Synthesis and Characterization of Hierarchical Structured Polyanionic Electrode Materials for Potassium-Ion-Batteries (PIBs)

Zur Erlangung des akademischen Grades eines

DOKTORS DER NATURWISSENSCHAFTEN

(Dr. rer. nat.)

von der KIT-Fakultät für Chemie und Biowissenschaften

des Karlsruher Instituts für Technologie (KIT)

genehmigte

DISSERTATION

Von

M.Sc. Andreas Heyn

1. Referent: Prof. Dr. Helmut Ehrenberg
2. Referent: Prof. Dr. Christine Kranz

Tag der mündlichen Prüfung: 09.12.2025

Affidavit

I hereby confirm that this thesis is the result of my own work. All sources and / or materials applied and used in and for this thesis are listed and quoted. The statutes for Good Research Practice of the KIT have been respected and followed.

Furthermore, I confirm that this thesis has not yet been submitted as part of another examination process neither in identical nor in similar form.

Karlsruhe, 04.11.2025

Kurzfassung

Im Rahmen dieser Dissertation werden sowohl die Synthese, als auch die Mikrostruktur und elektrochemische Performanz verschiedener hierarchisch strukturierter polyanionischer Elektrodenmaterialien für Kalium-Ionen-Batterien (PIBs) untersucht. Die Kombination von Sprühtrocknung und Festkörpersynthese erzeugte mikrometergroße, offenporige Granulate basierend auf nanokristallinen Primärpartikeln. Die erzeugten hierarchischen Kompositstrukturen ermöglichten eine optimierte elektrochemische Nutzung der Materialien durch eine Verbesserung der elektronischen Leitfähigkeit und Reaktionskinetik.

In Kapitel 6 wurden Kalium-Vanadium-Phosphat-Komposite ($K_3V_2(PO_4)_3$/C → KVP/C, $KVOPO_4$/C → KVPO/C) als Hochvolt-Kathodenmaterialien untersucht. Die systematische Variation von Kohlenstoffquellengehalt und Sintertemperatur führte zu einer verbesserten Zyklierbarkeit und erhöhten Leitfähigkeit durch die optimierten Mikrostrukturen für einen moderaten Kohlenstoffquellengehalt und eine Sinterung bei 750 °C – 800 °C der KVP/C Komposite. Die Anpassung des Syntheseprozess für KVPO/C-Komposite führte zu einer Verbesserung der elektrochemischen Performanz um 30 % bzw. 24 % hinsichtlich Kapazität respektive Energiedichte gegenüber der Literatur.

Kapitel 7 beschreibt die Entwicklung von Kalium-Titanium-Phosphat-Kompositen ($KTi_2(PO_4)_3$/C → KTP/C, $KTiOPO_4$/C → KTPO/C) als Referenz- und Diagnostikelektroden. Die Ti-basierten Komposite zeigen ein stabiles Redoxverhalten im Bereich 1.0 V – 1.6 V *vs.* K^+/K und weisen im Fall des KTP/C eine geringe Selbstentladung, sowie niedrige Polarisation von nur 50 mV bei C/20 für KTPO/C auf. Ihr Einsatz ermöglicht präzisere elektrochemische Charakterisierungen ohne die störenden, parasitären Nebeneffekte durch metallisches Kalium als Gegenelektroden in Halbzellen. Durch die Nutzung von KTP/C als Referenzelektrode konnte der große störende Einfluss auf die elektrochemische Charakterisierung in konventionellen Halbzellsetups nachgewiesen werden, wodurch die elektrochemische Performanz von KVP/C und KVPO/C unterschätzt wurde.

Kapitel 8 untersucht den Übergang von Halbzell- zu Vollzellsetups unter Verwendung der KTPO/C Diagnostikelektrode. Die resultierenden Vollzellen zeigten eine verbesserte Entladekapazität und C-Raten-Performanz bis C/2 sowie eine erhöhte Stabilität über mehrere Zyklen basierend auf einem minimierten Spannungsoffset gegenüber der Halbzellen.

Zusammenfassend wurde gezeigt, dass die hierarchische Mikrostrukturierung von Aktivmaterialien und die Nutzung stabiler Referenzelektrodensysteme entscheidend zur Verbesserung der elektrochemischen Performanz und präzisen und verlässlichen Charakterisierung von polyanionischen Aktivmaterialien in PIBs beitragen kann.

Abstract

In this thesis the synthesis, microstructure and electrochemical performance of hierarchically structured polyanionic electrode materials for potassium-ion-batteries was investigated. The spray-drying-assisted solid-state process led to micrometer sized, open-porous composite granules composed of nanocrystalline primary particles. The hierarchical architectures enabled an optimized electrochemical performance based on improved electronic conductivity and reaction kinetics.

In Chapter 6 two potassium–vanadium–phosphate composites (KVP/C, KVPO/C) as high-voltage cathodic materials were investigated. The systematic variation of the carbon source content and sintering temperature resulted in improved electrochemical performance based on a stable microstructure and improved conductivity for a moderate carbon source content and sintering at 750 °C – 800 °C. An adapted synthesis process for KVPO/C composites improved the capacity by 30 % respectively energy density by 24 % compared to previously reported literature.

In Chapter 7 potassium–titanium–phosphate composites (KTP/C, KTPO/C) were investigated as reference and diagnostic electrodes. The synthesized materials show a stable redox behavior in the range of 1.0 V – 1.6 V *vs.* K^+/K, while KTP/C showing low self-discharge and KTPO/C demonstrating low polarization of only 50 mV at C/20 in a conventional half-cell. The use of KTP/C and KTPO/C allows precise electrochemical characterizations without parasitic effects arising from the metallic potassium in half-cell configurations. By the use of a KTP/C reference electrode it was shown, that fluctuating potentials and large polarization of the potassium metal lead to an underestimation of the true electrochemical performance of KVP/C and KVPO/C composites in conventional half-cell setups.

In Chapter 8, the transition from half-cell to full-cell characterizations using the KTPO/C diagnostic electrode was investigated. The use of a precycled KTPO/C diagnostic electrodes instead of potassium metal counter electrodes significantly reduced the voltage offsets. The resulting full cells revealed an improved discharge capacity, enhanced rate capability up to C/2, and increased cycling stability for the KVP/C composites.

Overall, the results demonstrate that hierarchical structuring of polyanionic electrode materials combined with the use of stable reference sytems are inevitable for improving performance and enabling a reliable, accurate electrochemical characterization of polyanionic electrode materials in potassium-ion batteries (PIBs).

Table of Content

I. List of Figures

II. List of Tables

III. List of Appendix

IV. List of Abbreviations

LIB	Lithium-Ion-Battery
SIB	Sodium-Ion-Battery
PIB	Potassium-Ion-Battery
KVP	Potassium-Vanadium-Phosphate $K_3V_2(PO_4)_3$
KVPO	Potassium-Vanadyl-Phosphate $KVOPO_4$
KTP	Potassium-Titanium-Phosphate $KTi_2(PO_4)_3$
KTPO	Potassium-Titanyl-Phosphate $KTiOPO_4$
XRD	X-Ray Diffraction
DSC	Differential Scanning Calorimetry
TGA	Thermal Gravimetric Analysis
XPS	X-Ray Photoelectron-Spectroscopy
FT-IR	Fourier-Transformed Infrared-Spectroscopy
BET	Brunnauer-Emmet-Teller Method
ICP-OES	Inductive Coupled Plasma – Optical Emmision-Spectroscopy
SEM	Scanning Electron Microscopy
EDX	Energy Dispersive X-Ray Spectroscopy
I_{Obs}	Intensity Experimental Curve
I_{Calc}	Intensity Calculated Curve
Diff.	Difference Curve
NMP	N-Methyl-2-Pyrolidon
PVDF	Polyvinylidene fluoride
PEG	Polyethylene glycol

PAA	Polyacrylic acid
CEI	Cathode-Electrolyte-Interface
SEI	Solid-Electrolyte-Interface
FEC	Fluoroethylene carbonate
EC	Ethylene carbonate
PC	Propylene carbonate
PBA	Prussian-Blue-Analogue
NMC	Lithium-Nickel-Manganese-Cobalt-Oxide
LFP	Lithium-Iron-Phosphate $LiFePO_4$
RE	Reference Electrode
DE	Diagnostic Electrode
CE	Counter Electrode
DMC	Dimetyhl carbonate
DEC	Diethyl carbonate
KPF_6	Potassium-Hexafluorophosphate
KFSI	Potassium Bis(fluorosulfonyl)imide
KTFSI	Potassium Bis(Trifluoromethylsulfonyl)imide
K2-EDTA	Dipotassium ethylenediaminetetraacetic acid
MOF	Metal-Organic-Framework
LTMO	Layered Transition Metal Oxide

V. Acknowledgment

This thesis was created during my time as a research associate at the Institute of Applied Materials – Energy Storage Systems (IAM - ESS) and contributes to the work within the POLiS Cluster of Excellence funded by the German Research Foundation (DFG) under the Projec ID 390874152 (POLiS Cluster of Excellence, EXC 2154). Without the positive environment and contribution of all colleagues at the institute and the excellence cluster, this work would not have been possible.

Especially I want to thank Prof. Dr. Helmut Ehrenberg for the possibility to write this thesis at the IAM - ESS, his support through the last 3.5 years within the TAC and for taking over the examination.

Prof. Dr. Christine Kranz I want to thank for her support in the TAC and taking over the examination as well.

I want to sincerely thank Dr. Joachim Binder and Dr. Fabian Jeschull, the group leaders of my two research groups at the IAM-ESS. Both gave me the freedom to explore the research topics that I found valuable and I was able to profit from the expertise of both, to grow as a researcher and expert in the PIB field.

I am also very grateful to all my office colleagues in building 717, Ruochen Xu, Xuebin Wu, Marius Schmidt and Marcel Häringer for their support, motivation and help through the years.

Additionally, I want to thank a lot of people personally:

- Dr. Rob Armstrong and his research group at St. Andrews University to explore new synthesis methods and more sustainable materials for PIBs during my research stay in beautiful Scotland.
- Dr. Holger Geßwein for his support and expertise for all XRD analysis during the last years.
- Dr. Valeriu Mereacre for countless SEM images, his support in the lab and the great working atmosphere.
- Nicole Bohn for her support in solid-state synthesis and the application of the spray-drying method.
- Monika Raab for all the countless structural characterizations of my samples.
- Dr. Iurii Panasenko for his inevitable support in the lab during my first clumsy approaches to build PIB half-cells and the 3-electrode characterizations.

- Celine Röder for her work as a Master Student to find a suitable electrolyte for our PIB system and her continuous support in the lab and research through the last years.
- Joshua Psille and Tabea Sostmann for their contribution to this thesis as students in our research group.
- Dr. Thomas Bergfeldt for the ICP-OES analysis at the IAM-AWP.
- Dr. Martin Velazquez-Rizo and Dr. Ali Ahmadian from the INT for their approaches to find a structural solution for our KVP phase in several TEM sessions.
- All other colleagues from building 575 and 441 for the great and productive work atmosphere with countless discussions and funny moments to remember.

Finally, I want to thank my parents and my girlfriend for their unwavering support and encouragement to pursue a doctoral degree. Without their help, motivation and unconditional support through my whole life, my studies and all of my time as a PhD student, this work would not have been possible.

"Before I'm pushing up daisies,
Give me a long heady summer,
With arms open wide!"
Sam Fender

1 Introduction

An important marking point in the evolution of the battery technology was the successful development of LIBs by Goodenough, Whittingham and Yoshino, that has been awarded with the nobel prize in Chemistry 2019.[1-3] The Royal Swedish Academy of Sciences claimed in their press release: "This lightweight, rechargeable and powerful battery is now used in everything from mobile phones to laptops and electric vehicles. It can also store significant amounts of energy from solar and wind power, making possible a fossil fuel-free society."[4]

The biggest global challenge, human made climate change, and the following reduction of greenhouse gases opens new applications to LIBs beside small electronic devices. For storage and buffering of fluctuating renewable energies, large scale stationary storage systems are necessary.[5] To de-carbonize the on-road transportation and reduce the greenhouse emissions in the transportation sector, the electrification of vehicles is inevitable as well.[6] For these large-scale battery storage safety and costs play an important role, beside the overall performance of the LIBs.[7,8]

As LIBs are predicted to have a market share of more than 90% in the future[9] and lithium and cobalt resources for the state-of-the-art cathode materials (LFP and NMC)[7,10,11] are critical, prices for LIBs are predicted to increase dramatically in the next years.[9,12] Even as LFP does not rely on any critical elements like cobalt or nickel for NMC, the availability of lithium minerals will become critical by the increasing demands for large scale energy storage.[9,13,14] As a solution to overcome this shortage of resources and dramatic price changes, two options are possible. One option is the recycling of used battery cells and recovery of all elements used inside the cell. But recycling is just at the beginning of its development and starts with delay to battery production caused by the lifetime of the cells.[15,16]

The second and more practical solution is the development of post-lithium battery technologies, which rely on a more abundant mineral base compared to LIBs. Sodium and potassium are two other elements, which can be used as an alternative monovalent ion battery technology to complement LIBs.[17] Potassium and sodium are around three orders of magnitude more abundant in the earth crust compared to lithium, what would overcome the shortage of mineral resources.[18] Combined with their even distribution around the globe, what would prevent geopolitical restrictions, it will result in lower costs for battery production.[19-21] Both technologies are similar to LIBs in their "rocking chair" working principle. But the major drawback and challenge for these alternative technologies will remain the reduced energy density compared to LIBs.[17]

As SIBs are already commercialized by CATL[22], PIBs are the latest addition to the monovalent ion portfolio and an emerging field of ongoing research. Some benefits for PIBs over LIBs are their possible fast-charging capability, high redox-potentials and the use of aluminum current collectors on both sides of the battery, as potassium does not form any alloys with aluminum. The major benefit of PIBs over SIBs is the reversible intercalation of potassium ions into graphite, which makes it a real "drop-in" technology to LIBs on large scale. Based on these facts the main research fronts for PIBs arise: Development of electrolytes compatible with graphite and suitable high-voltage cathodic materials.[21,23-28]

In this thesis two polyanionic high-voltage cathodic materials for PIBs, KVPO and KVP, were synthesized and characterized thoroughly. The materials are synthesized *via* a spray-drying assisted solid-state synthesis to create hierarchical structured carbon-composites with improved electrochemical performance.

For KVP/C the influence of carbon source content and sintering temperature onto the microstructure of the composites is studied. These finding were transferred and adjusted to all other synthesis processes with respect to the underlying chemical reactions.

To study fundamental electrochemical processes at the different cathode materials, novel reference (RE) and diagnostic (DE) electrodes were developed, based on hierarchically structured KTP/C or KTPO/C, in order to mitigate the detrimental impact of potassium metal as counter or reference electrode in half-cell setups.

2 Potassium-Ion-Batteries

2.1 Working Principle

The main components of a PIB are cathode and anode coated onto an aluminum current collector, separator and electrolyte. The separator is an insulating layer to separate the electrodes spatially and prevent a short-circuit of the cell.[29] There are different classes of separators like polymers (Celgard), ceramics and glass-fibres. On lab scale a glass-fibre separator, like Whatman GF/C, is the most common type used.[30] In this work only Whatman GF/C separators were used. **Figure 1** schematically shows the basic components of a PIB cell.

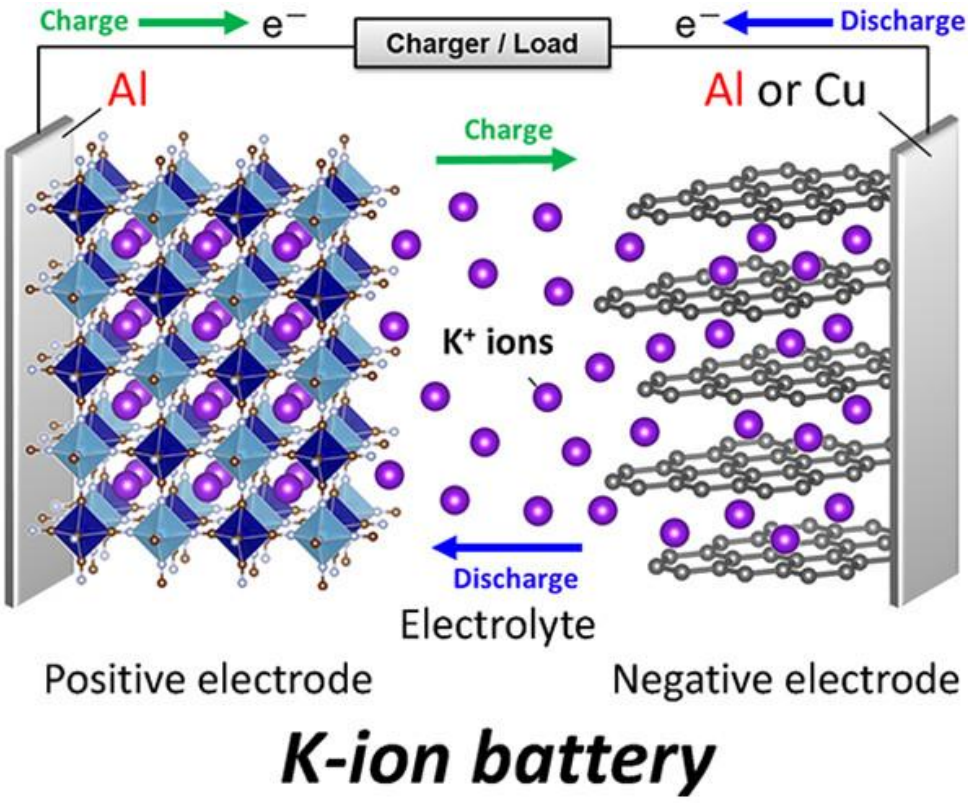

Figure 1: Schematically drawing of the basic components of a Potassium-Ion-Battery reproduced from Hosaka et al.[27], with permission from the American Chemical Society©.

The electrolyte allows ionic conduction between the two electrodes. At the electrolyte level, typically a potassium containing salt dissolved in different organic solvents is used. The most common solvent compositions are EC:DMC, EC:DEC or EC:PC. As conductive salts KPF_6 or others like KFSI, KTFSI, etc. are used.[31] To overcome issues associated with low Coulombic efficiencies caused by the formation of unstable SEI layers at the surface of the anode, highly concentrated organic electrolytes become a focus of research. But high viscosity, low conductivity, poor wettability and high costs limit their practical application in the future.[32] KPF_6 based electrolyte systems with small amount of additives will be the most promising

electrolyte composition for practical application of PIBs.[31] In addition, there are ever-increasing efforts in research into ionic liquids and solid-state electrolytes for improved safety and performance of PIBs.[32]

Anode and cathode materials are typically coated in similar way compared to LIBs and SIBs onto an aluminum current collector. The current collector allows the connection of the cell to an electric consumer.[29] At lab-scale the compositions of an electrode are typically 80% active material, 10% conductive additive (usually carbon C65) and 10% binder (usually PVDF).

The working principle for PIBs is similar to other monovalent ion batteries like LIBs and SIBs. It is based on the reversible de-/insertion of potassium ions into the cathodic and anodic active materials.[32,33] The definition of anodic and cathodic materials is based on the electrochemical standard potential of the materials. Usually materials with low potential are classified as anodic materials, while materials with high potential are called cathodic materials.[29]

During the charge process, potassium ions are deinserted from the cathode active material (oxidation), travel across the electrolyte and are inserted into the anode active material (reduction). As the charge process leads to an energetically unfavorable situation, a current needs to be applied to deliver the needed electrons for the redox-processes.

The discharge process follows the charge process *vice versa*. Potassium ions are deinserted from the anode active material (oxidation), travel across the electrolyte and are inserted into the cathode active material (reduction). As the discharge process leads to an energetically more favorable situation, the cell delivers a current/energy *via* the flowing electrons during discharge to power an electric device.

The simplified underlying electrochemical reaction scheme of a PIB with graphite as anodic material and polyanionic cathode material of the stochiometric formula $K_nM^{m+}XO_y$ (M= transition metal, XO_y= polyanionic group) for the charge process is shown below in **Equation 1 a-c**:

Equation 1: Simplified electrochemical reaction scheme during charge in the case of a) graphite as an anode, b) a polyanionic material as the cathode and c) the overall reaction.

a) Anode: $8\,C + K^+ + e^- \rightleftharpoons KC_8$

b) Cathode: $K_nM^{m^+}XO_y \rightleftharpoons K^+ + e^- + K_{n-1}M^{(m+1)^+}XO_y$

c) Overall: $8\,C + K_nM^{m^+}XO_y \rightleftharpoons KC_8 + K_{n-1}M^{(m+1)^+}XO_y$

2.2 Electrode Materials

Electrode materials for PIBs could be generally classified into anodic and cathodic materials based on their electrochemical potentials. The following chapter gives a brief overview about the most important anodic and cathodic materials for PIBs. As in this work the focus was laid onto hierarchical structured polyanionic materials, the polyanionic material class will be discussed more detailed compared to short overviews for the other material classes.

2.2.1 Anodic Materials

Anodic materials for PIBs could be divided into three different categories: alloying, intercalation and conversion type materials. As the focus of this work was on intercalation type polyanionic materials, only the two most relevant intercalation type material classes as an anodic material will be discussed in this chapter. A specific focus onto Ti-based polyanionic phosphates as an electrode material will be laid in Chapter 3.2.

2.2.1.1 Graphite

The intercalation of potassium ions into graphite is the main benefit of PIBs compared to SIBs as an alternative to LIBs. Graphite forms thermodynamically stable KC_8-graphite intercalation compounds (GIC) during reversible de-/intercalation of potassium-ions into the graphite sheets.[26] Intercalation of potassium ions occurs through a staging mechanism to the KC_8 close to 0.01 V, while the exact mechanisms are still under debate. The theoretical capacity of graphite in a PIB is 279 mAh g^{-1} with an average potassiation and depotassiation potential of 0.17 V and 0.27 V.[25] (**Figure 2**) The main issues associated with graphite as an anodic material for PIBs are the huge volume expansion of 61 % during cycling[25], leading to possible mechanical exfoliation[34], and the insufficient passivation by formation of a stable solid-

electrolyte-interface (SEI).[35] The formed SEI-layer is much more organic and thicker compared to LIBs, which leads to a higher dissolution tendency of the SEI-layer during cycling in organic electrolyte. As a consequence, the dissolution of parts of the SEI-layer leads to recurrent SEI formation reactions at the free graphite surfaces. This leads in fact to very low coulombic efficiencies (CE) and reduced cycling stability of graphite as an anode material.[36] The possible exfoliation caused by the huge volume expansion during intercalation, which leads to even more free graphite surfaces, could amplify these effects even more.[34]

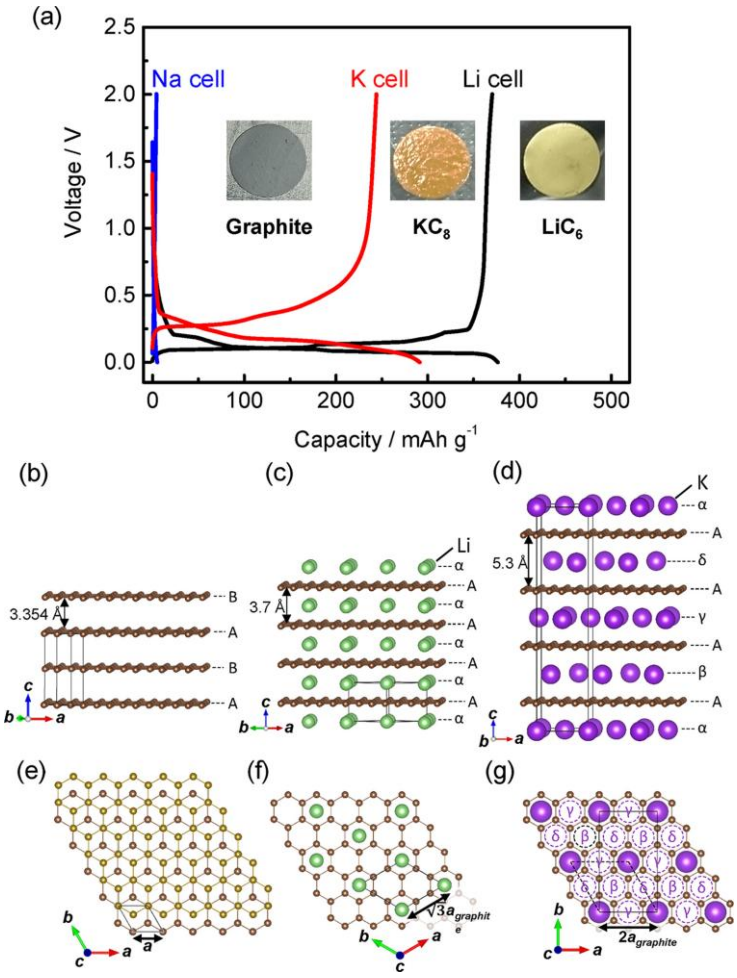

Figure 2: *(a) Typical charge–discharge curve of graphite in a Li-Ion cell with 1 M LiPF6/EC dimethyl carbonate (DMC; 1:1 v/v; black curve), Na-Ion cell with 1.0 M NaPF6/EC:DEC (1:1 v/v; blue curve), and K-Ion cell with 1 M KFSA/EC:DEC (1:1 v/v; red curve). Reproduced from Kubota et al.[37], with permission from The Chemical Society of Japan & Wiley-VCH©. Schematic illustrations of crystal structures of (b) graphite having a hexagonal lattice with the SG P63/mmc, (c) LiC6 having a hexagonal lattice with the SG P6/mmm, (d) KC8 having an orthorhombic lattice with the SG Fddd, and (e–g) their respective in-plane structures with alkali metal distribution. Reproduced from Hosaka et al.[27], with permission from American Chemical Society©.*

To address these issues, several strategies could be applied to improve the electrochemical characteristics of graphite for PIBs. Surface engineered graphite with introduced defects and a following coating with soft-carbon leads to an improved cycling stability. While the introduced defects increase the reversible capacity and C-rate capability of the graphite, the soft-carbon

coating leads to an even more increased capacity and cycling stability. The soft-carbon coating is able to alleviate the induced stress better during intercalation, leading to a reduced damage after the expansion of the graphite during potassium ion intercalation.[38] Other options to tune the electrochemical characteristics are structural modifications like the synthesis of expanded graphite[39] or to use hetero-atom doping strategies, which could modify ionic mobility and electronic conductivity.[40,41]

2.2.1.2 Ti-based Materials

As carbonaceous materials often suffer from structural degradation caused by huge volume changes during cycling, different Ti-based materials are a promising alternative to overcome these issues.[42] For LIBs and SIBs the application of several Ti-based candidates as anodic materials was shown successfully several times.[43,44] Typically, Ti-based materials show low electrochemical potentials around 1.0 V caused by the low redox-transition of the active Ti-metal site, which is in the electrolyte stability window of commonly used organic electrolytes. This leads to reduced irreversible losses caused by SEI formation, which is typically not required at potentials above 1.0 V.[45,46] Combined with the great structural and thermal stability of Ti-based materials, this makes them a well-suited candidate for the use as an anodic material with improved cycling stability and C-rate capability for PIBs.[42] Among Ti-based materials several different material classes have been studied for their application as an anode active material in PIBs. The most promising material classes are Titanates and several polyanionic compounds.[47]

Among the titanates, for example the layered $K_2Ti_4O_9$ shows a promising initial capacity of 97 mAh g^{-1} at 30 mA g^{-1}. But the de-/insertion of the big potassium ions (Li^+ 0.76 Å < Na^+ 1.02 Å < K^+ 1.38 Å[37]) results in poor cycling stability.[48] To overcome these issues, several modifications like nanostructuring can be applied. The synthesis of MXene derived nanoribbons leads to an improved electrochemical performance (151 mAh g^{-1} at 50 mA g^{-1}) and superior cycling stability for 900 cycles.[49] Another layered titanate, $K_2Ti_8O_{17}$, shows a suitable interlayer spacing and open channels for a fast potassium ion transport. Similar to the layered $K_2Ti_4O_9$, synthesized nanorods of $K_2Ti_8O_{17}$ showed improved potassium storage with an initial capacity of 182 mAh g^{-1} at 20 mA g^{-1} and good rate capability. But the cycling stability remains critical as only 110 mAh g^{-1} remain after 50 cycles at 20 mA g^{-1}.[50]

The most promising material class in terms of cycling stability among the Ti-based anode active materials are the polyanionic materials. Based on their unique crystal structure they offer great thermal and structural stability to allow reversible cycling.[51,52] A more detailed introduction

into the most prominent polyanionic phosphates and the two in this work synthesized potassium-titanium / titanyl-phosphates, KTP and KTPO, will be given in chapter 3.2.

2.2.2 Cathodic Materials

At the cathodic site of the potassium ion cell several different material classes were explored as possible active materials. The main cathodic materials could be categorized into 3 different groups: layered transition metal oxides, PBAs and polyanionic materials. **Figure 3** shows representative material characteristics including the pro and cons of the different material classes for PIBs. From a practical perspective an ideal cathodic material should: 1) have a high redox potential, 2) rely on highly abundant and low cost raw materials, 3) be easily synthesizable and storable, 4) have a high capacity, 5) allow a highly reversible potassium ion intercalation due to a robust structure and minimal volume variations, 6) have a good electronical and ionic conductivity for improved C-rate capability and 7) have a high tap and material density leading to higher volumetric energy densities.[53]

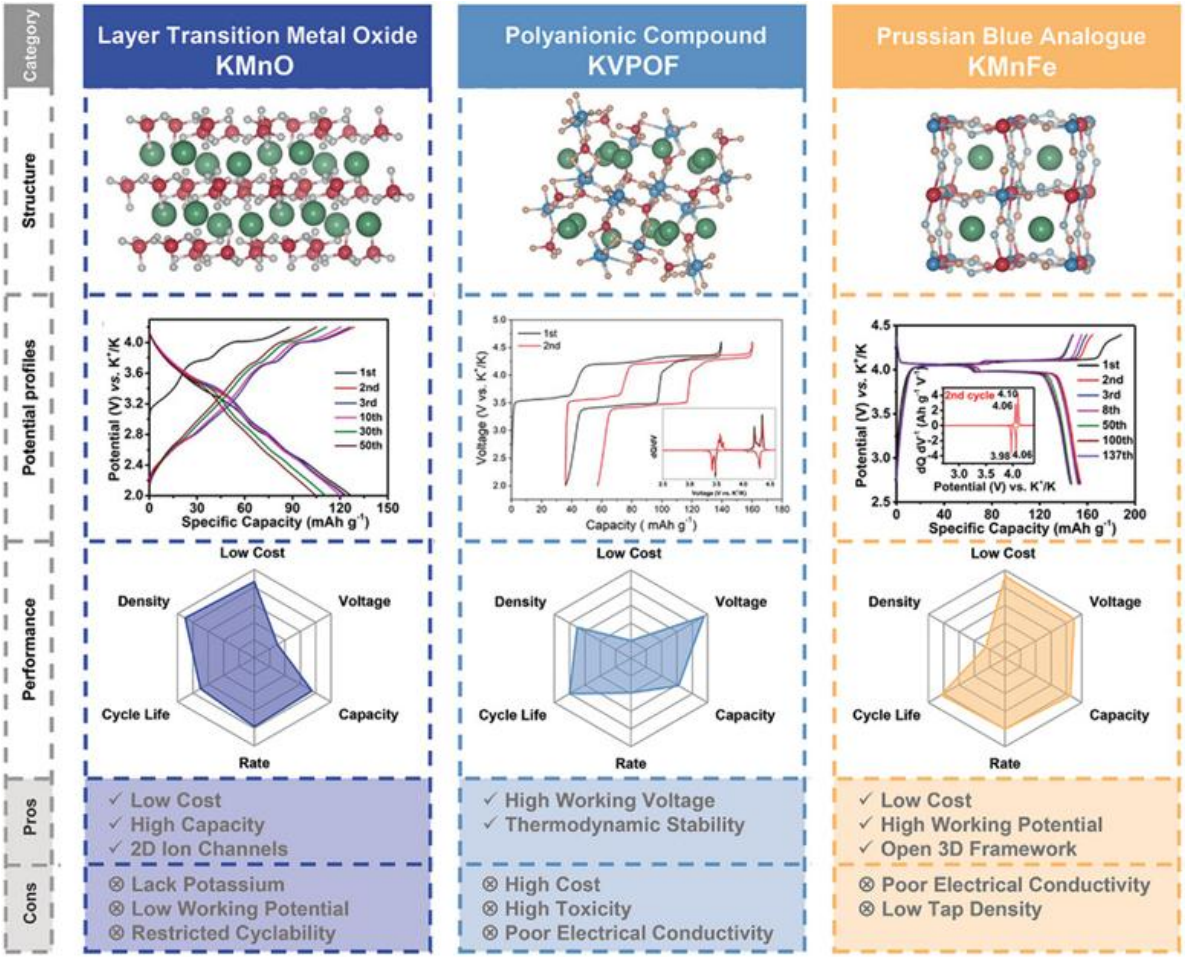

Figure 3: Representative Cathodic Materials of each material class together with its potential profile, performance assessment, pros and cons: LTMO, Polyanionic Material, PBA adapted from Wang et al.[53], with permission from Wiley VCH©.

In the following chapter the three most important material classes will be introduced, while a focus was set onto polyanionic materials. In this work four different polyanionic materials were synthesized, as these material class delivers the best trade-off of tunable high redox potential with great cyclability based on their wide range of structural composition and 3D crystal structure.

2.2.2.1 Layered Transition Metal Oxides (LTMO)

The search for suitable LTMOs was inspired by the successful application in the field of SIBs and LIBs, where LTMOs proved already their very good electrochemical performance.[28] LTMOs could be categorized into three different types based on their unique crystal structure P2, P3 and O3. P and O represent the coordination of the alkali metal ion either in prismatic or octahedral coordination, while 2 or 3 represents the number of Transition Metal Oxide layers in each unit cell.[54] Compared to Na^+ and Li^+, the insertion of large K^+ leads to significant structural instabilities in the O3 (octahedral) phases at higher K^+-content based on strong K^+-K^+ repulsion. This leads to a tendency of preferred crystallization in a prismatic coordination (P2 or P3) of the LTMOs for PIBs.[55] But as a positive consequence this strong K^+-K^+ repulsion can play a role in suppressing phase transitions as it makes transition metal migration less favorable compared to Li^+ and Na^+ analogues.[56] This results in more open pathways for K^+ diffusion for the P-type structures compared to O-type LTMOs, which could enhance ionic conductivity.[28] Similar to their sodium and lithium analogues, the main challenges associated with the LTMOs for PIBs are: 1) Jahn-Teller distortion for Mn-based LTMOs leading to structural deterioration and poor cycle life, 2) multiple phase transitions caused by the large ionic radius of K^+ leading ultimately to an increased layer gliding of adjacent oxygen layers, 3) intrinsically potassium deficiency and 4) air instability.[57]

Vaalma *et al.* was one of the first to show that birnessite type $K_{0.3}MnO_2$ achieved a reversible capacity of 70 mAh g^{-1} at a current density of 27.9 mA g^{-1} in a voltage window of 1.5 V – 3.5 V. The capacity faded to 40 mAh g^{-1} after 600 cycles. Nevertheless, a higher cut-off voltage of 4.0 V or even higher leads to a layer gliding mechanism of adjacent oxygen layers induced by high repulsion at lower potassium contents. As the layer gliding is accompanied with large volume changes, this process is partially irreversible leading to a fast capacity fading.[58] Additionally, the sloped voltage profile with average voltages often below 3.0 V limits the energy density of a practical PIB.[53]

Inspired by this first report many other LTMOs have been studied as a cathode material for PIBs, while the main research focus was on Mn-based LTMOs because of their cheap and

highly abundant raw materials. For example, Zhang *et al.* studied the impact of Co-doping onto structure and electrochemical performance of $K_{0.3}MnO_2$. The 5% Co-doping suppressed the Jahn-Teller-distortion usually induced by Mn^{3+}, which is leading usually to structural deterioration, resulting in an enhanced K^+ diffusion rate and rate performance of the cell. The Co-doped LTMO showed a capacity of 99 mAh g^{-1} at 22 mA g^{-1} compared to 77 mAh g^{-1} for $K_{0.3}MnO_2$, while the doped sample showed a 92% higher capacity at a high C-rate of 440 mA g^{-1}. Nevertheless, the CO-doping induced additional phase transitions and larger volume changes, leading ultimately to a faster capacity fade compared to $K_{0.3}MnO_2$.[59]

The success of the state-of-the-art cathode material NMC for LIBs, inspired researchers to study the substitution of Mn by Ni as well.[60-62] Bai *et al.* studied different Ni-content in $K_{0.67}Mn_{1-y}Ni_yO_2$, while P3-type $K_{0.67}Mn_{0.83}Ni_{0.17}O_2$ showed the best electrochemical performance with 122 mAh g^{-1} at 20 mA g^{-1}. This appropriate Ni-amount successfully suppressed the Jahn-Teller effect leading to reduced structural deterioration, improved C-rate capability due to more migration pathways for K^+ and extended cycle life of the cathode material.[62] Additionally studies on ternary metal oxides and beyond[63-65] or on more abundant substituting elements like Fe[66] were performed to address several of the issues associated with LTMOs for PIBs.

2.2.2.2 Prussian Blue Analogues

PBAs belong to the wide family of Metal-Organic-Frameworks (MOFs) and are widely studied as cathodic materials in the field of SIBs and PIBs. Their chemical formula is: $A_xM[M'(CN)_6]_{1-y}\cdot Vac_y\cdot n\ H_2O$ (M/M' = n-coordinated transition metal, Vac. = $M(CN)_6$ vacancy, A = alkali metal Na / K) and they offer an 3D-open framework with large interstitial sites, which allows reversible accommodation of K^+ with small volume changes.[67]

In 2004 Eftekhari *et al.* reported the use of PBA as a cathodic material for PIBs for the first time. They developed a first prototype of a PIB cell and used a PBA film as a cathode, which showed promising electrochemical performance with just 12% capacity fade after 500 cycles.[68] Due to their low cost and highly abundant raw materials, the most common studied PBAs as cathodic materials are Fe- or Mn-based like $K_2Mn[Fe(CN)_6]$ or $K_2Fe[Fe(CN)_6]$.[53] In particular $K_2Mn[Fe(CN)_6]$ showed a high reversible capacity of 141 mAh g^{-1}, which is close to the theoretical capacity of 156 mAh g^{-1}, and an average voltage up to 3.8 V with promising C-rate performance and cyclability.[69] Additionally the voltage step between the two intercalation plateaus in the voltage profile is smaller for $K_2Mn[Fe(CN)_6]$ compared to $K_2Fe[Fe(CN)_6]$, while the Mn-Fe-PBA tends to contain less interstitial water and $Fe(CN)_6$-vacancies as well.[70]

Beside the low density and intrinsically low electronic conductivity, one of the biggest issues associated with PBA's are the presence of interstitial water and $Fe(CN)_6$-vacancies. The role of these vacancies and its influence onto the electrochemical performance is still not completely understood and a focus of several studies.[71] To address these issues several studies have investigated the influence of different synthesis process parameters onto crystallinity and particle size of the material. For example, Fiore *et al.* studied 28 different compositions of Mn-Fe-PBA's by high-throughput synthesis to optimize the material in terms of defect content and particle size.[72] The addition of potassium citrate during the co-precipitation process could directly regulate the particle size and vacancy / interstitial water content. High amounts of added potassium citrate lead to an increasing particle size and reduced vacancy content of below 5 %. While smaller particle showed an increased maximum discharge capacity, the cycling stability of bigger particles with reduced vacancy and interstitial water content was much improved with 87% capacity remaining after 100 cycles in a half-cell setup. They propose that the potassium insertion gets kinetically limited at increasing particle size due to low ionic and electronic conductivity.[72] Hosaka *et al.* reports similar results regarding the influence of particle size onto electrochemical performance. But they could improve the electrochemical performance in terms of capacity and C-rate capability of bigger particles by the controlled introduction of $Fe(CN)_6$-vacancies. They propose that these vacancies lead to an enhancement of K^+ diffusion, which overcomes kinetically limitations and improves the electrochemical performance of bigger particles drastically.[71]

To address the common problem of Mn-dissolution in Mn-based PBAs, Ge *et al.* used a chelating agent assisted co-precipitation synthesis combined with a modified electrolyte by the addition of $Fe(CF_3SO_3)_3$ for their $K_2Mn[Fe(CN)_6]$.[73] The chelating agent leads to a low $Fe(CN)_6$-vacancy content, while the addition of the iron salt to the pure electrolyte leads to an in-situ Fe substitution into the Mn-vacancies caused by Mn-dissolution during repeated cycling. The results lead to a significantly improved cycling stability over several thousand cycles with low capacity fading and a high discharge capacity of 160 mAh g^{-1} at 300 mA g^{-1}.[73] The Low electronic conductivity could be addressed by compositing the PBAs with highly conductive additives like carbon based materials.[74,75]

2.2.2.3 Polyanionic Materials

Similar to PBAs, polyanionic materials offer an open and very stable 3D-framework, which makes them an interesting material class for cathodic materials for PIBs. The general formula of this material class is $K_yM_z(XO_4)_n$ with X = S, P, C, Si, Mo, while M = transition metal like

V, Mn, Ti, etc. Polyanionic materials generally consist of a series of tetrahedron anion units $(XO_4)^{n-}$ in which strong covalent linkages exist to adjacent M-O_x polyhedral.[52] The strong inductive effect of the anion group elevates the redox potential of this material class as the covalent M-O bond gets weakened by the strong electron withdrawing effect of the anion unit. The introduction of other electron withdrawing groups like F^- or O^{2-} elevates the redox potential even further. By use of this effect the redox potential becomes tunable by varying the structure and composition for a given transition metal.[76] The 3D-open framework structure of the polyanionic materials could provide large interstitial spaces for fast alkali ion diffusion.[77-79] As the oxygen atoms have strong covalent bonds inside the $(XO_4)^{n-}$anion units, polyanionic materials show a higher thermal stability, which make them more applicable in terms of safety for large scale battery production.[52] Usually polyanionic materials lack in electronic conductivity caused by their unique structure. To overcome this issue several approaches could be applied like microstructuring, carbon coating or doping with other elements.[52,80,81]

The polyanionic materials, which have been considered and explored as a cathodic material for PIBs so far, could be categorized into five different groups: sulfates (e.g., $KFeSO_4F$)[82], phosphates (e.g., $K_3V(PO_4)_2$)[83], pyrophosphates (e.g. KVP_2O_7)[84,85], fluoro-derivatives (e.g. $KTiPO_4F$)[86] and oxalates (e.g., $K_2Fe(C_2O_4)_2$)[85,87]. Typical synthesis processes are hydro/solvothermal methods or solid-state reactions, which make polyanionic materials applicable for large scale production.[52,78]

For PIBs mostly V-based materials were studied due to their multivalent oxidation states (+III - +V) and high working potential. Among more abundant Fe-containing materials only Fe-based sulfates and oxalates, as well as derivatives of these compounds with fluorine as additional anion have shown promising electrochemical performance. For example, Dong *et al.* synthesized $KFe(SO_4)F$ *via* a solvothermal method. Through a subsequent compositing with graphite by calcination the $KFe(SO_4)F$-composite showed a promising average voltage of 3.55 V and reversible capacity of 111.5 mAh g^{-1} at C/20 (1C = 128 mA g^{-1}).[82] Another promising Fe-based material, $K_2Fe(C_2O_4)_2$ could be synthesized *via* hydrothermal methods as well.[85,87] In a study by Wu *et al.* the iron oxalate showed a promising capacity of 78 mAh g^{-1} at C/5 (1C = 86 mA g^{-1}).[85] But as many other polyanionic materials $K_2Fe(C_2O_4)_2$ showed low electronic conductivity and needed to be ball-milled to reduce the particle size and composited with carbon additives to increase the electronic conductivity.[87]

Vanadium-based materials usually are studied as polyanionic phosphates or their fluoro-derivatives. As in this work several different phosphates were synthesized, a special focus onto two promising potassium-vanadium-phosphates is set in the next chapter.

3 Phosphate-based polyanionic electrode materials

Phosphate-based polyanionic electrode materials are well known from the successful exploration and application of NVP, LFP, etc. The polyanionic phosphates consist of the anionic PO_4^{3-} group, which strong inductive effect leads to high redox potentials of the materials.[78] In the research area of phosphate-based polyanionic materials for PIBs only Ti, V and Fe were studied as transition metals. As for the Fe-containing polyanionic phosphates only amorphous $FePO_4$ showed electrochemical activity and all other compositions were electrochemically inactive or have to be synthesized *via* electrochemical ion-exchange (which makes them unsuitable for large-scale application), research focused mainly on V-based polyanionic phosphates for cathodic materials.[88,89] Besides the V-based materials several Ti-based polyanionic phosphates have been studied as well, but mainly for their use as a possible anodic material due to the lower redox potential of Ti-based materials. **(Figure 4)**

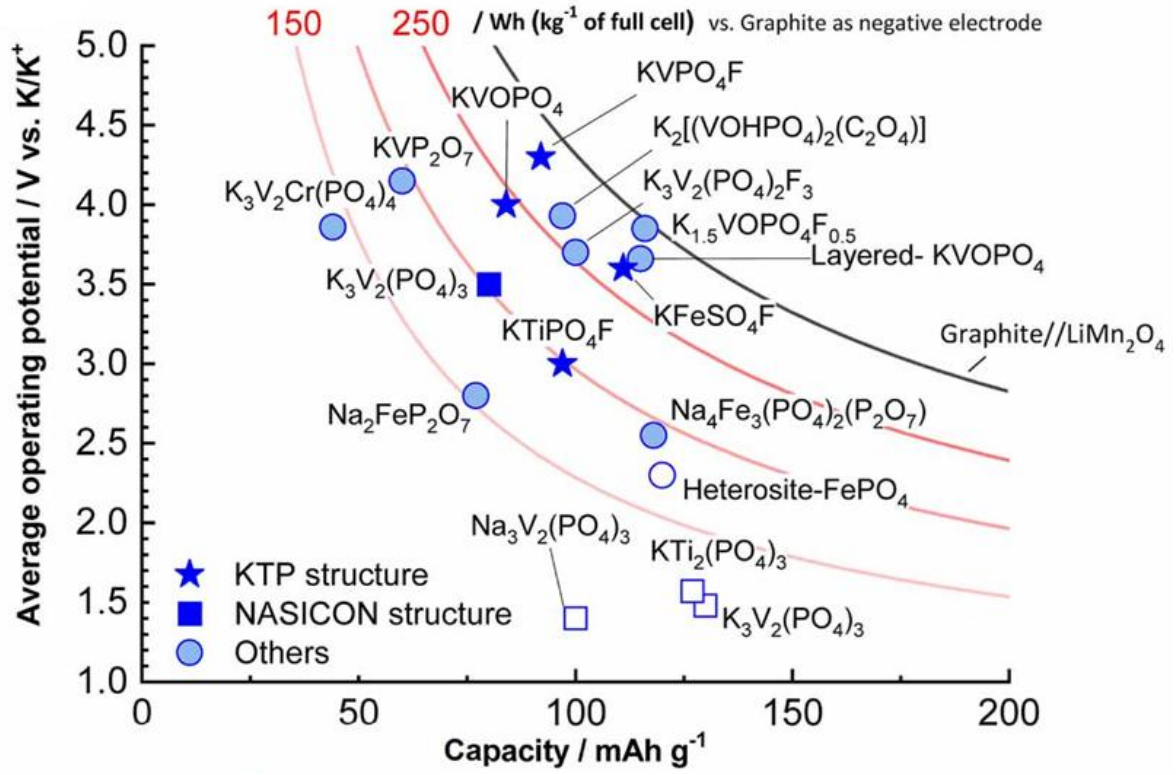

Figure 4: Average working potential versus gravimetric capacity for selected polyanionic materials as cathodic materials in PIB half-cell setups. The energy densities of the full cells were calculated assuming graphite as the anode material against the cathode materials. Open and filled plots represent K^+ insertion / extraction and extraction / insertion performance respectively, adapted from Xu et al©.[28]

3.1 Potassium-Vanadium-Phosphates

Several different V-based phosphatic materials have been explored as cathodic materials for PIBs.[84,90-94] For example, Park *et al.* performed a computational material screening with specific criteria for plausible electrode materials for PIBs through the inorganic compound structure

database (ICSD). Among the selected materials only KVP_2O_7 showed a promising electrochemical activity with a very high average voltage of around 4.2 V, but only a maximum discharge capacity of 60 mAh g^{-1}. This is caused by irreversible phase transition if more than 0.6 K^+ per formula are in- / deinserted.[84]

The most extensively studied material in literature is $KVPO_4F$.[92,95-101] This material possesses a high theoretical capacity of up to 131 mAh g^{-1} and working potential above 4.0 V. For example, Kim *et al.* achieved a high reversible capacity of 105 mAh g^{-1} with an average voltage of 4.3 V.[95] $KVPO_4F$ belongs to the KTPO type-structure, while its open 3D-structure and large channels for K^+ diffusion are beneficial for the C-rate capability of the material.[92,102]

As fluorinated derivatives are usually hard to prepare and need more safety precautions during synthesis and handling[102], in this work the isostructural compound KVPO was synthesized and studied. Beside KVPO and based on the successful application of NVP in SIBs[103], the stochiometric analogue to NVP $K_3V_2(PO_4)_3$ (KVP) was prepared and studied in this work. Those two compounds will be discussed in the following chapters more detailed.

3.1.1 KVP

Nanowires of KVP/C were first tested as cathodic materials for SIBs by Wang *et al.* in 2015. They delivered a reversible capacity of 119 mAh g^{-1} and retained 99% of capacity after 2000 cycles. As the collected XRD pattern in this study did not match any known structure in the ICSD, the crystal structure remained unclear at this time.[104] Zhang *et al.* proposed the crystal structure to be similar to NVP in the NASICON structure with the symmetry $R\bar{3}c$ based on in-situ synchrotron XRD analysis. But important data for an unambiguous structural analysis like atomic positions are missing in their study.[105] Jenkins *et al.* proposed that $K_3V_2(PO_4)_3$ is in fact a mixture of two different other potassium-vanadium-phosphates: $K_3V_3(PO_4)_4{\cdot}H_2O$ and $K_3V(PO_4)_2$. They propose an orthorhombic *Pnna* symmetry for their novel composition $K_3V_3(PO_4)_4{\cdot}H_2O$.[106] Today the crystal structure of KVP is still an open research question and remains a critical point in the optimization and understanding of the underlying electrochemical reaction mechanisms of KVP as a cathodic material for PIBs.

Theoretically KVP delivers a high capacity of up to 106 mAh g^{-1} with an average potential of 3.5 V, which makes it a promising polyanionic cathode material for PIBs.[79,90] Similar to other polyanionic materials KVP lacks of electronic conductivity, which limits the electrochemical performance of the KVP cathode material.[90] To overcome these limitations similar approaches

as mentioned in chapter 2.2.2 can be applied, like nanosizing, carbon compositing or transition / alkali metal substitution.

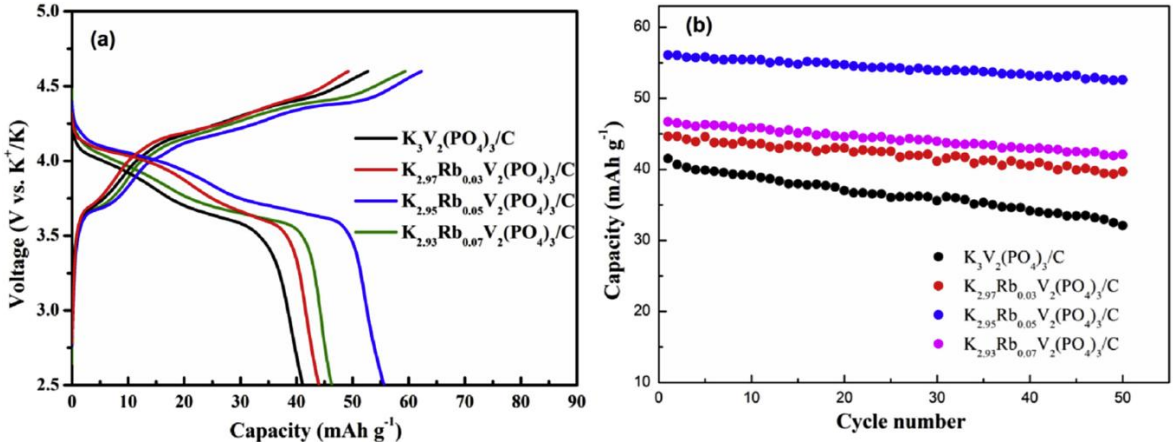

Figure 5: *a) Initial potential profile of with different amounts of Rb^+ doped KVP/C composites synthesized via a sol-gel method, b) Cycling performance of different doped KVP/C composites. Cycling was performed in half-cell setup between 2.5 V- 4.6 V at 20 mA g^{-1}. Reproduced from Zheng et al.[107], with permission from Elsevier B.V.©.*

The combination of nanosizing and carbon compositing *via* freeze-drying and solid-state synthesis led to a reversible capacity of about 90 mAh g^{-1} in the potential window of 2.0 V – 4.0 V in a study by Zhang *et al.*.[105] A study by Kuai *et al.* revealed instead an improved electrochemical performance of KVP/C composites at calcination temperature of 800 °C compared to the bulk KVP. They suggest an improved microstructure of the composites leads to a decent electrochemical performance and a reversible capacity of 76 mAh g^{-1}.[108] Beside carbon compositing and nanosizing to improve the low electronic conductivity and electrochemical performance of KVP, Zheng *et al.* studied the partial substitution of K^+ with Rb^+. According to their results the doping with 5 % Rb^+ instead of K^+ could lead to an increased K^+ diffusion and an improved electrochemical performance compared to the KVP/C composite without Rb^+-doping (**Figure 5**).[107] Nevertheless, a clear understanding of the macroscopic improvement by Rb^+-doping was not possible, as the crystal structure of KVP is unclear and no statement about a possible enlargement of K^+-diffusion pathways, etc. inside the KVP lattice can be made.[107]

3.1.2 KVPO

A particular material family of polyanionic materials, namely the $KTiOPO_4$-type electrode materials, has been identified as being of significant interest for their potential application as cathodic materials for PIBs. This is due to their unique structural characteristics, which include a rigid 3D-polyhedral framework with open channels for K^+ in- / deinsertion.[102] KVPO crystalizes in the $Pna2_1$ symmetry.[109] The crystal structure is build up of vertex sharing VO_6

octahedra, which build helical chains along the b axis. These helical chains are corner linked by PO_4 tetrahedra. The helical chains are composed of two different VO_6 octahedra, namely $V_{cis}O_6$ and $V_{trans}O_6$ octahedra.[110] As Vanadium is in the valent oxidation state +IV in KVPO, it usually shows a distorted octahedral coordination caused by the highly covalent V^{+IV}=O (vanadyl-)-bond.[111] This distortion is underlined by results from Wernert *et al.*, which showed different vanadyl bond length for the V_{cis} and V_{trans} positions.[93,111]

The arrangements into the corner linked helical chains results in open channels along the a and b axis. The potassium ions are located in these channels.[109,112] Within the structure, two symmetrically non-equivalent potassium ion positions are located, with K1 being coordinated eight times and K2 nine times.[93] Based on DFT calculations by Lian *et al.* the extraction of potassium ions could be described in four stages. Stage (I) is described as a two-phase mechanism, while 0.5 K^+ are extracted from the K_2 and the other 0.5 K^+ are moving from the K_1 position to a new K_3 position, which is energetically more favorable. Stage (II) between the extraction of 0.5 and 0.625 K^+ could be described as a solid solution mechanism, while the remaining K^+ stay at the K_3 position. Between the extraction of 0.625 and 0.75 K^+ the remaining K^+ at the K_3 position move back to the K_2, why stage (III) could be described as a two-phase mechanism as well. The extraction up to 1.0 K^+ in stage (IV) is described as a solid solution mechanism again, while all K^+ at the K_2 position are extracted. The complete extraction of the K^+ leads just to a 6.6% volume change for KVPO following the DFT calculations in this study.[110]

Based on the open channels inside the crystal structure of KVPO improved diffusion kinetics for K^+ and with this improved C-rate capability as a cathodic material for PIBs are expected.[92,110] Combined with the high average voltage (≥4.0 V) and the high theoretical capacity of 133 mAh g^{-1}, KVPO becomes one of the most attractive candidates as a polyanionic cathodic material for PIBs.[92,93]

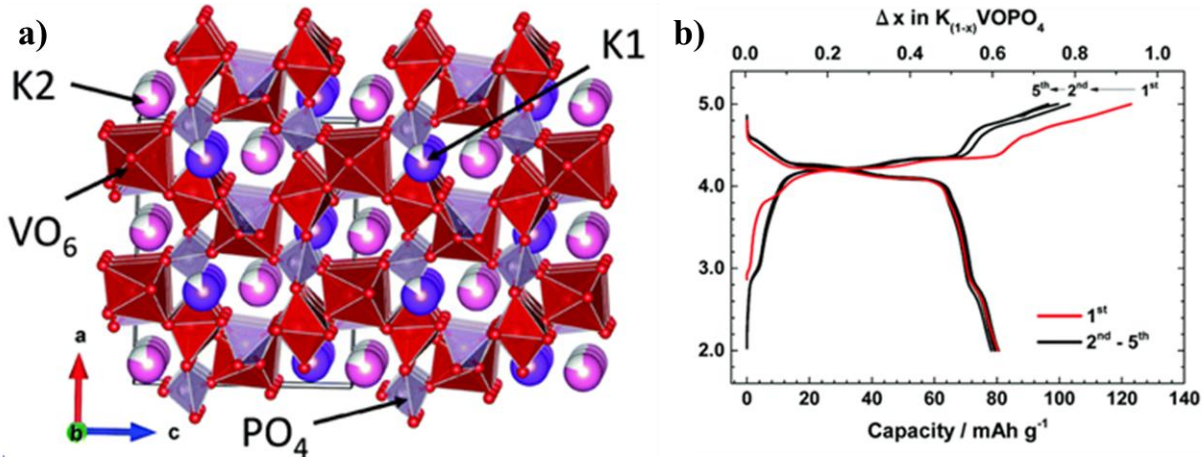

Figure 6: *a) Schematic representation of the crystal structure of KVPO along the b-axis, adapted from Chihara et al.[92], with permission from the Royal Society of Chemistry©, b) Voltage profile of KVPO/C at C/20 in a voltage window of 2.0-5.0 V in a PIB half-cell setup, adapted from Chihara et al. [92], with permission from the Royal Society of Chemistry©*

As the synthesis of compounds with vanadium in the valent oxidation state +IV is usually quite complicated[102], several different approaches like hydrothermal[113], solid state / carbothermal reduction[92,112,114] or comproportionation[93] reactions have been proposed. Chihara *et al.* studied the electrochemical performance of KVPO/C composited synthesized *via* a carbothermal reduction approach. Their KVPO/C composites achieved a reversible capacity of 84 mAh g^{-1} at an average working potential of 4.0 V (potential window 2.0 V – 5.0 V), which means 0.63 K^+ were reversibly extracted and inserted. During cycling a volume change of just 3.3 % was detected *via operando*-XRD analysis.[92] (**Figure 6**)

Wernert *et al.* used a comproportionation reaction for synthesis of pure KVPO particles. The synthesis procedure resulted in the formation of crystallites with a size of more than 1 µm. However, the KVPO exhibited a reversible capacity of only 65 mAh g^{-1} within the voltage range of 3.5 V - 5.0 V at C/20. They propose that a full extraction of K^+ would occur at voltages above 5.0 V, while their calculated average potential was already 4.35 V and much higher compared to the study of Chihara *et al.*.[93] Nevertheless, increasing the upper cut-off voltage above 5.0 V will lead to electrolyte stability issues and cause electrolyte decomposition.[92]

3.2 Potassium-Titanium-Phosphates

As already discussed in chapter 2.2.1.2 Ti-based polyanionic materials show low average voltages around 1.0 V and stable cycling performance due to the unique crystal structures of polyanionic compounds. This makes them suitable candidates for their use as anodic materials in PIBs. In the following chapters KTP and KTPO will be discussed detailed in regard to their application in PIBs.

3.2.1 KTP

With its high theoretical capacity of 128 mAh g^{-1} and relatively low average voltage around 1.6 V KTP seems a promising candidate as an anodic material for PIBs.[115] KTP crystalizes in the NASICON structure with the symmetry $R\bar{3}c$, which shows open channels for ionic migration and relatively fast ion diffusion like for other NASICON structures.[116] Nevertheless, KTP suffers from low electronic conductivity like other polyanionic compounds as well. A few approaches to overcome these limitations were reported in literature. Han *et al.* synthesized nanocubic KTP particles *via* a hydrothermal synthesis route. They combined their synthesis with a subsequent carbon coating *via* sintering and explored KTP as a possible anodic material for PIBs for the first time. In their study they proposed KTP to have a favorable host structure for K^+ in- / deinsertion and the applied carbon coating was an easy way to improve the electronic conductivity.[117]

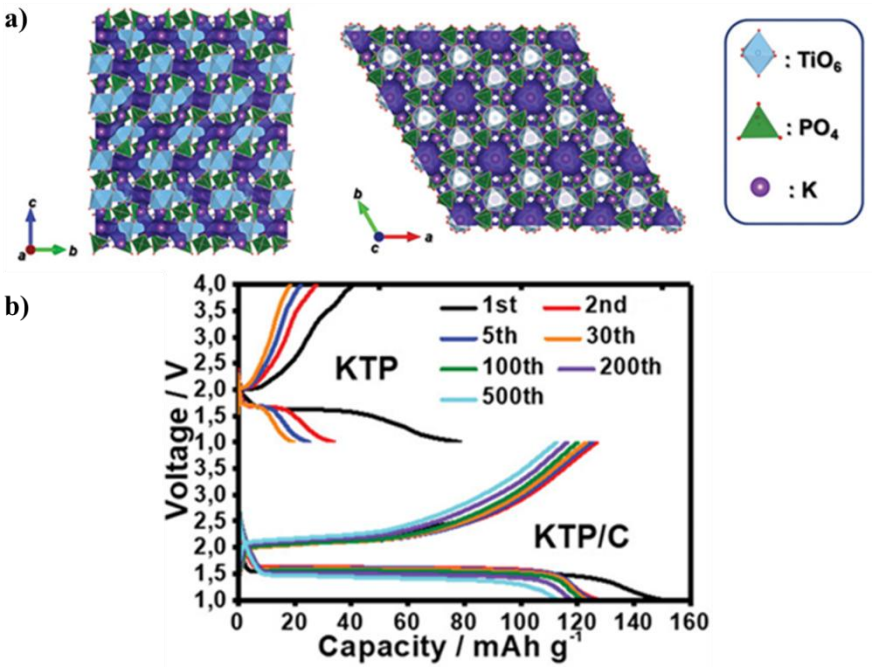

Figure 7: *a) Crystal structures of KTP with vacant sites for K^+ along bc-plane (left) and ab-plane (right) predicted through BVEL analyses, adapted from Voronina et al.[115] b) Potential profile of KTP and KTP/C in PIB half-cells at C/10, adapted from Voronina et al.[115], with permission from Wiley-VCH©.*

Instead Voronina *et al.* synthesized KTP/C-composites by terms of a classical solid-state reaction. Their KTP/C showed a prolonged voltage plateau at 1.69 V compared to uncoated KTP, which is a clear indication for the improved kinetics (**Figure 7**). They proposed an untypical biphasic redox process during discharge, while a single-phase reaction followed by a biphasic reaction was visible during charge in *operando*-XRD measurements. Upon intercalation of 2 K^+ just 11.7 % volume expansion were predicted.[115] Recently Dong *et al.* combined the synthesis of porous nanosized KTP particles with compositing by N-doped carbon coating. The composites achieved a reversible capacity of 98.9 mAh g^{-1} at C/2, while 93% capacity retention was achieved after 150 cycles at 1C in PIB half-cells. They propose that the porous structure and interconnected N-doped carbon network leads to enhanced ion diffusion and electronic conuctivity.[118]

3.2.2 KTPO

KTPO is known as a non-linear optics material and is an isostructural analogue to KVPO. It crystalizes in the same space group *Pna2₁*. Similar to KVPO the by PO_4 tetraeder corner linked TiO_6 octahedra build helical chains to build a rigid 3D-open framework. In the spacious cavities or channels along the a- and b-axis the K^+ are located.[119] Zhang *et al.* synthesized KTPO/C composites *via* a classical solid-state approach and evaluated it for the first time as an anodic material in PIBs. Their composites delivered a reversible capacity of just 102 mAh g^{-1}

(theoretical capacity 135 mAh g^{-1}) at an average voltage of 0.82 V. Due to a quasi 3D-lattice expansion just 9.5 % volume change and only a small strain onto the lattice were detected during cycling. As their material showed a small voltage hysteresis, they studied the K^+ diffusion kinetics more detailed. According to their study KTPO offers an about 10 times faster ionic diffusion compared to NASICON structured KTP caused by the unique crystal structure of the KTPO.[120] Kumar *et al.* synthesized KTPO/rGo composites *via* a solid-state reaction. In an optimized electrolyte their composites delivered a reversible capacity of 129 mAh g^{-1} at 0.075C, while without compositing with carbon barely any electrochemical activity was visible (**Figure** 8). *Operando*-XRD revealed highly reversible two-phase reactions for KTPO/rGO composites along seven different phases in a voltage window of 0.1 V - 2.5 V.[121]

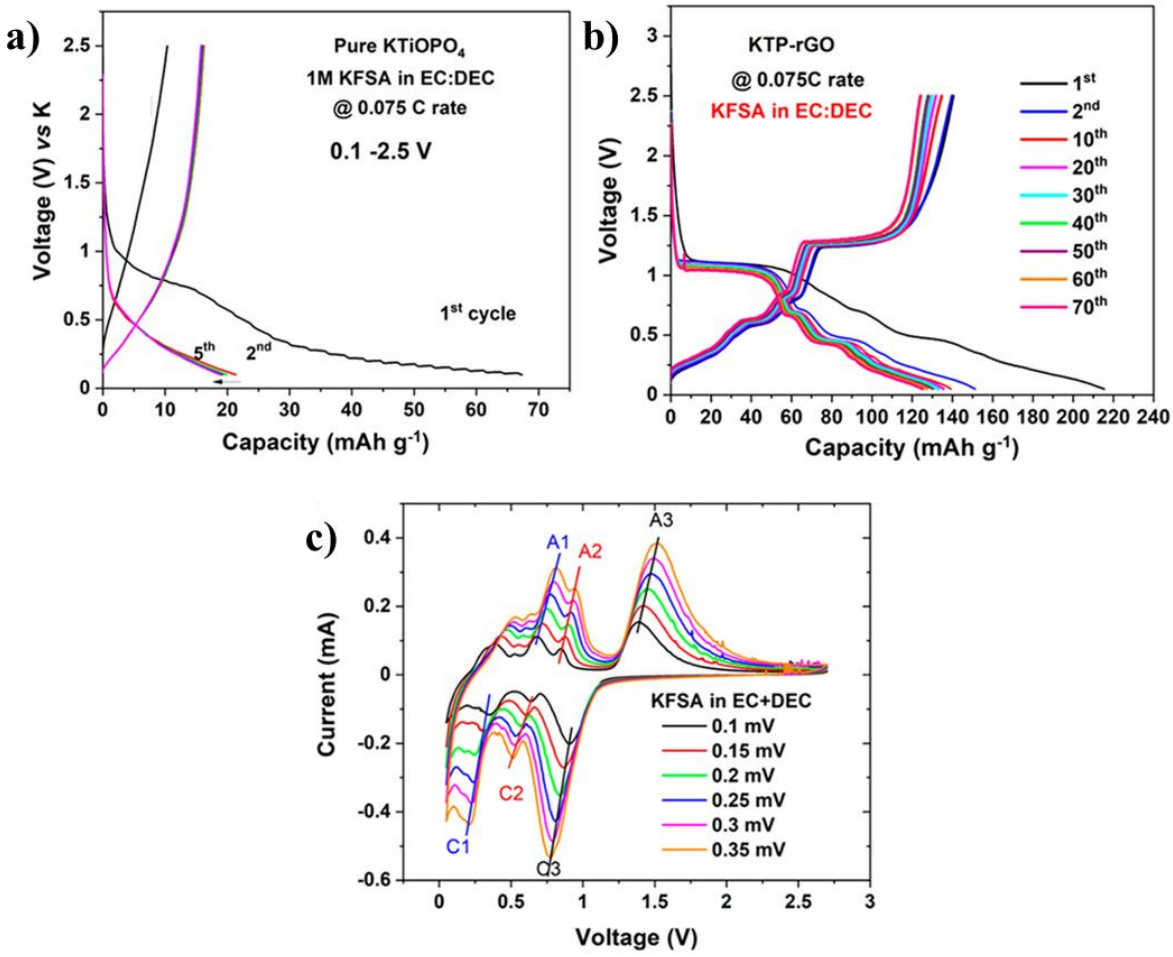

Figure 8: *Potential profile of a) pure KTPO and b) KTPO/rGO composites in a PIB half-cell with an optimized electrolyte at 0.075C, adapted from Kumar et al.[121] c) CV scan of KTPO/rGO composites at different scan rates in PIB half cells indicating the high reversibility of the underlying redox processes. Adapted from Kumar et al©.[121]*

As the Ti-O covalence is weaker compared to the O-P covalence, the inductive effect leads to a lowering of the potential, which could increase the possible full-cell voltage but still prevents severe dendrite formation.[76,120] Combined with the fast reaction kinetics and high reversible capacities, KTPO/C composites is a promising candidate for anodic materials in PIBs.

4 Spray Drying for the Design of Hierarchical Structured Electrode Materials

As demonstrated by numerous studies, the electrochemical performance of a cell is significantly influenced by the particle size and morphology of electrode materials.[122,123] To illustrate, nanosized particles offer numerous advantages, including a reduction in the diffusion length within the bulk particle and an enhancement in the mechanical stability of the particles, thereby facilitating better accommodation of volume changes.[124] Conversely, the large-scale processing of these nanoparticles into electrodes could result in a number of challenges, like particle agglomeration, low tap density or increased parasitic side reactions.[125] In order to overcome the processing issues referenced above and still benefiting from nanosized particle properties, the utilization of hierarchical structured materials could provide a viable solution.

In material science, hierarchical structures are described as the arrangement of smaller particles, often nanosized, into larger secondary particles / granules. This process could result in the formation of open porous structures.[126] Spray drying represents an ideal process, that is easily scalable for the creation of hierarchical structures for a variety of purposes like pharmaceutical industry or the development of novel cathodic materials for post-lithium energy storage.[124,127,128]

Basically, spray drying is described in three steps: 1) atomization to increase the reactive / specific surface as a liquid dispersion / solution is fed into an atomizer, 2) droplet-to-particle conversion as the heated flow of a carrier gas evaporates the solvent completely and solid particles remain, 3) particle collection of completely dried solid particles.[129] To tune particle characteristics adjustments to the gas properties (temperature, flow rate, type of gas), feed properties, solid concentration in the dispersion or spray properties (droplet size) can be made. *Via* spray drying a variety of different particle compositions like inorganic-organic, single component, multi-component, core-shell or hollow particles could be created.[130]

For example, an optimized spray-drying process in presence of a β-lactose improved the electrochemical performance of NVP/C composites after sintering due to a beneficial microstructure with open porosities up to 52% and pore sizes of just 76 nm.[103] As discussed above, the use of nanosized primary particles has the potential to overcome the limitations of solid-state diffusion. Additionally, larger secondary granules, created by spray-drying, could improve the electronic conductivity. This could be attributed to one or two factors: improved intra- and interparticle connections or / and *in-situ* carbon coatings achieved by subsequent thermal treatments.[103,131] In summary, the creation of secondary granules with open

nanoporosity by spray drying is beneficial for the electrochemical performance of electrode materials. Again, this could be attributed to several factors: shortening of diffusion length, improved electrolyte penetration, improved mechanical stability of the particles during cycling due to better accommodation of the volume expansion and homogenous carbon coating onto the surface of the particles.

The combination of these benefits, in conjunction with the well-known scalability of the spray-drying process itself and the enhanced processability of the resulting granules, results in the utilization of the spray-drying process in the synthesis process of all the different electrode materials for PIBs investigated in this thesis. In the following chapter all relevant experimental setups and synthesis processes will be discussed.

5 Materials and Methods

5.1 Synthesis Strategy to design Hierarchical Structured Electrode Materials

The basic principle for the synthesis of all hierarchical structured electrode materials was similar. All materials were synthesized according to the synthesis procedure previously published as part of this thesis (Heyn *et al.*[132]). Based on the underlying chemical reaction minor modifications were made to the synthesis process of each electrode material.

In **Figure 9** the synthesis process for hierarchical structured electrode materials, in this case for KVP/C, is schematically visualized.

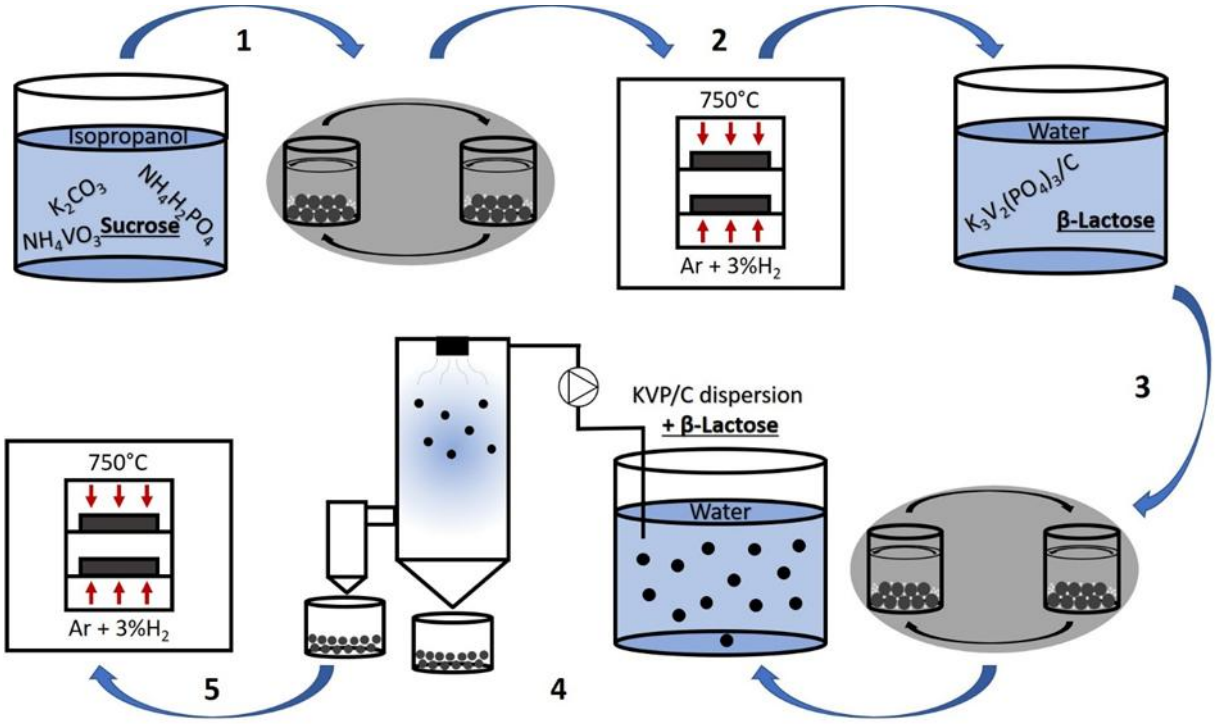

Figure 9: Schematic drawing of the synthesis process of hierarchically structured KVP/C-composites with: 1) Mixing of reactants by planetary ball-milling in isopropanol with subsequent drying, 2) Calcination under Ar + 3 % H_2-atmosphere in a chamber oven at 750 °C, 3) Mixing and grinding of KVP/C with β-lactose in water by planetary ball-milling, 4) Spray-drying of the KVP/C dispersion in water with β-lactose, 5) Sintering of hierarchical structured secondary KVP/C particles under Ar + 3 % H_2-atmosphere in a chamber oven at 750 °C, reproduced from Heyn et al.©.[132]

The fundamental principle of synthesizing the various electrode materials remained consistent, and the process can be summarized as follows:

1 mixing step, either by ball-milling or mortar mill, of the reactants / precursors
2 calcination under specific atmosphere at given temperature and time for synthesis of the desired compound

3 ball-milling step with β-lactose in deionized water to reduce primary particle size to nanoscale
4 spray-drying of a dispersion of primary active material particles in water with a defined solid content of 8 – 10 wt. %, PEG and PAA were added with 1 wt. % as dispersing agent and binder additive respectively
5 thermal treatment under specific atmosphere at given temperature and time to mechanically stabilize the secondary granules and form an *in-situ* carbon coating on the particles surface.

5.1.1 KVP/C

The synthesis process of KVP/C followed the same two-step solid state synthesis process previously published as part of this thesis (Heyn *et al.*).[132]

As reactants K_2CO_3 (VWR, Germany), NH_4VO_3 (Thermo Scientific, USA) and $NH_4H_2PO_4$ (VWR, Germany), as well as sucrose (Sigma-Aldrich, USA) and β-lactose (Sigma-Aldrich, USA) as carbon sources were used. First the reactants K_2CO_3, NH_4VO_3 and $NH_4H_2PO_4$ were thoroughly mixed in the stochiometric ratio of 3:4:6 together with different weight percentages of sucrose (5 / 7.5 / 10 wt. %) by ball-milling in 2-Propanol in a planetary ball-mill for 8 h (alternating 1 h milling and 1 h break). 300 g ZrO_2 balls with a diameter of 3 mm were used for milling, while the reactants were dispersed and milled in 2-Propanol. The ratio of reactants:milling balls:2-Propanol was about 1:3:2.3. Afterwards the 2-Propanol was evaporated and the mixture of reactants dried over night at 80 °C.

The calcination of the materials was performed under reducing Ar + 3 % H_2-atmosphere in a retort oven. The heating rate was 1 K min^{-1} till 450 °C, where the temperature was held for 2 h. Afterwards the heating rate was increased to 3 K min^{-1} until 750 °C for the calcination of 5 h at this temperature for synthesis of KVP/C composites *via* a carbothermal reduction. The samples were naturally cooled down to room temperature afterwards. KVP/C composites were obtained as a fine black powder.

Subsequently the samples were prepared for the spray-drying process to create hierarchical microstructures. Therefore, different amounts of β-lactose (5 / 15 wt. %) were added to the composites and the samples were ball-milled in a planetary ball-mill with deionized water as dispersion media. Milling time was 12 h in total (2 x 6 h milling with 3 h break) at 250 rpm, while 300 g deionized water were used per 50 g of KVP/C and β-lactose mixture. 300 g ZrO_2 balls with a diameter of 3 mm were used for milling. For the following spray-drying process

the solid content was adjusted to 8-10 wt.% and 1 wt.% of PEG and PAA, as dispersing agent and binder additive were added. The inlet temperature was 210 °C, the outlet temperature 112 °C, as a process gas nitrogen was used. The samples were spray-dried with 30.000 - 35.000 rpm of the atomizer. The tower and cyclone fraction were combined and then subjected to a further heat treatment in a retort oven under reducing Ar + 3 % H_2-atmosphere. The heating rate was 5 K min^{-1} till 750 °C, where the temperature was held for 5 h. Afterwards the samples were cooled naturally to room temperature, sieved and stored in an exsiccator under vacuum.[132]

To investigate the influence of different sintering temperatures on the microstructure and electrochemical performance, the KVP/C sample with the best electrochemical performance (KVP/C-2) was chosen. The sintering temperature was varied between 650 °C – 850 °C with steps of 50 °C in between.

In **Table 1** the composition for each KVP/C sample is summarized. The exact amounts of the used reactants, etc. are summarized in **Appendix 1**.

Table 1: Composition of all different synthesized and evaluated KVP/C samples with respect to their different carbon source contents, sintering temperature and nomenclature.

Sample	Calcination Temperature / °C	Sucrose / wt.%	Sintering Temperature / °C	β-Lactose / wt.%
KVP/C-1	750	5	750	5
KVP/C-2	750	7.5	750	5
KVP/C-3	750	10	750	5
KVP/C-4	750	5	750	15
KVP/C-5	750	7.5	750	15
KVP/C-6	750	10	750	15
KVP/C-2_650	750	7.5	650	5
KVP/C-2_700	750	7.5	700	5
KVP/C-2_750	750	7.5	750	5
KVP/C-2_800	750	7.5	800	5
KVP/C-2_850	750	7.5	850	5

5.1.2 KVPO/C

The synthesis of phase pure KVPO followed the proposed comproportionation reaction scheme by Wernert *et al.* based on the two precursors VPO_4 (+III) and $VOPO_4$ (+V)[93], and was further optimized within the framework of a deepening thesis project (Tabea Sostmann, 2025).[133]

The VPO_4 precursor was prepared by planetary ball-milling stochiometric amounts of the reactants NH_4VO_3 and $NH_4H_2PO_4$ (1:1) in 2-Propanol for 8 h in total (alternating 1 h milling and 1 h break). For ball-milling 300 g ZrO_2 balls with a diameter of 3 mm were used. The ratio of reactants:milling balls:2-Propanol was set to about 1:4:3. Subsequently the 2-Propanol was evaporated and the mixture of reactants dried over night at 80 °C.

The calcination of VPO_4 was performed under reducing Ar + 3 % H_2-atmosphere in a retort oven. The heating rate was 1 K min^{-1} till 400 °C, where the temperature was held for 2 h. Afterwards the heating rate was increased to 3 K min^{-1} until 800 °C for the calcination of 10 h at this temperature. The samples were naturally cooled down to room temperature afterwards. VPO_4 was obtained as a gray powder.

The $VOPO_4$ precursor was prepared by dry mixing stochiometric amounts of the reactants NH_4VO_3 and $NH_4H_2PO_4$ (1:1) in a mortar mill for 10 minutes. The calcination of the precursor was performed under synthetic air (80 % O_2 / 20 % N_2) in a retort oven. The heating rate was 1 K min^{-1} till 450 °C, where the temperature was held for 2 h. Afterwards the heating rate was increased to 3 K min^{-1} until 750 °C for the calcination of 5 h at this temperature for synthesis of $VOPO_4$. The samples were naturally cooled down to room temperature afterwards. $VOPO_4$ was obtained as yellow powder.

The desired $KVOPO_4$ compound was prepared by dry mixing stochiometric amounts of VPO_4, $VOPO_4$ and K_2CO_3 (2:2:1) in a mortar mill for 10 minutes. Subsequently the powder was calcined in a retort oven under inert Ar-atmosphere. The heating rate was 5 K min^{-1} till 750 °C, while this temperature was held for 6 h. The samples were naturally cooled down to room temperature afterwards. $KVOPO_4$ was obtained as a brown powder.

The preparation for the spray drying process and the spray dryings itself, were performed completely analogue to chapter 5.1.1, except just 5 wt.% of β-lactose were added as a carbon source for the KVPO/C composites. The sintering process was performed in a retort oven under Ar-atmosphere, while the sintering temperature and sintering duration were varied. KVPO/C samples were sieved with 32 µm sieve and stored under ambient conditions after completion of the sintering process.

The nomenclature and sintering parameters are summarized in **Table 2**. The exact masses of the reactants, etc. are summarized in **Appendix 2**.

Table 2: Nomenclature and Sintering parameters for all evaluated KVPO/C compounds.

Sample	Sintering Temperature / °C	Sintering Duration / h
KVPO/C-500°C_1h	500	1
KVPO/C-500°C_5h	500	5
KVPO/C-650°C_1h	650	1
KVPO/C-650°C_5h	650	5
KVPO/C-750°C_1h	750	1

5.1.3 KTP/C

The synthesis of the KTP/C composites followed the two-step solid state synthesis process of the KVP/C composites, except only for spray drying and subsequent sintering β-Lactose as a carbon source was added for the KTP/C composites. The discussed hierarchical structured KTP/C composites were optimized in the framework of a master thesis project (Joshua A. Psille, 2025)[134].

For synthesis of the phase pure KTP stochiometric amounts of TiO_2 (Degussa / Evonik, Germany) and $NH_4H_2PO_4$ were used, while for K_2CO_3 10 wt. % excess was used (4:6:1 + 10 wt. %).[134] The reactants were thoroughly homogenized by planetary ball-milling at 250 rpm in 2-Propanol for 8 h in total (alternating 1 h milling and 1 h break). 300 g ZrO_2 ball with a diameter of 3 mm were used for milling, while the reactants were dispersed and milled in 2-Propanol. The ratio of reactants:milling balls:2-Propanol was about 1:4:3.5. Afterwards the 2-Propanol was evaporated and the precursor dried over night at 80 °C.

The calcination of the pure KTP was performed under synthetic air (80 % O_2 / 20 % N_2) in a retort oven. The heating rate was 1 K min^{-1} till 400 °C, where the temperature was held for 2 h. Afterwards the heating rate was increased to 3 K min^{-1} until 850 °C for the calcination of 5 h at this temperature. The samples were naturally cooled down to room temperature afterwards. KTP was obtained as a white powder.

Subsequently the samples were prepared for the spray-drying process to create hierarchical microstructures. Therefore, 12.5 wt. % of β-lactose were added to the pure KTP and the samples were ball-milled in a planetary ball-mill with deionized water as dispersion media. Milling time was 12 h in total (2 x 6 h milling and 3 h break) at 250 rpm, while 300 g deionized water were used per 50 g of KTP and β-lactose mixture. 300 g ZrO_2 balls with a diameter of 3 mm were used for milling. For the following spray-drying process the solid content was adjusted to 8 - 10 wt. % and 1 wt. % of PEG and PAA, as dispersing agent and binder additive, were added.

The inlet temperature was 210 °C, the outlet temperature 112 °C, as a process gas nitrogen was used. The samples were spray-dried with 30.000 - 35.000 rpm of the atomizer. The tower and cyclone fraction were combined and then subjected to a further heat treatment in a retort oven under inert Ar-atmosphere. The heating rate was 5 K min^{-1} till 700 °C, where the temperature was held for 5 h. Afterwards the samples were cooled naturally to room temperature, sieved with a 32 µm sieve and stored under ambient conditions. The exact masses of the reactants, etc. are summarized in **Appendix 3**.

5.1.4 KTPO/C

The synthesis process for the KTPO/C composites was analogue to the two-step solid state approach used for the KVP/C samples.

For preparation of KTPO/C composites stochiometric amounts of the reactants K_2CO_3, TiO_2 and $NH_4H_2PO_4$ (1:2:2) together with 7.5 wt. % sucrose were thoroughly mixed by planetary ball milling in 2-Propanol for 8 h (alternating 1 h milling and 1 h break) at 250 rpm. The ratio of reactants:milling balls:2-Propanol was set to about 1:3:2.5. Afterwards the 2-Propanol was evaporated and the precursor dried over night at 80 °C.

The calcination of the materials was performed under inert Ar-atmosphere in a retort oven. The heating rate was 1 K min^{-1} till 450 °C, where the temperature was held for 2 h. Afterwards the heating rate was increased to 3 K min^{-1} until 850 °C for the calcination of 12 h at this temperature for synthesis of KTPO/C composites. The samples were naturally cooled down to room temperature afterwards. KTPO/C composites were obtained as a fine black powder.

Subsequently the samples were prepared for the spray-drying process to create hierarchical microstructures. Therefore, 15 wt. % of β-lactose were added to the composites and the samples were ball-milled in a planetary ball-mill with deionized water as dispersion media. Milling time was 12 h in total (2 x 6 h milling with 3 h break) at 250 rpm, while 300 g deionized water were used per 50 g of KTPO/C and β-lactose mixture. 300 g ZrO_2 balls with a diameter of 3 mm were used for milling. For the following spray-drying process the solid content was adjusted to 8-10 wt. % and 1 wt. % of PEG and PAA, as dispersing agent and binder additive, were added. The inlet temperature was 210 °C, the outlet temperature 112 °C, as a process gas nitrogen was used. The samples were spray-dried with 30.000 - 35.000 rpm of the atomizer. The tower and cyclone fraction were combined and then subjected to a further heat treatment in a retort oven under inert Ar-atmosphere. The heating rate was 5 K min^{-1} till 850 °C, where the temperature was held for 5 h. Afterwards the samples were cooled naturally to room temperature, sieved

with a 32 µm sieve and stored under ambient conditions. The exact masses of the reactants, etc. are summarized in **Appendix 4**.

5.2 Electrochemical Characterization

5.2.1 Electrode Coating

For preparation of the working electrodes the different active material samples were first dried at 120 °C under vacuum in an BUCHI-oven. Subsequently the active material samples were mixed in a Speedmixer at 2000 rpm for at least 10 minutes with a premixed slurry containing PVDF, C65 and NMP in a ratio of active material:C65:PVDF of 80:10:10. The well-mixed and homogenous slurry was then casted onto Al-foil with a wet-film thickness of 200 µm by a doctor blade. The electrode sheets were cut into 12 mm (half-cell setup), 14 mm (anodes full-cell setup) or 16 mm with 8 mm hole in the middle (3-electrode setup, working electrode) disks and dried at 120 °C under vacuum in an BUCHI-oven. The specific mass loadings of the electrodes of all shown electrochemical characterizations are summarized in **Appendix 5**.

5.2.2 Half-Cell-Setup vs. K^+/K

Coin-cells of type 2032 in a half-cell setup were assembled in Ar-filled gloveboxes (H_2O & O_2 < 0.1 ppm). As the working electrode, the different active material samples were used, while potassium metal was used as the anode. The potassium metal was cut into small pieces, washed thoroughly in and stored over n-Hexane inside the glovebox. For preparation of the potassium metal anodes, the potassium metal was rolled and squeezed into thin sheets inside a nitrile glove. After that, 14 mm disk electrodes were punched out of the thin potassium metal sheets to use them as the anode.

As an electrolyte a solution of 0.5 M KPF_6 in EC:PC (1:1 by volume) was used. The electrolyte volume was set to 150 µl.

As a separator two Whatman GF/C-separators with a diameter of 16.5 mm were used. Separators were pre-dried in a BUCHI-Oven at 120 °C under vacuum for 12 h.

Galvanostatic charging (CCCV) with a CV step were performed at a Biologic BCS, VMP or VSP. The voltage range depends on the active material and is summarized in **Table 3**. The CV step was performed at the lower and upper cut-off voltages respectively. The cut-off current for the CV step was defined as half of the applied current in the CC step. 1C corresponded to the current density equal to the theoretical capacity of the respective active material (see **Table 3**). CCCV measurements were performed at the following C-rates: C/20, C/10, C/5, C/2, 1C for 10

cycles at each C-rate. All stated capacities are referred to the active material-carbon composite mass and not the bare active material content. For KTP/C and KTPO/C cycling starts always with discharge, as they are used as anodic materials. For KVP/C and KVPO/C cycling starts with charge as they are used as cathodic materials.

For the *operando*-XRD measurements in a reflection setup the same coating process was used as described in chapter 5.2.1, only the wet-film thickness was increased to 250 µm and an Al-mesh instead of an Al-foil was used as a current collector to minimize the background of the current collector in the XRD pattern. The electrode size for the *operando*-XRD measurements was 14 mm for potassium metal and the respective working electrode, the separator size was set to 18 mm. Galvanostatic cycling was performed at C/20, while the electrolyte volume of 0.5 M KPF_6 in EC:PC (1:1 by volume) was set to 300 µl. The voltage ranges used for *operando*-XRD are similar to the half-cell setups for coin-cells (**Table 3**).

Table 3: Voltage range and theoretical capacity / current density at 1C for all evaluated active materials in a half-cell setup against a potassium metal anode.

Active Material	**Voltage range / V**	**1C / Theoretical Capacity / mA g^{-1} / mAh g^{-1}**
KVP/C	2.0 – 4.5	106
KVPO/C	2.0 – 4.8	133
KTP/C	1.0 – 4.0	128
KTPO/C	0.1 – 2.5	135

5.2.3 3-Electrode-Setup

The basic setup, which was used for all 3-electrode measurements is shown in a recent study of Panasenko *et al.*[135] For a first evaluation of KVP/C and analysis of limitations in a PIB half-cell setup this configuration with a Ag / AgCl-RE was used. Galvanostatic cycling with potential limitation in a voltage range of 2.5 V - 4.5 V (WE vs. CE) at C/20 was performed. As a WE 16 mm KVP/C electrodes with a 8 mm hole in the middle were used, while the CE was a 14 mm potassium metal anode. The setup from Panasenko *et al.*[135] is schematically shown in **Figure 10 a**. The separators used were 18 mm Whatman GF/C, while the electrolyte was the same as for the half-cell measurements in coin-cells. The electrolyte volume was set to 300 µl.

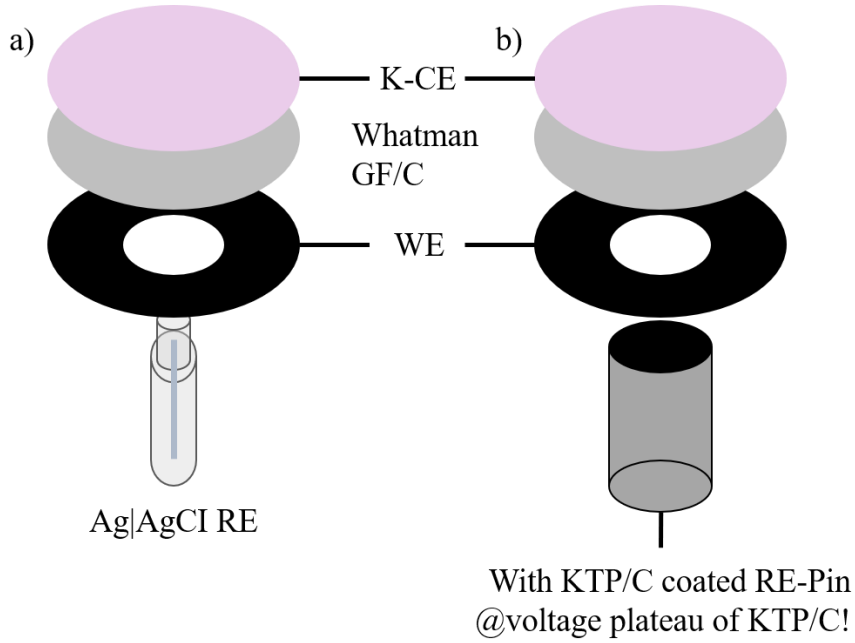

Figure 10: Schematically drawing of the used 3-electrode setup in this work with a) Ag / AgCl-RE according to Panasenko et al.[135] and b) KTP/C RE-Pin at the voltage plateau of KTP/C.

For evaluation of all the other synthesized materials in this work, a to its voltage plateau precycled KTP/C pin was used as RE (**Figure 10 b**). In this setup galvanostatic cycling at C/20 were performed according to the parameters summarized for the half-cell measurements in **Table 3**. All other relevant cell parameters (electrolyte, electrode diameters, separators) were kept constant to evaluation of KVP/C in a 3-electrode setup as described above. The precycling procedure for the KTP/C pin is shown in **Appendix 6**. After precycling of the KTP/C RE-pin the potassium metal counter electrode was exchanged for further 3-electrode measurements.

For 3-electrode measurements in full cell configuration the potassium metal counter electrode was exchanged by a 14 mm KTPO/C disk electrode, while all other parameters in the cell configuration were kept constant. C-Rate and applied current was calculated based on the active material mass at the WE.

5.2.4 Full-Cell-Setup vs. a Diagnostic Electrode as Anode

As the synthesized KTPO/C should be used as a diagnostic electrode (DE), a proof of concept of a full cell setup for more precise characterization of different electrode materials was developed.

For this purpose, 14 mm KTPO/C disk electrodes were preconditioned at C/20 in voltage range of 0.9 V – 1.5 V in a PIB half-cell setup *versus* a potassium metal counter electrode for two cycles to reduce irreversible losses in the full cell. After the second cycle the cells were stopped

at the voltage plateau of KTPO/C and disassembled. For its use in a full cell setup the preconditioned KTPO/C electrodes were either used in a classical coin cell format against a 12 mm KVP/C disk electrode or in a 3-electrode setup against a 16 mm KVP/C disk electrode with a 8 mm hole in the middle and the KTP/C-pin used as RE. The wet film thickness for the used KVP/C WE was reduced to 100 µm due to mass balancing issues, which excludes the capacity limitation of the full cell due to the capacity of the KTPO/C DE. The full cells were cycled similar to the cycling procedure in chapter 5.2.2, while the voltage window was adjusted to 0.8 V – 3.7 V (WE vs. KTPO/C DE). Electrolyte and electrolyte volume were used analogue to cycling in half-cell or 3-electrode configuration.

5.3 Material Characterization

Nitrogen Sorption. To evaluate the specific surface of the different hierarchical structured composites the method of nitrogen sorption with the BET (Brunnauer-Emmet-Teller)-method was used at Gemini VII 2390a (Micrometrics, USA). BET-evaluation was used in the linear region of the adsorption isotherm with a positive C-value. Prior to the characterization by nitrogen sorption all samples were pre-dried over night at 120 °C under vacuum.

Mercury-porosimetry. To determine the internal porosity and pore sizes of the secondary granules, mercury-porosimetry at a CEI PASCAL 1.05 (Thermo Electron, USA) was used. For the evaluation of the porosity all samples were pre-dried over night at 120 °C under vacuum. The internal porosity P was calculated by use of the internal specific pore volume V_P below a defined threshold value (1000 nm) based on the following equation: $P = \frac{V_P}{V_P + \frac{1}{\rho}}$ with the density of the different composite materials ρ. The threshold was used and necessary to distinguish between intragranular and intergranular porosity. The used densities ρ of the different composite materials are summarized in **Table 4**:

Table 4: Composite densities for the different electrode material composites used for the calculation of the intragranular porosity.

Composite	Density ρ / g cm^{-3}
KVP/C-1	2.82
KVP/C-2	2.80
KVP/C-3	2.78
KVP/C-4	2.78
KVP/C-5	2.73
KVP/C-6	2.68
KVP/C-2-650	2.77
KVP/C-2-700	2.77
KVP/C-2-750	2.77
KVP/C-2-800	2.79
KVP/C-2-850	2.81
KVP/C-2_CR	2.80
KVPO/C	3.13
KTP/C	2.99
KTPO/C	3.03

The densities for the composites KVP/C-1 and KVP/C-2 were determined by He-pycnometry prior to the porosity measurements. The densities for the other KVP/C composites were calculated based on the KVP/C-1 / -2 densities and according to their carbon content. The densities used for the other electrode materials are based on the CIF-files for the corresponding pure materials. (KVPO/C: Wernert *et al.*[93], ICSD-47829, ICSD release 2025.1; KTP/C: Lunezheva *et al.*[136], ICSD-67091, ICSD release 2025.1; KTPO/C: Norberg *et al.*[137], ICSD-182657, ICSD release 2025.1)

Particle Size Distribution. Particle size distributions were determined by static light scattering at a Horiba LA950 (Retsch Technology, Germany). Internal sonification was used to destroy possible particle agglomerates prior to analysis. Five measurements per sample were performed and mean values for the volume weighted particle size distribution were determined.

ICP-OES. Chemical composition of the different active materials was evaluated by use of ICP-OES with iCAP7600 due (Thermo Scientific, USA). Samples were dissolved in nitric and / or

hydrochloric acid prior to measurements. All samples were measured three times and mean values were calculated. All measurements were carried out by Dr. Thomas Bergfeldt and his team at the IAM-AWP. The carbon content was analyzed *via* a CS-analyzer.

Thermal Analysis. Thermal characterization of the materials and synthesis process was performed with a TGA STA449 (Netzsch, Germany) directly coupled with a FT-IR Vertex 70 (Bruker, Germany) to analyze gaseous reaction products. The transfer-line and FT-IR measurement cell were heated to 200 °C in advance, while the coupling and FT-IR were flooded with nitrogen all the time to reduce measurement artifacts by ambient air. The heating rate for all characterizations was 5 K min^{-1} till 1000 °C, while the cooling rate was 20 K min^{-1}. The reaction atmosphere was selected respective to the synthesis processes of the different materials described in chapter 5.1. IR-traces of the respective gaseous byproducts were determined by subtracting a baseline in the IR-spectra to eliminate influences of ambient atmosphere inside the IR gas measurement cell.

XRD analysis. Powder-XRD measurements were recorded either at a D8 or D2 diffractometer (Bruker, Germany) by using Cu-Kα-radiation with a step size of 0.02°. As a sample holder a zero-background silicium wafer was used. For Rietveld-refinements the TOPAS-software was used. For estimation of the crystallite size a double-Voigt approach as implemented in the TOPAS software was used.

Operando-XRD. Operando-XRD measurements were performed at a Huber diffractometer by using Mo-Kα-radiation developed by Gesswein *et al.*.[138] For measurements a asymmetric reflexion geometry under the use of parallel X-ray radiation and an areal detector was used. The measurements were performed in a for the reflection mode especially designed *operando*-cell from MTI (MTI Corporation, Richmond, USA) by use of a berrylium window, which was transparent to the radiation in the used angular ranges. The selected angular range was 7 ° - 17 ° for all different electrode materials. Cycling of the cells was performed at C/20 with a IVIUM CompactStat Potentiostat (Ivium Technologies B.V., Netherlands) according to chapter 5.2.2.

Electron Microscopy. The sample for TEM analysis was a lift-out lamella prepared using a Strata 400 S (ThermoFisher Scientific) dual-beam gallium focused ion-beam (FIB) / SEM system. The surface of the KVP/C-2 granule was protected before preparation using electron- and Ga-beam-deposited platinum. The TEM measurements were conducted using a probe-corrected Themis 300 TEM (ThermoFisher Scientific) operated at 300 kV in TEM mode. SEM images were recorded with a Supra55 SEM (Zeiss, Germany) at different acceleration voltages

and magnifications. For preparation of cross-sections for SEM investigations usually prepared electrodes were cut and etched by ion-etching for the further analysis with SEM.

XAS. X-Ray-Absorption-Spectroscopy was used to analyze the valent oxidation state of vanadium of different KVPO/C samples. Analysis was performed by using an EasyXAFS300 laboratory spectrometer (easyXAFS, USA). All measurement and analysis were performed by Ramon Zimmermanns at IAM-ESS.

6 Hierarchical Structured Potassium-Vanadium-Phosphate-Carbon-Composites as Cathodic Materials for PIBs

6.1 KVP/C as a Cathodic Material for PIBs

Based on the successful application of hierarchical structured NVP/C composites within the POLiS Cluster of Excellence as a cathodic reference material in SIBs[139], the stochiometric analogue KVP/C was studies as a hierarchical structured cathodic material for PIBs in the following chapters. First, the structural evolution and microstructural characterization of different KVP/C composites will be discussed (Chapter 6.1.1), as in the following chapter 6.1.2 the electrochemical behavior and performance of the KVP/C composites will be studied and correlated with the microstructural properties.

6.1.1 Structural Evolution and Microstructural Characterization

The findings discussed in this chapter are previously published in ChemSusChem, Volume 18, Issue 16 on June 20th 2025 as "Hierarchical Microstructured $K_3V_2(PO_4)_3$/C Composite Electrode Through Scalable Spray Drying Approach"[132].

Structural evolution during Synthesis and Crystal Structure of KVP

To study the underlying solid-state reaction and crystallization of the KVP-phase, TG/DSC analysis coupled with FT-IR measurements were performed. The thermal analysis results of the KVP/C-2 precursor are shown in **Figure 11**. The IR-traces of the respective gaseous byproducts were determined by subtracting a baseline in the IR-spectra to eliminate influences of ambient atmosphere inside the IR gas measurement cell.

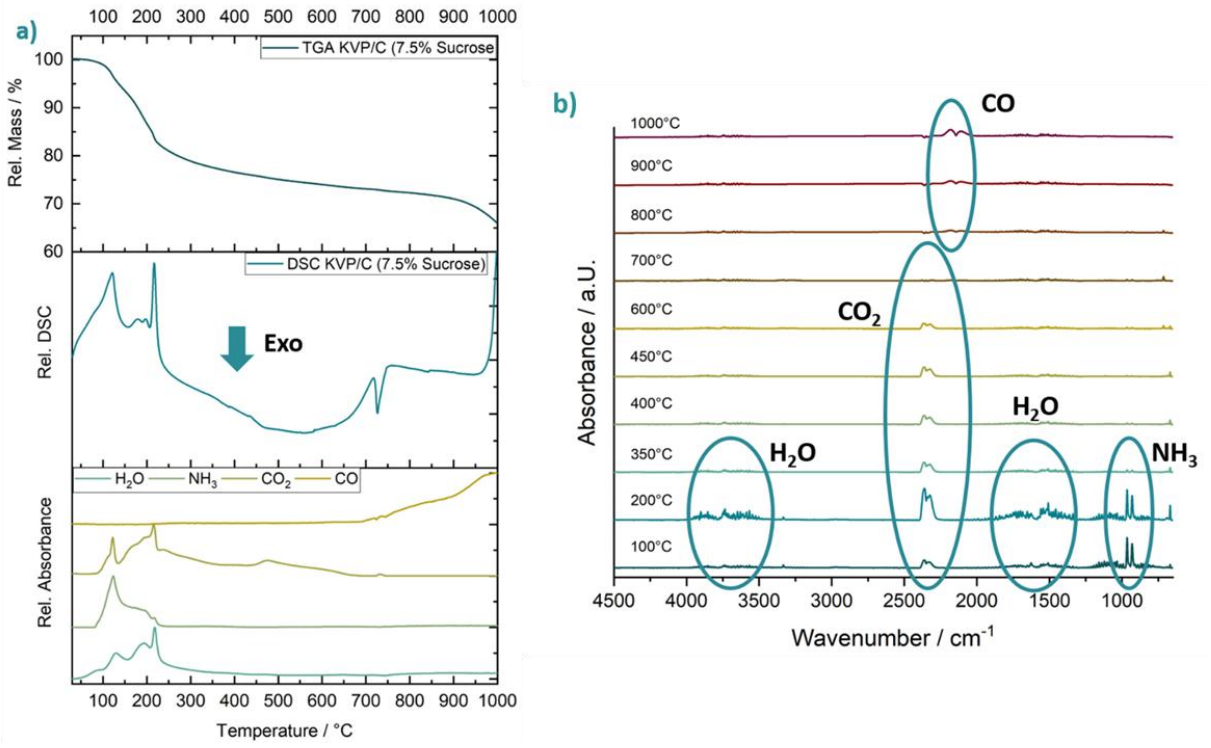

Figure 11: TG/DSC-IR analysis on KVP/C-2 precursors under Ar + 3 % H2 atmosphere. a) TGA (top), DSC (middle) and FTIR-traces of main gaseous byproducts (bottom), b) FTIR-spectra with marked gaseous byproducts at different temperatures during thermal analysis, reproduced from Heyn et al.©[132].

A distinct mass loss until temperatures up to approximately 350 °C was observed, which correlates with the release of NH_3 and H_2O accompanied with a continuous release of CO_2 extending up to 600 °C - 700 °C. This indicates the decomposition of the reactants NH_4VO_3, $NH_4H_2PO_4$ and sucrose.[132] The potassium source used prior to ball milling, K_2CO_3, decomposed during precursor preparation *via* ball-milling or storage of the precursor. This could lead to the formation KOH or a partwise as the potassium source for the synthesis of the KVP phase. Furthermore, a partwise reaction of the used K_2CO_3 or the formed KOH during precursor preparation with the reactant $NH_4H_2PO_4$ could lead to the formation of K_2HPO_4 or KH_2PO_4 as potassium source. Additional FT-IR measurements of the precursor and reactants could indicate the formation of KOH during precursor preparation (**Appendix 7**). A distinct exothermic peak at around 720 °C (**Figure 11 a**, middle) indicates the crystallization of the KVP phase. Above 800 °C a continuous release of CO instead of CO_2 becomes apparent. This suggests a possible reaction of the KVP phase with the carbon coating leading to a possible impurity phase formation.[103,132] This is underlined by the beginning of a strong endothermic signal in the DSC curve (**Figure 11 a**, middle) at around 900 °C with an increased mass loss, indicating a possible decomposition reaction of the KVP phase.[103,140] Based on these results a calcination temperature of 750 °C was selected for all KVP/C-composites. This temperature is above the crystallization temperature of 700 °C and below a possible impurity phase formation

above 800 °C. A powder XRD measurement of a KVP/C-2 precursor calcinated below 700 °C confirms an amorphous phase (**Appendix 8**). The observed mass losses, suggested decomposition products and onset temperatures are summarized in **Appendix 9**.[132]

Based on the presented thermal analysis of the calcination process of KVP/C composites the following reaction scheme is proposed (**Equation 2**):[132]

Equation 2: Proposed reaction scheme for the synthesis of KVP/C composites under reductive Ar + 3 % H_2-atmosphere in presence of sucrose as a carbon source, reproduced from Heyn et al.©.[132]

$$3\,K_2CO_3 + 4\,NH_4VO_3 + 6\,NH_4H_2PO_4 + 4\,H_2 + \mathrm{n\,C} \xrightarrow{Ar+3\,\%\,H_2,\,\Delta T} 2\,K_3V_2(PO_4)_3/C_n + 10\,NH_3 + 15\,H_2O + 3\,CO_2$$

In absence of any carbon according to **Equation 2**, theoretically a reaction turnover of 64 % would be expected. The residual mass after thermal analysis of the KVP/C-2 precursor was 66 %, which is in good agreement with the theoretical reaction turnover. Differences arise due to a partwise decomposition or reaction of the reactants during precursor preparation, as shown via additional FT-IR measurements (**Appendix 7)**. For example, assuming a complete reaction of K_2CO_3 with $NH_4H_2PO_4$ to K_2HPO_4 during the precursor preparation, this would increase the theoretical reaction turnover to about 75 %. Instead, assuming KOH as the potassium source, due to a complete decomposition of K_2CO_3 during storage or precursor preparation, this would lead to an increase of the theoretical reaction turnover to 67 %. Additionally, suggesting a complete carbonization of the 7.5 wt. % sucrose present in the KVP/C-2 precursor, this would reduce the theoretical reaction turnover to 62 % according to **Equation 2**. All these calculations further underline the partwise decomposition or reaction of the reactants during precursor preparation and prior to calcination as the experimental reaction was slightly higher as expected according to **Equation 2**.

Assuming the complete carbonization of the 7.5 wt. % sucrose during calcination, a residual content of 3.2 % carbon in the KVP/C-2 composite was expected. After completion of the calcination for 5 h at 750 °C under reductive Ar + 3 % H_2-atmosphere the carbon content for KVP/C-2 was determined as 2.3 % (**Table 5**). The difference of the experimental to the expected theoretical carbon content was attributed to the consumption of 0.9 wt. % carbon during the necessary reduction of V(+V) to V(+III) in the synthesis of the KVP/C composites under reductive Ar + 3 % H_2-atmosphere. If the reduction of vanadium is assumed to be exclusively caused by the present carbon matrix, a complete reduction of V(+V) to V(+III) would consume 1.5 wt. % of carbon during synthesis of the KVP phase. The difference to these theoretical values arises from a partial reduction of V(+V) to V(+III) by the reductive Ar + 3 % H_2-atmosphere during calcination. The amount of carbon used for the reduction of V(+V) to

V(+III) during calcination decreases from KVP/C composites with 5 wt. % sucrose with 1.2 wt. % to composites with 10 wt. % sucrose with 0.4 wt. %. This could be explained by an increased specific surface area of the KVP/C composites calcinated with higher amounts of sucrose, which increase the reactive surface to reduction by the Ar + 3 % H_2-atmosphere (**Table 5**).[132]

Table 5: Theoretical and experimental carbon content combined with the amount of carbon used for the reduction of vanadium and the specific surface of the different KVP/C-composites after calcination at 750 °C for 5 h under Ar + 3 % H_2-atmosphere.

Composite	Sucrose Content / wt. %	Theoretical Carbon Content / wt. %	Experimental Carbon Content / wt. %	Carbon used for V-Reduction / wt. %	Specific Surface / $m^2 g^{-1}$
KVP/C-1/4	5	2.1	0.9	1.2	3.3
KVP/C-2/5	7.5	3.2	2.3	0.9	9.5
KVP/C-3/6	10	4.2	3.8	0.4	27.7

As the crystal structure of KVP remains under debate in literature and no structure solution is available in the ICSD, the crystal structure of the KVP/C composites was studied by the combining electron diffraction (SAED) *via* TEM imaging and powder XRD measurements. The obtained powder diffraction pattern of KVP/C-1 is shown in **Figure 12 c.** It visually matches well with the diffraction patterns reported by Zhang *et al.*, particularly in the angular range of 28 ° and 34 ° 2θ.[107] As there are different structural models of KVP under discussion in literature, several attempts to fit different models reported in literature did not yield any satisfying results. (**Appendix 10**) The most promising fit is based on the assumption of the co-existence of at least two main phases in our composites: orthorhombic $K_3V_3(PO_4)_4 \cdot H_2O$[106] or crystal-water free $K_3V_3(PO_4)_4$[91] with the symmetry *Pnna* and monoclinic $K_3V(PO_4)_2$ with the symmetry $P12_1/c1$. Jenkins *et al.* proposed, that a phase in the stoichiometry of $K_3V_2(PO_4)_3$ does not exist and all synthesis approaches lead to the formation of at least the two main phases, which are mentioned above. Depending on the calcination atmosphere and exact stoichiometric ratio, several different main phases and impurities can be found. However, their study reveals also some weaknesses like the identification of crystal water.[106]

The presence of microstrains and small crystallite sizes in nm-range in the KVP/C composites are indicated by relatively broad diffraction reflexes visible in the powder diffraction pattern. These small crystallites are confirmed by TEM images (**Figure 12 a & b**) together with the imaging of lattice fringes. Due to the porosity of the KVP/C granules (which limited the thinning-down process during lamella preparation) and the small grain size of the crystallites,

it was not possible to obtain direct single-crystalline low-index TEM imaging.[132] In the electron diffraction pattern a significant dynamic scattering is visible caused by the thickness of the sample, which generates double spots. Combined with the nanosized crystallites it makes it difficult to obtain diffraction pattern circles, as rather preferential reflections (strong spots) are visible. (**Figure 13a**) Nevertheless, an extrapolation could reveal the actual position of the diffraction discs and most of the single crystal diffraction pattern match a given set of lattice parameters. Based on SAED on different single crystal diffraction pattern a triclinic crystal structure was proposed for the KVP/C composites. The fitted lattice parameters with a SAED-pattern along the [100] zone axis for KVP/C-2 are shown in **Appendix 11.** However, all attempts to find a structure solution based on the triclinic lattice parameter set obtained *via* SAED and the recorded powder diffraction patterns did not lead to an unambiguous structure solution for KVP. Even approaches to increase primary particle and crystallite size of the KVP/C composites *via* a calcination for 48 h at 750 °C under Ar + 3 % H_2-atmosphere did not improve the obtained data quality of electron or powder X-ray diffraction to create an unambiguous structure solution for the KVP phase. For example, if the triclinic lattice parameter set from the SAED results is assumed, the first significant reflex in the XRD pattern should appear at around $2\theta = 4.87$ ° (for Cu Kα radiation) and corresponds to the [010] lattice plane. This reflex is not visible in the XRD patterns for the KVP/C composites, indicating that a triclinic space group cannot describe the KVP/C structure. (**Appendix 12**)

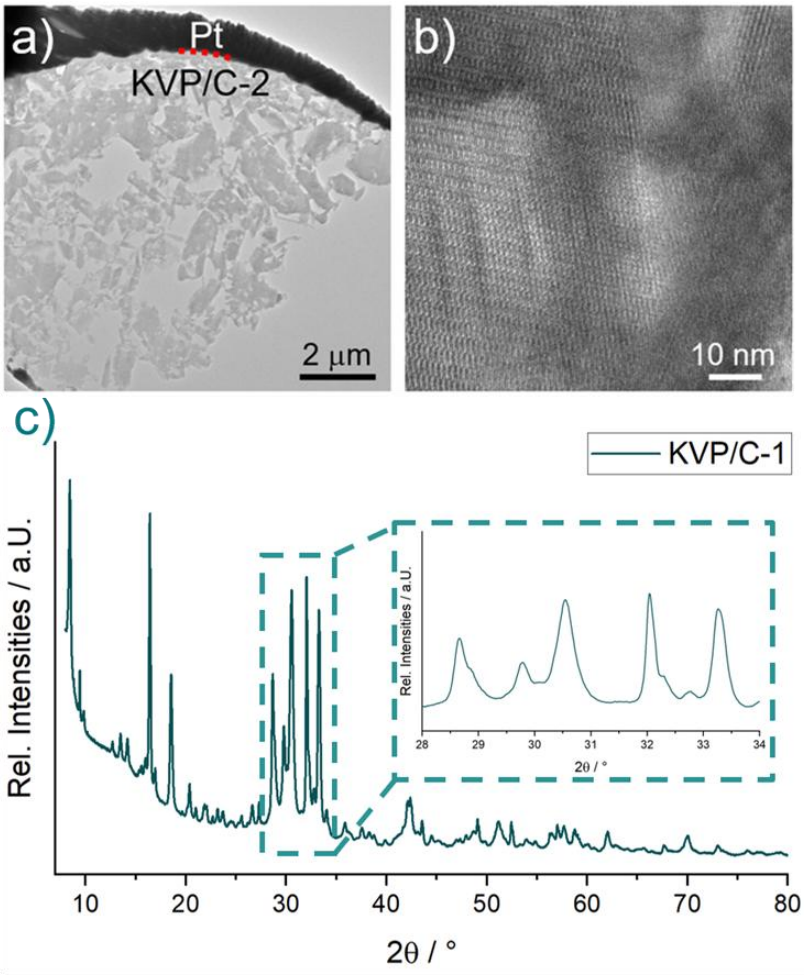

Figure 12: a) Prepared TEM-lamella of a typical KVP/C-2 granule, b) HR-TEM image of the lattice fringes of KVP/C-2, c) Collected XRD pattern of KVP/C-1, adapted from Heyn et al.©[132]

Based on the discussions in literature regarding a possible phase mixture, a Rietveld-refinement of the structural models for $K_3V_3(PO_4)_4$ (*Pnna* symmetry, ICSD-69792, ICSD release 2025.1, Benhamada *et al.*[141]) and $K_3V(PO_4)_2$ (*P12₁/c1* symmetry, ICSD-149167, ICSD release 2025.1, Li *et al.*[91]) as main phases against the obtained diffraction pattern for KVP/C-2 is shown in **Figure 13 b**. The fit shows at least a reasonable match with the obtained diffraction pattern, which supports the hypothesis of a phase mixture discussed by Jenkins *et al.*[106] Nevertheless, assuming a phase mixture and non-existence of $K_3V_2(PO_4)_3$ phase is contradictory to the findings *via* TEM imaging and SAED. Assuming a statistical distribution of the primary particles in a cross-section of a porous secondary KVP/C granule, the possible different main phase in the KVP/C composites should be directly visible during SAED and TEM imaging at different primary particles. This was not the case for all electron diffraction experiments performed at cross-sections of the KVP/C-2 granules or primary particles. In all cases, similar images of the lattice fringes and selected area electron diffraction (SAED) patterns were obtained, displaying diffraction rings that could be indexed to a specific set of

lattice parameters (**Figure 13a**). ICP-OES measurements confirm the stoichiometry of KVP/C-2 according to $K_3V_2(PO_4)_3$ (**Appendix 13**).

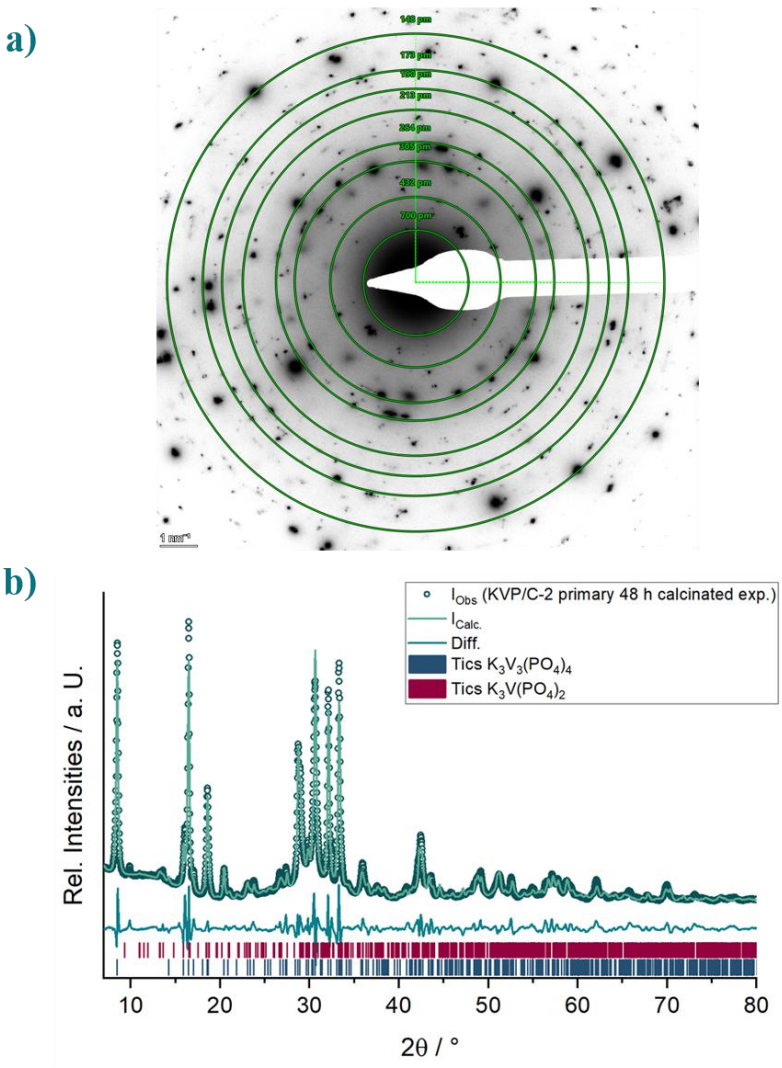

Figure 13: *a) Exemplary SAED diffraction pattern of KVP/C-2 granules with extrapolated diffraction rings and b) Rietveld-refinement of the structural model against the collected XRD pattern of KVP/C-2 primary particles calcinated for 48 h based on the main phases $K_3V_3(PO_4)_4$ ($P12_1/c1$ symmetry, ICSD-149167, ICSD release 2025.1, Li* et al.[91]) *with around 84 wt. % and $K_3V(PO_4)_2$ (Pnna symmetry, ICSD-69792, ICSD release 2025.1, Benhamada* et al.[141]) with around 16 wt. %.

It seems that the synthesis process of the KVP/C composites is highly sensitive to the applied calcination conditions. Combined with the presence of different amount of carbon sources, minor differences in reaction atmosphere or temperature could alter the vanadium valence state. This in turn, could lead to the formation of different impurity phases, or changes in the crystallographic structure as visible in different peak broadenings or reflex intensities of the different KVP/C composites (**Appendix 14**).[132] A complete structure solution for the KVP phase remains challenging and should be considered as a key research objective in the future, as it is a critical point in the improvement and understanding of KVP/C composites as cathodic materials for PIBs.

Influence of Carbon Source Content onto Microstructure of the KVP/C Granules

Firstly, the carbon source content of the KVP/C-2 composites was varied to study the influence onto the microstructure and electrochemical performance. All KVP/C composites with different carbon source content were calcinated and sintered at 750 °C for 5 h under Ar + 3 % H_2-atmosphere. All relevant powder characteristics are summarized in **Table 6**.

Table 6: Summary of all powder characteristics after completion of the sintering process for all different KVP/C compositions, reproduced from Heyn et al.©.[132]

Composite	Sucrose / wt. %	β-Lactose / wt. %	C-Content after Sintering / wt. %	Median Secondary Particle Size / µm	Specific Surface / $m^2 g^{-1}$	Porosity / %	Pore size / nm
KVP/C-1	5	5	2.4	13.4	11.1	35.7	232
KVP/C-2	7.5	5	3.6	13.6	20.7	38.3	153
KVP/C-3	10	5	4.4	13.1	3.5	11.4	-
KVP/C-4	5	15	4.4	14.9	41.1	30.4	191
KVP/C-5	7.5	15	5.7	14.5	46.3	28.5	157
KVP/C-6	10	15	7.2	13.9	56.3	30.9	186

The median secondary granule size of the KVP/C composites was nearly independent of the carbon source content, ranging from 13.1 µm - 13.6 µm for samples with 5 wt. % of β-lactose and from 13.9 µm - 14.9 µm for samples with 15 wt.% of β-lactose. The carbon content after completion of the synthesis process increased from 2.4 wt. % (KVP/C-1) to 7.2 wt. % (KVP/C-6) with increasing carbon source content, as expected (**Table 6**). An increased carbon source content leads also to an increased specific surface after calcination (**Table 5**) and also after completion of the sintering process (**Table 6**). This is mainly caused due to apparent carbon matrix formed during the thermal treatments, which increases the specific surface of the composites.[103] Additionally, the carbonization of the carbon sources has the potential to result in the formation of more nanosized crystallites. This, in turn, can impede the particle growth, thereby contributing to an increase in specific surface area.[132,142] Nevertheless, the stated specific surfaces are an effective surface area of the combined contributions of both, the carbon matrix and KVP particles. A clear correlation between the specific surface area and the electrochemical performance in chapter 6.1.2.2 could not be made.[103,132] The composites KVP/C-1 and KVP/C-2 exhibited the highest open intragranular porosity with 35.7 % and 38.3 % respectively, which were higher compared to KVP/C composites with 15 wt. % β-lactose (≈30 %). Modal pore sizes are comparable for all different KVP/C composites and all

KVP/C composites could be categorized into macroporous materials (pore size > 50 nm). Composite KVP/C-3 shows an exceptionally low specific surface area (3.5 m^2 g^{-1}) and porosity (11.4 %) with barely an open porosity, why no pore sizes were measurable (**Figure 14**).[132]

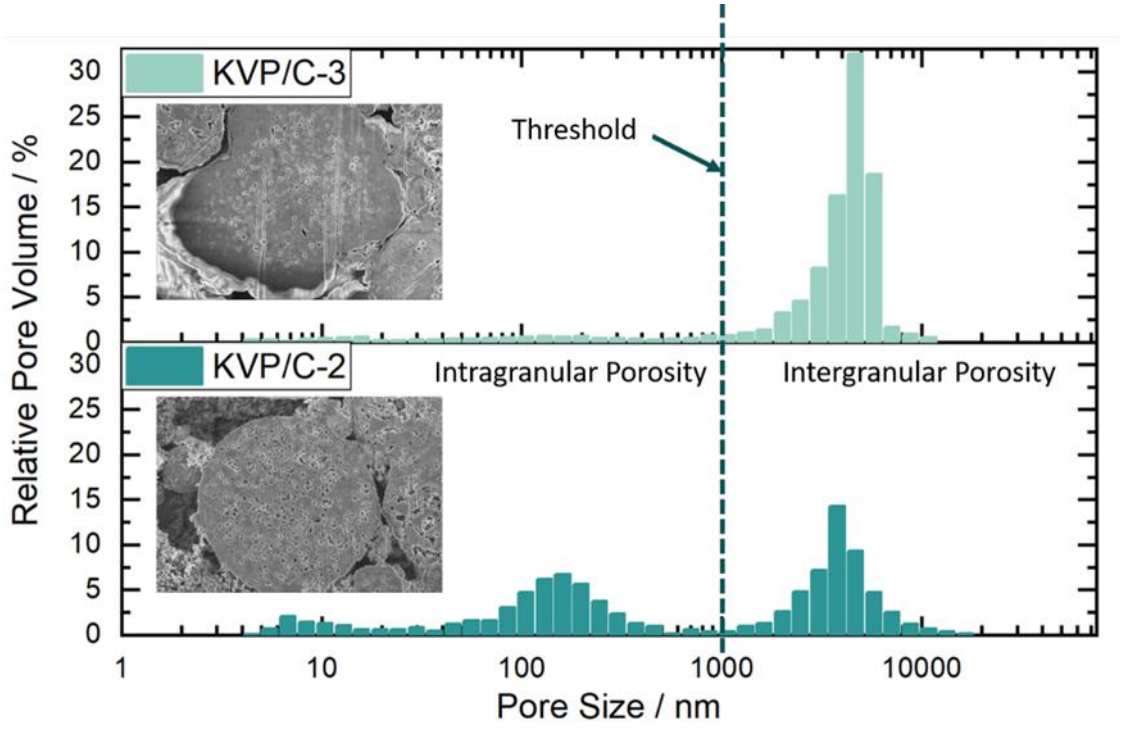

Figure 14: Exemplary Pore size distribution of KVP/C-2 and KVP/C-3 with intra- and intergranular porosity. The threshold was used for calculation of the total intragranular porosities of all materials, reproduced from Heyn et al.©[132]

The SEM images show a homogenous spherical morphology and well distributed open porosity through the cross-sections of all KVP/C composites. KVP/C-3 represented an exception, consistent with the porosimetry measurements as no open porosity was observed (**Figure 15**). Spray drying of small particles leads to the arrangement of the smallest particles at the border of the granules.[129] During subsequent sintering these smallest particles sintered more rapidly, forming a denser surface layer. This was clearly visible for KVP/C-3, where an almost completely closed surface was observed. For all other KVP/C composites this effect is obvious as well, but not as pronounced as for KVP/C-3. The dense surface layer of KVP/C-3 results in a lower specific surface and porosity compared to the other KVP/C composites.[132]

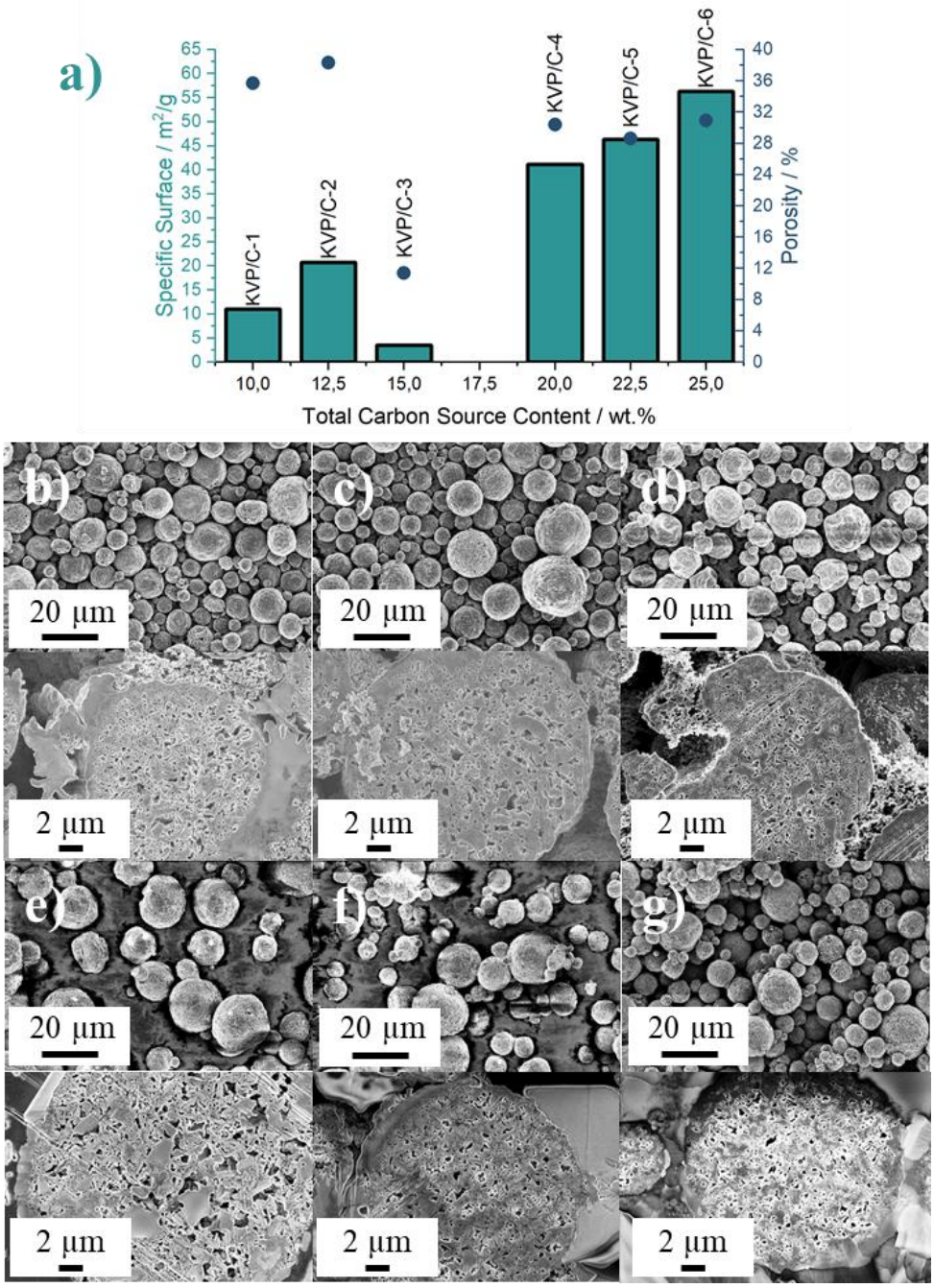

Figure 15: *a) Correlation between specific surface (bars), intragranular porosity (bullets) and total carbon source content (sucrose + β-lactose) after completion of the synthesis process of all KVP/C-composites, b)-g) SEM images of the morphology and cross-sections of the secondary granules with b) KVP/C-1, c) KVP/C-2, d) KVP/C-3, e) KVP/C-4, f) KVP/C-5 and g) KVP/C-6, adapted from Heyn et al.©*[132]

Influence of Sintering Temperature onto Microstructure of the KVP/C Granules

The effect of different sintering temperatures was studied using the KVP/C-2 composite, as this composite showed the most promising electrochemical performance (chapter 6.1.2). In **Table** 7 all relevant powder characteristics for the KVP/C-2 composites sintered at different temperatures are summarized.

Table 7: Summary of all relevant powder characteristics after completion of the synthesis process for all KVP/C-2 composites sintered at different temperatures.

Composite	Sintering Temperature / °C	C-Content after Sintering / wt. %	Median Secondary Particle Size / µm	Specific Surface / $m^2 g^{-1}$	Porosity / %	Pore size / nm
KVP/C-2-650	650	4.2	14.2	14.0	29.8	110
KVP/C-2-700	700	4.2	12.5	21.8	33.1	108
KVP/C-2-750	750	4.1	12.7	20.0	33.9	110
KVP/C-2-800	800	3.5	12.2	20.0	32.4	110
KVP/C-2-850	850	2.9	11.9	8.1	28.3	118

The carbon content, specific surface, secondary particle size and porosity are decreasing with increasing temperature starting from 700 °C, as expected. The pore sizes are nearly similar for all different KVP/C composites. The deviation of this trend observed for KVP/C-2-650 could possibly be explained with the formation of small new crystallites of the KVP phase at temperature of 700 °C and above. As discussed before, the crystallization temperature of KVP was determined at around 700 °C *via* thermal analysis (**Figure 11**), which could lead to the formation of new crystals during sintering at temperatures above 700 °C. This in turn, increases the specific surface of the composites.[140] At temperatures below 750 °C some minor reflexes appear in the powder diffraction pattern. These reflexes are likely associated with small amounts of impurity phase inside the composites KVP/C-2-650 and KVP/C-2-700, which could underline the formation of new small crystallites at temperatures of 700 °C and above. The corresponding powder XRD pattern of the different KVP/C composites (**Appendix 15**) visually match well with the XRD pattern from KVP/C-1 (**Figure 12**) and literature.[107] Another probable reason for the increase in the specific surface from 650 °C to 700 °C and above may be attributable to different carbon matrices apparent in the various composites, which could alter the specific surface.[103] Morphology and cross sections of the secondary granules are shown in **Figure 16** and **Appendix 16**. The morphology of all KVP/C-2 composites sintered at different temperatures appeared similar and was nearly spherical. The surface of the granules appeared

to be similar for the composites calcined at temperatures between 650 °C and 800 °C. Their surfaces showed a carbonaceous network or matrix structure. In contrast, the surface of the composite sintered at 850 °C showed fewer carbon residues and larger pores enclosed to the surface. The cross sections for all composites revealed a well distributed open porosity through the cross-sections of all granules. **(Appendix 16**).

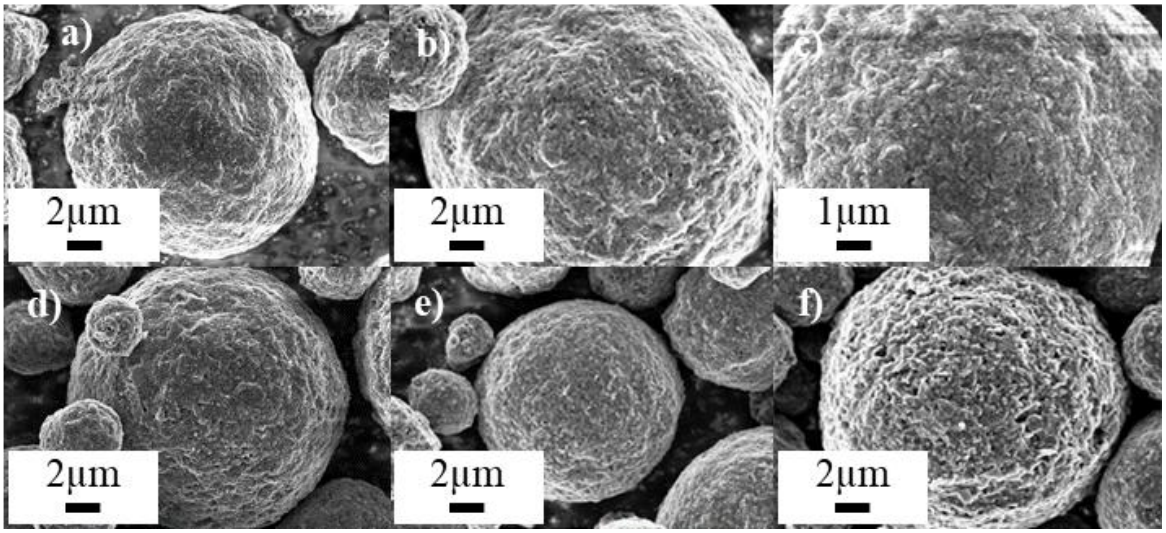

Figure 16: SEM images for visualization of the morphology of different KVP/C-2 composites with a) secondary granules after spray-drying without sintering and b)-f) KVP/C-2 composites sintered at different temperatures with b) KVP/C-2-650 (650 °C), c) KVP/C-2-700 (700 °C), d) KVP/C-2-750 (750 °C), e) KVP/C-2-800 (800 °C) and f) KVP/C-2-850 (850 °C).

6.1.2 Electrochemical Performance of Hierarchical Structured KVP/C-Composites

6.1.2.1 Electrochemical Behavior

Figure 17 visualizes the electrochemical behavior of the KVP/C-2-800 composite investigated *via operando*-XRD measurements in a PIB half-cell setup.

Since the exact crystal structure and possible phase composition of the KVP/C composites are still unknown, only a qualitative interpretation of the *operando*-XRD data can be provided. The *operando*-XRD cell was cycled at C/20 (1C = 106 mA g^{-1}) in a PIB half-cell setup for two cycles. The angular range between 13 ° and 15 ° was selected for discussion, as several intense main reflexes are observed in this range.

During the first charge cycle, the reflexes at 13.2 ° and 14.8 ° gradually shifts to higher reflex angels and broaden continuously, especially in the high voltage region above 4.2 V – 4.3 V. In contrast, the reflexes around 13.6 ° and 14.1 ° progressively weakened and disappear upon charging to the upper cut-off voltage of 4.5 V. The reflex around 13.6 ° already vanishes around 4.1 V, before the high voltage region above 4.0 V these reflex shifts to lower angels. The reflex around 14.1 ° gradually shifts to lower angels until a voltage of around 4.2 V – 4.3 V, while it is nearly completely vanished above this voltage. This opposite reflex shift compared to higher or respectively lower angels could indicate the contraction of the unit cell in one lattice direction, while it expands in another lattice direction. During discharge, this behavior is obtained *vice versa*, the reflexes around 13.2 ° and 14.8 ° shift gradually back to their pristine positions and smaller angels. Instead, the reflexes around 13.6 ° and 14.1 ° appear again with stepwise increasing reflex intensity and shift back to their pristine position as well. Notably, the reflex around 13.6 ° shows a progressive peak broadening and reduced intensity upon continuous cycling. This could indicate a possible structural rearrangement or change in symmetry / crystal structure during continuous cycling and probably explain the increasing capacity during the first cycles (**Figure 18a**).

Nevertheless, the electrochemical reaction mechanism seems quite complicated based on the obtained *operando*-XRD data. The observed opposite peak shifts, peak broadening, and partial disappearance of reflections during cycling suggest changes in symmetry or the coexistence of multiple phases within the KVP/C composites In order to facilitate a more detailed understanding of the electrochemical reaction mechanism, it is imperative that an unambiguous

structural solution is obtained for the KVP/C composites. This will assist in further improving and understanding the electrochemical performance of the KVP/C composites.

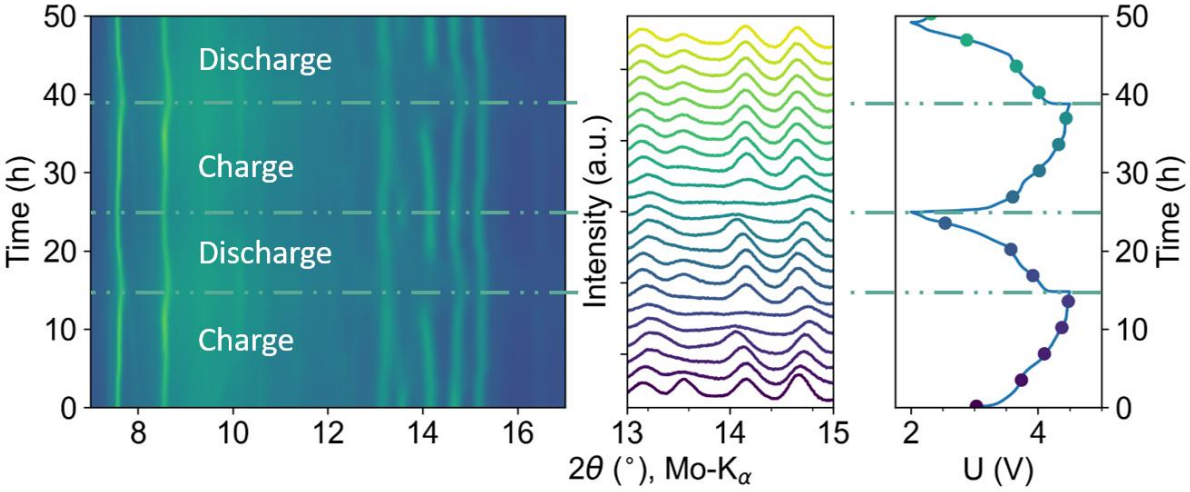

Figure 17: *Operando XRD measurement on composite KVP/C-2 in PIB half-cell setup for two cycles with contour plot during cycling in the range of 7 ° - 17 ° (left), selected diffraction pattern in an angular range of 13 ° - 15 ° (middle) and corresponding voltage profile over time (right).*

The voltage profiles and dq/dV-plots of the KVP/C-2-800 composites are visualized in **Figure** 18. During cycling in the potential window of 2.0 V - 4.5 V, distinct pairs of redox peaks appear in the dq/dV-plot, which correlate with small steps int the voltage profile around 3.7 V - 3.8 V, 4.0 V and 4.2 V (charge) and 3.6 V and 4.1 V (discharge). Additionally, following continuous cycling a minor redox peak during charge at around 3.3 V appears (peak 4). This peak also emerges during discharge with high polarization at 2.1 V (peak 4). As the redox peak at 3.6 V during discharge shows a small shoulder, this could be assigned to the small redox peak around 4.0 V during charge. Generally, the assigned pair of redox peaks have a high polarization of at least 150 mV - 200 mV (peak 1) and up to 1.2 V (peak 4) in common. A high polarization already at low C-rates is not uncommon in PIB half-cell setups. The high reactivity of the potassium metal anode could result in the formation of resistive surface layers, which are increasing the polarization.[37] Nevertheless, a polarization of more than 1.0 V has probably its origin in structure related properties of the material or structural rearrangement during insertion / deinsertion of K^+. Combined with *operando* XRD measurements a partly reversibility of the redox processes at C/20 is determined, while the reaction mechanism remains unclear due to missing crystallographic information of the KVP/C phase.

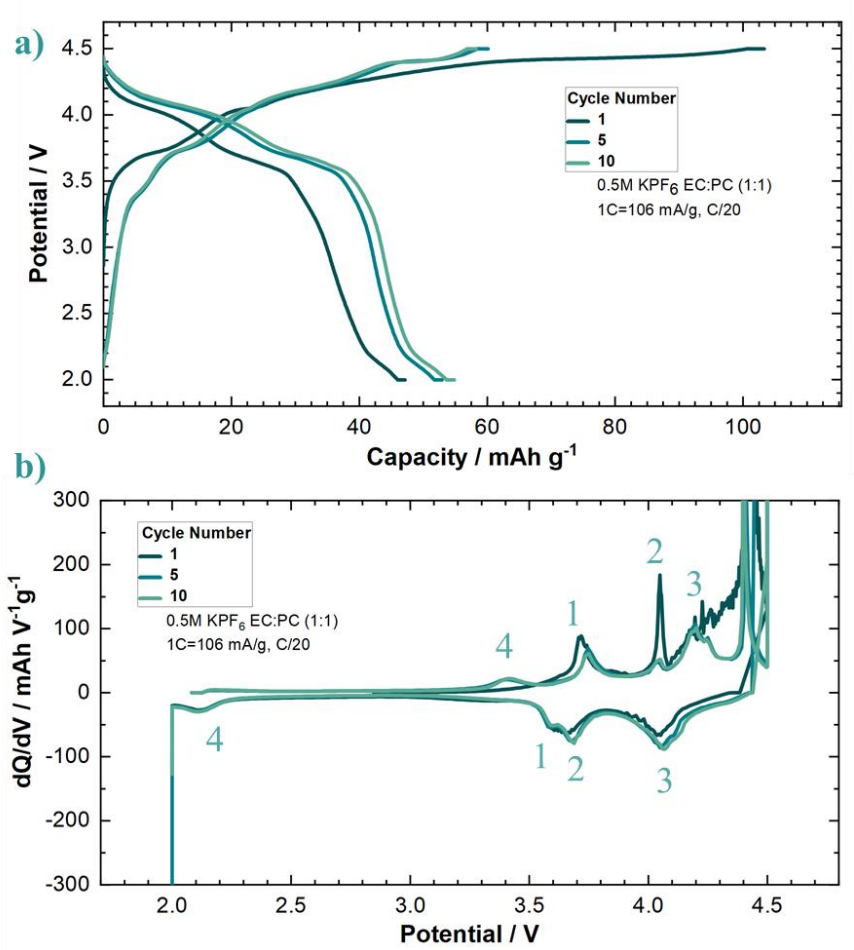

Figure 18: Electrochemical data from composite KVP/C-2 in a PIB half-cell setup (2-electrode) at C/20 with a) potential profile and b) corresponding dq/dV-plot for the 1st, 5th and 10th cycle. As an electrolyte 0.5 M KPF_6 in EC:PC (1:1) was used.

6.1.2.2 Influence of Carbon Source Content

To determine the maximum discharge capacity of the KVP/C-composites with different carbon source content, galvanostatic cycling at C/20 (1C = 106 mA g^{-1}) in PIB half-cells in the potential window of 2.0 V - 4.5 V was performed. All stated capacities are based on the KVP/C active material mass. In terms of specific discharge capacity an increase in sucrose content leads to an increased specific discharge capacity at C/20, while an optimum of 7.5 wt. % sucrose was obtained (KVP/C-2). After 25 cycles, KVP/C-2 showed the highest specific discharge capacity of 58 mAh g^{-1}, while KVP/C composites with the lowest sucrose content of just 5 wt. % showed the lowest discharge capacities (KVP/C-1 & KVP/C-4, **Figure 19**). An increase in the specific discharge capacity is obtained for all KVP/C composites with 5 wt. % of β-lactose, which could be attributed to an activation process of inactive secondary particle domains. Compared to literature our synthesis process leads to easily processable and µm-sized secondary granules. This in turn, could lead to some inactive domains at the beginning with subsequent activation of this domains during continuous galvanostatic cycling. KVP/C composites with 15 wt. % β-

lactose just show minor differences in the electrochemical performance. The increase in the amount of added β-lactose for the spray-drying does not lead to any further increase in discharge capacity at C/20. Even if the discharge capacities are calculated without the contribution of the residual carbon content the same trends are obtained (**Appendix 17**).[132]

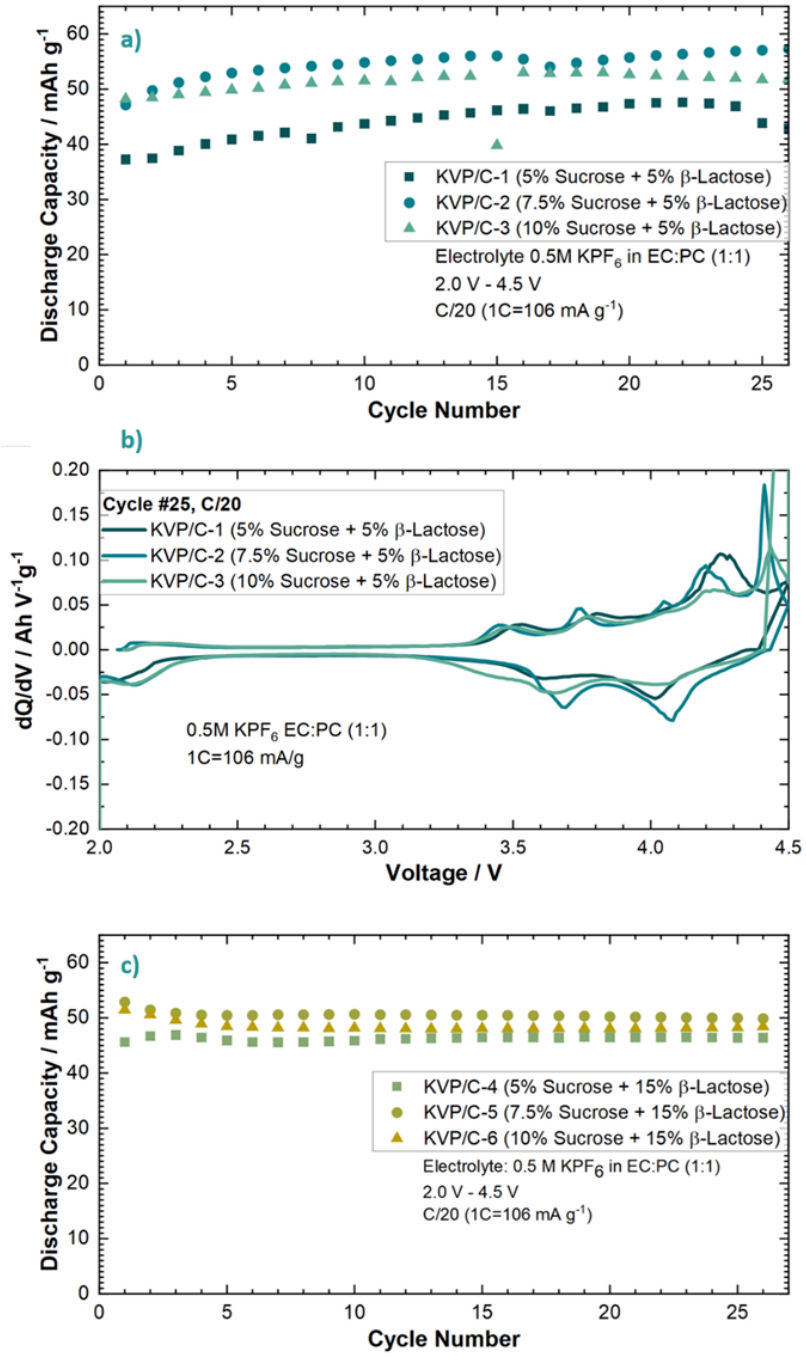

Figure 19: Specific discharge capacities of KVP/C composites depending on the sucrose content in PIB half-cells at C/20 for a) KVP/C composites with 5 wt. % β-lactose, b) dq/dV-plot of KVP/C composites with 5 wt. % β-lactose at cycle 25 and c) discharge capacity of KVP/C composites with 15 wt. % β-lactose, reproduced from Heyn et al©.[132]

The rate capability of the different KVP/C composites was evaluated in PIB half-cells from C/20 to 1C. The tests were limited to 1C for two reasons: Firstly, a potassium metal counter electrode tends to build up a high resistivity itself by the build-up of thick resistive surface layers due to the high reactivity toward electrolyte components. The recurrent electrolyte degradation processes amplify the surface layer growth at the potassium metal electrode and could lead to parasitic side reactions by soluble species. These are the main causes for high cell polarization in PIB half cells.[135,143-146] With increasing C-rate and increasing current densities this is causing an increasing bias in rate capability evaluation of different electrode materials in PIB half cells.[37] Secondly, the rate capability tests should identify viable C-rates, which do not suffer form rate induced capacity losses for further material characterization or electrolyte development and surface analysis.[132]

At low and moderate C-rate until C/2, KVP/C-2 performs best with the highest discharge capacity. At 1C the discharge capacity of KVP/C-1 and KVP/C-2 is similar, while KVP/C-3 shows the worst C-rate capability (**Figure 20**). KVP/C-3 not only shows the lowest discharge capacities, its voltage profiles undergo drastic changes with increasing C-rate (**Figure 21**). The KVP/C composites with 15 wt. % β-lactose showed a similar C-rate capability, which seems to be caused by the nearly similar open intragranular porosity. The composites with 15 wt. % β-lactose generally maintained lower discharge capacities compared to the KVP/C composites with 5 wt. % β-lactose. Even if the different residual carbon contents are considered and discharge capacities are calculated without the carbon content, the same trends are obtained (**Appendix 18**). The corresponding dq/dV-plots and potential profiles for KVP/C composites with 15 wt. % β-lactose are shown in **Appendix 19** and **Appendix 20**.[132]

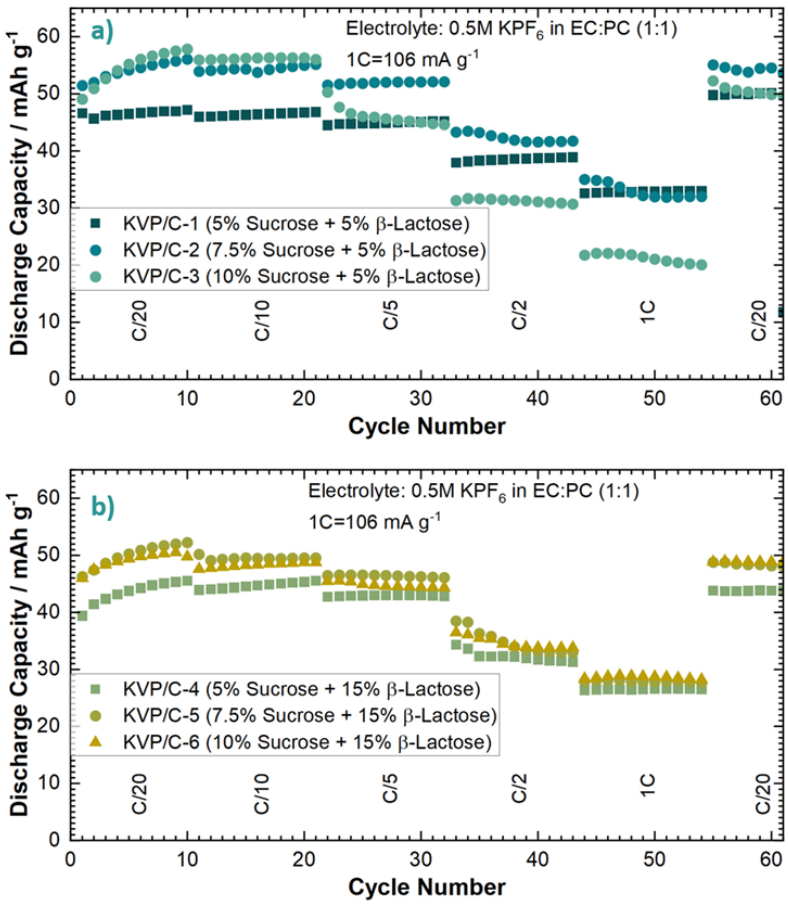

Figure 20: *C-Rate capability test of KVP/C composites with different carbon source content in PIB half-cells with a) KVP/C composites with 5 wt. % β-lactose and b) KVP/C composites with 15 wt. % β-lactose, reproduced from Heyn et al.©.*[132]

Summarizing the results above, a sucrose content of 7.5 wt. % seems to be the optimum in terms of maximum specific discharge capacity (58 mAh g^{-1} at C/20 after 25 cycles) and C-rate capability. A further increase in sucrose content does not further improve the maximum specific discharge capacities of the KVP/C composites. Conversely, an increase in sucrose content leads to much poorer C-rate capability, higher polarization and lower maximum discharge capacity, which could be directly linked to the microstructure of the KVP/C secondary granules. For example, KVP/C-3 shows the lowest open intragranular porosity and poorest C-rate capability as well. Increasing sucrose content could inhibit the particle growth and lead to nanocrystalline particles.[103] Accordingly, sucrose contents above 7.5 wt. % could lead to much thicker and dense carbon coatings at the surface of the primary KVP/C particles. This could limit K^+-diffusion from the liquid electrolyte phase into the active material and thus render more domains of the KVP/C granules electrochemically inactive.[147,148] In the dq/dV plots for KVP/C composites with 5 wt. % β-lactose this effect becomes directly visible, as a clear shift in the redox peaks during discharge to higher potentials for KVP/C-2 with less polarization compared

to KVP/C-3 is obvious (**Figure 19 b**). The higher open intragranular porosities of KVP/C-1 and KVP/C-2 (**Table 6**) could explain the improved C-rate capability compared to KVP/C-3 with barely any open porosity. This low intragranular porosity combined with the thick carbon coating for KVP/C-3 contribute to the poor mass-transport properties in the electrolyte and particle phase. It generates a poorly percolated electronic network inside the secondary KVP/C-3 granules, which results in high polarization effects at higher C-rates (**Figure 21**). Concluding, the carbon coating of KVP/C-2 with its high specific surface and open intragranular porosity, shortens the diffusion length inside the active KVP/C phase. Additionally, this could promote the electrolyte penetration and interfacial contact, which leads to increased potassium ion diffusion and depth of discharge with higher maximum discharge capacities at low C-rates and improved C-rate capability.[90,103,108,142]

Based on the discussed results, KVP/C-1 and KVP/C-2 have an improved C-rate capability compared to the KVP/C-composites with 15 wt. % β-lactose, which could be directly linked to the unique microstructure of the secondary granules. The high open intragranular porosity up to 38 % (KVP/C-2) leads to a shortening of diffusion length inside the nanostructured granules, which improves the electrochemical performance.

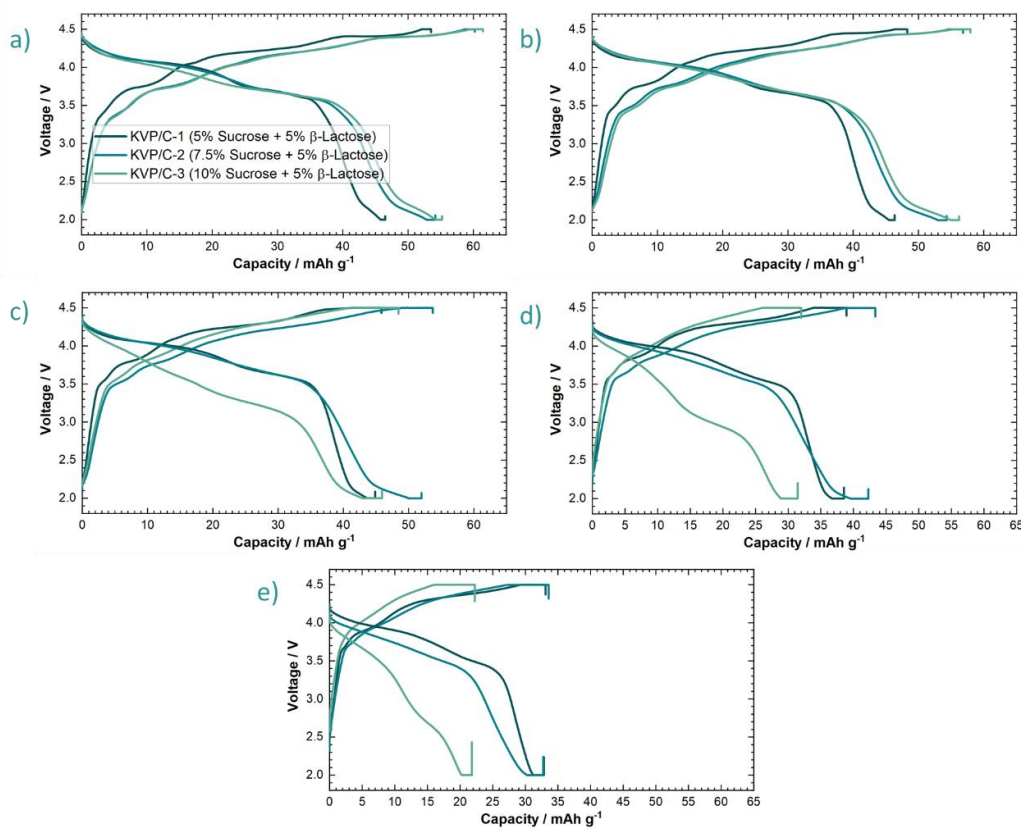

Figure 21: Potential profiles of KVP/C composites with 5 wt.% of β-lactose in PIB half cells at different C-Rates in the 5th cycle at each C-rate. a) C/20, b) C/10, c) C/5, d) C/2 and e) 1C. 1C=106 mA g^{-1}, adapted from Heyn et al.©.[132]

6.1.2.3 Influence of the Sintering Temperature

The impact of different sintering temperatures on the C-rate capability of KVP/C composites was studied in the temperature range from 650 °C - 850 °C. The rate capability of the different KVP/C composites was evaluated in PIB half-cells from C/20 to 1C. In **Figure 22** the C-rate capability test and voltage profiles of the composites at the 5th cycle of each C-rate are shown. Due to the minor differences in microstructure, the differences seen in the electrochemical performance are quite small as well. At a low C-rate of C/20 the maximum discharge capacity of the KVP/C composite sintered at just 650 °C is slightly compared to the other KVP/C composites with 63 mAh g^{-1} in the 10th cycle. Nevertheless, the composite KVP/C-2-650 shows the worst C-rate capability as the specific discharge capacity is limited to only 41 mAh g^{-1} at C/2 and 29 mAh g^{-1} at 1C, which is the lowest for all investigated sintering temperatures. All other composites show similar C-rate capability, while the KVP/C composites sintered at 800 °C and 850 °C show slightly higher discharge capacities at higher C-rates of C/2 and 1C. Based on the voltage profiles shown in **Figure 22 b-g**, the voltage drop of KVP/C composites sintered at temperatures up to 750 °C appears at lower C-rates compared to composites sintered at 800 °C and 850 °C. This is especially the case for composite KVP/C-2-650, where a clear polarization at higher C-rates is obtained. As the specific surface is quite low and the carbon content is the highest for KVP/C-2-650, it seems a kind of similar behavior to the composite with a high sucrose content (KVP/C-3, chapter 6.1.2.2). A thicker carbon coating and possibly different carbon matrix at the surface of the granules could limit the potassium ion diffusion into the particles, which results in higher polarization and low discharge capacities at higher C-rates.[103,147,148] The overpotential of the composites sintered at temperatures of 800 °C and 850 °C seems to stay the lowest during the C-rate capability test. The polarization of KVP/C-2-850 stays lower at higher C-rates of C/2 and 1C compared to KVP/C-2-800. Nevertheless, the discharge capacity of the composite sintered at 850 °C is lower at moderate C-rates until C/5. Based on the microstructural data (**Table 7**) a sintering temperature of 850 °C seems to intensify the sintering process and builds up a better connectivity / larger area of contact between the primary particles, which could enhance the effective conductivity of the composites.[131] At low C-rates (C/20 to C/5) this effect does not seem to dominate as the specific discharge capacity for KVP/C-2-800 is higher with 62 mAh g^{-1} at C/20 and 55 mAh g^{-1} at C/5 in the 10th cycle of the corresponding C-rate (KVP/C-2-850: 58 mAh g^{-1} at C/20 and 52 mAh g^{-1} at C/5).

In summary, sintering temperatures of 800 °C and 850 °C for KVP/C-2 composites are slightly beneficial for C-rate capability based on the improved microstructural characteristics. This could be especially seen at a C-rate of C/2 with lower polarization and higher specific discharge capacity for KVP/C-2-800/850 compared to the other composites. At low and moderate C-rates up to C/5 a sintering temperature of 800 °C seems to be the optimum as the specific discharge capacity is higher compared to the composites sintered at 850 °C. At 1C discharge capacities of all KVP/C composites seems nearly similar, except for KVP/C-2-650 with the highest polarization and lowest discharge capacity at increasing C-rates. Nevertheless, KVP/C-2-800 seems to be the best compromise in terms of maximum depth of discharge at low C-rates and improved C-rate capability with relatively low polarization apparent at increasing C-rate.

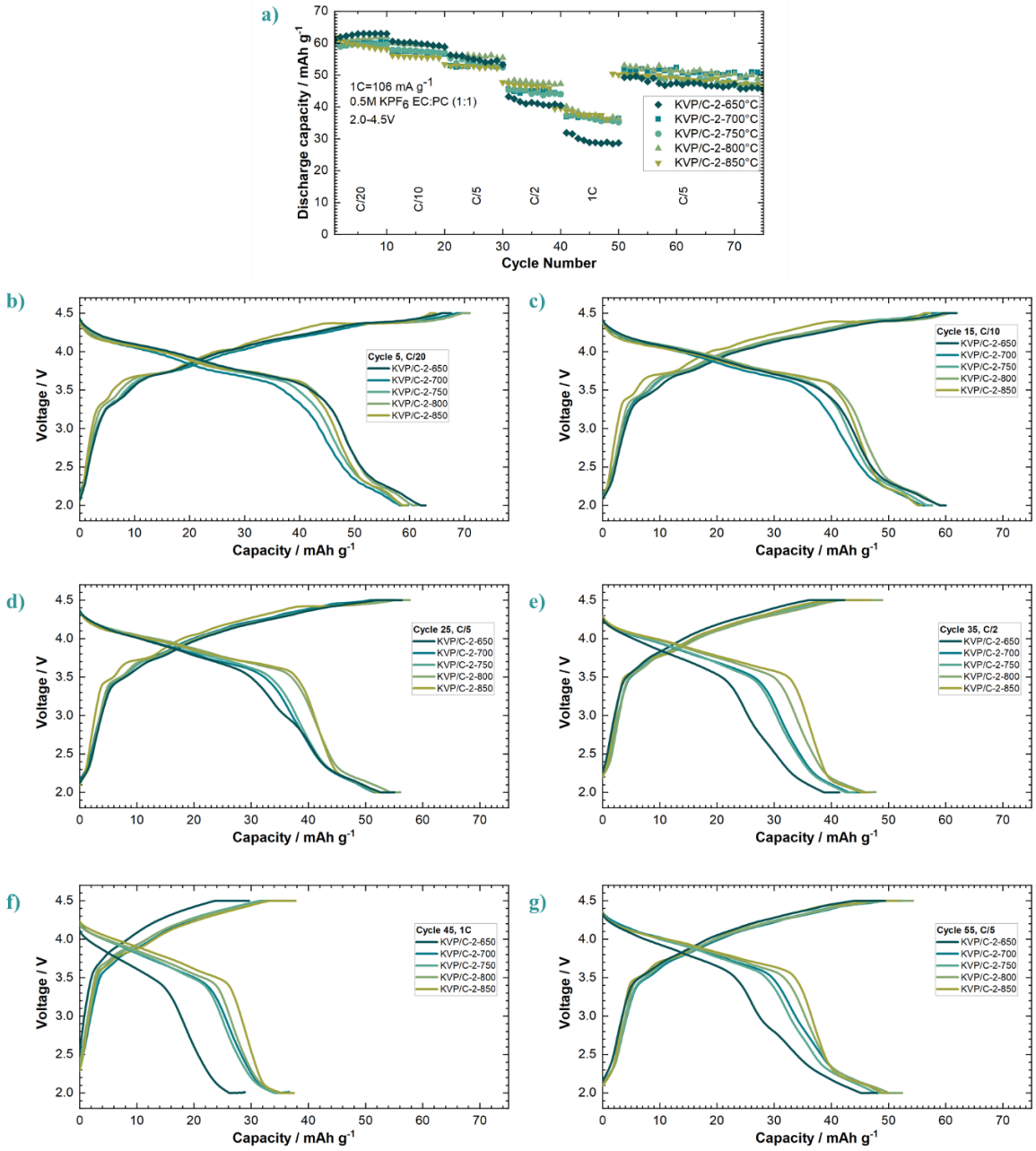

Figure 22: Electrochemical performance of KVP/C- composites (7.5 wt. % sucrose + 5 wt. % β-lactose) sintered at different temperatures with a) C-rate capability test, b)-g) voltage profiles in the 5th cycle at each studied C-rate during C-rate capability test. All tests were performed in PIB half-cells in potential window of 2.0 V - 4.5V, as an electrolyte 0.5M KPF_6 EC:PC was used.

As the differences in the microstructure and electrochemical performance are quite small for KVP/C composites sintered at different temperatures, the reproducibility of the complete synthesis process is shown for different batches of KVP/C-2 composites (composition of 7.5 wt. % sucrose + 5 wt. % β-lactose and sintered at 750 °C). The corresponding microstructural properties and maximum discharge capacities at C/20 in a PIB half-cell setup with their standard deviation are summarized in **Table 8.** The results obtained, show a high reproducibility of the developed synthesis process for hierarchical structured materials with just

minor deviations in the relevant powder characteristics and maximum discharge capacity at C/20. This indicates that the obtained electrochemical and microstructural characteristics for different sintering temperatures of the KVP/C composites show meaningful and reliable results in terms of material characterization. This should be even more the case if it is considered, that the different sintering temperatures were studied at one batch of the spray-dried KVP/C-2 composition. This further eliminates sources of error for the shown results of the KVP/C composites sintered at different temperatures.

It should be noted that the maximum specific discharge capacity at C/20 stated for batch KVP/C-2_CR was only studied within an electrolyte 0.5 M KPF_6 EC:PC with the addition of 0.5 vol. % of TMSP in PIB half-cells during a master thesis.[149] Later experiments revealed only minor differences in specific discharge capacities at C/20 caused by the addition of small amounts of electrolyte additives to the base electrolyte of 0.5M KPF_6 EC:PC.[132] Accordingly, the stated specific discharge capacity at C/20 of the composite KVP/C-2_CR is still comparable to the results from the other KVP/C-2 batches characterized in the base electrolyte 0.5 M KPF_6 EC:PC.

Table 8: Comparison of maximum discharge capacity and all relevant powder characteristics for three different batches of KVP/C composites with the composition of KVP/C-2 (7.5 wt. % sucrose + 5 wt. % β-lactose, sintered at 750 °C). Note: Specific discharge capacity for batch KVP/C-2_CR was studied in an electrolyte of 0.5 M KPF_6 EC:PC + 0.5 vol. % TMSP, while the other batches were studied in the base electrolyte of 0.5 M KPF_6 EC:PC.

Composite	**Max. Discharge Capacity at C/20 / mAh g^{-1}**	**C-Content after Sintering / wt. %**	**Median Secondary Particle Size / wt. %**	**Specific Surface / m^2 g^{-1}**	**Porosity / %**	**Pore size / nm**
KVP/C-2	58	3.6	13.6	20.7	38.3	153
KVP/C-2-750	60	4.1	12.7	20.0	33.9	110
KVP/C-2_CR	56	3.6	14.9	26.8	34.4	105
Mean KVP/C-2	**58 ± 1.6**	**3.8 ± 0.3**	**13.7 ± 0.9**	**22.4 ± 2.9**	**35.5 ± 2.0**	**123 ± 22**

6.2 KVPO/C

As introduced in chapter 3.1.2, KVPO is one of the most promising polyanionic cathode materials for PIBs, as it combines high intrinsic ionic conductivity with high average discharge potential. Due to these intrinsic properties of KVPO, a synthesis process for hierarchical structured KVPO/C composites similar to KVP/C was developed. Firstly, the structural evolution and microstructural characterization is discussed in chapter 6.2.1, while secondly the electrochemical behavior and performance is investigated in chapter 6.2.2.

For the synthesis of hierarchical structured KVPO/C composites some adjustments to the synthesis process of the KVP/C had to be made, as compounds with vanadium in valent oxidation state V(+IV) are hard to prepare *via* direct carbothermal reduction.[102]

Prior to the creation of hierarchical structured KVPO/C composites, the phase pure KVPO composite had to be synthesized as all approaches for direct synthesis of KVPO/C composites *via* a carbothermal reduction failed. The synthesis process of hierarchical structured KVPO/C composites was based on a comproportionation reaction scheme by Wernert *et al.* [93] and was further optimized in the framework of a student internship by Tabea Sostmann.[133]

Some of the results shown in this chapter are based on results of the student internship, which will be referenced to at each appropriate section.[133]

6.2.1 Structural Evolution and Characterization

6.2.1.1 Precursor Synthesis of VPO_4 and $VOPO_4$

The synthesis approach for KVPO was based on a comproportionation reaction out of a V(+III), VPO_4, and a V(+V), $VOPO_4$ precursor with K_2CO_3. The synthesis approach for both precursors is based on a classical solid-state reaction adapted from Wernert *et al*.[111]

Firstly, the synthesis reaction and structural evolution of the precursors was studied by TG/DSC-IR analysis to determine the appropriate synthesis conditions. In **Figure 23** the thermal analysis for both precursor syntheses are shown. Thermal analysis for VPO_4 was performed under Ar + 3 % H_2 atmosphere, while analysis for $VOPO_4$ was performed under synthetic air. The corresponding IR-spectra at the most important temperatures recorded during thermal analysis are shown in **Appendix 21**. The IR-traces of the respective gaseous byproducts were determined by subtracting a baseline in the IR-spectra to eliminate influences of ambient atmosphere inside the IR gas measurement cell, which could cause for example a continuous CO_2 and H_2O signal in the IR-spectra (**Appendix 21**).

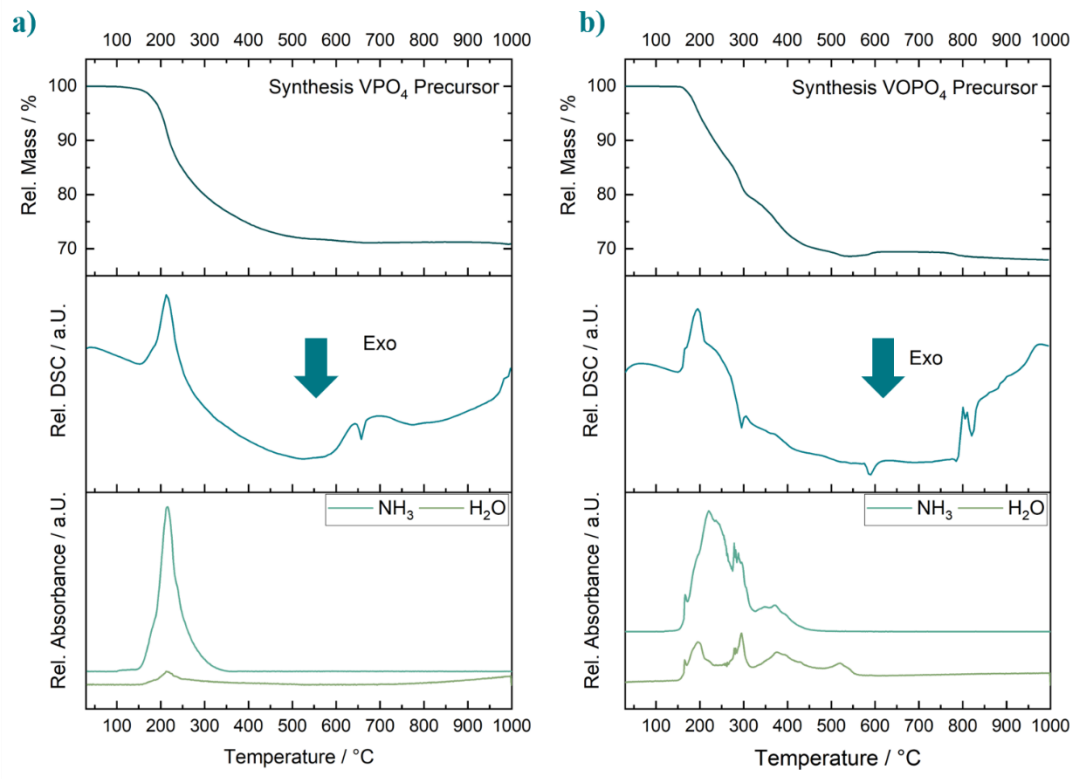

Figure 23: TG/DSC-IR analysis for the two precursors a) VPO_4 (under Ar + 3 % H_2) and b) $VOPO_4$ (under synthetic air) with TGA (top), DSC (middle) and FTIR-traces of main gaseous byproducts (bottom).

Synthesis of the VPO_4 precursors.

In the TG/DSC-IR analysis (**Figure 23a**) a distinct mass loss up to approximately 650 °C is observed. This distinct mass loss is caused by the release of H_2O and NH_3 due to the decomposition of the reactants NH_4VO_3 and $NH_4H_2PO_4$. Additionally, the mass loss is accompanied by a prominent endothermic peak in the DSC signal coupled with the main release peak in the IR-traces for these two gases at around 200 – 250 °C. The exothermic signal in the DSC curve around 650 °C is attributed to the crystallization of VPO_4. Based on these results a reaction temperature of 800 °C was selected, as it is above the crystallization temperature of around 650 °C. The following reaction scheme is proposed (**Equation 3**):

Equation 3: Proposed reaction scheme for the synthesis of precursor VPO_4 under reductive Ar + 3 % H_2 atmosphere.

$$NH_4VO_3 + NH_4H_2PO_4 + H_2 \xrightarrow{Ar+3\ \%\ H_2,\ \Delta T} VPO_4 + 2\ NH_3 + 3\ H_2O$$

A theoretical reaction turnover of around 63 % is expected for the synthesis of VPO_4. The relative mass after completion of the thermal analysis is about 70 %, which indicates a higher experimental reaction turnover compared to the theoretical calculated reaction turnover based on **Equation 3**. This difference becomes plausible if the homogenization and mixing of the

reactants for the VPO_4 synthesis is considered. The homogenization of the reactants was performed by high-energy planetary ball-milling in 2-propanol with subsequent evaporation of the 2-propanol at a rotary evaporator. Due to the high energy input during milling and evaporation of the 2-propanol, a partly decomposition of the reactants could be expected. This leads already to a release of NH_3 and H_2O during the preparation of the precursor prior to calcination. After mixing of the reactants and evaporation of the 2-propanol a typical smell of ammonia was usually observed. Mass losses, suggested decomposition products or reaction processes combined with onset temperatures for the TG/DSC-IR analysis are summarized in **Appendix 22**.

Synthesis of the $VOPO_4$ precursor.

A distinct mass loss until around 600 °C is observed in the TGA signal during synthesis of $VOPO_4$ under synthetic air (**Figure 23b**). A prominent endothermic signal around 200 – 250 °C is apparent in the DSC signal, coinciding with the primary peaks in the IR-traces of the gaseous byproducts NH_3 and H_2O. This phenomenon could be attributed to the decomposition of the reactants NH_4VO_3 and $NH_4H_2PO_4$. Around 300 °C a minor exothermic signal becomes apparent, which could be caused by the evolution of an intermediate compound or structural polymorph of β-$VOPO_4$ during synthesis.[150-152] At a temperature of 600 °C, another exothermic peak is obtained indicating the crystallization of the β-$VOPO_4$ precursor.[151] Accompanied with the exothermic signal around 600 °C, a mass increase around this temperature is visible in the TGA signal. This could be explained due to a prior reduction of $VOPO_4$ by the released NH_3 from the reactant decomposition with a subsequent oxidation under synthetic air at temperatures above 600 °C, as similar seen in literature before by Bagnasco *et al.*[153] As the temperature increased to around 800 °C some additional exothermic and endothermic signal appear in the DSC curve. This could either indicate further structural rearrangements into different polymorphs of the β-$VOPO_4$ or the start of a decomposition reaction.[150-152] According to literature above 800 °C a decomposition reaction of the $VOPO_4$ is taken place.[153] Based on these results, a calcination temperature of 750 °C was chosen for the synthesis of the β-$VOPO_4$ precursor, as this temperature is above the crystallization temperature of around 600 °C, but below the temperature at which decomposition begins, around 800 °C.

The following reaction scheme is proposed based on the discusses thermal analysis (**Equation 4)**:

Equation 4: Proposed reaction scheme for the synthesis of $VOPO_4$ precursor under synthetic air atmosphere.

$$NH_4VO_3 + NH_4H_2PO_4 \xrightarrow{syn.\,air,\,\Delta T} VOPO_4 + 2\,NH_3 + 2\,H_2O$$

According to the proposed reaction scheme, a reaction turnover of about 70 % is expected theoretically. This coincides with the relative mass during thermal analysis at the chosen calcination temperature of 750 °C with about 69.3 %, which further indicates the complete reaction to the proposed precursor β-$VOPO_4$. In **Appendix 23** the relative mass losses, suggested decomposition products or reaction processes combined with their onset temperatures for the TG/DSC-IR analysis are summarized.

In **Figure 24** the corresponding XRD pattern of the precursor materials are shown. The collected powder XRD pattern further confirm the findings of the thermal analysis and the complete reaction to the desired precursors VPO_4 and β-$VOPO_4$. The precursors were obtained as a greyish powder for the VPO_4 and a bright yellow powder for the β-$VOPO_4$ precursor (**Appendix 26a & b**). The XRD pattern of VPO_4 indicates phase purity for the precursor as no other reflexes are apparent, while for β-$VOPO_4$ some minor additional reflexes are apparent. These reflexes could be attributed to small amounts of impurity phase formed during synthesis of the β-$VOPO_4$.[133] As the amount of impurity phase formed is rather small, no further optimization of the precursor synthesis was performed and the two precursors were as used for the comproportionation reaction for KVPO synthesis discussed in the next chapter 6.2.1.2.

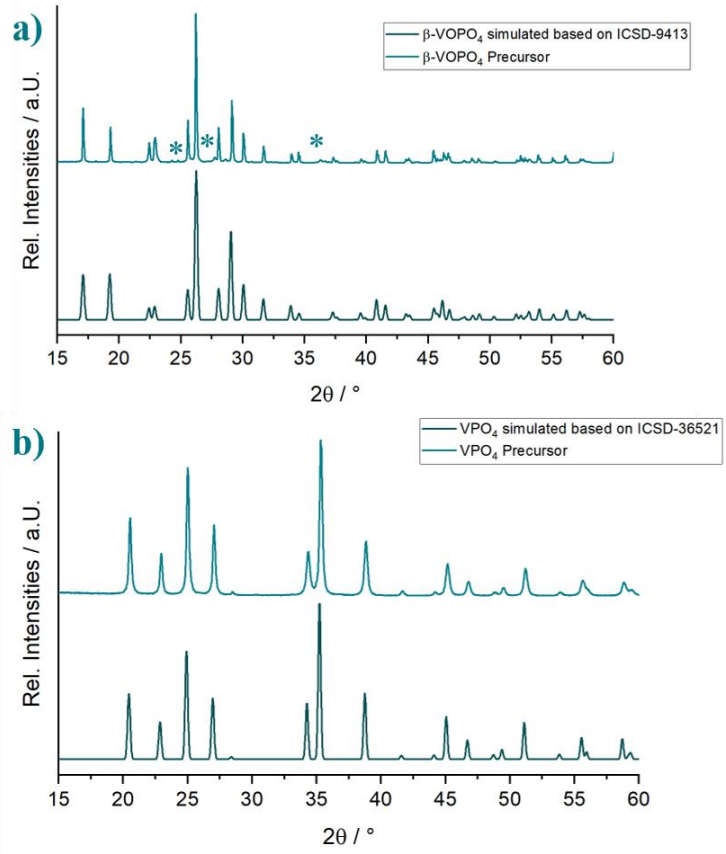

*Figure 24: Collected powder diffraction pattern for the two precursor materials with simulated diffraction pattern based on the structural models of a) β-$VOPO_4$ (ICSD-9413, ICSD release 2025.1, Gopal et al.[154]) and b) VPO_4 (ICSD-36521, ICSD release 2025.1, Glaum et al.[155]). Unknown impurity reflexes are marked with *. Adapted from student internship by Tabea Sostmann.[133]*

6.2.1.2 KVPO/C as Cathodic Material for PIBs

The principle idea for the synthesis of hierarchical structured KVPO/C composites was a 2-step-solid-state synthesis assisted by a spray-drying process. Firstly, *via* a comproportionation based on the previously discussed precursors $VOPO_4$ and VPO_4, the pure KVPO phase should be obtained. Secondly, a milling and spray-drying step followed by sintering in presence of β-lactose should create hierarchical structured KVPO/C granules similar to the KVP/C composites.

To study the phase evolution and comproportionation reaction, the KVPO synthesis was investigated by TG/DSC-IR analysis under Ar-atmosphere. The thermal analysis results for the comproportionation reaction of KVPO are provided in **Figure 25.**

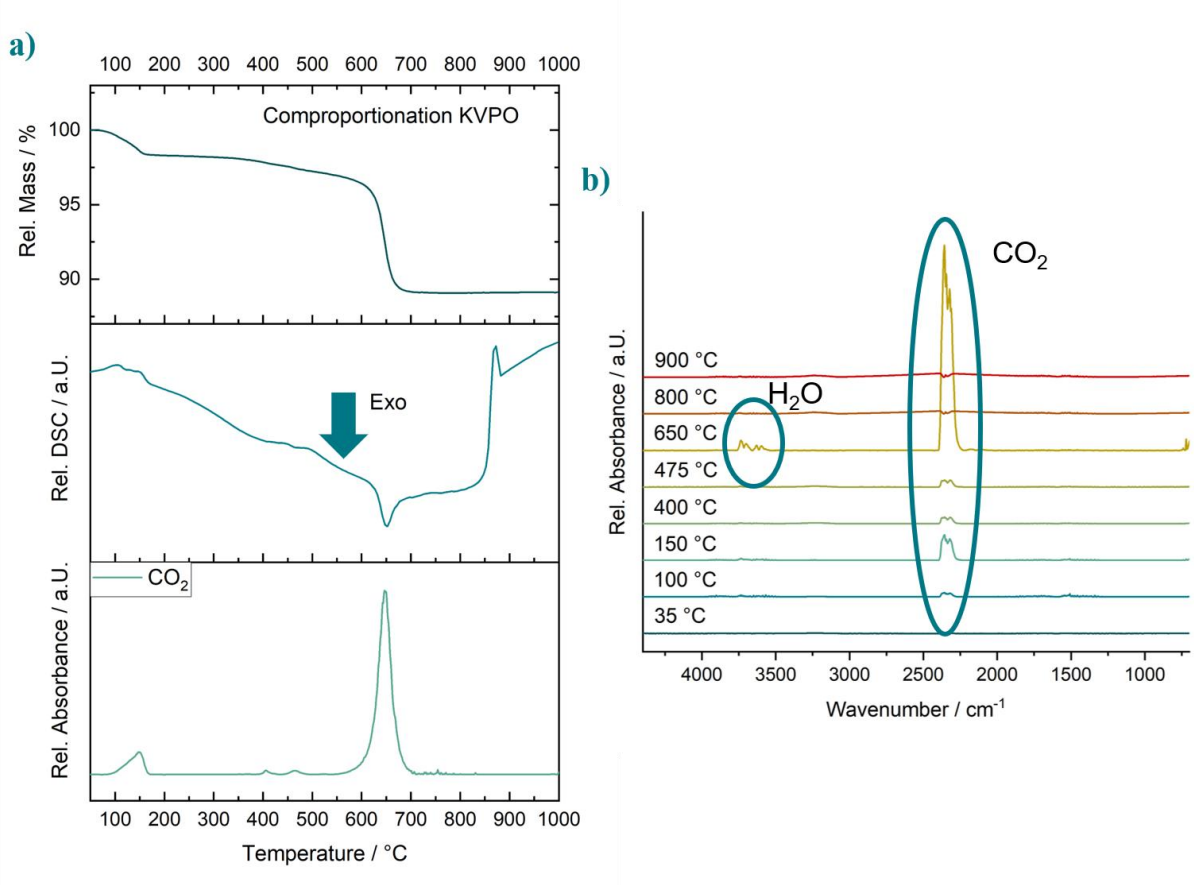

Figure 25: TG/DSC-IR analysis on the comproportionation reaction of KVPO under Ar-atmosphere. a) TGA (top), DSC (middle) and FTIR-traces of main gaseous byproducts (bottom), b) FTIR-spectra with marked gaseous byproducts at different temperatures during thermal analysis.

At temperatures between 100 – 200 °C a minor step in the TGA signal, accompanied with a small endothermic signal in the DSC curve and the release of CO_2 and H_2O apparent in the IR-traces is observed. This could be attributed to a beginning decomposition of the K_2CO_3 and evaporation of water adsorbed to the reactants. Between 550 °C and 700 °C the main mass

change appears, while a prominent exothermic peak in the DSC curve and the release of CO_2 indicates the crystallization of the KVPO phase. At temperatures around 850 °C, an endothermic peak in the DSC curve is observed, while no mass change or release of any gaseous byproducts is determined. This could be an indication for a melting process without any further decomposition reaction under Ar-atmosphere as additionally a dark brown glassy solid was obtained after completion of the thermal analysis. Based on these results a reaction temperature of 750 °C was chosen for the comproportionation reaction of KVPO. After calcination a brown powder was obtained (**Appendix 26c & d**). Based on the discussed results the following reaction scheme is proposed (**Equation 5**):

Equation 5: Proposed reaction scheme for the comproportionation reaction of KVPO under Ar-atmosphere based on the thermal analysis results.

$$K_2CO_3 + VOPO_4 + VPO_4 \xrightarrow{Ar,\Delta T} 2\,KVOPO_4 + CO_2$$

According to **Equation 5,** a reaction turnover of 90 % is expected theoretically. After completion of the thermal analysis a residual mass of 89 % was obtained, indicating a complete reaction during thermal analysis of the comproportionation reaction. Nevertheless, the powder diffraction pattern obtained for KVPO calcinated for 6 h at 750 °C under Ar-atmosphere (**Figure 26**) shows minor additional reflexes between 20 ° and 30 °. This indicates the formation of minor amounts of unknown impurity phases. As these reflexes are rather small, the amount of impurity phases formed could be assumed negligible.[133] Additionally, ICP-OES analysis (**Appendix 25**) revealed a stochiometric ratio for K:V:P of 1:1.06:1.06, which is probably the cause for the formation of the impurity phases formed as the amount of potassium is below the desired K:V:P-ratio of 1:1:1. The reflexes of the collected diffraction pattern are quite sharp with low background, indicating a high crystallinity of the KVPO sample. The crystallite size of the KVPO phase was estimated with 50 (1) nm.

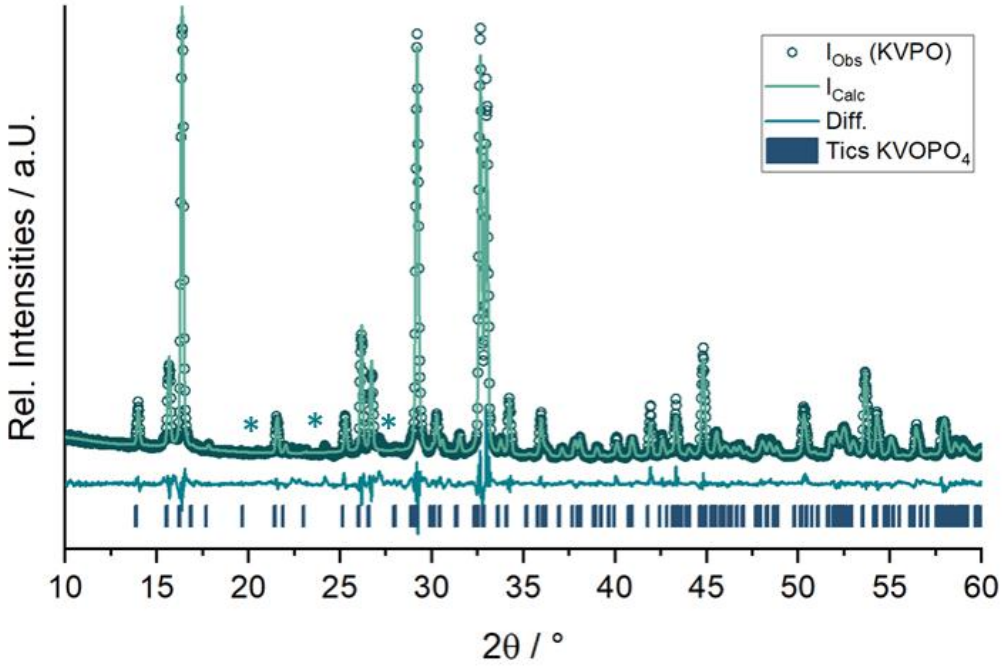

*Figure 26: Rietveld refinement on the orthorhombic structural model by Wernert et al.[93] (ICSD-47829, ICSD release 2025.1) with the symmetry $Pna2_1$ for KVPO against the obtained powder diffraction pattern of KVPO. Unknown impurity reflexes are marked with *. Adapted from student internship by Tabea Sostmann.[133]*

To obtain hierarchical structured KVPO/C composites, the KVPO material had to be ball-milled in presence of β-lactose and spray-dried afterwards. Subsequently, the secondary granules were sintered under Ar-atmosphere to obtain open porous KVPO/C composites. As V(+IV)-containing compounds are highly sensitive to carbothermal reduction in presence of a carbon source[102], several sintering temperatures and holding times of 1 h and 5 h were studied to maintain phase purity of the KVPO/C composites completion of the synthesis process. The collected powder diffraction pattern of KVPO/C composites sintered at different temperatures and holding times are summarized in **Appendix 27**. It is clearly observed, that the KVPO/C composites undergo severe decomposition / carbothermal reduction reaction at sintering temperatures of 700 °C and above. At these temperatures, several different phases with vanadium in the valent oxidation state V(+III) become apparent, like KVP_2O_7, V_2O_3 or $K_6V_2(PO_4)_4$. As a consequence, a sintering temperature of 650 °C was chosen, while the holding time was set to 1 h to keep the impurity formation due to carbothermal reduction as low as possible.[133] The resulting powder diffraction pattern of the KVPO/C composites sintered at 650 °C for 1 h under Ar-atmosphere is shown in **Figure 27**.

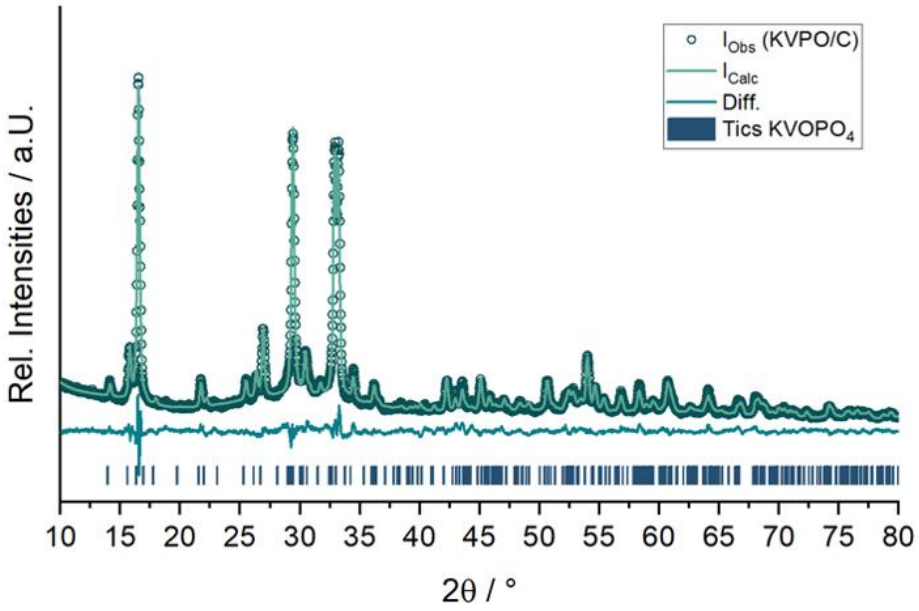

Figure 27: Rietveld refinement on the orthorhombic structural model by Wernert et al.[93](ICSD-47829, ICSD release 2025.1) with the symmetry $Pna2_1$ for KVPO against the obtained powder diffraction pattern of KVPO/C.

Table 9: All relevant powder characteristics for the synthesized KVPO/C composites.

Composite	Sintering Temperatue / °C	C-Content after Sintering / wt. %	Median Secondary Particle Size / µm	Specific Surface / $m^2 g^{-1}$	Porosity / %	Pore size / nm
KVPO/C	650	1.6	15.5	15.1	39.2	82

The Rietveld-refinement of the orthorhombic structural KVPO model (symmetry $Pna2_1$) against the obtained XRD data for the KVPO/C composite indicates nanocrystallinity (38 (1) nm crystallite size) inside the KVPO/C granules. The refined lattice parameters for KVPO/C are in good agreement with literature[92,93] (refined: a= 12.6789(8) Å, b= 6.3451(4) Å, c= 10.4667(4) Å, α=β=γ= 90 °, V= 853.98 $Å^3$). The necessary ball-milling process combined with the *in-situ* carbon coating decreased the crystallinity / crystallite size of the KVPO/C samples compared to the phase pure KVPO, which is indicated by a reflex broadening and increased background due to the apparent carbon coating in **Figure 27**. In **Table 9** the observed powder characteristics of the KVPO/C composites are summarized. Assuming a complete carbonization of the 5 wt. % β-lactose added, after sintering a carbon content of 2.1 % is expected theoretically. After completion of the synthesis process, the carbon content for KVPO/C was found to be less than the theoretical value, measuring only 1.6 %. The minor difference could arise due to a partly consumption of the carbon for reduction of minor amounts of vanadium from V(+IV) to V(+III). This correlates with the formation of minor amounts of

V(+III) containing compounds during sintering, as observed in the powder diffraction pattern of KVPO/C composites sintered at different temperatures (**Appendix 27**).[133]

Similar to the KVP/C composites, the developed synthesis process leads to an open intragranular porosity of 39.2 % with modal pore sizes of 82 nm. The specific surface of the composites was found to be 15.5 $m^2 g^{-1}$. SEM images of the KVPO/C composites confirm a spherical morphology of the secondary granules with open intragranular porosity. Cross-sections of the secondary particles reveal a homogenous distribution of the porosity throughout the secondary granules, while a thin denser surface layer is apparent (**Figure 28**). All the relevant powder characteristics of KVPO/C are quite similar to the KVP/C-2 composites (**Table** 6) with an optimized microstructure to improve the electrochemical performance.[133] This should lead to improved electrochemical performance based on the unique microstructure of the KVPO/C composites as well, which will be discussed in the next chapter 6.2.2.

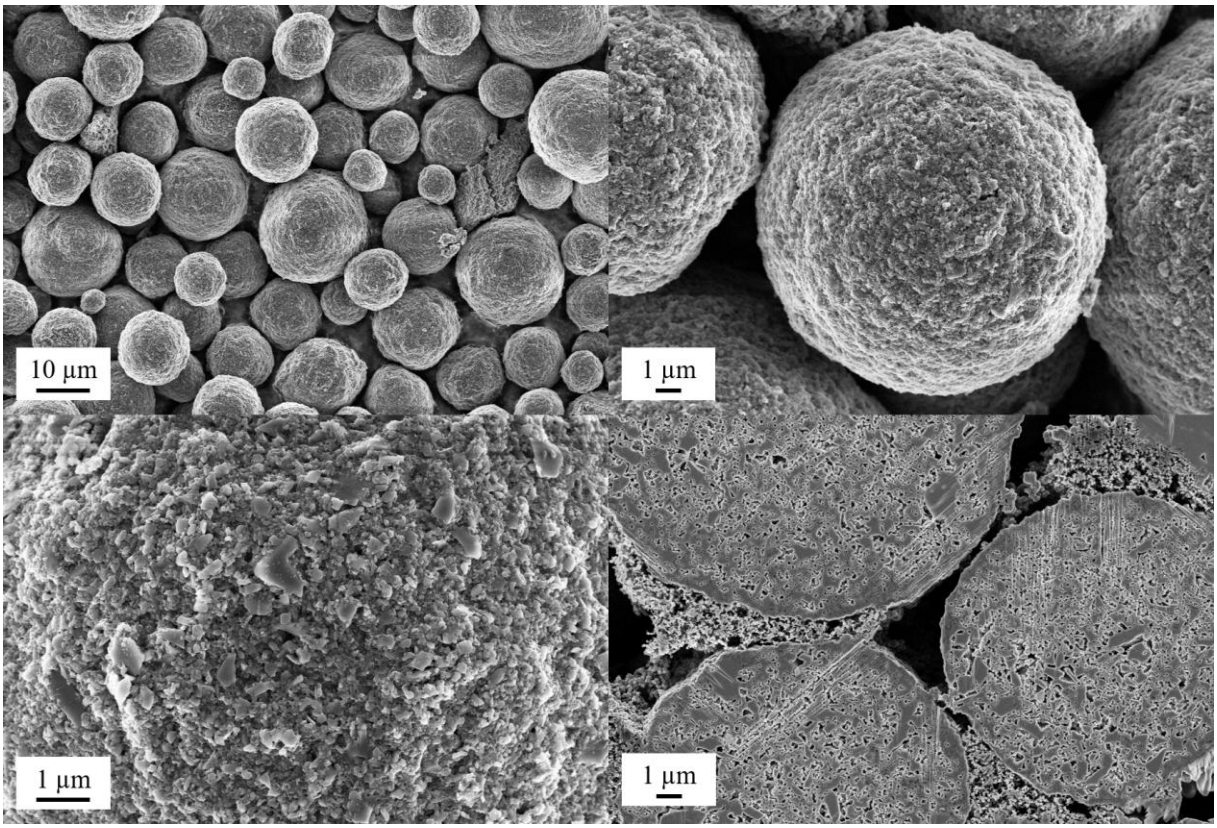

Figure 28: SEM images at different magnifications of the secondary KVPO/C granules to visualize the morphology and unique microstructure of the KVPO/C granules.

6.2.2 Electrochemical Performance of Hierarchical Structured KVPO/C-Composites

C-rate capability tests were performed at C-rates ranging from C/20 to 1C (1C = 133 mA g^{-1}) in a PIB half-cell setup. The C-rate capability and voltage profiles of the KVPO/C composite at the 5th cycle of each C-rate are visualized in **Figure 29**.

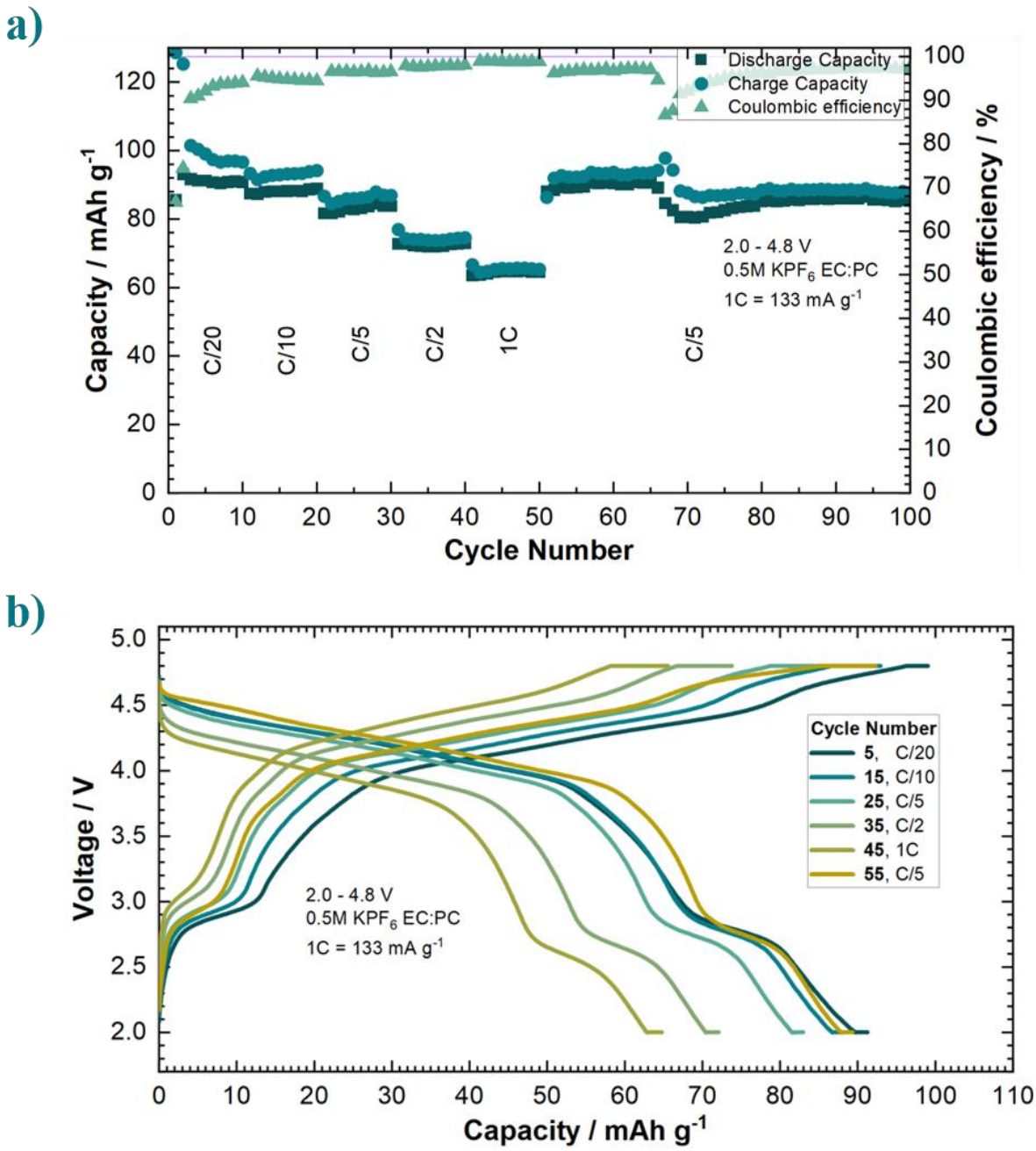

Figure 29: C-Rate capability test of the KVPO/C composite in a PIB half-cell setup, a) Specific charge and discharge capacity at different C-rates (1C = 133 mA g^{-1}), b) voltage profile of KVPO/C in the 5th cycle at each C-rate. As an electrolyte 0.5 M KPF_6 in EC:PC was used.

A maximum specific discharge capacity of 93 mAh g^{-1} at C/20 was observed for the hierarchical structured KVPO/C composite, while still 65 mAh g^{-1} remain at 1C. Compared to literature a significant enhancement in the performance is observed, where capacities of just 70 mAh g^{-1} or even below in similar voltage windows and low concentrated electrolytes were achieved.[92,93] The enhanced electrochemical performance compared to literature could be directly linked to the unique microstructure of the KVPO/C composites. As seen for the KVP/C composites before, the open porosity of 39.2 % combined with the high specific surface area (15.5 m^2 g^{-1}) and thin carbon coating, are beneficial for the electrochemical performance. These unique microstructural properties generate a highly percolated electronic network inside the KVPO/C composites, resulting in low polarization effects and improved reaction kinetics. The shortening of diffusion length inside the active KVPO/C phase combined with the nanocrystallinity (38 (1) nm crystallite size) of the active material could promote electrolyte penetration and interfacial contact. These effects result ultimately in an increased depth of discharge and potassium ion diffusion with improved C-rate capability compared to literature.[103,132] The drop in capacity between cycle 60 and 70 at C/5 could possibly be attributed to phenomena happening at the highly reactive potassium metal anode. The capacity stabilizes again after 70 cycles at around 82 mAh g^{-1} at C/5, which is comparable to the capacity achieved at C/5 between cycle 20 and 30. Possibly some parts of the formed organic SEI were dissolved leading to new free potassium surfaces, resulting in increased side reactions and formation of fresh SEI.[135,143,144,146] The drop in capacity coincides clearly with the drop in coulombic efficiency and strengthens this argument. Generally, the coulombic efficiencies stay low during the C-rate capability test. This could be mainly attributed to two reasons: Firstly, increased decomposition reactions of the used organic liquid electrolyte at the high potentials of up to 4.8 V.[92,132] Secondly, the continuous SEI formation on the potassium metal anode surface due to stability issues caused by the chemical composition of the SEI in PIB half-cells, as discussed before.[135,143,144,146]

Even if the relatively low average discharge voltage of around 3.7 V compared to literature (3.9 V - 4.0 V)[92,93] is considered, the obtained gravimetric energy density (based on half-cell data) of the KVPO/C composites with 344 Wh kg^{-1} (277 Wh kg^{-1} at C/20 in literature)[92] remains still improved. The relatively low average discharge voltage is mainly caused by a clear step in the voltage profile observed between 2.5 V and 3.0 V. The step in the voltage profile is observed in several other studies as well, but to our knowledge no explanation is given so far.[92,93] As discussed in chapter 6.2.1.2, it is possible that small amounts of vanadium are further reduced to V(+III) during sintering of the KVPO/C composites due to the apparent carbon in the

composites. This could provide a possible explanation for the observed step in the voltage profile between 2.5 V and 3.0 V, as the redox transition of V(+III) to V(+IV) is expected to occur at different potentials compared to the transition of V(+IV) to V(+V). Ding *et al.* studied the insertion of Na^+ into a partly depotassiated KVPO ($K_{0.36}VOPO_4$) and revealed an average voltage of the V(+III) ↔ V(+IV) transition of around 1.9 V - 2.0 V *vs.* Na^+/Na based on electrochemical data and DFT calculations. They conclude, that both redox transitions from V(+V) → V(+IV) and V(+IV) → V(+III) are electrochemically active in KVPO used in SIBs and PIBs.[112] To proof this hypothesis for the PIB case and the underlying electrochemical reaction mechanism for the potassiation / depotassiation for KVPO, XAS measurements of the pristine KVPO/C powder and the KVPO phase, combined with *operando* XRD measurements of KVPO/C in a PIB half-cell setup were performed.

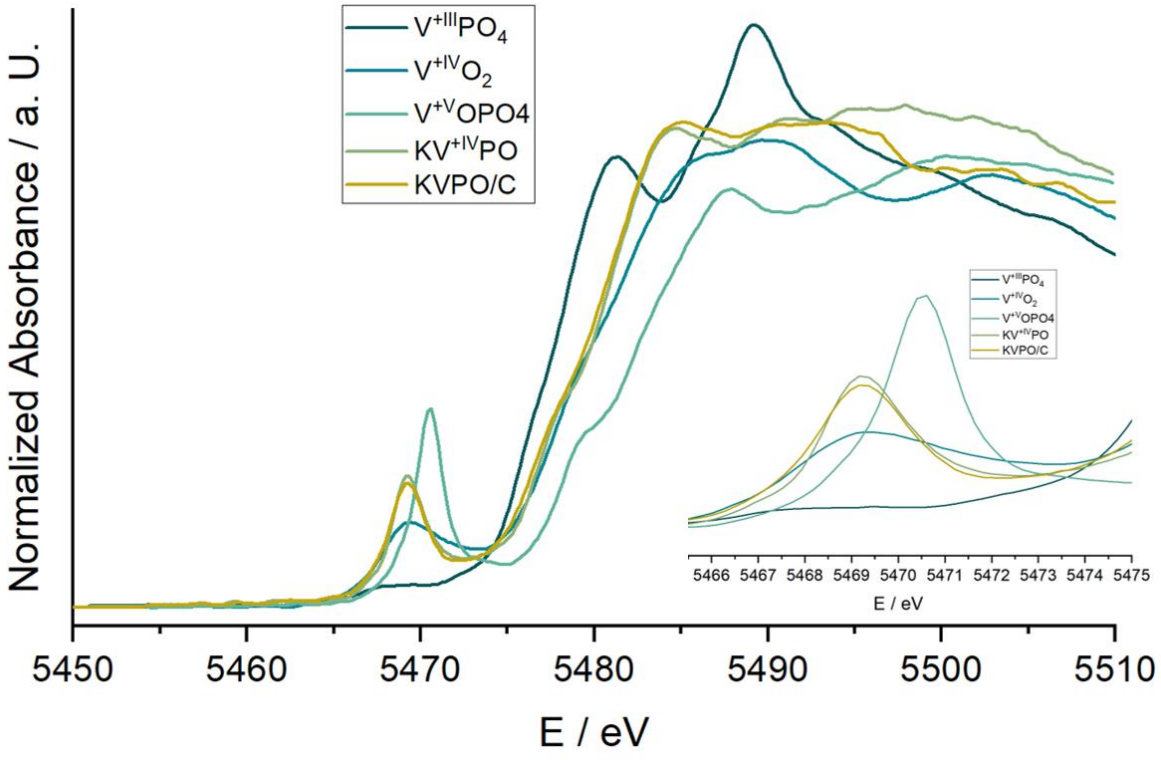

Figure 30: XAS measurements to determine the valent oxidation state of vanadium in the KVPO/C composites and pure KVPO with reference spectra for V(+III) (VPO_4), V(+IV) (VO_2) and V(+V) ($VOPO_4$).

The shown XAS measurements in **Figure 30** indicates the presence of V(+III) in the pristine KVPO/C powder. Based on the normalized data, the pre-edge peak for the KVPO/C composites is slightly shifted and decreased in amplitude compared to the pure KVPO phase. This could be seen as an indication for the presence of small amounts of V(+III) in the KVPO/C composites, as the pre-edge region is highly sensitive to the valent oxidation state of vanadium.[93] Additionally, the edge position for KVPO/C is minimal shifted to lower energies compared to

the pure KVPO phase, which could be seen as a further indication for the presence of V(+III) in KVPO/C. These small amounts of V(+III) could theoretically participate in the electrochemical reaction. The small redox peak in the first cycle around 2.8 V (oxidation) or 2.6 V (reduction) is electrochemically active from the first cycle and highly reversible, which further indicates the participation of small amounts of V(+III) and V(+IV) in the electrochemical reaction of the KVPO/C granules (**Appendix 29**). It should be mentioned, that the possible redox transition of the V(+III) to V(+IV) occurs at a higher voltage compared to the study by the Ding *et al.* (around 2.0 V) for KVPO in their PIB setup[112], which could be possibly caused by the highly reactive potassium metal anode itself or small amounts of another unknown electrochemically active phases with vanadium in the valent oxidation state V(+III) apparent in the KVPO/C composites.

Nevertheless, in the XAS spectra of two electrodes of KVPO/C precycled and stopped at 2.0 V ("fully" reduced to V(+III)) or 3.5 V ("fully" oxidized to V(+IV)) only a minor difference in the pre-edge peak region was revealed (**Appendix 28**). During the recurrent measurement for four times, the "fully" reduced electrode seems to oxidize continuously at the ambient atmosphere. In the first measurements, a small shift to lower energies and a reduced pre-edge peak intensity is visible compared to the "fully" oxidized sample. This indicates the presence of small amounts and active participation of V(+III) in the electrochemical reaction of the KVPO/C composites around 2.5 V – 3.0 V.

To study the underlying electrochemical reaction mechanism and possible impact of the transition from V(+III) to V(+IV) onto the crystal structure of KVPO, the *operando* XRD data in a voltage window from 2.0 V – 4.8 V for the first two cycles are shown in **Figure 31**. The *operando*-XRD cell was cycled at C/20 (1C = 133 mAh g^{-1}) in a PIB half-cell setup. Due to the quality of the obtained diffraction patterns (peak broadening at higher reflex angles due to the experimental diffraction geometry and lower intensity) only a qualitative analysis of the reaction mechanisms was possible at the reflexes at lower reflex angles. Exact calculations of lattice parameters or amount of K^+ de- / inserted were not possible and reliable enough.

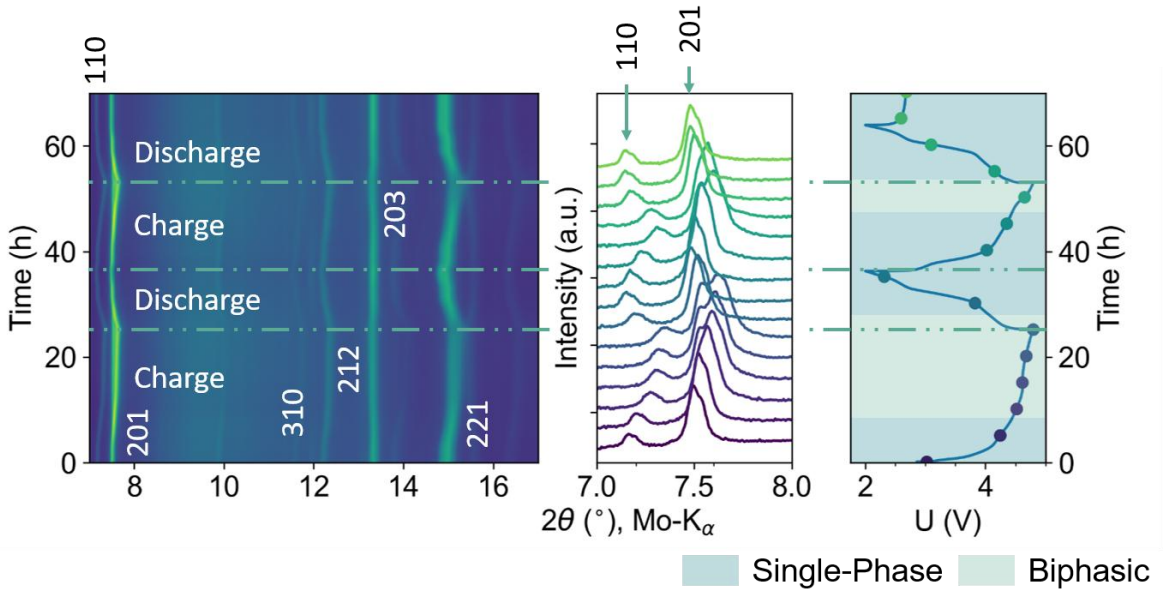

Figure 31: Collected operando XRD data of KVPO/C composite to study the electrochemical reaction mechanism in a PIB half-cell setup in a voltage window of 2.0 V – 4.8 V at C/20. The corresponding charge / discharge cycles (dashed lines) and indexed hkl reflexes are marked. As an electrolyte 0.5M KPF_6 in EC:PC was used.

During the first charge process, the hkl reflexes 110 and 201 shift gradually to higher angles until around 4.5 V and no additional reflexes appear in this region. Additionally, the reflexes are quite sharp until 4.5 V. Based on this behavior, the reaction mechanism could be described as a single-phase or solid-solution mechanism in this voltage region. Between 4.5 V and 4.8 V, the pristine reflexes shift to higher angles, broaden and an additional shoulder / reflex at the main 201 reflex appears. This indicates the transition to a two-phases or biphasic reaction. The high voltage phase transition could possibly be caused by the existence of small fractions of fully depotassiated particles leading to isostructural $VOPO_4$.[114] The main 203 reflex continuously broadens during charge and discharge respectively, with reflex maxima at the pristine states of KVPO/C. During discharge the same behavior is obtained *vice versa,* indicating the high reversibility of the underlying redox reactions. This is underlined by additional CV measurements with high reversibility of the corresponding redox peaks (**Appendix 29)**.

Especially in the low voltage region between 2.0 V and 3.0 V no additional reflexes appear and only a gradual shift of the 110 and 201 reflexes is obtained. This indicates a solid-solution reaction mechanism in this voltage region during the redox transition from small amounts of V(+III) to or from V(+IV). The same behavior is obtained for the 221 reflex, as observed in the contour plot. The minor pristine 310 reflex around 12 ° is only observed in this low voltage region and vanishes during cycling above 4.5 V, which is a further indication for the solid-solution behavior till 4.5 V. With increasing / decreasing voltage during cycling, the KVPO is

depotassiated / potassiated, which could lead to a change in reflex intensity or symmetry due to different amounts of potassium inside the crystal structure. As previously discussed by Li *et al.*, the 310 reflex vanishes due to a phase transition caused by the relaxation of the residual potassium ions into new positions of the KVPO framework.[110,114] The results of the *operando*-XRD measurements correlate well with the literature regarding the electrochemical reaction mechanism.[92,110,114] For a more in-depth and quantitative analysis of the electrochemical reaction mechanism, *ex-situ* XRD on KVPO/C samples charged / discharged to different state-of-charges are necessary. Based on this *ex-situ* XRD data changes in the lattice parameters and potassium contents could be calculated *via* Rietveld-refinements at different state-of-charge to allow a more detailed view onto the electrochemical reaction mechanism.

As the contour-plot after the second cycle (discharge) looks completely similar to the pristine state and no additional impurity was found in the pristine powder of KVPO/C (**Figure 27**), the hypothesis of an reversible intercalation of more than one K^+ per formula into the KVPO/C structure leading to the redox transition V(+IV) → V(+III) becomes plausible, as previously described by Ding *et al.* as well.[112] This is underlined by the previously discussed XAS results indicating the presence of V(+III) already in the pristine KVPO/C samples.

In summary, a clearly improved electrochemical performance is achieved for hierarchical structured KVPO/C composites. These improvements rely mainly onto the unique microstructure with high intragranular porosity and specific surface area combined with a thin carbon coating. Additionally, the underlying electrochemical reaction mechanism and cause for the lowering in average discharge voltage were determined by *operando*-XRD and XAS. The lowering in average discharge voltage could be caused by the redox transition of small amounts of V(+III), formed during the sintering in presence of carbon and determined by XAS, to V(+IV). Nevertheless, this redox transition has no negative impact onto the reversibility of the electrochemical processes of the KVPO/C composite, ultimately resulting in good cyclability with improved electrochemical performance.

6.3 Limitations of Electrochemical Characterizations in Half-Cells

The development of advanced cathode materials and electrolytes for PIBs makes precise and reliable electrochemical characterization techniques inevitable.[21,156] Traditionally, most electrochemical characterization for alkali ion batteries are performed in half-cell setups, where the metallic counter electrode (CE), in the case of PIBs metallic potassium, is utilized to study the insertion characteristics of an electrode material as the working electrode (WE).[135,146,157,158] Nevertheless, several recent studies revealed serious issues accompanied with metallic counter electrodes in Post-Lithium-systems, especially for PIBs. The practical problems associated with metallic potassium counter electrodes include high resistivity of the metal itself, resulting in increased cell polarization, fast formation of resistive surface layers and growth of mossy structures and dendrites.[135,143-146] One of the main issues is the poor passivation of the potassium metal from recurrent electrolyte degradation processes, which could amplify resistive surface layer growth and side reactions from the formation of parasitic soluble electrolyte degradation products. As the potassium metal counter electrode builds up high resistivity and polarization during cycling, which is additionally strongly dependent onto applied currents, it causes an increased bias during C-rate capability tests and cycle life assessment for different electrode materials.[37]

All of the mentioned issues above could massively influence the electrochemical characterization of electrode materials and lead to underestimated material properties if potassium metal is used as CE.[135,156,158-160] To gain first insights and study the limitations of the potassium metal counter electrode onto the electrochemical performance of the KVP/C composites in PIB half-cells, the 3-electrode setup with a Ag / AgCl RE from Panasenko *et al.* was used.[135] In **Figure 32** the corresponding 3-electrode-cell data for KVP/C-2 as a WE with potassium metal as a CE and Ag / AgCl as the RE is shown. Compared to the PIB half-cell tests, the investigated potential window was reduced to 2.5 V – 4.5 V as otherwise the cell setup did not work due to problems associated with the RE. As an electrolyte 0.5 M KPF_6 in EC:PC was used, while the C-rate was set to C/20 (1C = 106 mA g^{-1}).

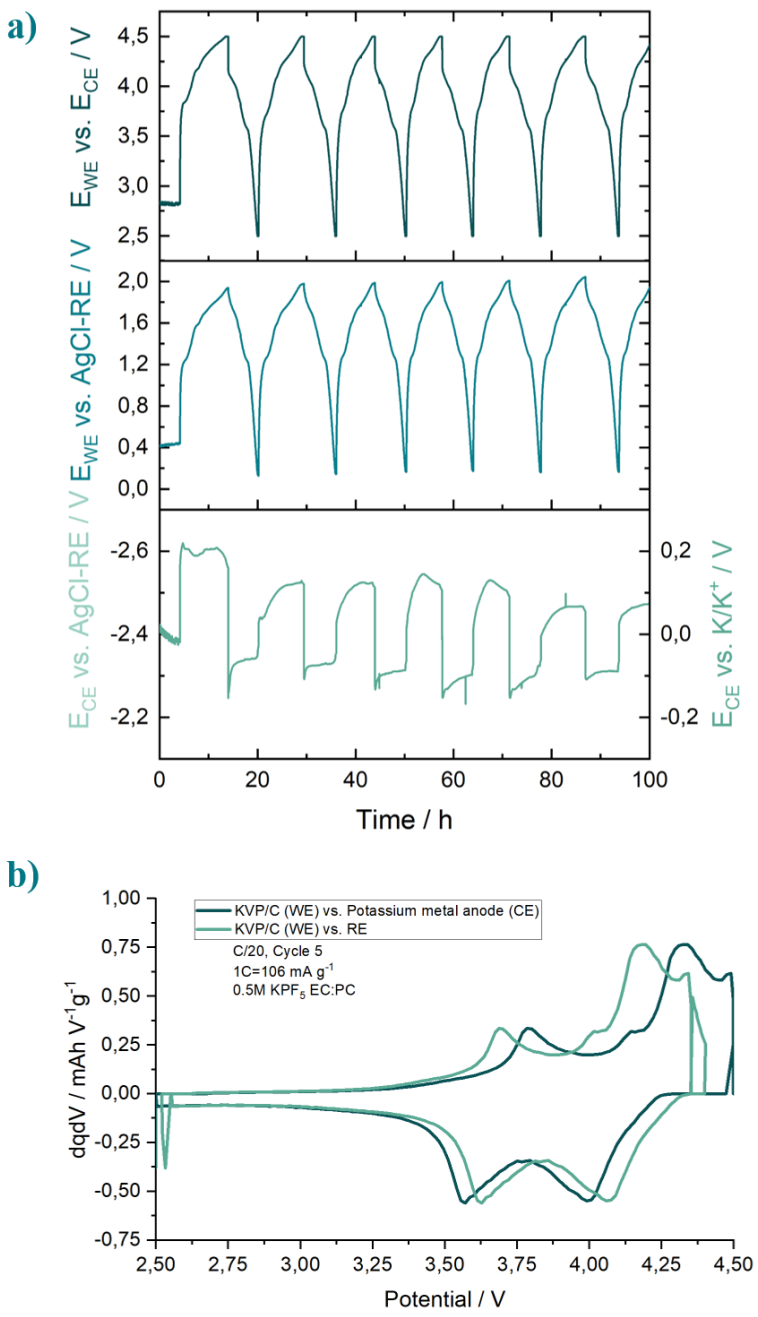

Figure 32: 3-electrode-cell measurement with KVP/C-2 as WE, potassium metal as CE and Ag / AgCl as RE with a) WE vs CE-potential (upper), WE vs. RE-potential and CE vs. RE-potential over time and b) dq/dV-plot of the 5th cycle for KVP/C-2 vs. CE and KVP/C-2 vs. RE.

Based on the 3-electrode-cell measurement it becomes obvious how strongly the electrochemical characterization of the KVP/C-2 composite is influenced by the potassium metal counter electrode in a PIB half-cell setup. Not only a huge polarization of about 300 mV in total (±150 mV), but also a highly drifting potential during cycling is obtained for the potassium metal counter electrode (**Figure 32 a, lower**). This significantly alters the cut-off potentials of the KVP/C-2 WE during cycling (**Figure 32 a, middle**) and leads to an increased overpotential in the cell voltage already apparent at low C-rates (C/20). The increased

polarization becomes immediately visible in the dq/dV-plot of the fifth cycle at C/20 (**Figure 32 b**). The dq/dV-plot for the cell voltage in a half-cell setup (KVP/C-2 WE vs. potassium metal CE) shows a high polarization between the corresponding redox-peaks apparent for the KVP/C-2. Conversely, the dq/dV-plot of the KVP/C-2 (WE) potential against the Ag / AgCl RE shows a small polarization of onyl 70-80 mV indicating the improved electronic and ionic conductivity of the KVP/C composites discussed in chapter 6.1. As the huge impact of the potassium metal counter electrode becomes directly visible in this 3-electrode-setup, it is raising the question:

How reliable and precise are electrochemical characterizations performed in PIB half-cell setups?

To obtain reliable and more precise electrochemical characterization results, the introduction of an additional RE in a 3-electrode setup or a suitable diagnostic electrode (DE) instead of the potassium metals in a classical half-cell setup is inevitable. One of the main prerequisites for a RE is its well-defined redox potential and stability over time without any applied current. Additionally, the RE should be chemically inert and work in the electrochemical stability window of the electrolyte.[135,156,157,161] Conversely, a DE should provide a stable potential with a well-defined redox reaction during cycling and faster reaction kinetics than the WE to prevent or keep the impact of polarization effects as small as possible in a half-cell configuration.[161-164]

Three different categories for RE are practically described in literature: the metal itself, alloys or insertion type materials.[161] In the research area of PIBs only a few reports on the development of different RE for PIBs are available. For example, Komaba *et al.* utilized potassium metal after a pretreatment as a RE to overcome limitations of the inaccurate rest potential of the potassium metal electrode.[158] Nevertheless, potassium stays highly reactive to the electrolyte on contact, which could lead to parasitic side reactions by electrolyte degradation products.[135] Finally, this could massively influence the electrochemical performance of the WE. Jagger *et al.* studied different potassium alloys regarding their application as RE in PIB setups. Their Bi-Bi_2-K system stabilized its potential quickly with low drift rates, enabling its use as a RE in 3-electrode-setups for PIBs.[156]

To our knowledge no studies utilizing insertion type materials as RE or DE for PIBs are reported so far. Inspired by the successful application of LTO or semi-charged LFP as RE and / or DE in the field of LIBs[162,163,165,166], two different potassium titanium phosphates were evaluated regarding their possible utilization as a RE or DE for PIBs in the following chapter.

7 Development of Polyanionic Reference and Diagnostic Electrodes for PIBs

Based on the intrinsic properties of the previously introduced Ti-based polyanionic materials KTP/C and KTPO/C (chapter 3.2), these two materials were studied as RE and DE. The synthesis of the materials followed the developed process of the KVP/C composites, while minor adjustments were made with respect to the underlying chemical reactions.

Firstly, the synthesis and characterization will be discussed in chapter 7.1.1 and 7.1.2 respectively for KTP/C and KTPO/C. Secondly, the utilization of the two Ti-based polyanionic materials as RE and DE is studied (chapter 7.2 and 7.3) to allow a precise and more reliable characterization of electrode active materials for PIBs.

7.1 Synthesis and Characterization of Hierarchical Structured Potassium-Titanium-Phosphate-Carbon Composites

7.1.1 KTP/C as Electrode Material for PIBs

It should be noted that some of the results shown in this chapter are based on a master thesis project from Joshua Atencio Psille under the supervision of the author, which will be referenced to at each appropriate section.

The synthesis of the hierarchical structured KTP/C composites followed the classical 2-step solid-state approach combined with a spray-drying step analogue to the KVP/C composites. As the addition of a carbon source for the calcination step led to increased impurity phase formation, just for the spray-drying step a carbon source (12.5 wt. % β-lactose) was added. The calcination of the KTP phase was performed without any carbon / carbon source apparent under synthetic air at 850 °C.[134] To study the phase evolution and crystallization behavior of KTP, TG/DSC-IR analysis was performed under synthetic air. The corresponding analysis data is shown in **Figure 33**.

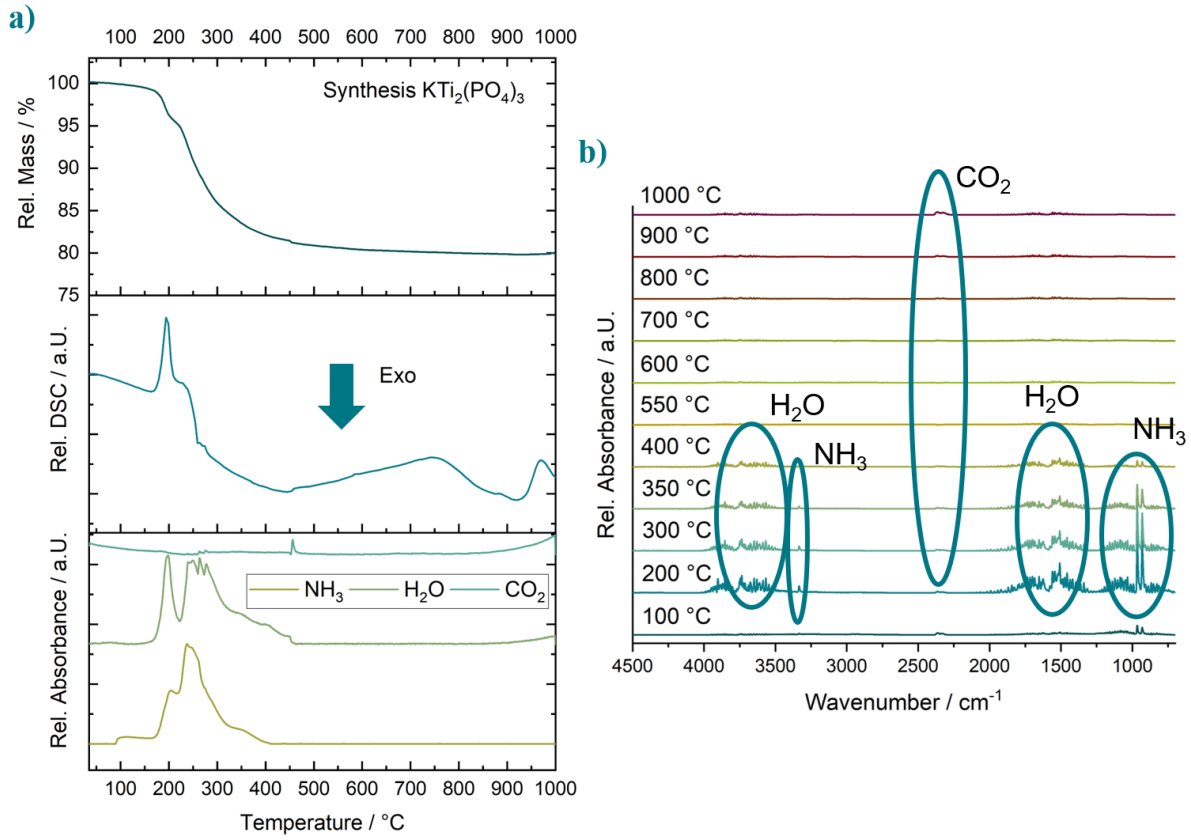

Figure 33: TG/DSC-IR analysis on the synthesis reaction of KTP under synthetic air. a) TGA (top), DSC (middle) and FTIR-traces of main gaseous byproducts (bottom), b) FTIR-spectra with marked gaseous byproducts at different temperatures during thermal analysis.

A continuous mass loss is observed until around 600 °C. At higher temperatures no further mass loss is detected. The mass loss coincides with an endothermic peak in the DSC signal around 200 °C and the release of NH_3 and H_2O (150 °C - 400 °C) indicating the decomposition of the reactant $NH_4H_2PO_4$. Additionally, as CO_2 is quite IR-sensitive a significant peak for CO_2 should be observed in the IR-traces due to the decomposition of K_2CO_3. Beside a minor peak in the IR-trace at around 450 °C, no further IR-signal of CO_2 was detected. During preparation of the precursor *via* ball-milling in 2-propanol or during storage of the precursor the K_2CO_3 decomposes, leading possibly to KOH as a potassium source. This was confirmed by additional FT-IR measurements on the precursor and reactants (**Appendix 30**) Decomposition of KOH is accompanied with a loss of water at elevated temperatures, which correlates well with the IR-trace for water and explains the missing CO_2 signal in the IR-traces. Additionally, small amounts of the K_2CO_3 could react with the $NH_4H_2PO_4$ to K_2HPO_4 during precursor preparation, as discussed for the KVP/C composites before. At around 750 °C and up to 950 °C a broad exothermic area is apparent in the DSC signal, which indicates the crystallization of the KTP

phase during synthesis under synthetic air. Based on the discussion above and the assumption of KOH as potassium source, the following reaction scheme is proposed (**Equation 6**):

Equation 6: Proposed reaction scheme for the synthesis of KTP under synthetic air based on the thermal analysis results.

$$2\,KOH + 4\,TiO_2 + 6\,NH_4H_2PO_4 \xrightarrow{syn.\ \text{air},\ \Delta T} 2\,KTi_2(PO_4)_3 + 6\,NH_3 + 10\,H_2O$$

Based on **Equation 6** a reaction turnover of around 75 % is expected theoretically after synthesis. After completion of the thermal analysis a residual mass of 80 % was detected. The differences in the reaction turnover could arise due to a possible decomposition of the reactant $NH_4H_2PO_4$ during ball-milling in 2-propanol and subsequent evaporation of the 2-propanol or storage, leading to the release of NH_3 and H_2O. Similar to the synthesis of the VPO_4 precursor, after ball milling a typical smell of ammonia was obtained during preparation of the KTP precursor. Additionally, similar to the precursor preparation of KVP/C, a reaction of $NH_4H_2PO_4$ with the potassium source KOH / K_2CO_3 during the precursor preparation is possible. This could lead in fact to an increase in the theoretical reaction turnover as similar discussed for the KVP/C precursor.

Based on the results from thermal analysis, the calcination temperature for the synthesis was set to 850 °C, as this temperature is located in the center of the broad crystallization area of the KTP phase. ICP-OES analysis of the as synthesized KTP phase reveals a stochiometric ratio of K:Ti:P of 1.07:2:3.08, which shows a minor Ti-deficiency. Nevertheless, the obtained diffraction pattern of the as synthesized KTP phase revealed no additional impurity reflexes, indicating phase purity based on the XRD analysis (**Figure 34a**). Similar to the pure KVPO, the reflexes of the KTP phase are quite narrow with low background, indicating a high crystallinity. The crystallite size was estimated as 81 (2) nm *via* the Rietveld-refinement.

For synthesis of hierarchical structured KTP/C composites, a spray-drying step with subsequent sintering in the presence of 12.5 wt. % β-lactose has to be applied. For sintering of the secondary granules under Ar-atmosphere, a lower temperature was necessary to prevent carbothermal reduction of Ti(+IV) and remain phase purity. At sintering temperatures above 700 °C, additional impurity reflexes corresponding to the formation of the cubic $K_2Ti_2(PO_4)_3$ and indicating the partwise reduction of Ti(+IV) to Ti(+III) become apparent **(Appendix 31**).[134] As a consequence to these results, a sintering temperature of 700 °C for the synthesis of hierarchical structured KTP/C composites was used. The corresponding diffraction pattern with the performed Rietveld-refinement on the structural model of the rhombohedral KTP phase (symmetry $R\bar{3}c$, ICSD-67091, ICSD release 2025.1, Lunezheva *et al.*[136]) for KTP/C sintered at

700 °C under Ar-atmosphere is shown in **Figure 34 b**. The performed refinement is indicating nanocrystallinity (40 (1) nm crystallite size) of the KTP/C granules. The necessary ball-milling step and *in-situ* carbon coating is reducing the crystallinity / crystallite size compared to the pure KTP phase, which is further indicated by broader reflexes and increased background due to the apparent carbon coating. Nevertheless, a good agreement between the observed and calculated pattern is observed. The refined lattice parameters for KTP/C correlate well with the literature[115,117] (refined: a=b= 8.3615(1) Å, c= 23.1005(6) Å, α=β= 90 °, γ=120 °, V= 1398.92 Å^3).

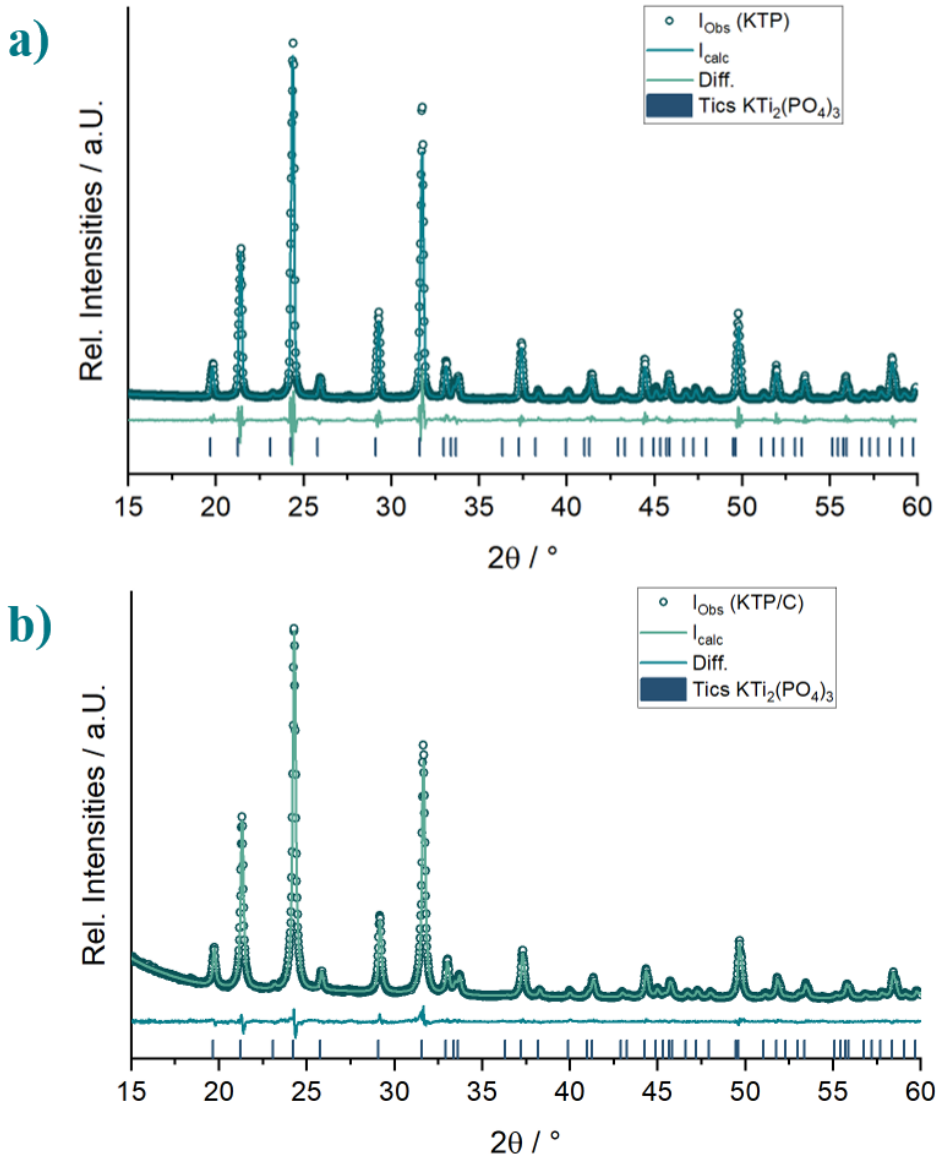

Figure 34: Rietveld-refinement on the rhombohedral structural model with the symmetry $R\bar{3}c$ of KTP (ICSD-67091, ICSD release 2025.1, Lunezheva et al.*[136]) against the obtained powder diffraction pattern of a) KTP and b) KTP/C. Adapted from master thesis project from Psille.[134]*

In **Figure 35** SEM images of the nearly spherical KTP/C granules with the corresponding cross-sections are shown, while in **Table 10** all powder characteristics are summarized. The granules

appear to be spherical with grooves on their surface. This indicates that the binder (PAA) or the solid content in the spray-drying dispersion is too low to stabilize the spherical morphology.[140] Nevertheless, similar to the vanadium-based active materials, KTP/C granules with an open intragranular porosity of 49.3 % and nanometer sized primary KTP/C particles are successfully synthesized *via* the developed synthesis process in this thesis.[134]

Table 10: Summary of all powder characteristics after completion of the synthesis process for the KTP/C composite sintered at 700 °C, according to the master thesis project from Psille.[134]

Composite	Sintering Temperatue / °C	C-Content after Sintering / wt. %	Median Secondary Particle Size / µm	Specific Surface / $m^2 g^{-1}$	Porosity / %	Pore size / nm
KTP/C	700	4.2	10.2	49.4	49.3	66

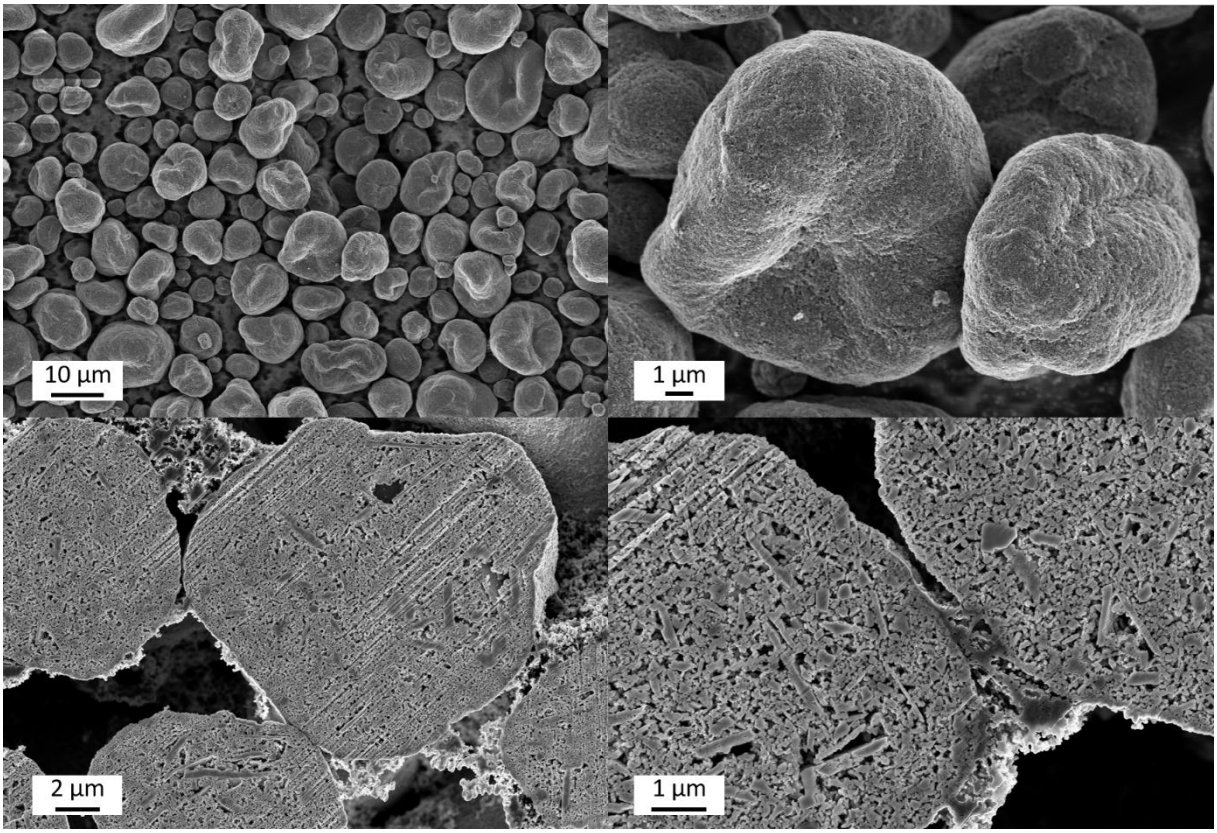

Figure 35: SEM images of the morphology of the KTP/C granules (top) and the corresponding cross-sections (bottom) after sintering at 700 °C under Ar-atmosphere, adapted from master thesis project from Psille.[134]

Assuming a complete carbonization of the β-lactose, a carbon content of 5.3 % is expected theoretically. Conversely, just 4.2 % of residual carbon were measured after sintering for 5 h at 700 °C under Ar-atmosphere. The differences could arise due to a partial reduction of Ti(+IV) to Ti(+III) by carbon, which does not influence the obtained XRD pattern as possibly the

impurity phase formation is too small to detect *via* XRD analysis. Another explanation could be an incomplete carbonization of the β-lactose, which means that not every C-atom of the β-lactose was carbonized and released as gaseous byproducts in form of lower molecular species like CO_2 or CO during decomposition of the β-lactose. The release of CO_2 and CO at elevated temperatures was visible during the calcination reaction of KVP/C in presence of sucrose (**Figure 11**) as well, which could further strengthen this argument.[132]

The cross-sections of the KTP/C granules reveal an open and homogenous distributed intragranular porosity, while no dense surface layer was visible for the KTP/C granules compared to the other composites. The open porosity without any dense surface layer at the surface of the granules is beneficial for electrolyte penetration, as no hindrance is apparent at the surface of the granules. Combined with the high specific surface of 49.4 $m^2\ g^{-1}$, the open porosity (49.3 %) and the high carbon content of the KTP/C creating a unique microstructure, which should be beneficial for the electrochemical performance overall due to the improved electronic conductivity and diffusion kinetics, as discussed previously for the vanadium-based composites.[132,134]

To characterize the basic electrochemical properties like maximum charge capacity and C-rate capability of the KTP/C composites, galvanostatic cycling at different C-rates (1C = 128 mA g^{-1}) in a voltage window between 1.0 V – 4.0 V in a PIB half-cell setup was performed. To study the underlying electrochemical reactions *operando*-XRD measurements during galvanostatic cycling at C/20 in a PIB half-cell setup was performed. All galvanostatic cycling experiments start with discharge (reduction) for the KTP/C composite, as it is evaluated as an anodic active material. The corresponding *operando*-XRD measurement is shown in **Figure 36**. The horizontal line in **Figure 36** is caused by a short-term X-ray beam interruption, but does not influence the qualitative analysis of the *operando*-XRD data. Due to the quality of the obtained diffraction patterns (peak broadening at higher reflex angles due to the experimental diffraction geometry and lower intensity), only a qualitative analysis of the reaction mechanisms was possible. Exact calculations of lattice parameters or amount of K^+ de-/ inserted were not possible and reliable enough.

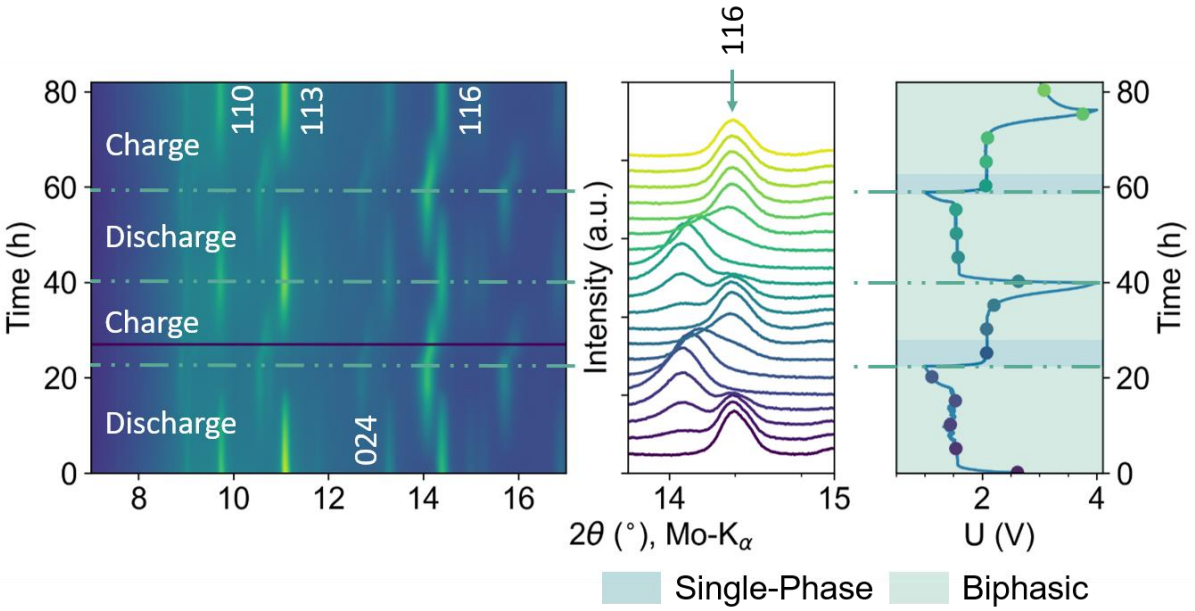

Figure 36: Collected operando XRD data of KTP/C composite to study the electrochemical reaction mechanism in a PIB half-cell setup in a voltage window of 1.0 V – 4.0 V at C/20. The corresponding charge / discharge cycles and indexed hkl reflexes are marked. As an electrolyte 0.5M KPF_6 in EC:PC was used.

During discharge a biphasic reaction was obtained. The main hkl reflexes 113 and 116 in the corresponding XRD pattern (contour plot) gradually vanish and new reflexes at lower reflex angels appear, leading ultimately to the fully discharged $K_3Ti_2(PO_4)_3$ at 1.0 V starting from $KTi_2(PO_4)_3$. The potassium-rich compound could be indexed to the same space group $R\bar{3}c$ as the pristine KTP phase according to literature.[115] During charge an untypical biphasic reaction was obtained. Until a potential of around 2.1 V, a solid-solution mechanism leading to an intermediate KTP compound is observed due to a gradually shift of the reflexes 113 and 116 to higher angels. Due to an increase of the potential over 2.1 V, the reflexes at around 11.2 ° (113) and 14.3 ° (116) of the intermediate compound vanish again. This leads in fact to the starting $KTi_2(PO_4)_3$ phase *via* a biphasic reaction with the 113 and 116 reflexes back at their pristine position. A similar behavior is obtained for the 024 and 110 reflexes. Voronina *et al.* stated, that the untypical phase behavior during charge is caused by different intrinsic electronic conductivities of the potassium-rich $K_3Ti_2(PO_4)_3$ and potassium-deficient $KTi_2(PO_4)_3$ compounds. Sufficiently high electronic conductivity is required for the insertion and/or extraction of large K^+ ions, which can directly affect the electrochemical behaviour of electrode materials. As the electronic conductivity of the potassium rich compound is remarkably higher than for the pristine KTP phase, it was concluded that the untypical phase transition during charge is based on the differences in intrinsic electronic conductivity and thus different ionic diffusion in the electrode material.[115] For a more in-depth and quantitative analysis of the electrochemical reaction mechanism, *ex-situ* XRD on KTP/C samples charged / discharged to

different state-of-charges are necessary. Based on this *ex-situ* XRD data, changes in the lattice parameters and potassium contents could be calculated via Rietveld-refinements at different state-of-charges to allow a more detailed view onto the electrochemical reaction mechanism.

In **Figure 37** the C-rate capability test for the KTP/C composite combined with the voltage profiles at the 5th cycle of each C-rate are shown.

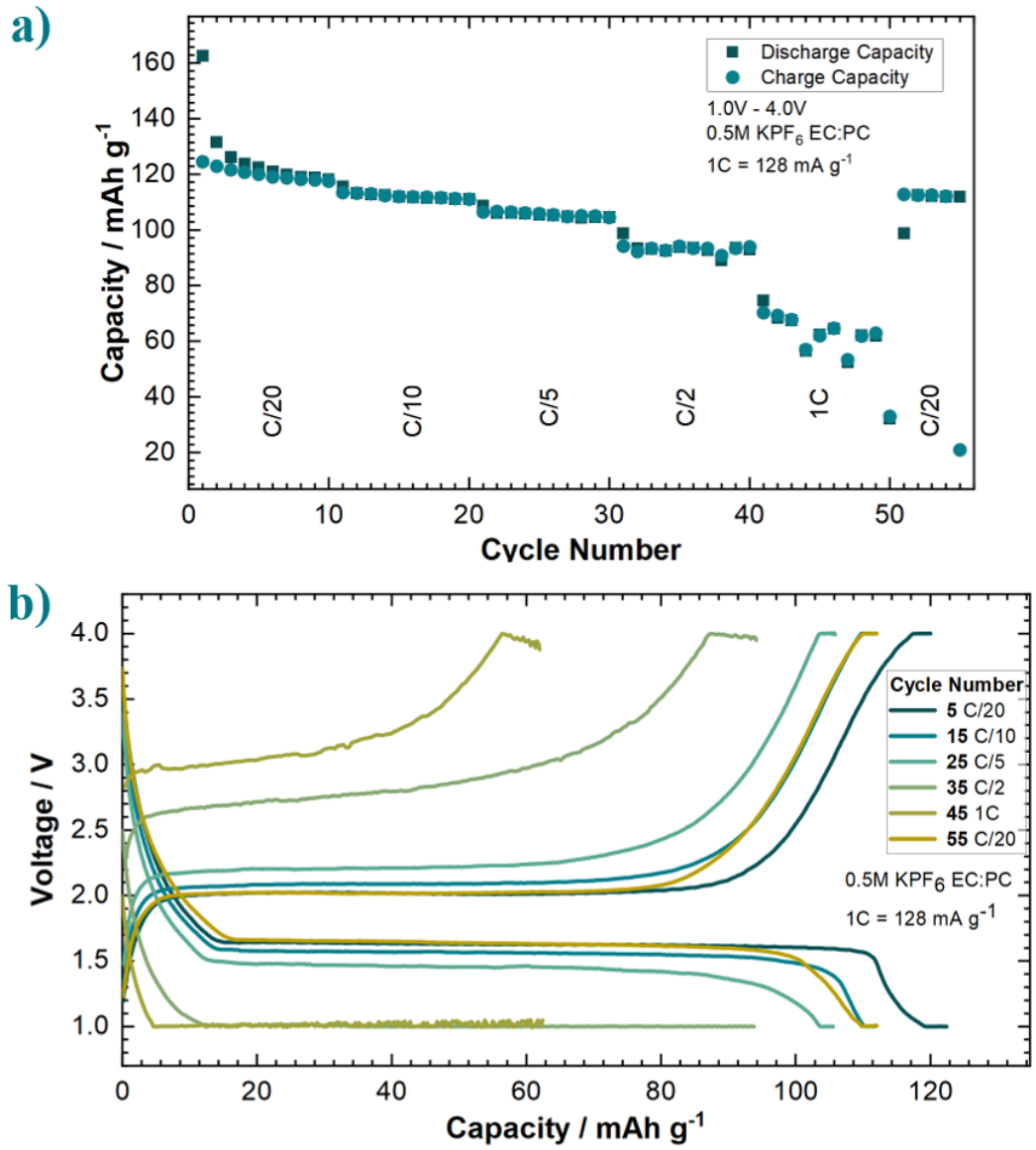

Figure 37: C-Rate capability test of KTP/C composite in a PIB half-cell setup, a) Specific charge and discharge capacity at different C-rates (1C = 128 mA g^{-1}), b) voltage profile of KTP/C in the 5th cycle at each C-rate, adapted from master thesis project from Psille.[134]

At C/20 the maximum charge capacity of the KTP/C composite is reaching 123 mAh g^{-1}, which is close to the theoretical capacity of 128 mAh g^{-1}. At low and moderate C-rates until C/5, the voltage profile stays nearly constant with a distinct flat voltage plateau around 1.5 V - 1.7 V (discharge) and 1.8 V - 2.0 V (charge). The polarization at low and moderate C-rate is low for

PIBs with around 500 mV at C/5, which could be linked to the improved electrochemical performance due to the unique microstructure of the hierarchical structured KTP/C composites and the intrinsic good ionic conductivity of the KTP phase. Previously published studies showed only similar or even higher polarizations for KTP in PIB half-cell setups.[115,117,118,167] The open porosity (≈50 %) with the high specific surface area and carbon coating of the KTP/C leads to a shortening of the diffusion length inside the solid KTP/C granules and a highly percolated electronic network, similar seen for the vanadium-based active materials.[132,134] Combined with the nanocrystallinity (40 (1) nm crystallite size), this leads in fact to improved charge transfer kinetics during de- / insertion of K^+, thus yielding an increased charge capacity and C-rate performance of the KTP/C composite.[115,132,140,167,168] At higher C-rates of C/2 and 1C, an increased polarization in the voltage profile of the KTP/C composite becomes apparent, while during discharge most of the capacity arise from the constant voltage-step (CV). This could be possibly caused by increased polarization of the potassium metal anode itself due to resistive surface layer formation.[135,143-146] Additionally, intrinsic limitation in solid-state diffusion of the potassium ions inside the KTP/C granules could limit the reaction kinetics at higher C-rates as well.[28,52,169,170]

Nevertheless, the KTP/C composite shows a relatively low polarization for a PIB active material with a well-defined redox potential at around 1.5 V (discharge at C/20). Additionally, it works within the electrochemical stability window of commonly used organic liquid electrolytes.[171] This in fact, make the KTP/C granules theoretically suited as a RE for PIBs, as discussed in chapter 6.3.[134] To study its possible utilization as a RE for PIBs, further electrochemical tests like testing the stability of the potential over time (self-discharge) were performed and are discussed in chapter 7.2.

7.1.2 KTPO/C as Electrode Material for PIBs

The synthesis of the KTPO/C composites followed the classical 2-step solid-state approach assisted by a spray-drying step analogue to the KVP/C composites. Instead of 5 wt. % β-lactose for the KVP/C composites, 15 wt. % β-lactose were added for the KTPO/C composites. The idea behind the increase in β-lactose content was to enhance the open porosity and specific surface of the KTPO/C composites, to further improve the electrochemical reaction kinetics and keep the polarization during cycling as low as possible. To study the phase evolution and synthesis reaction of the KTPO/C phase, TG/DSC-IR under Ar-atmosphere was measured. The obtained thermal analysis data is summarized in **Figure 38**, while onset temperatures, mass losses or ongoing reactions are summarized in **Appendix 32**.

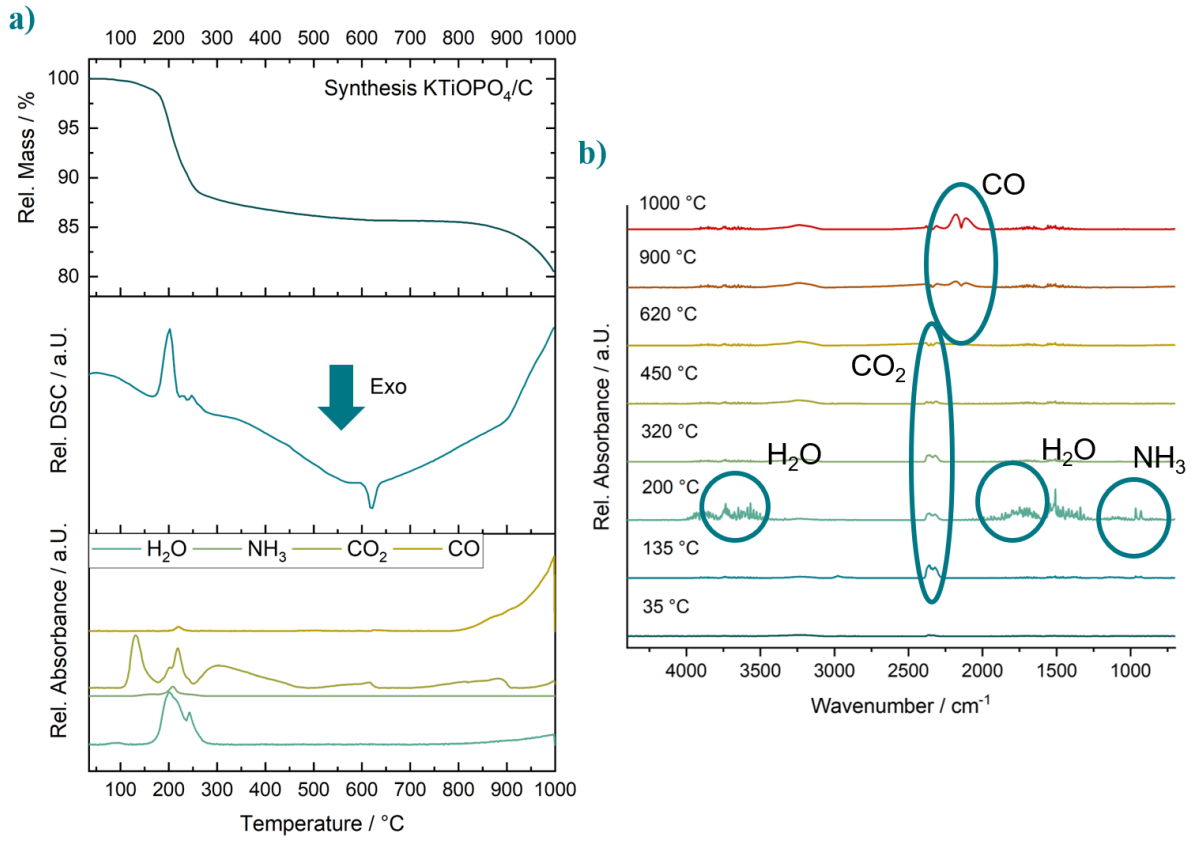

Figure 38: TG/DSC-IR analysis on the synthesis reaction of KTPO/C under Ar-atmosphere. a) TGA (top), DSC (middle) and FTIR-traces of main gaseous byproducts (bottom), b) FTIR-spectra with marked gaseous byproducts at different temperatures during thermal analysis.

In the TGA signal, two distinct mass losses are observed. The first mass loss between 100 °C and 300 °C is accompanied with a sharp endothermic peak in the DSC signal. This indicates the decomposition of the reactants $NH_4H_2PO_4$ and sucrose, which becomes obvious in the FTIR-traces as the main peaks for H_2O, NH_3 and CO_2 are located between 100 °C and 300 °C. Between 600 °C and 650 °C, a sharp exothermic signal in the DSC curve is indicating the

crystallization of the KTPO phase. At temperatures above 850 °C, another beginning mass loss in the TGA signal is apparent. This mass loss coincides with a strong endothermic signal in the DSC curve and a release of CO instead of CO_2, observed in the FTIR-traces. This could be an indication for a beginning decomposition or a reaction of the KTPO phase with the formed carbon coating, leading to impurity phase formation. All CO_2 signals in the FT-IR traces arise due to the carbonization of the sucrose. It has been shown for the synthesis of the other materials, that the K_2CO_3 could decompose or react with the $NH_4H_2PO_4$ during the ball-milling process or storage of the precursor. This has been confirmed by additional FT-IR measurements on the precursor and the reactants, which have shown the absence of K_2CO_3 in the precursor (**Appendix 33**). Based on the thermal analysis results and the assumption of KOH as the potassium source in the precursor, the following reaction scheme for the synthesis of KTPO/C is proposed (**Equation 7**):

Equation 7: Proposed reaction scheme for the synthesis reaction of KTPO/C composites based on the thermal analysis results.

$$KOH + TiO_2 + NH_4H_2PO_4 \xrightarrow{Ar,\ C,\ \Delta T} KTiOPO_4/C + NH_3 + 2\,H_2O$$

According to **Equation 7**, a theoretical reaction turnover of around 76 % is expected after completion of the KTPO synthesis and complete carbonization of the 7.5 wt. % sucrose for the calcination step. After completion of the thermal analysis, a residual relative mass of around 81 % was detected. It has to be considered, that at temperatures above 850 °C a decomposition or reaction of the KTPO with the formed carbon matrix accompanied with a CO release occurs. This leads in fact to an increased mass loss and should lead to a lower reaction turnover than theoretically expected. Nevertheless, if the precursor preparation by planetary ball-milling in 2-propanol and subsequent evaporation of the 2-propanol is considered, similar to the KTP and KVPO precursors, a starting decomposition of the $NH_4H_2PO_4$ with release of NH_3 during precursor preparation is possible. Additionally, the reaction of the potassium source with $NH_4H_2PO_4$ to K_2HPO_4, as similar discussed for the KVP/C precursor, seems plausible. After precursor preparation, a typical smell of ammonia was obtained similar to the other precursors. This leads in fact to the differences in theoretical and experimental reaction turnover, even if the residual mass before 850 °C (starting decomposition) is considered with around 86 %. Based on the thermal analysis results the calcination and sintering temperature for the KTPO/C composites was set to 850 °C.

Assuming a complete carbonization of the 7.5 wt. % sucrose, after calcination of the KTPO/C precursor under Ar-atmosphere a carbon content of 3.2 % is expected theoretically.

Experimentally, a carbon content of only 2.2 % for the KTPO/C after calcination was determined. The differences could arise due to an incomplete carbonization of the sucrose, a beginning reaction of the KTPO / reactants with the formed carbon coating or decomposition at the calcination temperature of 850 °C. All of these options could reduce the experimentally obtained carbon content. The obtained diffraction pattern of the KTPO/C composite with the performed Rietveld-refinement on the orthorhombic structural model of KTPO (symmetry *Pna2₁*) after calcination is shown in **Figure 39 a**.

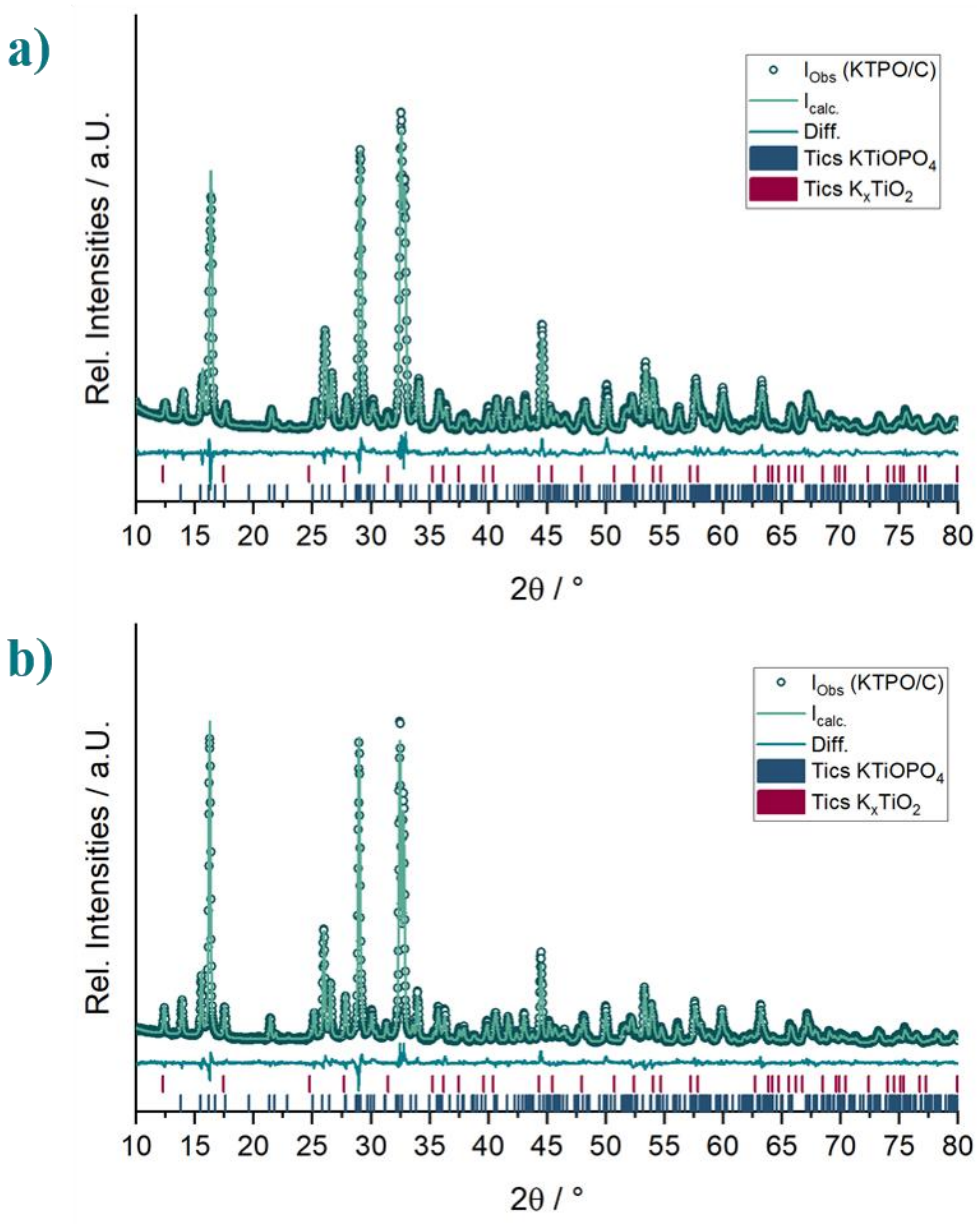

Figure 39: Rietveld-refinement on the structural model of KTPO (symmetry Pna2₁, ICSD-182657, ICSD release 2025.1, Norberg et. al[137]) and K_xTiO_2 (symmetry I4/m, ICSD-247826, ICSD release 2025.1, Sakao et al.[172]) against the obtained powder diffraction pattern of a) KTPO/C after calcination and b) KTPO/C after completion of the sintering process.

The XRD analysis and Rietveld-refinement strengthen the argument, that a minor amount of the carbon from the carbonized sucrose is consumed for reduction of Ti(+IV) to Ti(+III) under Ar-atmosphere. Around 6 wt. % of a tetragonal hollandite-type K_xTiO_2 bronze (symmetry *I4/m*) was formed as an impurity phase.[172] This causes mainly the difference between theoretically expected and experimentally determined carbon contents after the calcination reaction of the KTPO/C composite. An ICP-OES analysis reveals a stochiometric ratio of K:Ti:P of 1:1.02:0.98, which could be seen as a further indication for the formation of Ti-rich impurity phases and coincides with the obtained XRD analysis.

For synthesis of the hierarchical structured KTPO/C composites, a spray-drying step with subsequent sintering in the presence of 15 wt. % β-lactose has to be applied. As a sintering temperature 850 °C was chosen based on the thermal analysis results. The obtained diffraction pattern with the performed Rietveld-refinement is shown in **Figure 39 b**. A good agreement between the observed and calculated pattern is observed. The narrow reflexes and low background of the obtained diffraction pattern indicate a high crystallinity. The calculated lattice parameter for the KTPO/C after sintering are in good agreement with the literature[121,173] (refined: a= 12.8179(4) Å, b= 6.4045(2) Å, c= 10.5844(2) Å, α=β=γ= 90 ° and V= 867.26 $Å^3$). The crystallite size is estimated as 50 (1) nm, indicating nanocrystallinity of the KTPO/C granules. Similar to the KTPO/C composite after calcination, the impurity phase of the tetragonal hollandite-type K_xTiO_2 bronze (symmetry *I4/m*) is present in the hierarchical structured KTPO/C composites after spray-drying and sintering. The relative fraction of the impurity phase increases to 8.5 wt. % after sintering in presence of β-lactose according to the Rietveld-refinement. This reveals the additional consumption of some of the formed carbon coating for further reduction of Ti(+IV) to Ti(+III). Assuming a complete carbonization of the β-lactose (15 wt. %), an additional carbon content of 6.3 % would have been expected after sintering. Experimentally, for the spray-dried KTPO/C granules at 850 °C a total carbon content of only 5.2 % was detected. This means, the carbonization of β-lactose led to an increase in carbon content of only 3.0 % compared to the carbon content after calcination (**Table 11**). Similar to the calcination reaction of the KTPO/C composite, an incomplete carbonization of the β-lactose with the volatilization of lower molecular species like CO_2 and CO and / or the consumption of carbon for reduction during formation of the Ti-rich impurity phase K_xTiO_2 could be the main cause for this deviation. In **Table 11** all powder characteristics of the hierarchically structured KTPO/C composites are summarized, while in **Figure 40** SEM images of the morphology and cross-sections of the KTPO/C granules are shown.

Table 11: Summary of all powder characteristics after completion of the synthesis process for the KTPO/C composite sintered at 850 °C.

Composite	Sintering Temperatue / °C	C-Content after Calcination / wt. %	C-Content after Sintering / wt. %	Median Secondary Particle Size / µm	Specific Surface / $m^2 g^{-1}$	Porosity / %	Pore size / nm
KTPO/C	850	2.2	5.2	11.7	27.7	39.8	42

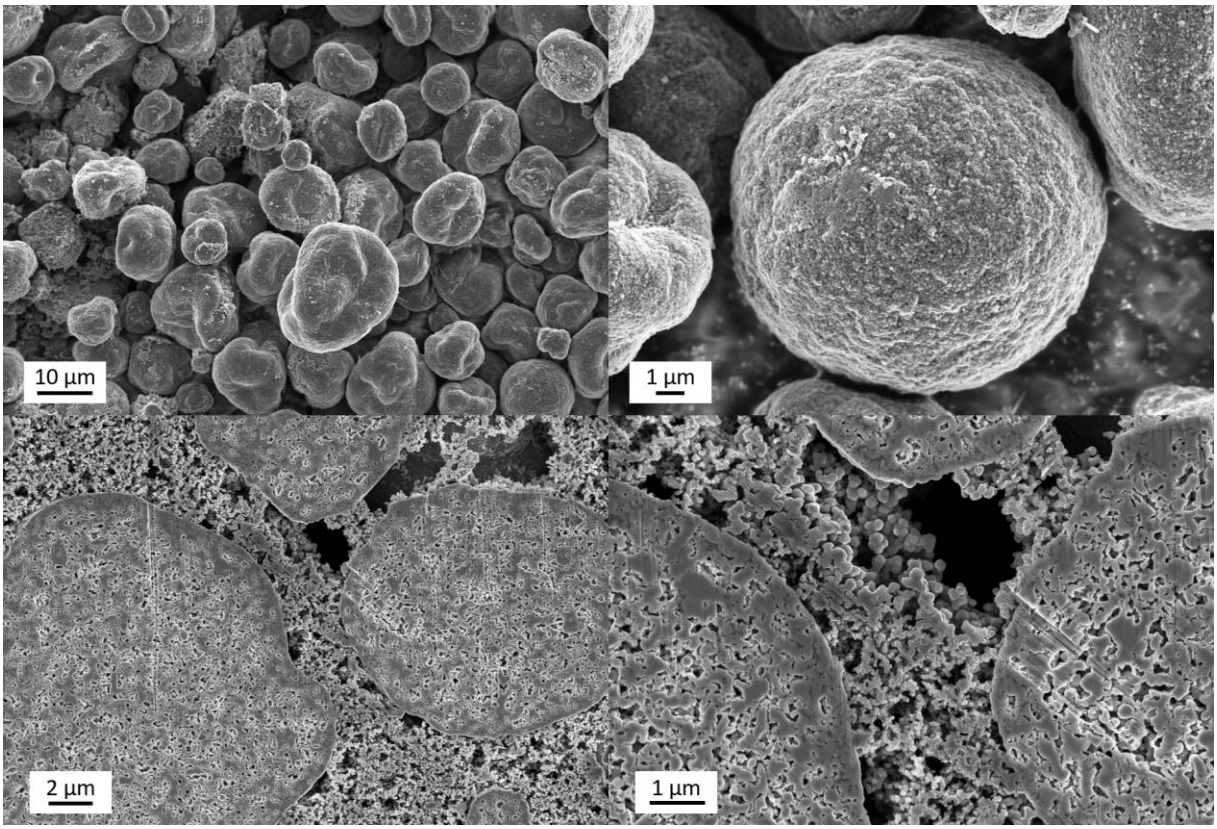

Figure 40: SEM images of the morphology of the KTPO/C granules (top) and the corresponding cross-sections (bottom) after sintering at 850 °C under Ar-atmosphere.

Similar to the KTP/C composites, the KTPO/C granules show a nearly spherical morphology with grooves at the surface of the granules. This indicates a too low binder (PAA) or solid content in the dispersion for spray-drying, which could consequently not stabilize the spherical morphology similarly seen for to the KTP/C composites.[140] The cross-sections of the KTPO/C granules reveal a homogenous distribution of the open intragranular porosity (39.8 %, **Table** 11). A thin, denser surface layer was observed at the border of the KTPO/C granules. Similar to the vanadium-based granules (**Figure 15** & **Figure 28**), this is not uncommon for the spray-drying process as the smallest particles tend to arrange at the borders of the granules, resulting

in an increased sintering activity and ultimately in a denser surface layer at the borders of the KTPO/C granules.[129,132,140]

Based on the previous discussed results, the open porosity (39.8%) combined with the high specific surface area (27.7 m^2 g^{-1}) and carbon content of 5.2 % should be beneficial for the overall electrochemical performance of the KTPO/C composite and lead to improved electronic conductivity and diffusion kinetics.[132] Additionally, the intrinsic material properties (high ionic conductivity, flat voltage plateau around 1.0 V)[120] combined with the unique microstructure should lead to a low polarization during cycling, even at higher C-rates. These properties render the hierarchically structured KTPO/C composites an ideal candidate as a diagnostic electrode (DE).

To study the basic electrochemical properties of the KTPO/C composites, galvanostatic cycling in a PIB half-cell setup at different C-rates (1C = 135 mA g^{-1}) in a voltage window of 0.1 V – 2.5 V were performed. The underlying electrochemical reactions were studied *via operando*-XRD measurements at C/20 in a PIB half-cell setup as well. All galvanostatic cycling experiments start with discharge (reduction) for the KTPO/C composites, as it is evaluated as an anodic active material. The obtained *operando*-XRD analysis of the KTPO/C composite is shown in **Figure 41**. Due to the quality of the obtained diffraction patterns (peak broadening at higher reflex angles due to the experimental diffraction geometry and lower intensity) only a qualitative analysis of the reaction mechanisms was possible. Exact calculations of lattice parameters or amount of K^+ de-/inserted were not possible and reliable enough.

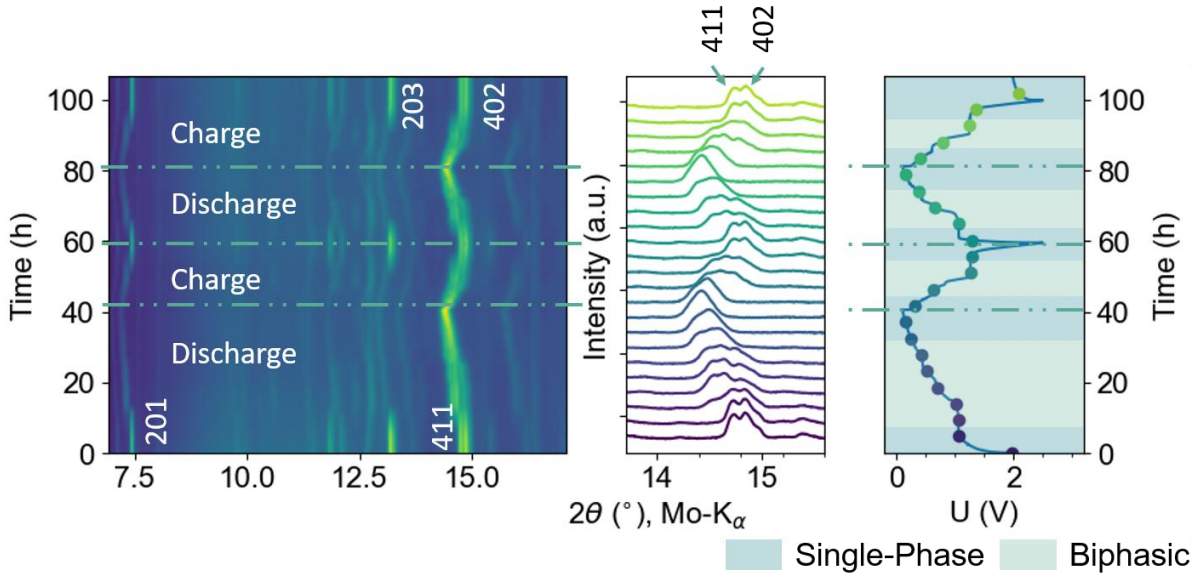

Figure 41: Collected operando XRD data of the KTPO/C composite to study the electrochemical reaction mechanism in a PIB half-cell setup in a voltage window of 0.1 V – 2.5 V at C/20. The corresponding charge / discharge cycles and indexed hkl reflexes are marked. As an electrolyte 0.5M KPF_6 in EC:PC was used.

During the first discharge all reflexes remain at the same position until the center of the first voltage plateau around 1.0 V due to SEI formation and a solid solution mechanism. At the center of the first voltage plateau around 1.0 V, the hkl reflexes 411 and 402 start to gradually disappear and a new reflex (411) at lower reflection angels with increasing reflex intensity appears. This indicates the formation of a new potassium rich KTPO-phase, which crystallizes in the same space group according to literature.[120] A similar behavior for the 201 and 203 reflexes is visible. Contrary to literature, this process is happening until a voltage of around 0.4 V during discharge and could be described as a biphasic reaction at this stage. Additional reflex maxima at the 201 and 411 reflexes between 1.0 V and 0.4 V in the contour plot indicating the formation of a different intermediate potassium-rich KTPO compound, similar to the findings from Kumar *et al.*.[121] Nevertheless, contrary to these findings no additional single-phase region in the voltage range between 0.4 V and 1.0 V was obtained during discharge revealing a continuous biphasic reaction mechanism. It should be noted, that due to the experimental setup the reflexes are quite broad, which limits the resolution and could possibly lead to overlooking of minor single-phase regions in the voltage range between 0.4 V and 1.0 V as stated by Kumar *et al.*.[121] The ongoing insertion of K^+ until the lower cut-off voltage of 0.1 V could be described as a solid-solution mechanism as only a peak shift to lower reflex-angels is obtained and no additional reflexes appear or disappear. During charge the opposite behavior is obtained, meaning a solid-solution mechanism until around 0.4 V - 0.5 V, followed by a biphasic reaction until the voltage plateau around 1.1 V, while intermediate potassium-rich

KTPO phases seems apparent in the XRD pattern. This is indicated by different reflex maxima at the 201 and 411 reflexes. The mechanism at the beginning (reduction / discharge) or end (oxidation / charge) of the voltage plateau around 1.0 V and above this voltage could be described as a solid-solution mechanism as well, as only the reflexes of the pristine KTPO phase are visible. The performed *operando*-XRD measurements reveal a highly reversible in- / deinsertion of the K^+ as all structural changes during cycling seem to be completely reversible. The corresponding dq/dV-plot of the KTPO/C cycled at C/20 in the 2nd cycle is shown in **Figure** 42 and reveals six corresponding redox peaks, similar to the study from Kumar *et al.*.[121] According to their study, this could indicate several phase transformations and structural changes during cycling. This coincides well with the obtained *operando*-XRD pattern as several reflexes appear and disappear during cycling revealing the structural transformations. Additionally, the dq/dV-plot confirms the high reversibility of the underlying electrochemical reactions of the KTPO/C composites during cycling.

For a more in-depth and quantitative analysis of the electrochemical reaction mechanism, *ex-situ* XRD on KTPO/C samples charged / discharged to different state-of-charge are necessary. Based on this *ex-situ* XRD data, changes in the lattice parameters and potassium contents could be calculated via Rietveld-refinements at different state-of-charges to allow a more detailed view onto the electrochemical reaction mechanism.

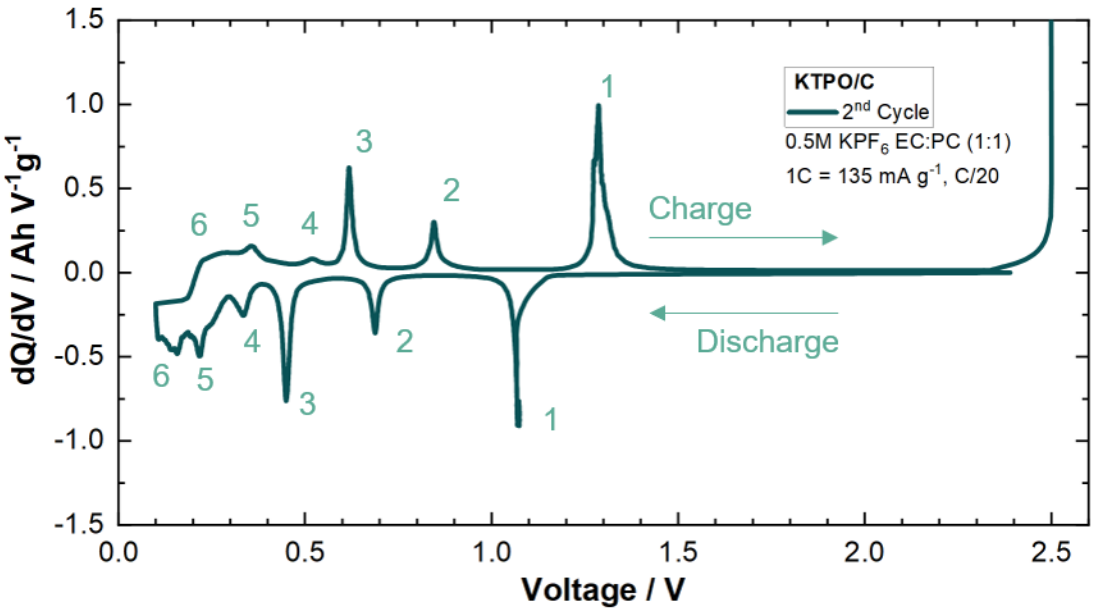

Figure 42: dq/dV-plot of the 2nd cycle of KTPO/C composites cycled at C/20 in PIB half-cell setup against a potassium metal anode. As an electrolyte 0.5M KPF_6 in EC:PC (1:1) was used. The corresponding redox peaks during charge and discharge marked. Note: To suppress the noise, the data in the dq/dV-plot was smoothed.

In **Figure 43** the C-rate capability test for the KTPO/C composite combined with the voltage profile for the 5th cycle at each C-rate is shown. At C/20 the maximum charge capacity of the KTPO/C composites reaches the theoretical capacity of 135 mAh g^{-1}. The specific charge capacity in the first cycle at C/20 was lower than the theoretical value as the lower cut-off voltage was not reached during the first discharge due to a step time limit for cycling at C/20. The polarization of the wide voltage plateau at around 1.0 V is low for a PIB half-cell setup with around 250 mV at C/20 and comparable or lower to previous studies for Ti-based active materials.[115,117,120,121,167] At C/10 the polarization increases already to around 450 mV, while still 118 mAh g^{-1} of charge capacity are reached. The high charge capacity and low to moderate polarization at C/20 and C/10 could be linked to the unique microstructure of the KTPO/C granules. The nanocrystallinity (50 (1) nm crystallite size according to Rietveld-refinement, see **Figure 39**) of the KTPO/C granules combined with the open porosity, high specific surface area and the carbon coating lead to a highly percolated electronic network with shortened diffusion length. This leads ultimately to an improved electrochemical performance, similarly seen for the other hierarchical structured composites studied in this thesis.[132,140] Beginning at C/5, the voltage profile of the KTPO/C composites tested in a PIB half-cell setup dramatically changes and the polarization increases strongly. At C/2 and 1C barely any charge capacity of the KTPO/C during cycling is measurable. All of the capacity reached at C/2 is caused due to the insertion / deinsertion during the constant voltage (CV) step at the end of the charge or discharge step. Instead of an increase in polarization, the unique microstructure of the hierarchical structured KTPO/C granules should lead to improved electrochemical reaction kinetics as seen for the vanadium-based materials and the KTP/C composite. Combined with the highest intrinsic ionic conductivity among the polyanionic electrode materials for PIBs[120], the polarization should be low and the C-rate capability improved instead of the dramatical changes in the voltage profile and high polarization seen in **Figure 43 b**. Nevertheless, ongoing cycling at C/5 for another 45 cycles reveals a relaxation of the charge capacity to 118 mAh g^{-1} in the 95th cycle. The charge capacity at C/5 thereby increases from 89 mAh g^{-1} in cycle 51 to 118 mAh g^{-1} in cycle 95, while the polarization obtained during cycling is dramatically reduced at the 95th cycle compared to the 51st cycle (**Figure 43 a**). This could indicate, that a majority of the polarization visible in the voltage profile of the KTPO/C composite (**Figure 43 b**), even at C/2 and 1C, is caused by resistive surface layer formation at and the high reactivity of the potassium metal anode. This in fact, strongly alters the electrochemical characterization results of PIB half-cell setups as shown in chapter 6.3.[37,135,143-146] With increasing cycle number it seems reasonable that the potassium metal electrode becomes less resistive by the formation of

porous and mossy surface layers. As the surface area of the potassium metal electrode increases, the plating / stripping overpotential at any given current density decreases, which leads in fact to the increased electrochemical performance of the KTPO/C composites tested in the PIB half-cell setup.[145] An activation process of the KTPO/C granules similarly seen for the KVP/C composites seems unlikely, as at C/20 already the theoretical capacity of 135 mAh g^{-1} was reached during the first 10 cycles.

As the KTPO/C composite shows a well-defined voltage plateau around 1.0 V (discharge C/20) and works in the electrochemical stability window of commonly used electrolyte, the material was further evaluated as a possible RE for PIBs.[171] Additionally, as the polarization at C/20 and C/10 was relatively low and the KTPO phase is known for its high intrinsic ionic conductivity, the material was further evaluated for its use as a DE for PIBs to develop an easy and more precise full-cell setup for characterization of different electrode active materials.

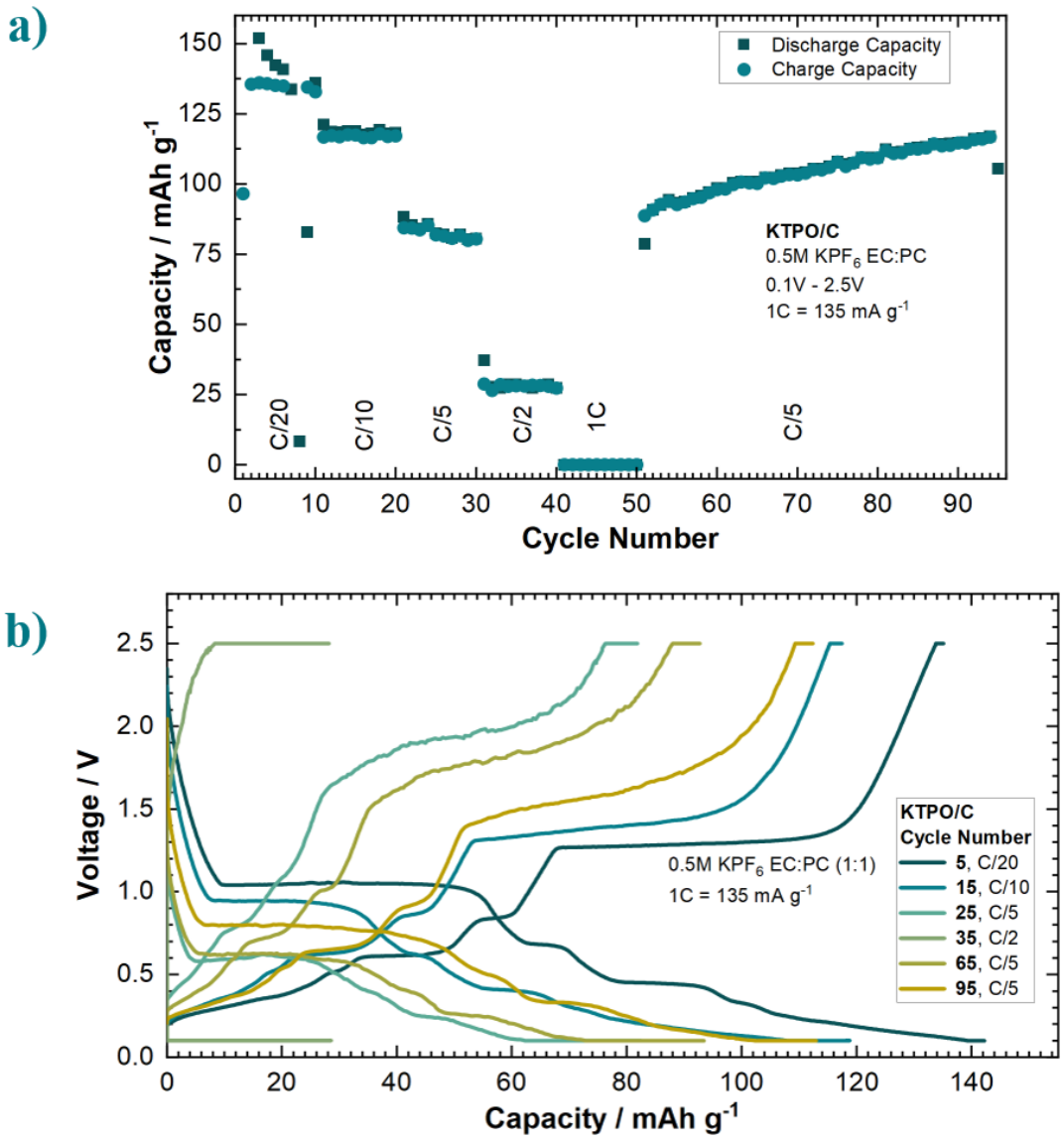

Figure 43: *C-Rate capability test of the KTPO/C composite in a PIB half-cell setup, a) Specific charge and discharge capacity at different C-rates (1C = 135 mA g^{-1}), b) voltage profile of KTPO/C in the 5th cycle at each C-rate with additional cycles at C/5.*

7.2 Utilization of KTP/C and KTPO/C as Reference and Diagnostic Electrode

A fundamental prerequisites of a RE is a stable and well-defined redox potential over time.[135,156,161] As both Ti-based composites possess a well-defined voltage plateau / redox potential at around 1.6 V for KTP/C and 1.0 V for KTPO/C *vs.* K^+ / K at C/20 during discharge respectively, both materials were discharged to this voltage plateau in a PIB half-cell setup at C/20. As the voltage plateau was reached, the applied current was stopped and the open-circuit voltage (OCV) was measured over several days to study the self-discharge and stability of the redox potential over time. The corresponding data for the self-discharge test is shown in **Figure** 44.

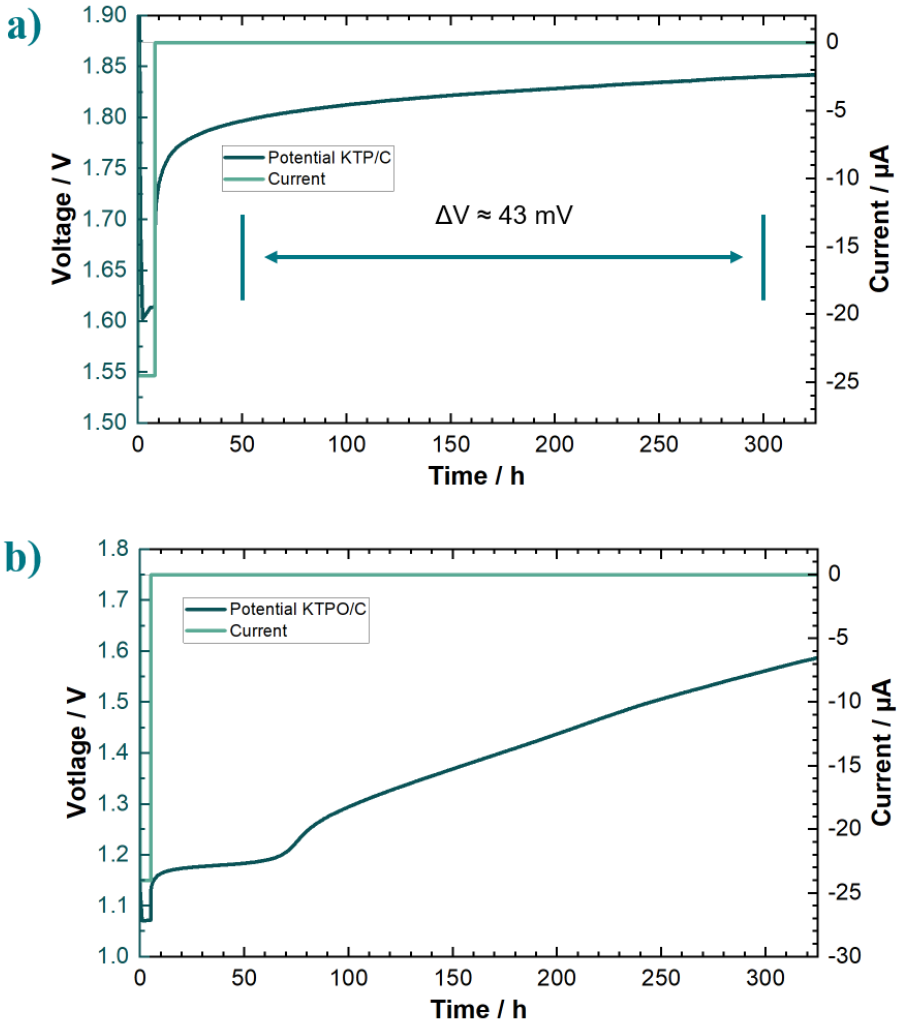

Figure 44: Self-discharge test for a) KTP/C and b) KTPO/C in a PIB half-cell setup against a potassium metal anode. The cells were cycled at C/20 to the voltage plateau around 1.6 V and 1.05 V for KTP/C and KTPO/C vs. K^+ / K respectively. As an electrolyte 0.5M KPF_6 EC:PC (1:1) was used. Note: Self-discharge for KTP/C was studied on granules sintered at 650 °C instead of 700 °C.

The two different potassium titanium phosphates show an opposite behavior during the self-discharge test. As the potential of KTP/C stabilizes after a relaxation period of around 48 h, the potential of the KTPO/C is stable for around 48 h and drifts strongly to higher potentials *versus* potassium afterwards. The KTPO/C composites are therefore not suited as a RE for PIBs due to the severe potential drift after 48 h. Ideally, the RE potential is stable over mid- to long-term durations ranging from several days to week, if the aim is to study the aging of electrode materials over many cycles. The potential of the KTP/C stabilizes at around 1.84 V after around 325 h in the PIB half-cell setup. The potential drift over 275 h (t= 50 h – 325 h) is minor with about 43 mV for the KTP/C composites, which corresponds to a drift rate of 0.16 mV h^{-1} in the PIB half-cell setup. As the drift rate of the KTP/C is quite comparable to the values obtained from Jagger *et al.* for their Bi-Bi_2K alloy (0.1 mV h^{-1} ± 0.1 mV h^{-1}), the KTP/C was further evaluated as a potential RE for PIBs.[156] For this purpose, the basic 3-electrode setup from Panasenko *et al.* was used, while the Ag / AgCl – RE capillary was exchanged with a RE pin.[135] The RE pin was coated with a standard electrode slurry containing the ratio of KTP/C:C65:PVDF of 8:1:1, according to chapter 5.2.3. For the use of the KTP/C composites as a RE, the RE-pin had to be precycled to the voltage plateau of the KTP/C composite around 1.6 V *vs.* K^+/K. An exemplary precycling of the KTP/C RE-pin is shown in **Appendix 6**. For an evaluation of the KTP/C-RE, a 3-electrode measurement with KTP/C as WE and a fresh potassium metal anode (CE) was performed. The corresponding data is displayed in **Figure 45** at different time scales for better readability and visibility combined with the voltage profile over capacity for the KTP/C WE *vs.* KTP/C-RE potential.

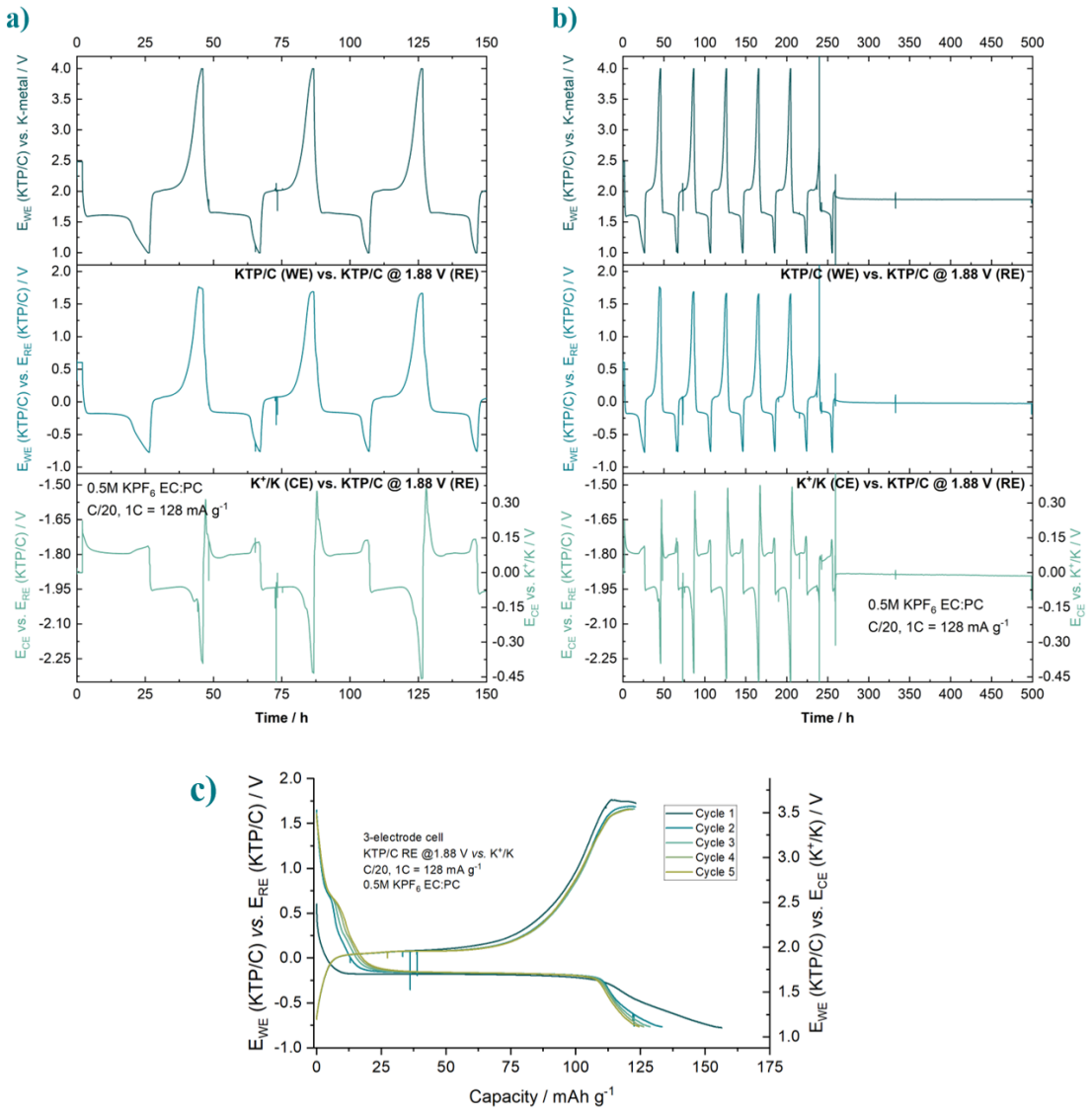

Figure 45: 3-electrode-cell measurement with KTP/C as WE, potassium metal as CE and precycled KTP/C as RE at different time scales for better visibility with a) t= 0 h – 150 h, b) t= 0 h – 500 h and c) KTP/C WE potentials specific capacity. The exact potential of the KTP/C RE was determined by measuring the OCV for several hours prior to cycling. Galvanostatic cycling was performed at C/20 (1C = 128 mA g^{-1}). As an electrolyte 0.5M KPF_6 EC:PC (1:1) was used.

After the measurement of the OCV for several hours prior to cycling, the potential of the KTP/C-RE was determined as 1.88 V *vs.* K^+/K. In the top image of **Figure 45** the cell potential (KTP/C WE *vs.* potassium metal CE), in the middle image the potential of KTP/C WE *vs.* KTP/C-RE and in the bottom image the potential of the potassium metal CE *vs.* KTP/C-RE is plotted. The polarization was calculated at the corresponding potential in the center of the charge / discharge plateau of the KTP/C WE in the first cycle. During cycling at C/20 a polarization of more than 400 mV at the first cycle of the cell potential becomes obvious (**Figure 45a, top**). More than 200 mV of the polarization arise from the KTP/C WE, while about 200 mV of the polarization arise from the potassium metal counter electrode at this low C-rate (**Figure 45a, middle and bottom**). Similar to the results with the Ag / AgCl-RE (**Figure**

32**,** chapter 6.3), the huge impact of the potassium metal anode onto the observed overpotentials becomes obvious with the KTP/C-RE in the first cycles. Not only the high polarization of about 200 mV, but a drifting potential of the potassium metal anode during cycling with huge overpotentials at the beginning of discharge and end of charge becomes visible as well. This alters dramatically the electrochemical characterization results obtained in PIB half-cell setups.[135,143,145,146,156,158,159] Although the polarization of the KTP/C WE was relatively high (≈200 mV), the stability of the KTP/C potential as a RE was significantly improved compared to the commonly used potassium metal reference electrode[158] and similar or better to previously reported alternative REs.[135,156] As the potential of the KTP/C WE *vs.* the KTP/C-RE and the potential of the potassium metal CE *vs.* the KTP/C-RE shows a drift in potential of only about 10 mV over 250 h after cycling was stopped, the KTP/C-RE could be expected to be stable over this time scale. As another benefit, the potential of the KTP/C-RE is within the electrolyte stability window of commonly used organic electrolytes[171] and the coating of the pin did not show any form of visual dissolution or degradation phenomena after disassembling of the used 3-electrode-cell. Additionally, the KTP/C-RE could be used several times without preparing a new KTP/C-RE for every 3-electrode-measurement. For re-use the KTP/C-RE was washed with 0.5 ml of pure EC:PC (solvents of the standard electrolyte 0.5M KPF_6 EC:PC) after disassembly of the cell and dried inside the glovebox overnight. Afterwards, the KTP/C-RE could be repeatedly used for several 3-electrode-measurement with different WE and CE configurations. Even if the potential of the KTP/C-RE drifted to much after several measurements, it could be used again. It was possible to charge / discharge the KTP/C-RE back to the plateau around 1.6 V and was left to a relaxation period for several days. Afterwards, the KTP/C RE-pin was again at a stable potential of 1.88 V *vs.* K^+/K. This represents a significant improvement over the basic setup from Panasenko *et al.* with a Ag / AgCl-RE. As this setup could not be sealed tightly due to setup related issues, the potential of the Ag / AgCl-RE was very sensitive to different contact pressures of the RE membrane to the separator or evaporation of the electrolyte solution during operation inside the glovebox. This directly affects long-term cycling leading to biased results on a long-term scale.[135]

Additionally, the maximum specific charge capacity of the KTP/C WE reached 123 mAh g^{-1}, which is similar to the previously discussed results of KTP/C in a coin-cell setup *vs.* a potassium metal CE (**Figure 37**). This further underlines the suitability of the developed 3-electrode setup for and a low impact of the cell setup (low geometric overlap of WE and CE due to 16 mm WE with 8 mm hole in middle, see **Figure 10**) onto the in-depth characterization of different active materials for PIBs.

All the discussed properties of the KTP/C composites from above, underline its great potential as a RE for PIBs, while to our knowledge the use of an insertion type material as a RE for PIBs is shown for the first time. These findings simplify the precise characterization of electrode active materials and electrolyte properties in PIBs. In addition, it theoretically allows a more precise characterization of electrode material performance at higher C-rate as the WE potential *vs.* RE potential could be controlled to bypass the overpotentials caused by the potassium metal anode. Based on these results, all synthesized electrode materials were characterized in a 3-electrode setup with the KTP/C RE-pin and a potassium metal CE at least over several cycles at C/20. With the developed 3-electrode setup the impact of the potassium metal CE onto the obtained electrode active material performance could be analyzed and discussed with respect to the results from PIB half-cells as shown before. The 3-electrode-cell data for KVPO/C as WE cycled against a potassium metal CE, similar to the PIB half-cell setup, is shown in **Figure** 46. Additionally, the voltage profile over capacity for the KVPO/C WE *vs.* KTP/C-RE potential is shown.

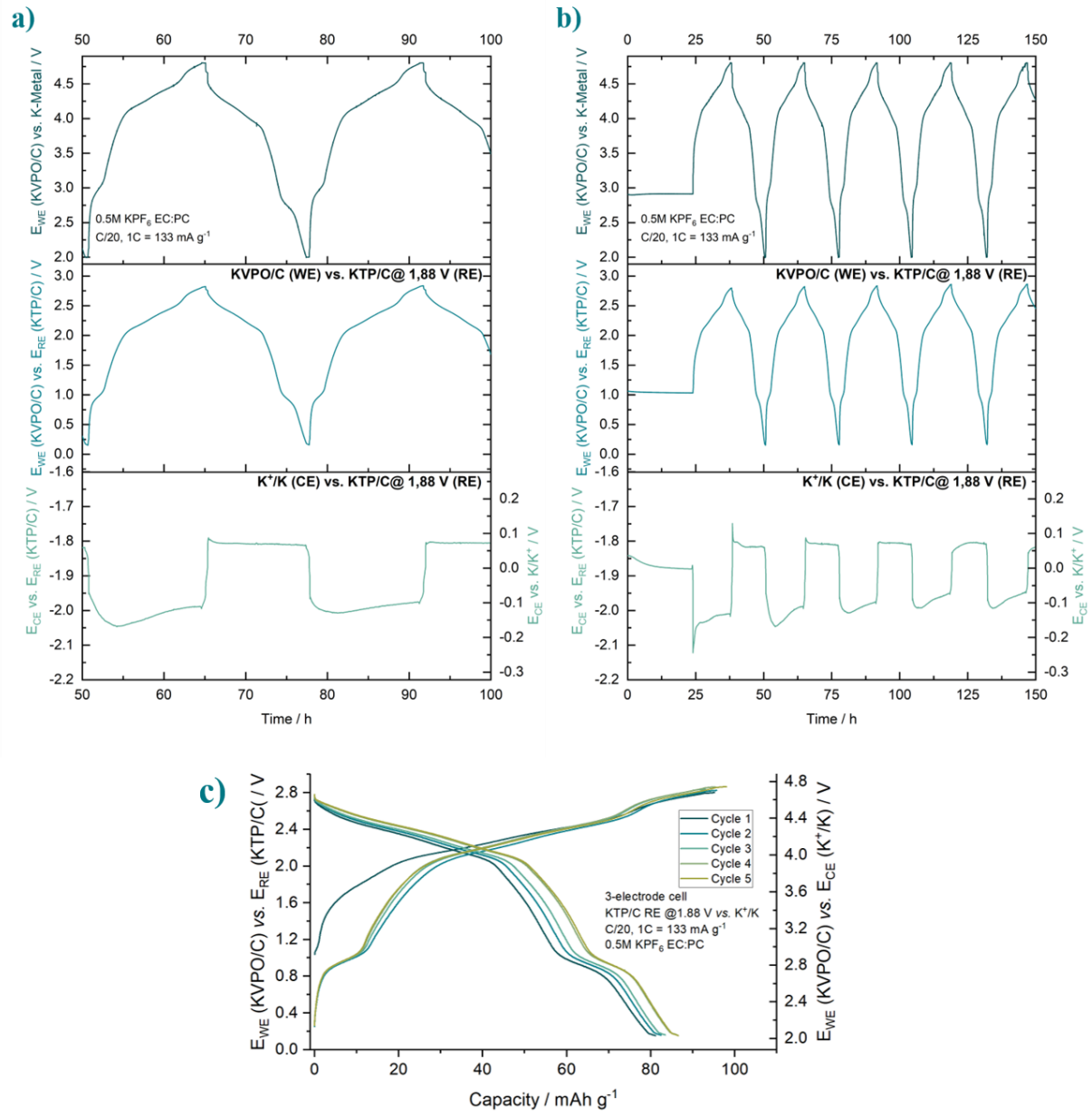

Figure 46: *3-electrode-cell measurement with KVPO/C as WE, potassium metal as CE and KTP/C as RE-pin at different time scales for improved visibility with a) t= 50 h – 100 h, b) t= 0 h – 150 h and c) KVPO/C WE vs. KTP/C-RE potential vs. specific capacity. Galvanostatic cycling was performed at C/20 (1C = 133 mA g^{-1}). As an electrolyte 0.5M KPF_6 in EC:PC was used.*

A polarization of up to 200 mV caused by the potassium metal anode becomes directly obvious in the 3-electrode-cell data with KVPO/C as WE (**Figure 46 a&b, bottom**). The polarization was calculated in the center of the small charge / discharge step of the cell potential (WE *vs.* CE) at around 2.5 V -3.0 V during the first cycle. The polarization of the KVPO/C composite apparent in the 3-electrode setup seems to be low at C/20, as the steps in the voltage profile around 1.0 V and 2.0 – 2.5 V *versus* the KTP/C-RE (1.88 V *vs.* K^+/K) or potassium metal CE respectively are at the same potential for charge and discharge during cycling (**Figure** 46 **a&b, middle**). The low polarization of the KVPO/C WE underlines the improved electronic

conductivity and reaction kinetics of the hierarchical structured KVPO/C composite due to the highly percolating electronic network inside the granules, as discussed in chapter 6.2.2. These properties, combined with the intrinsically high ionic conductivity of the KVPO material class render the KVPO/C granules a highly promising cathodic material for PIBs with improved C-rate capability. Additionally, the maximum discharge capacity of KVPO/C obtained in the 3-electrode setup is comparable to the coin-cell type half-cell setup (**Figure 29**) with 87 mAh g^{-1}, which further underlines the suitability of the developed 3-electrode setup for in-depth characterization (**Figure 46c**). Nevertheless, the high polarization and drifting potential of the potassium metal CE again reveals the huge impact onto electrochemical characterization performed in PIBs half-cell setups. As the resistivity and polarization of the potassium metal during cycling seems highly dependent onto applied currents[37], the caused bias of the potassium metal anode onto C-rate capability test of the KVP/C-2 composites was studied in the 3-electrode-cell with the KTP/C-RE as well.

In **Figure 47** the 3-electrode-cell data with KVP/C-2-800 as the WE, potassium metal as the CE and the KTP/C pin as the RE is shown, combined with the voltage profile over capacity for the KVP/C-2-800 WE *vs.* KTP/C RE potential at the fifth cycle for each C-rate.

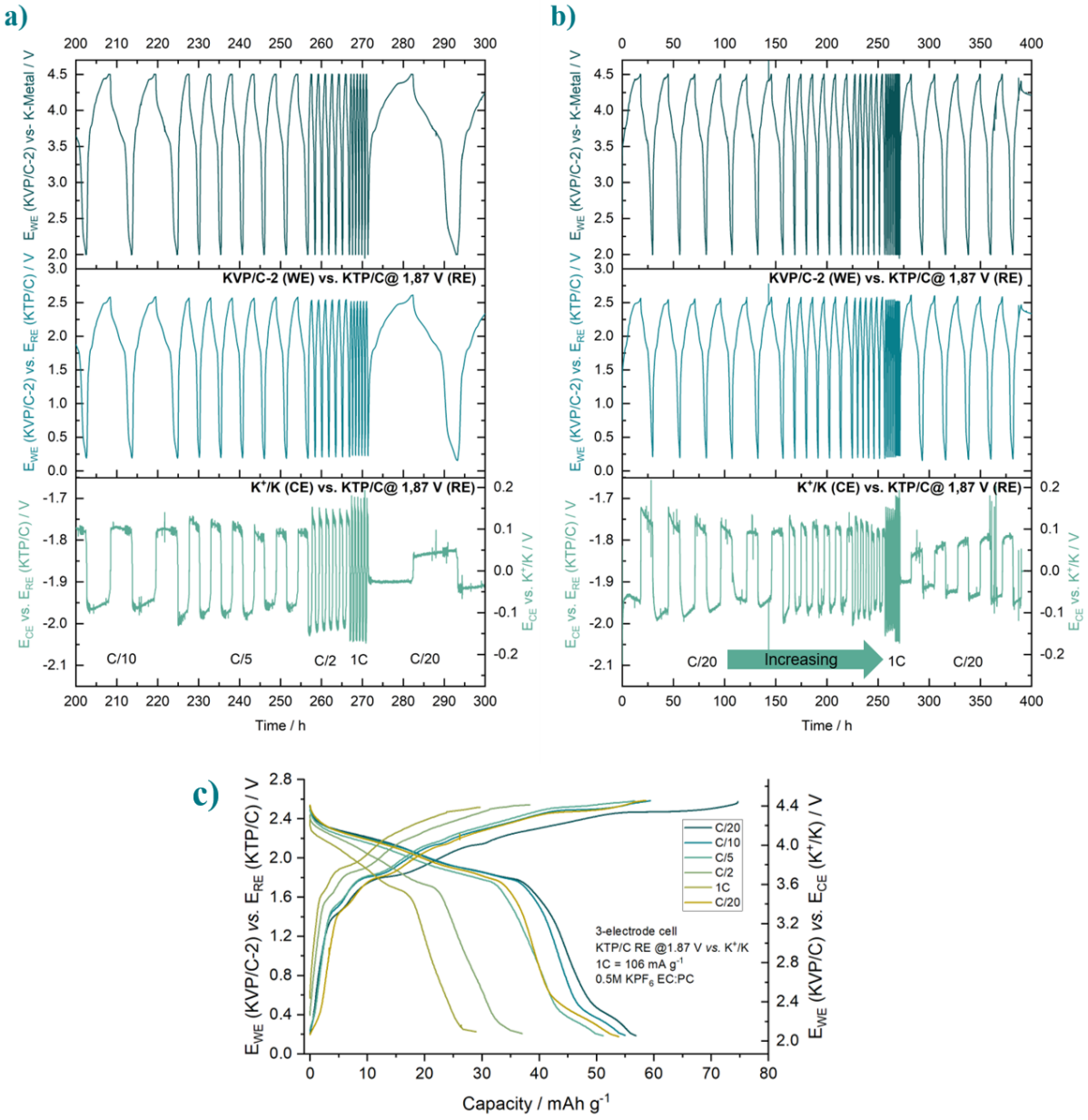

Figure 47: 3-electrode-cell measurement with KVP/C-2-800 as WE, potassium metal as CE and KTP/C as RE-pin at different time scales for improved visibility with a) t= 200 h – 300 h, b) t= 0 h – 400 h and c) KVP/C-2-800 WE vs. KTP/C-RE potential vs. specific capacity. The C-rate (1C = 106 mA g^{-1}) was varied similar to the PIB half-cell setup. As an electrolyte 0.5M KPF_6 in EC:PC was used.

The 3-electrode-cell data for the KVP/C composites clearly reveals the increasing overpotential at the potassium metal anode (CE) with increasing C-rate / current. However, the specific discharge capacities demonstrate a correlation with the coin-cell type half-cell setups of the KVP/C-2-800 composites (**Figure 22a**). This coincidence is similarly observed for the KTP/C and KVPO/C 3-electrode setups.

Additionally, at all different C-rates a highly drifting potential of the potassium metal anode is visible. This correlates well with results from Komaba *et al.*, where they obtained a strong increase of the measured overpotential in symmetric cells of potassium metal with increasing currents.[37] The cut-off potentials for the KVP/C-2-800 were set to 4.5 V and 2.0 V *versus* the potassium metal CE in the 3-electrode setup. Those cut-offs potentials are never reached in the realistic PIB half-cell setup. The experimental realistic upper cut-off potential was around 2.6 V / 4.47 V at C/20, which was reduced to below 2.5 V / 4.37 V at 1C *versus* the KTP/C-RE or potassium metal CE respectively. The lower cut-off potential was biased in the opposite way as it was around 0.2 V / 2.07 V at C/20 and above 0.25 V / 2.13 V at 1 C *versus* the KTP/C-RE or potassium metal CE respectively. Based on these results, an increased bias onto the C-rate capability test from the potassium metal CE is clearly revealed. This demonstrates an increased underestimation of the electrochemical performance of the different electrode active materials with increasing C-rate in PIB half-cell setups. The reproducibility of the electrochemical performance of electrode active materials determined in PIB half-cells could be also questioned based on these results. The potassium metal potential is highly dependent onto the applied current and is drifting continuously during cycling. Due to different mass loadings of the characterized WE in PIB half-cell setups, a different current is applied at each C-rate of each cell leading to different bias caused by the potassium metal anode. This leads in fact to different impacts onto the achievable realistic cut-off potentials and electrochemical performance of the investigated WE. Similar to the KVPO/C composites, the polarization of the KVP/C-2-800 composite is low compared to the polarization caused by the potassium metal anode (**Figure** 47 **middle**). This further confirms the results from chapter 6.3, where a Ag / AgCl RE was used and underlines the potential of and precise characterization with the KTP/C-RE in a 3-electrode-setup. As demonstrated by the results presented above, it is evident that the electrochemical characterization of electrode active materials, electrolytes, etc. is significantly biased by the presence of a potassium metal anode. To enhance the reliability and precision of the electrochemical characterization, it is inevitable that the characterizations are conducted within 3-electrode cells or utilizing an alternative CE or DE within a conventional half-cell configuration.

KTPO/C seems to be a promising candidate as a DE due to its distinct voltage plateau / redox reaction at around 1.0 V *versus* K^+ / K and intrinsically high ionic conductivity based on the crystal structure of the KTPO material class.[120,121] Combined with the unique microstructure and improved electronic conductivity of the KTPO/C granules, this should lead to low polarization and improved reaction kinetics of the KTPO/C composites (see chapter 7.1.2), making them suitable as a DE at the voltage plateau of around 1.0 V. To prove the polarization and reaction kinetics of the KTPO/C composite, a 3-electrode-cell with KTPO/C as WE, potassium metal as CE and the KTP/C-RE was cycled at C/20. The corresponding 3-electrode-cell data is shown in **Figure 48,** combined with the voltage profile over capacity for the KTPO/C WE *vs.* KTP/C-RE potential. The specific charge capacity obtained in the 3-electrode setup for the KTPO/C composite correlates well with the results of the coin-cell type half-cells (**Figure 43**) with about 130 mAh g^{-1} (**Figure 48c**). The small deviations can be explained by setup related issues like low geometric overlap of WE and CE due to the WE design (16 mm with 8 mm hole in the middle).

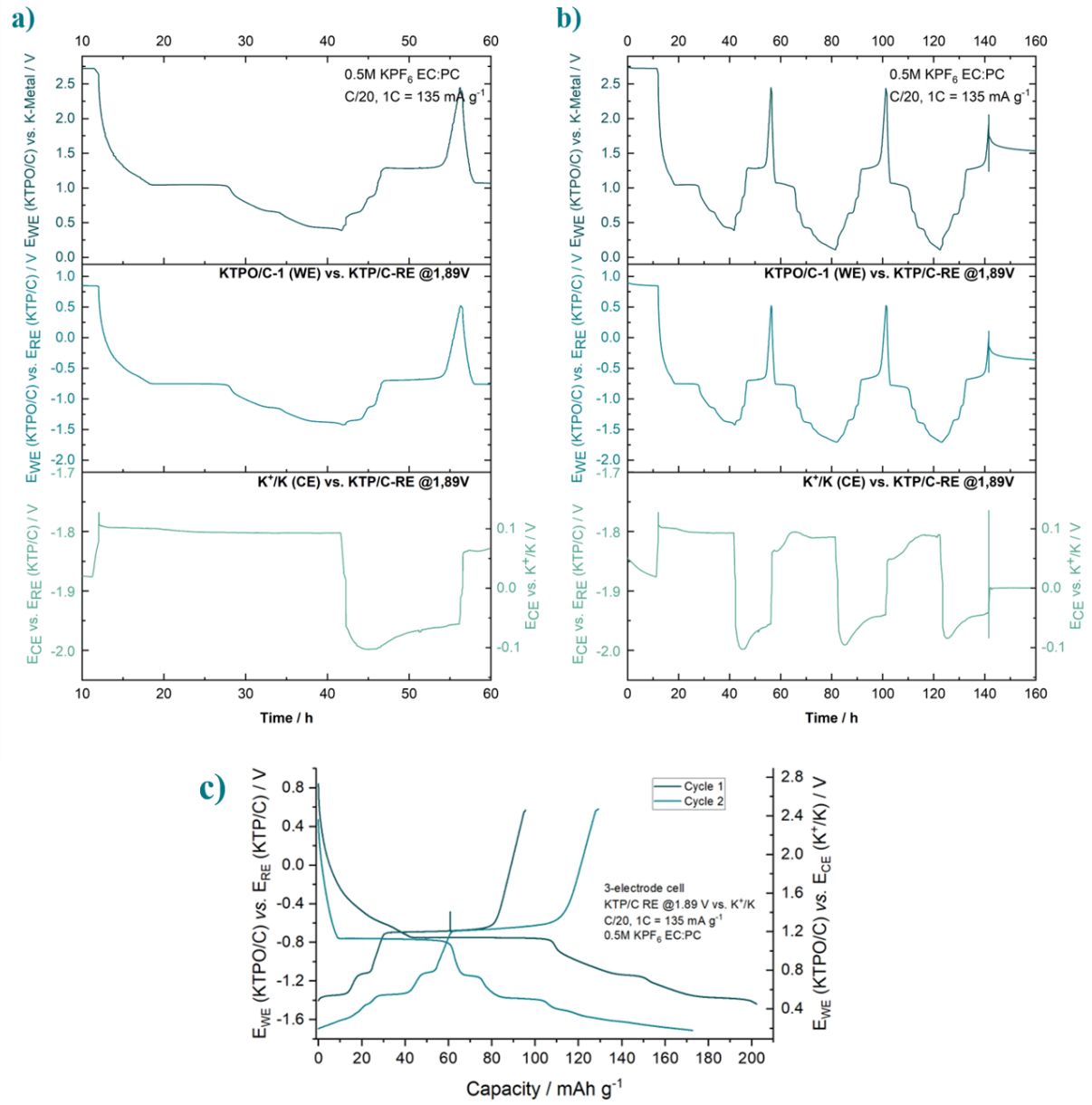

Figure 48: *3-electrode-cell measurement with KTPO/C as WE, potassium metal as CE and KTP/C as RE-pin at different time scales for improved visibility with a) t= 10 h – 60 h, b) t= 0 h – 160 h and c) KTPO/C WE vs. KTP/C-RE potential vs. specific capacity. Galvanostatic cycling was performed at C/20 (1C = 135 mA g^{-1}). As an electrolyte 0.5M KPF_6 in EC:PC was used. Note: During the first cycle the lower cut-off potential of 0.1 V versus K^+/K was not reached due to a time limitation for each cycling step.*

Similar to the KVP/C-2-800 and KVPO/C composites tested in a 3-electrode-setup, the high polarization of around 200 mV and drifting potential of the potassium metal CE at C/20 becomes directly obvious (**Figure 48 bottom**). Again, the polarization was calculated in the center of the corresponding charge / discharge plateau at around 1.1 V / 1.3 V of the cell potential during the first cycle. More interestingly, for the KTPO/C composite a polarization of less than 50 mV is obtained at the voltage plateau around -0.75 V / 1.14 V *versus* KTP/C-RE or K^+/K respectively. This underlines the improved reaction kinetics based on good electronic and ionic conductivity of the KTPO/C composites, render them an ideal candidate as a DE for

a more reliable and fast characterization of different electrode active materials for PIBs. This is absolutely necessary due to several practical problems associated with a potassium metal CE like high resistivity of the metal, growth of mossy structures, formation of resistive surface layers and unstable SEI with recurrent parasitic side reactions.[135,143-146,156,160] The utilization of the KTPO/C composites at its voltage plateau around 1.0 V as a DE in a full-cell setup for PIBs will be discussed in the following chapter.

7.3 Development of a Full-Cell-Setup for Electrochemical Characterization of Cathodic Materials

The idea for the utilization of the KTPO/C composite as a DE was to use it as counter electrode discharged to its voltage plateau around 1.0 V *versus* K^+/K. As shown in **Figure 48**, the polarization of the KTPO/C composite between charge and discharge at this voltage plateau was below 50 mV at C/20. This in fact, should lead to a stable potential of the CE during cycling in a full-cell setup, similar reported for LTO as a counter electrode in LIBs.[165] In a first setup, a 14 mm KTPO/C DE / anode with similar mass loading to the 12 mm KVP/C-2-800 cathodes was used to study the proof-of-concept. The remaining cell setup (electrolyte, separator, spacer, etc.) was kept constant compared to the conventional half-cell setup with a potassium metal CE. In **Figure 49** a 3-electrode-cell measurement with KVP/C-2-800 as WE, the KTPO/C as DE and the KTP/C-RE is shown. In the initial measurement, the potential window was selected as 0.6 V - 3.8 V to circumvent any limitations imposed by the cell setup, particularly those arising from erroneous cut-off potentials. This was done to definitely attain the voltage plateau of the KTPO/C, which is at approximately 1.0 V *versus* K^+ / K.

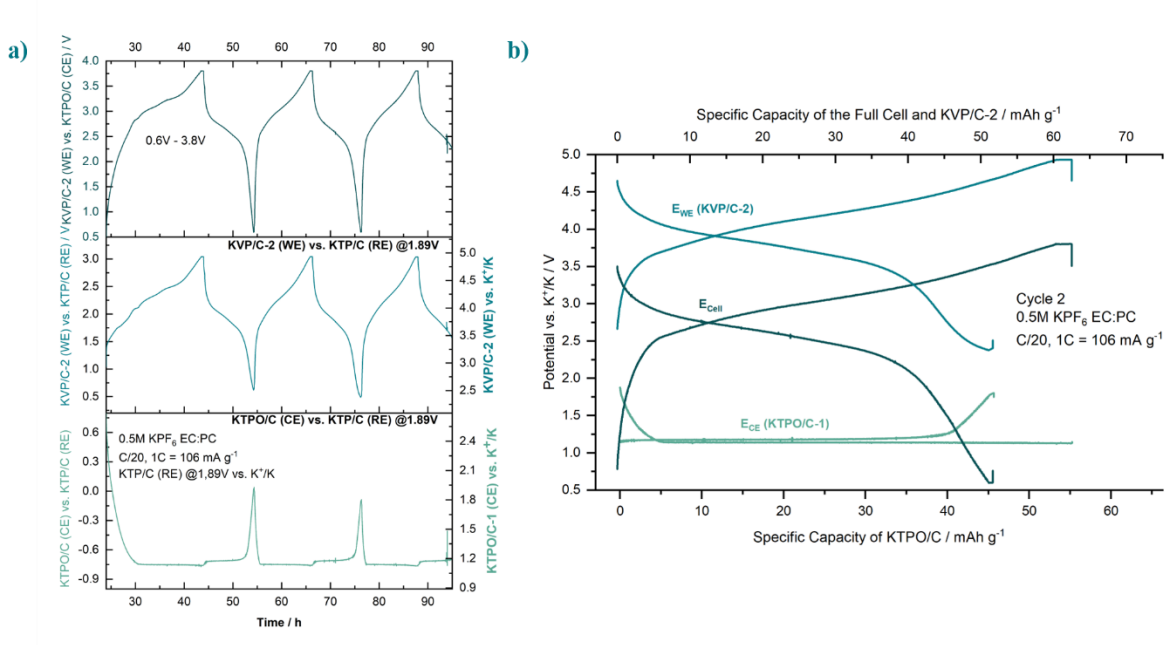

Figure 49: 3-electrode-cell measurement with KVP/C-2-800 as WE, an unconditioned KTPO/C DE and the KTP/C RE-pin with a) potential profiles of the cell, WE and DE over time and b) potential profiles of the cell, WE and DE over the specific capacity of KVP/C or KTPO/C respectively. Galvanostatic cycling was performed at C/20 (1C = 106 mA g^{-1}), as an electrolyte 0.5M KPF_6 EC:PC (1:1) was used.

During the first charge of the full cell, the potential of the KTPO/C DE is lowered to around -0.75 V *vs.* KTP/C-RE and 1.14 V *vs.* K^+/K, respectively, due to insertion of potassium ions into the KTPO structure (**Figure 49 a, bottom**). Simultaneously, the potential of the

KVP/C-2-800 rises to around 3.1 V *vs.* KTP/C-RE and 4.99 V *vs.* K^+/K, respectively, due to the deinsertion of potassium ions (**Figure 49 a, center**). During charge, the cell does not get limited by the potential of the KTPO/C DE as its potential stays constant around -0.75 V *vs.* KTP/C-RE and 1.14 V *vs.* K^+/K till the upper cut-off potential is reached due to the increase in potential of the KVP/C-2-800 WE. During discharge, the small polarization of around 50 mV for the KTPO/C DE compared to charge, similar to the results from the 3-electrode-measurements of a KTPO/C WE against a potassium metal CE, is observed (**Figure 49 a, bottom**). Based on the 3-electrode-cell measurement with KVP/C-2-800 as WE and KTPO/C as DE it is clearly revealed that cycling of a cathodic material against a KTPO/C DE at its plateau around 1.1 V is plausible.

Nevertheless, at the end of the discharge step the cell is characterized by a strong increase in potential of the KTPO/C DE limiting the overall cell performance in terms of capacity, as shown for the 2nd cycle in **Figure 49 b**. A possible cause for the limitation of the overall cell performance could be the huge irreversible capacity losses in the first cycle at the KTPO/C DE, which becomes obvious by the prolonged lowering of the potential of the KTPO/C DE in the first charging step. To overcome the limitations caused by irreversible losses in the first cycle, an improved mass balancing or improved electrolyte composition could be an option for further improvements of the setup. As this thesis is mainly focused onto the synthesis and characterization of different cathode active materials and not onto electrode or electrolyte optimization, a more hands-on driven approach was used. To reduce the irreversible losses in the first cycle, the KTPO/C composite electrodes were preconditioned in a PIB half-cell setup for two cycles within the voltage range of 0.9 V – 1.5 V *vs.* K^+/K at C/20. An exemplary preconditioning of the KTPO/C CE is shown in **Appendix 34**. Additionally, KVP/C-2-800 WE with lower mass loadings were used to ensure an overbalancing of the KTPO/C DE, which should exclude the risk of capacity limitation caused by the KTPO/C DE.

The corresponding 3-electrode-measurement of a KVP/C-2-800 as WE with a preconditioned KTPO/C DE and the KTP/C RE-pin is shown in **Figure 50**.

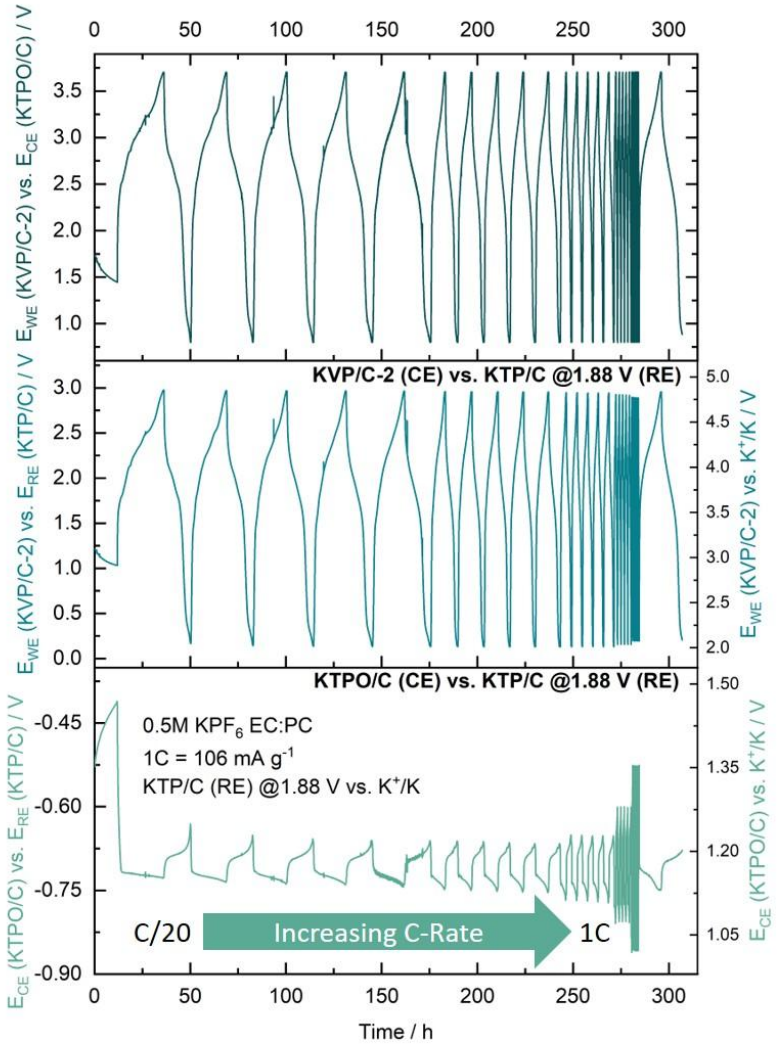

Figure 50: *3-electrode-cell data for a full-cell with KVP/C-2-800 WE, preconditioned KTPO/C DE and the KTP/C-RE with potential profiles of the cell (top), KVP/C-2-800 WE (middle) and preconditioned KTPO/C DE over time. Galvanostatic cycling was performed at C-rates similar to the half-cell setup (1C = 106 mA g^{-1}), as an electrolyte 0.5M KPF_6 EC:PC (1:1) was used.*

Based on the results from the first full-cell setup, the voltage range was reduced to 0.8 V – 3.7 V as the KTPO/C DE shows a stable potential around 1.1 V – 1.2 V at C/20. Within this voltage range, the KVP/C-2 WE-800 is cycled around 2.0 V – 4.8 V *versus* K^+/K, which means an increased upper cut-off voltage compared to the KVP/C-2 half-cell characterization. During C-rate capability test of the full-cell setup with a preconditioned KTPO/C CE, a very low polarization of just up to 80 mV until C/5 (**Figure 50**), compared to more than 200 mV in the half-cell setup for the potassium metal CE (**Figure 47**), is observed for the KTPO/C CE. At C/2 and 1C the polarization of the KTPO/C CE is increasing to around 200 mV and 300 mV

respectively, which is still about 100 mV lower than for a potassium metal CE (**Figure 47**) in the 3-electrode setup *versus* a KVP/C-2-800 WE. These values indicate already the great potential of the KTPO/C composites as a stable DE to replace the potassium metal CE. Another benefit of the KTPO/C DE seems its stable potential and polarization during C-rate capability test, at least for the five cycles at each C-rate. This allows theoretically a more precise and stable electrochemical characterization of the tested electrode active materials compared to the use of a potassium metal CE. To obtain a first impression of the underestimation of the electrochemical performance of different electrode active materials in terms of specific capacity, coin-cells with a preconditioned KTPO/C as DE *vs.* a KVP/C-2-800 WE are compared with the half-cell characterization of the KVP/C-2-800 composites in the next chapter.

8 Comparison of Half-Cell and Full-Cell Performance of KVP/C

In **Figure 51** a comparison of the full-cell performance of the KVP/C-2-800 composite *versus* a preconditioned KTPO/C DE and the half-cell performance of the KVP/C-2-800 composite is shown. Again, a lower mass loading for the KVP/C-2-800 WE compared to the KTPO/C DE was used to ensure an overbalancing of the KTPO/C DE.

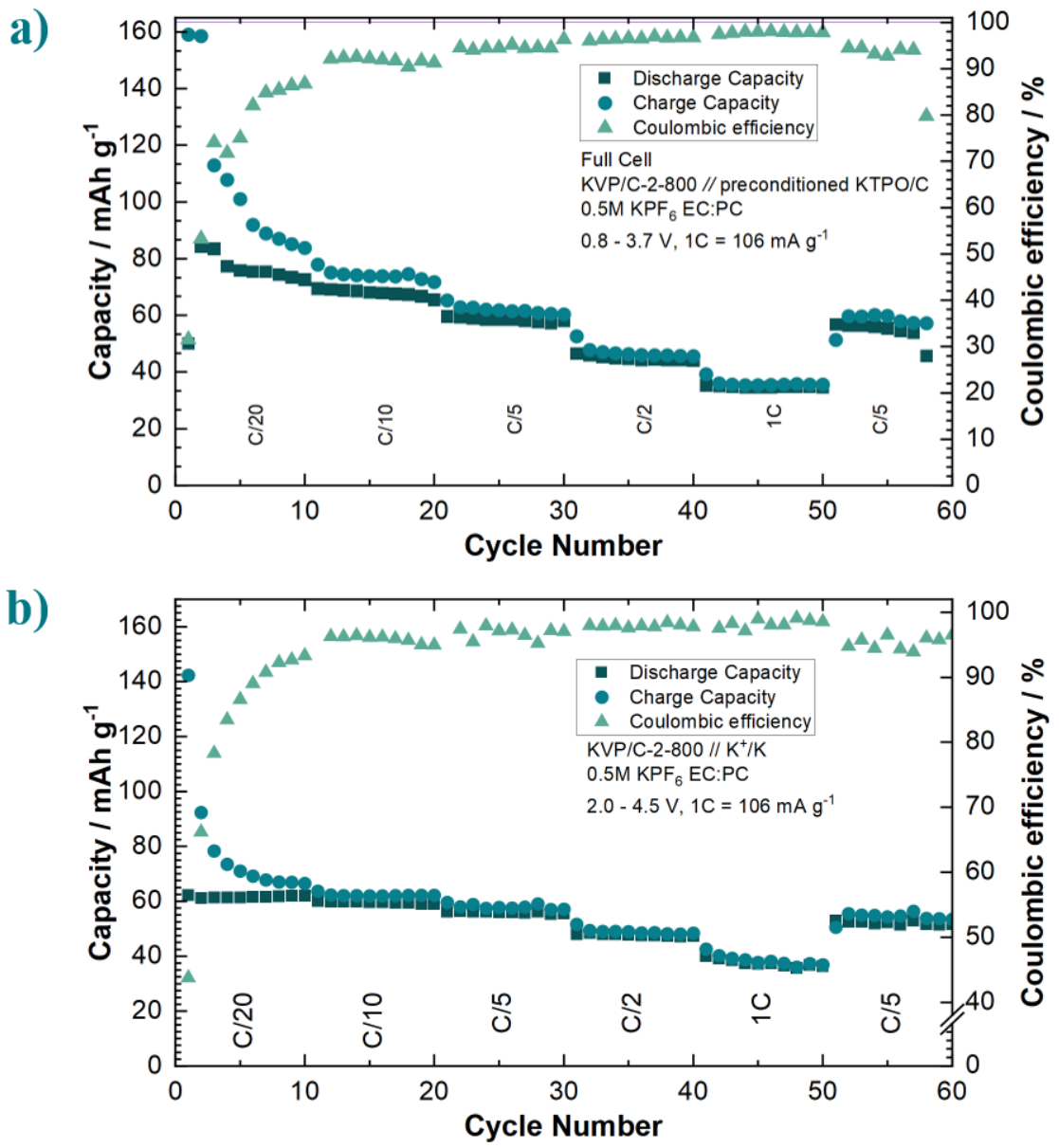

Figure 51: Comparison of the electrochemical characterization of a KVP/C-2-800 WE in a) a full-cell setup versus a preconditioned KTPO/C DE and b) a conventional half-cell setup versus a potassium metal CE. As an electrolyte 0.5M KPF_6 in EC:PC was used.

It is directly obvious that the KVP/C-2-800 composites exhibit an improved specific discharge capacity at C/20 of more than 10 mAh g^{-1} in the full-cell setup, compared to the half-cell data. One reason is definitely the reduced bias caused by the DE, another reason could be the

increased upper cut-off voltage of the KVP/C-2-800 in the full-cell setup compared to the half-cell setup. In literature the upper cut-off voltage for KVP/C composite was always limited to maximum 4.5 V. This higher cut-off voltage could lead to possible higher specific discharge capacities as potentially more potassium ions could be inserted / deinserted into the KVP/C structure at these high potentials. Additionally, the C-rate capability of the KVP/C-2-800 composites in the full-cell setup is improved compared to the half-cell setup until C-rates of C/2. This effect is mainly caused by the reduced polarization of the KTPO/C DE compared to the potassium metal. The voltage profiles appear to be similar between half- and full-cell setup (**Appendix 35**), indicating the stable potential of the KTPO/C DE shown in **Figure 50**. At 1 C the specific discharge capacity of the half-cell and full cell setup seems to be similar around 36 - 37 mAh g^{-1}. This could be explained by a similar polarization of the KTPO/C DE (**Figure** 50) compared to the potassium metal CE at 1C, leading to a decrease of the specific discharge capacity due to a biased cut-off voltage of the KVP/C-2-800 WE. These first results of the developed full-cell setup with a preconditioned KTPO/C DE approve the great potential of a possible DE, in this case KTPO/C composites. Firstly, it is possible to reduce the bias introduced by an unstable CE until moderate C-rates (C/2). Secondly, it allows a more precise, reliable and fast characterization of the electrode active materials compared to the conventional half-cell setup with the highly reactive potassium metal CE. With further studies on the different Ti-phosphate composites to improve their C-rate capability and lower the polarization at higher C-rates, further improvements onto this full-cell setup could be made. This optimization, when combined with improved electrolytes to reduce irreversible losses, has the potential to result in improved full-cell configurations. This approach eliminates the requirement for a preconditioning step of the DE, facilitating more precise and reliable studies of diverse electrode active materials.

9 Conclusion

One major research challenge for the development of PIBs is the lack of suitable cathodic materials with high energy density and stable cycling performance. Polyanionic potassium-vanadium-phosphates are ideally suited as they possess high average discharge potentials, leading to high energy densities, combined with a stable structural framework for stable cycling performance. As polyanionic materials typically lack of electronic conductivity, an easily scalable spray-drying assisted solid-state approach for the synthesis of hierarchically structured carbon composites was successfully developed in this thesis. Additionally, due to the design of the secondary granules on a micrometer scale with an open porosity and nanosized primary particles, the benefits of nanoscopic materials with improved reaction kinetics and microscopic materials with improved processability were combined. For KVP/C, one promising cathodic material, different carbon source contents and sintering temperatures were studied to tackle the low bulk ionic and electronic conductivity of polyanionic materials by an optimized microstructural design. A medium carbon source content and a sintering temperature of 800 °C are beneficial, leading to improved electrochemical performance due to the microstructural design with open porosity, nanocrystallinity and in-situ carbon coating. Nevertheless, the maximum discharge capacity of the KVP/C composites is somehow limited to around 60 % of the theoretical capacity (106 mAh g^{-1}) and the crystal structure of the KVP phase is still an open question, leaving room for further improvement of the KVP/C composites on the microstructural level.

Based on the developed synthesis process, KVPO/C composites, another promising cathodic material, were successfully synthesized. Due to the microstructural design of the granules, which leads in fact to beneficial reaction kinetics, an improvement of 30 % (93 mAh g^{-1} at C/20) in terms of capacity and 24 % (344 Wh kg^{-1} at C/20) in terms of energy density compared to literature was achieved.

As the conventional characterization of electrode active materials in PIB half-cells is accompanied with severe issues caused by the potassium metal anode like resistive surface layer and unstable SEI formation or growth of mossy structures and dendrites, two Ti-based electrode materials were established as RE and DE respectively. A stable RE and DE is inevitable to allow a precise and reliable characterization of different high-voltage electrode active materials for PIBs. For this purpose, the developed synthesis process for the vanadium-based materials was transferred to the KTP/C and KTPO/C composites to improve their electrochemical characteristics based on a beneficial microstructural design of the granules. Both Ti-based

materials revealed improved reaction kinetics with low polarization, an operation potential around 1.0 V in the stability region of commonly used liquid organic electrolytes and reached their theoretical charge capacities at low C-rates. As the synthesized KTP/C granules showed a stable potential on the mid- to long-term time scale (1.88 V *vs.* K^+/K, drift rate 0.16 mV h^{-1}), the with the C-rate increasing bias of the potassium metal anode onto electrochemical characterization in half-cells was directly measurable with the developed KTP/C as a RE. Additionally, the use of KTP/C as RE revealed a low polarization, meaning improved reaction kinetics of all hierarchically structured active materials due to the optimized microstructure of the granules and a highly drifting potential of the potassium metal anode. Based on the intrinsic material properties and optimized microstructure, the KTPO/C granules showed a stable polarization of only 50 mV at C/20 making them suitable as a DE for a fast and reliable characterization of electrode active materials. A coin-cell type full-cell with KVP/C as WE and KTPO/C as DE revealed an underestimation of the discharge capacity of KVP/C of more than 10 mAh g^{-1} at low to moderate C-rates compared to the PIB half-cell setups due to potassium metal CE related issues.

In conclusion, the easily scalable synthesis approach improved the electrochemical performance of different promising cathodic materials, while a good processability was still maintained. Combined with the developed Ti-based RE / DE and improved electrochemical characterization methods, important steps on the way to large-scale testing of different electrode active materials on the pouch-cell level and a facilitated electrolyte development for PIBs were taken in this work.

10 Outlook

As the anodic active material for a commercialization of PIBs in the future is fixed with graphite due to its high capacity (up to 272 mAh g^{-1}) and known production processes, the cathode materials remain the limiting factor for PIBs. The studied potassium-vanadium-phosphates KVPO and KVP rely mainly on the highly toxic and expensive element vanadium, which makes them unfavorable for a further industrialization on the way to a more environmentally friendly battery technology of PIBs. In the class of polyanionic materials, a wide range of possible other cathode active materials, which rely on more abundant and non-toxic elements like Mn or Fe, should be explored as alternatives to complement PBAs as the most promising cathode active material for PIBs so far. A possible alternative could be the class of potassium-iron-oxalates. Pramanik *et al.* synthesized several different compounds via hydrothermal methods and explored their potential as a cathodic material for SIBs and LIBs, but did not utilize them as a cathodic material for PIBs.[87,174,175] The synthesis of $K_2Fe(C_2O_4)_2$ (KFeOx) and $KFe(C_2O_4)F$ (KFeOxF) analogue to Pramanik *et al. via* a hydrothermal synthesis route relies only on non-critical elements and leads to large yellowish-orange crystals after synthesis (**Figure 52a**).[87,175]

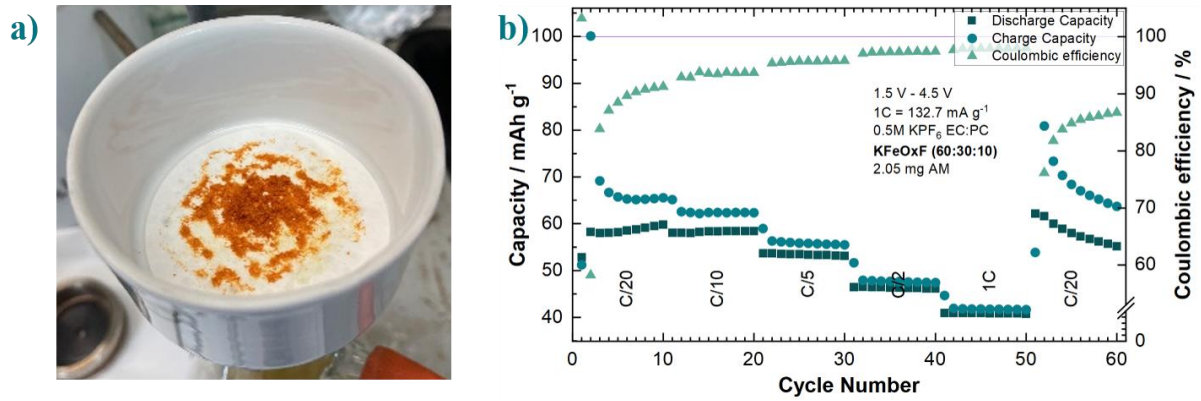

Figure 52: a) Exemplary yellowish-orange crystals of the as-synthesized KFeOxF crystals via hydrothermal methods, b) C-rate capability test of KFeOxF in a conventional PIB half-cell setup (1C = 132.7 mA g^{-1}). As an electrolyte 0.5M KPF_6 EC:PC (1:1) was used.

A first evaluation of these two materials as cathodic materials for PIBs leads to specific capacities of up to 60 mAh g^{-1}, but with a reduced average voltage (<3.0 V) compared to the vanadium phosphates (**Figure 52b**). Due to the low electronic conductivity of these materials the C-rate performance remains a critical issue if utilized as a cathodic material. Nevertheless, the different potassium iron oxalates show a promising electrochemical performance in the first electrochemical tests. Further improvement could be achieved if the synthesis of the potassium iron oxalates could be scaled for example *via* precipitation instead of hydrothermal methods, which is quite common for oxalate-based materials. A scaled synthesis could be ultimately

combined with the during this work established spray-drying process, leading to improved electrochemical performance. The combination with a carbon coating and / or carbon additive during hierarchical structuring could enhance the electronic conductivity and overcome kinetic limitations.

Beside the exploration of different polyanionic materials, a partly or complete substitution of vanadium for the KVPO or KVP could be promising due to cost- and toxicity issues. Another possible optimization of the developed synthesis process could be achieved by varying the primary particle size or used carbon sources. A different milling time or milling ball size could lead to optimized primary particle sizes, which ultimately improves the electrochemical performance.

The developed DE and RE based on potassium titanium phosphates have the potential to improve strongly the precision and reliability of electrochemical characterization in the field of PIBs. Further optimization could be done on several levels like 3-electrode-cell design, electrode coating, electrolyte or the materials itself. For example, improved reaction kinetics and C-rate capability of the KTPO/C by an improved synthesis process could lead to lower overpotentials at high C-rates. Beside this an optimized and standardized electrode coating process with an improved electrolyte for stable SEI formation, could allow the use of the KTPO/C DE without any preconditioning. This would simplify and fasten the characterization of different cathodic materials, etc. even more. On the 3-electrode-cell level an improved design of the KTP/C-RE as a mesh between two separators could be an optimization and simplify the use of the RE in classical 3-electrode-cell setups. The evaluation of specific discharge capacities in this setup would be much easier as well, as similar electrodes to coin cells could be used. This guarantees a good and complete geometric overlap of the WE and DE to determine the specific capacities more precisely compared to the 3-electrode setup used in this work.

11 References

1 Whittingham, M. S. Electrical Energy Storage and Intercalation Chemistry. *Science* **192**, 1126-1127 (1976). https://doi.org/10.1126/science.192.4244.1126

2 Mizushima, K., Jones, P. C., Wiseman, P. J. & Goodenough, J. B. LixCoO2 (0<x<-1): A new cathode material for batteries of high energy density. *Materials Research Bulletin* **15**, 783-789 (1980). https://doi.org/https://doi.org/10.1016/0025-5408(80)90012-4

3 Yoshino, A. The birth of the lithium-ion battery. *Angew Chem Int Ed Engl* **51**, 5798-5800 (2012). https://doi.org/10.1002/anie.201105006

4 Nobelprize.org. *Press release*, <https://www.nobelprize.org/prizes/chemistry/2019/press-release/> (2019).

5 Wali, S. B. *et al.* Battery storage systems integrated renewable energy sources: A biblio metric analysis towards future directions. *Journal of Energy Storage* **35** (2021). https://doi.org/10.1016/j.est.2021.102296

6 IEA. Global Supply Chains of EV Batteries. (IEA, Paris, 2022). https://www.iea.org/reports/global-supply-chains-of-ev-batteries

7 Schmuch, R., Wagner, R., Hörpel, G., Placke, T. & Winter, M. Performance and cost of materials for lithium-based rechargeable automotive batteries. *Nature Energy* **3**, 267-278 (2018). https://doi.org/10.1038/s41560-018-0107-2

8 Baumann, M. *et al.* Prospective Sustainability Screening of Sodium-Ion Battery Cathode Materials. *Advanced Energy Materials* **12** (2022). https://doi.org/10.1002/aenm.202202636

9 IEA. Global Critical Minerals Outlook 2024. (IEA, Paris, 2024). https://www.iea.org/reports/global-critical-minerals-outlook-2024

10 Andre, D. *et al.* Future generations of cathode materials: an automotive industry perspective. *Journal of Materials Chemistry A* **3**, 6709-6732 (2015). https://doi.org/10.1039/c5ta00361j

11 Yi, T.-F., Mei, J. & Zhu, Y.-R. Key strategies for enhancing the cycling stability and rate capacity of LiNi0.5Mn1.5O4 as high-voltage cathode materials for high power lithium-ion batteries. *Journal of Power Sources* **316**, 85-105 (2016). https://doi.org/10.1016/j.jpowsour.2016.03.070

12 Vaalma, C., Buchholz, D., Weil, M. & Passerini, S. A cost and resource analysis of sodium-ion batteries. *Nature Reviews Materials* **3**, 18013 (2018). https://doi.org/10.1038/natrevmats.2018.13

13 Yang, S., Song, Y., Zavalij, P. Y. & Stanley Whittingham, M. Reactivity, stability and electrochemical behavior of lithium iron phosphates. *Electrochemistry Communications* **4**, 239-244 (2002). https://doi.org/https://doi.org/10.1016/S1388-2481(01)00298-3

14 Jugović, D. & Uskoković, D. A review of recent developments in the synthesis procedures of lithium iron phosphate powders. *Journal of Power Sources* **190**, 538-544 (2009). https://doi.org/10.1016/j.jpowsour.2009.01.074

15 Mayyas, A., Steward, D. & Mann, M. The case for recycling: Overview and challenges in the material supply chain for automotive li-ion batteries. *Sustainable Materials and Technologies* **19** (2019). https://doi.org/10.1016/j.susmat.2018.e00087

16 Pinegar, H. & Smith, Y. R. Recycling of End-of-Life Lithium Ion Batteries, Part I: Commercial Processes. *Journal of Sustainable Metallurgy* **5**, 402-416 (2019). https://doi.org/10.1007/s40831-019-00235-9

17 Sada, K., Darga, J. & Manthiram, A. Challenges and Prospects of Sodium-Ion and Potassium-Ion Batteries for Mass Production. *Advanced Energy Materials* **13** (2023). https://doi.org/10.1002/aenm.202302321

18 Taylor, S. R. Abundance of chemical elements in the continental crust: a new table. *Geochimica et Cosmochimica Acta* **28**, 1273-1285 (1964).
19 Zhang, J. *et al.* Development status and future prospect of non-aqueous potassium ion batteries for large scale energy storage. *Nano Energy* **60**, 340-361 (2019). https://doi.org/10.1016/j.nanoen.2019.03.078
20 Mineral commodity summaries 2020. 204 (Reston, VA, 2020).
21 Dhir, S., Wheeler, S., Capone, I. & Pasta, M. Outlook on K-Ion Batteries. *Chem* **6**, 2442-2460 (2020). https://doi.org/10.1016/j.chempr.2020.08.012
22 CATL. *Naxtra Battery Breakthrough & Dual-Power Architecture: CATL Pioneers the Multi-Power Era*, <https://www.catl.com/en/news/6401.html#:~:text=CATL%27s%20Naxtra%20passenger%20EV%20Battery,and%20battery%20ages%20as%20one.> (2025).
23 Matsuda, Y., Nakashima, H., Morita, M. & Takasu, Y. Behavior of Some Ions in Mixed Organic Electrolytes of High Energy Density Batteries. *Journal of The Electrochemical Society* **128**, 2552 (1981). https://doi.org/10.1149/1.2127289
24 Marcus, Y. Thermodynamic Functions of Transfer of Single Ions from Water to Nonaqueous and Mixed Solvents, Part 3: Standard Potentials of Selected Electrodes. *Pure & Appl. Chem.* **57**, 1129-1132 (1985).
25 Jian, Z., Luo, W. & Ji, X. Carbon Electrodes for K-Ion Batteries. *J Am Chem Soc* **137**, 11566-11569 (2015). https://doi.org/10.1021/jacs.5b06809
26 Komaba, S., Hasegawa, T., Dahbi, M. & Kubota, K. Potassium intercalation into graphite to realize high-voltage/high-power potassium-ion batteries and potassium-ion capacitors. *Electrochemistry Communications* **60**, 172-175 (2015). https://doi.org/10.1016/j.elecom.2015.09.002
27 Hosaka, T., Kubota, K., Hameed, A. S. & Komaba, S. Research Development on K-Ion Batteries. *Chem Rev* **120**, 6358-6466 (2020). https://doi.org/10.1021/acs.chemrev.9b00463
28 Xu, Y. *et al.* 2023 roadmap for potassium-ion batteries. *Journal of Physics: Energy* **5** (2023). https://doi.org/10.1088/2515-7655/acbf76
29 Winter, M. R. J. B. What are Batteries, Fuel Cells, and Supercapacitors? *Chemical Reviews* **104**, 4245-4270 (2004). https://doi.org/https://doi.org/10.1021/cr020730k
30 Larhrib, B., Larbi, L. & Madec, L. Nonaqueous potassium-ion full-cells: Mapping the progress and identifying missing puzzle pieces. *Journal of Energy Chemistry* **93**, 384-399 (2024). https://doi.org/10.1016/j.jechem.2024.01.033
31 Hosaka, T. & Komaba, S. Development of Nonaqueous Electrolytes for High-Voltage K-Ion Batteries. *Bulletin of the Chemical Society of Japan* **95**, 569-581 (2022). https://doi.org/10.1246/bcsj.20210412
32 Xu, Y., Ding, T., Sun, D., Ji, X. & Zhou, X. Recent Advances in Electrolytes for Potassium-Ion Batteries. *Advanced Functional Materials* **33** (2022). https://doi.org/10.1002/adfm.202211290
33 Eftekhari, A., Jian, Z. & Ji, X. Potassium Secondary Batteries. *ACS Appl Mater Interfaces* **9**, 4404-4419 (2017). https://doi.org/10.1021/acsami.6b07989
34 Naylor, A. J., Carboni, M., Valvo, M. & Younesi, R. Interfacial Reaction Mechanisms on Graphite Anodes for K-Ion Batteries. *ACS Appl Mater Interfaces* **11**, 45636-45645 (2019). https://doi.org/10.1021/acsami.9b15453
35 Zhao, J., Zou, X., Zhu, Y., Xu, Y. & Wang, C. Electrochemical Intercalation of Potassium into Graphite. *Advanced Functional Materials* **26**, 8103-8110 (2016). https://doi.org/10.1002/adfm.201602248
36 Allgayer, F., Maibach, J. & Jeschull, F. Comparing the Solid Electrolyte Interphases on Graphite Electrodes in K and Li Half Cells. *ACS Applied Energy Materials* **5**, 1136-1148 (2022). https://doi.org/10.1021/acsaem.1c03491

37 Kubota, K., Dahbi, M., Hosaka, T., Kumakura, S. & Komaba, S. Towards K-Ion and Na-Ion Batteries as "Beyond Li-Ion". *Chem Rec* **18**, 459-479 (2018). https://doi.org/10.1002/tcr.201700057
38 Chang, X., Sun, N., Zhou, H., Soomro, R. A. & Xu, B. Soft carbon-coated bulk graphite for improved potassium ion storage. *Chinese Chemical Letters* **34**, 107312 (2023). https://doi.org/https://doi.org/10.1016/j.cclet.2022.03.035
39 An, Y. *et al.* Commercial expanded graphite as a low–cost, long-cycling life anode for potassium–ion batteries with conventional carbonate electrolyte. *Journal of Power Sources* **378**, 66-72 (2018). https://doi.org/10.1016/j.jpowsour.2017.12.033
40 Gong, J. *et al.* Controllable Phosphorylation Strategy for Free-Standing Phosphorus/Nitrogen Cofunctionalized Porous Carbon Monoliths as High-Performance Potassium Ion Battery Anodes. *ACS Nano* **14**, 14057-14069 (2020). https://doi.org/10.1021/acsnano.0c06690
41 Li, D. *et al.* Facile Fabrication of Nitrogen-Doped Porous Carbon as Superior Anode Material for Potassium-Ion Batteries. *Advanced Energy Materials* **8** (2018). https://doi.org/10.1002/aenm.201802386
42 Piernas-Munoz, M. J. & Zarrabeitia, M. Revisiting Intercalation Anode Materials for Potassium-Ion Batteries. *Materials (Basel)* **18** (2025). https://doi.org/10.3390/ma18010190
43 Mahmoud, A., Amarilla, J. M. & Saadoune, I. Effect of thermal treatment used in the sol–gel synthesis of Li 4 Ti 5 O 12 spinel on its electrochemical properties as anode for lithium ion batteries. *Electrochimica Acta* **163**, 213-222 (2015). https://doi.org/10.1016/j.electacta.2015.02.111
44 Xie, F., Zhang, L., Su, D., Jaroniec, M. & Qiao, S. Z. Na(2) Ti(3) O(7) @N-Doped Carbon Hollow Spheres for Sodium-Ion Batteries with Excellent Rate Performance. *Adv Mater* **29** (2017). https://doi.org/10.1002/adma.201700989
45 Chen, Z., Belharouak, I., Sun, Y. K. & Amine, K. Titanium-Based Anode Materials for Safe Lithium-Ion Batteries. *Advanced Functional Materials* **23**, 959-969 (2012). https://doi.org/10.1002/adfm.201200698
46 Ghosh, A. & Ghamouss, F. Role of Electrolytes in the Stability and Safety of Lithium Titanate-Based Batteries. *Frontiers in Materials* **7** (2020). https://doi.org/10.3389/fmats.2020.00186
47 Sha, M., Liu, L., Zhao, H. & Lei, Y. Anode materials for potassium-ion batteries: Current status and prospects. *Carbon Energy* **2**, 350-369 (2020). https://doi.org/10.1002/cey2.57
48 Kishore, B., G, V. & Munichandraiah, N. K2Ti4O9: A Promising Anode Material for Potassium Ion Batteries. *Journal of The Electrochemical Society* **163**, A2551-A2554 (2016). https://doi.org/10.1149/2.0421613jes
49 Dong, Y. *et al.* Ti(3)C(2) MXene-Derived Sodium/Potassium Titanate Nanoribbons for High-Performance Sodium/Potassium Ion Batteries with Enhanced Capacities. *ACS Nano* **11**, 4792-4800 (2017). https://doi.org/10.1021/acsnano.7b01165
50 Han, J. *et al.* Exploration of K(2)Ti(8)O(17) as an anode material for potassium-ion batteries. *Chem Commun (Camb)* **52**, 11274-11276 (2016). https://doi.org/10.1039/c6cc05102b
51 Jian, Z., Hu, Y. S., Ji, X. & Chen, W. NASICON-Structured Materials for Energy Storage. *Adv Mater* **29** (2017). https://doi.org/10.1002/adma.201601925
52 Zhang, C. & Zhou, L. in *Electrochemical Potassium Storage - Principles, Materials and Technological Development* (ed Yang Xu) 101-128 (WOODHEAD Publishing, 2025).
53 Wang, L. *et al.* Prospects and Challenges of Practical Nonaqueous Potassium-Ion Batteries. *Advanced Functional Materials* **34** (2024). https://doi.org/10.1002/adfm.202408965

54 C. Delmas, C. F., P. Hagenmuller. Structural Classification and Properties of the Layered Oxides. *Physica B+C* **99**, 81-85 (1980).
55 Kim, H. *et al.* Stoichiometric Layered Potassium Transition Metal Oxide for Rechargeable Potassium Batteries. *Chemistry of Materials* **30**, 6532-6539 (2018). https://doi.org/10.1021/acs.chemmater.8b03228
56 Kim, H. *et al.* Investigation of Potassium Storage in Layered P3-Type K(0.5) MnO(2) Cathode. *Adv Mater* **29** (2017). https://doi.org/10.1002/adma.201702480
57 Zhang, B., Choi, Y., Zhu, Z., Zhao, S. & Guo, S. Manganese-Based Layered Oxide Cathodes for Potassium-Ion Batteries: Progress and Outlook. *Advanced Energy Materials* (2025). https://doi.org/10.1002/aenm.202501657
58 Vaalma, C., Giffin, G. A., Buchholz, D. & Passerini, S. Non-Aqueous K-Ion Battery Based on Layered K0.3MnO2and Hard Carbon/Carbon Black. *Journal of The Electrochemical Society* **163**, A1295-A1299 (2016). https://doi.org/10.1149/2.0921607jes
59 Zhang, Q. *et al.* Structural Insight into Layer Gliding and Lattice Distortion in Layered Manganese Oxide Electrodes for Potassium-Ion Batteries. *Advanced Energy Materials* **9** (2019). https://doi.org/10.1002/aenm.201900568
60 Zhang, X. *et al.* Layered P2-Type K0.44Ni0.22Mn0.78O2 as a High-Performance Cathode for Potassium-Ion Batteries. *Advanced Functional Materials* **29** (2019). https://doi.org/10.1002/adfm.201905679
61 Bai, P. *et al.* Ni-Doped Layered Manganese Oxide as a Stable Cathode for Potassium-Ion Batteries. *ACS Appl Mater Interfaces* **12**, 10490-10495 (2020). https://doi.org/10.1021/acsami.9b22237
62 Jo, J. H. *et al.* P2-K0.75[Ni1/3Mn2/3]O2 Cathode Material for High Power and Long Life Potassium-Ion Batteries. *Advanced Energy Materials* **10** (2020). https://doi.org/10.1002/aenm.201903605
63 Ding, X. *et al.* Multi-element doping induced transition metal disordered layered oxide for rapid and stable potassium storage. *Chemical Engineering Journal* **466** (2023). https://doi.org/10.1016/j.cej.2023.143331
64 Duan, L. *et al.* A high-performance cathode for potassium-ion batteries based on uniform P3-type K0.5Mn0.8Co0.1Ni0.1O2porous microcuboids. *Journal of Materials Chemistry A* **9**, 22820-22826 (2021). https://doi.org/10.1039/d1ta07108d
65 Li, S. *et al.* Entropy-Tuned Layered Oxide Cathodes for Potassium-Ion Batteries. *Small Methods* **7**, e2300893 (2023). https://doi.org/10.1002/smtd.202300893
66 Deng, T. *et al.* Layered P2-Type K0.65Fe0.5Mn0.5O2 Microspheres as Superior Cathode for High-Energy Potassium-Ion Batteries. *Advanced Functional Materials* **28** (2018). https://doi.org/10.1002/adfm.201800219
67 Zhao, S. *et al.* The Rise of Prussian Blue Analogs: Challenges and Opportunities for High-Performance Cathode Materials in Potassium-Ion Batteries. *Small Structures* **2** (2020). https://doi.org/10.1002/sstr.202000054
68 Eftekhari, A. Potassium secondary cell based on Prussian blue cathode. *Journal of Power Sources* **126**, 221-228 (2004). https://doi.org/10.1016/j.jpowsour.2003.08.007
69 Bie, X., Kubota, K., Hosaka, T., Chihara, K. & Komaba, S. A novel K-ion battery: hexacyanoferrate(ii)/graphite cell. *Journal of Materials Chemistry A* **5**, 4325-4330 (2017). https://doi.org/10.1039/c7ta00220c
70 Xue, L. *et al.* Low-Cost High-Energy Potassium Cathode. *J Am Chem Soc* **139**, 2164-2167 (2017). https://doi.org/10.1021/jacs.6b12598
71 Hosaka, T., Fukabori, T., Kojima, H., Kubota, K. & Komaba, S. Effect of Particle Size and Anion Vacancy on Electrochemical Potassium Ion Insertion into Potassium Manganese Hexacyanoferrates. *ChemSusChem* **14**, 1166-1175 (2021). https://doi.org/10.1002/cssc.202002628

72 Fiore, M. *et al.* Paving the Way toward Highly Efficient, High-Energy Potassium-Ion Batteries with Ionic Liquid Electrolytes. *Chemistry of Materials* **32**, 7653-7661 (2020). https://doi.org/10.1021/acs.chemmater.0c01347
73 Ge, J., Fan, L., Rao, A. M., Zhou, J. & Lu, B. Surface-substituted Prussian blue analogue cathode for sustainable potassium-ion batteries. *Nature Sustainability* **5**, 225-234 (2021). https://doi.org/10.1038/s41893-021-00810-7
74 Xue, Q. *et al.* Polypyrrole-Modified Prussian Blue Cathode Material for Potassium Ion Batteries via In Situ Polymerization Coating. *ACS Applied Materials & Interfaces* **11**, 22339-22345 (2019). https://doi.org/10.1021/acsami.9b04579
75 Shi, W. *et al.* Self-supporting Prussian blue@CNF based battery-capacitor with superhigh adsorption capacity and selectivity for potassium recovery. *Chemical Engineering Journal* **388** (2020). https://doi.org/10.1016/j.cej.2020.124162
76 Manthiram, A. & Goodenough, J. B. Lithium insertion into Fe2(SO4)3 frameworks. *Journal of Power Sources* **26**, 403-408 (1989). https://doi.org/https://doi.org/10.1016/0378-7753(89)80153-3
77 Goodenough, J. B., Hong, H. Y. P. & Kafalas, J. A. Fast Na+-ion transport in skeleton structures. *Materials Research Bulletin* **11**, 203-220 (1976). https://doi.org/https://doi.org/10.1016/0025-5408(76)90077-5
78 Masquelier, C. & Croguennec, L. Polyanionic (phosphates, silicates, sulfates) frameworks as electrode materials for rechargeable Li (or Na) batteries. *Chem Rev* **113**, 6552-6591 (2013). https://doi.org/10.1021/cr3001862
79 Hosaka, T., Shimamura, T., Kubota, K. & Komaba, S. Polyanionic Compounds for Potassium-Ion Batteries. *Chem Rec* **19**, 735-745 (2019). https://doi.org/10.1002/tcr.201800143
80 Huang, H. *et al.* Polyanionic Cathode Materials: A Comparison Between Na-Ion and K-Ion Batteries. *Advanced Energy Materials* **14** (2024). https://doi.org/10.1002/aenm.202304251
81 Li, M. *et al.* 10 Years Development of Potassium-Ion Batteries. *Adv Mater*, e2416717 (2025). https://doi.org/10.1002/adma.202416717
82 Dong, J. *et al.* Graphene encircled KFeSO(4)F cathode composite for high energy density potassium-ion batteries. *Chem Commun (Camb)* **56**, 10050-10053 (2020). https://doi.org/10.1039/d0cc03795h
83 Bodart, J. *et al.* Spray-dried K3V(PO4)2/C composites as novel cathode materials for K-ion batteries with superior electrochemical performance. *Journal of Power Sources* **480** (2020). https://doi.org/10.1016/j.jpowsour.2020.229057
84 Park, W. B. *et al.* KVP2O7 as a Robust High-Energy Cathode for Potassium-Ion Batteries: Pinpointed by a Full Screening of the Inorganic Registry under Specific Search Conditions. *Advanced Energy Materials* **8** (2018). https://doi.org/10.1002/aenm.201703099
85 Wu, N. *et al.* K-Ion Battery Cathode Design Utilizing Trigonal Prismatic Ligand Field. *Adv Mater* **33**, e2101788 (2021). https://doi.org/10.1002/adma.202101788
86 Fedotov, S. S. *et al.* Titanium-based potassium-ion battery positive electrode with extraordinarily high redox potential. *Nat Commun* **11**, 1484 (2020). https://doi.org/10.1038/s41467-020-15244-6
87 Pramanik, A. *et al.* K(2)Fe(C(2)O(4))(2): An Oxalate Cathode for Li/Na-Ion Batteries Exhibiting a Combination of Multielectron Cation and Anion Redox. *Chem Mater* **35**, 2600-2611 (2023). https://doi.org/10.1021/acs.chemmater.3c00063
88 Mathew, V. *et al.* Amorphous iron phosphate: potential host for various charge carrier ions. *NPG Asia Materials* **6**, e138-e138 (2014). https://doi.org/10.1038/am.2014.98
89 Park, H. *et al.* Development of K4Fe3(PO4)2(P2O7) as a novel Fe-based cathode with high energy densities and excellent cyclability in rechargeable potassium batteries.

Energy Storage Materials **28**, 47-54 (2020). https://doi.org/10.1016/j.ensm.2020.02.031

90 Han, J. *et al.* Investigation of K(3)V(2)(PO(4))(3)/C nanocomposites as high-potential cathode materials for potassium-ion batteries. *Chem Commun (Camb)* **53**, 1805-1808 (2017). https://doi.org/10.1039/c6cc10065a

91 Li, S. *et al.* K3V3(PO4)4/C: A new carbon-coated layered structure cathode material for potassium-ion batteries. *Journal of Alloys and Compounds* **969** (2023). https://doi.org/10.1016/j.jallcom.2023.172446

92 Chihara, K., Katogi, A., Kubota, K. & Komaba, S. KVPO(4)F and KVOPO(4) toward 4 volt-class potassium-ion batteries. *Chem Commun (Camb)* **53**, 5208-5211 (2017). https://doi.org/10.1039/c6cc10280h

93 Wernert, R. *et al.* Controlling the Cathodic Potential of KVPO4F through Oxygen Substitution. *Chemistry of Materials* **34**, 4523-4535 (2022). https://doi.org/10.1021/acs.chemmater.2c00295

94 He, H. *et al.* Vanadium-Based Pyrophosphate Material K2(VO)3(P2O7)2 as a High Voltage Cathode for Potassium Ion Batteries. *ACS Applied Energy Materials* **7**, 41-47 (2023). https://doi.org/10.1021/acsaem.3c02153

95 Kim, H. *et al.* A New Strategy for High-Voltage Cathodes for K-Ion Batteries: Stoichiometric KVPO4F. *Advanced Energy Materials* **8** (2018). https://doi.org/10.1002/aenm.201801591

96 Caracciolo, L. *et al.* Electrochemical Redox Processes Involved in Carbon-Coated KVPO4F for High Voltage K-Ion Batteries Revealed by XPS Analysis. *Journal of The Electrochemical Society* **167** (2020). https://doi.org/10.1149/1945-7111/abbb0c

97 Kim, H., Tian, Y. & Ceder, G. Origin of Capacity Degradation of High-Voltage KVPO4F Cathode. *Journal of The Electrochemical Society* **167** (2020). https://doi.org/10.1149/1945-7111/aba54e

98 Liao, J. *et al.* A long lifespan potassium-ion full battery based on KVPO4F cathode and VPO4 anode. *Journal of Power Sources* **451** (2020). https://doi.org/10.1016/j.jpowsour.2020.227739

99 Liu, Z., Wang, J. & Lu, B. Plum pudding model inspired KVPO(4)F@3DC as high-voltage and hyperstable cathode for potassium ion batteries. *Sci Bull (Beijing)* **65**, 1242-1251 (2020). https://doi.org/10.1016/j.scib.2020.04.010

100 Wernert, R. *et al.* Self-Discharge Mechanism of High-Voltage KVPO4F for K-Ion Batteries. *ACS Applied Energy Materials* **5**, 14913-14921 (2022). https://doi.org/10.1021/acsaem.2c02379

101 Heng, Y. *et al.* Low-Strain and High-Energy KVPO4F Cathode with Multifunctional Stabilizer for Advanced Potassium-Ion Batteries. *Energy & Environmental Materials* **7** (2024). https://doi.org/10.1002/eem2.12721

102 Fedotov, S. S., Samarin, A. S. & Antipov, E. V. KTiOPO4-structured electrode materials for metal-ion batteries: A review. *Journal of Power Sources* **480** (2020). https://doi.org/10.1016/j.jpowsour.2020.228840

103 Häringer, M., Geßwein, H., Bohn, N., Ehrenberg, H. & Binder, J. R. Influence of Process Parameters on the Electrochemical Properties of Hierarchically Structured Na3V2(PO4)3/C Composites. *ChemElectroChem* **11** (2023). https://doi.org/10.1002/celc.202300401

104 Wang, X. *et al.* Novel K3V2(PO4)3/C Bundled Nanowires as Superior Sodium-Ion Battery Electrode with Ultrahigh Cycling Stability. *Advanced Energy Materials* **5** (2015). https://doi.org/10.1002/aenm.201500716

105 Zhang, L. *et al.* Constructing the best symmetric full K-ion battery with the NASICON-type K3V2(PO4)3. *Nano Energy* **60**, 432-439 (2019). https://doi.org/10.1016/j.nanoen.2019.03.085

106 Jenkins, T., Alarco, J. A. & Mackinnon, I. D. R. Synthesis and Characterization of a Novel Hydrated Layered Vanadium(III) Phosphate Phase K(3)V(3)(PO(4))(4).H(2)O: A Functional Cathode Material for Potassium-Ion Batteries. *ACS Omega* **6**, 1917-1929 (2021). https://doi.org/10.1021/acsomega.0c04675

107 Zheng, S. *et al.* Partial replacement of K by Rb to improve electrochemical performance of K3V2(PO4)3 cathode material for potassium-ion batteries. *Journal of Alloys and Compounds* **815** (2020). https://doi.org/10.1016/j.jallcom.2019.152379

108 Kuai, H.-X. *et al.* High-performance, three-dimensional and porous K3V2(PO4)3/C cathode material for potassium-ion batteries. *Ionics* **28**, 3817-3831 (2022). https://doi.org/10.1007/s11581-022-04612-5

109 Benhamada, L., Grandin, A., Borel, M. M., Leclaire, A. & Raveau, B. KVPO5, an intersecting tunnel structure closely related to the hexagonal tungsten bronze. *Acta Crystallographica Section C* **47**, 1138-1141 (1991). https://doi.org/https://doi.org/10.1107/S0108270190014044

110 Lian, R. *et al.* Phase transformation, ionic diffusion, and charge transfer mechanisms of KVOPO4 in potassium ion batteries: first-principles calculations. *Journal of Materials Chemistry A* **6**, 16228-16234 (2018). https://doi.org/10.1039/c8ta06708b

111 Wernert, R. *Crystal Chemistry and redox mechanisms of vanadium phosphates and Prussian Blue analogues for K-ion batteries* PhD thesis, Université de Bordeaux, (2023).

112 Ding, J. *et al.* KVOPO4: A New High Capacity Multielectron Na-Ion Battery Cathode. *Advanced Energy Materials* **8** (2018). https://doi.org/10.1002/aenm.201800221

113 Katorova, N. S. *et al.* Effect of Concentrated Diglyme-Based Electrolytes on the Electrochemical Performance of Potassium-Ion Batteries. *ACS Applied Energy Materials* **2**, 6051-6059 (2019). https://doi.org/10.1021/acsaem.9b01173

114 Li, J. *et al.* Enhanced K-storage performance in ultralong cycle-life potassium-ion batteries achieved via carbothermal-reduction-synthesized KVOPO4 cathode. *Energy Storage Materials* **61** (2023). https://doi.org/10.1016/j.ensm.2023.102852

115 Voronina, N., Jo, J. H., Konarov, A., Kim, J. & Myung, S. T. KTi(2) (PO(4))(3) Electrode with a Long Cycling Stability for Potassium-Ion Batteries. *Small* **16**, e2001090 (2020). https://doi.org/10.1002/smll.202001090

116 Sheng, J. *et al.* KTi2(PO4)3 with Large Ion Diffusion Channel for High-Efficiency Sodium Storage. *Advanced Energy Materials* **7** (2017). https://doi.org/10.1002/aenm.201700247

117 Han, J. *et al.* Nanocubic KTi(2)(PO(4))(3) electrodes for potassium-ion batteries. *Chem Commun (Camb)* **52**, 11661-11664 (2016). https://doi.org/10.1039/c6cc06177j

118 Dong, J. *et al.* Optimized Porous KTi2(PO4)3@N-Doped Carbon Electrode for Enhanced Sodium/Potassium-Storage and Accelerated Activation Process. *ACS Applied Materials & Interfaces* **17**, 18319-18328 (2025). https://doi.org/10.1021/acsami.4c22245

119 Thomas, P. A., Glazer, A. M. & Watts, B. E. Crystal structure and nonlinear optical properties of KSnOPO4 and their comparison with KTiOPO4. *Acta Crystallographica Section B* **46**, 333-343 (1990). https://doi.org/doi:10.1107/S0108768190001318

120 Zhang, R. *et al.* Safe, Low-Cost, Fast-Kinetics and Low-Strain Inorganic-Open-Framework Anode for Potassium-Ion Batteries. *Angew Chem Int Ed Engl* **58**, 16474-16479 (2019). https://doi.org/10.1002/anie.201909202

121 Kumar, P. R., Kubota, K., Igarashi, D. & Komaba, S. Enhanced Electrochemical Properties of KTiOPO4–rGO Negative Electrode for Sodium and Potassium Ion Batteries. *The Journal of Physical Chemistry C* **125**, 24823-24830 (2021). https://doi.org/10.1021/acs.jpcc.1c08339

122 Yu, S. *et al.* Morphology Dependency of Li3V2(PO4)3/C Cathode Material Regarding to Rate Capability and Cycle Life in Lithium-ion Batteries. *Electrochimica Acta* **232**, 310-322 (2017). https://doi.org/10.1016/j.electacta.2017.02.136
123 Chen, Z., Chao, D., Chen, M. & Shen, Z. Hierarchical porous LiNi(1/3)Co(1/3)Mn(1/3)O(2) with yolk-shell-like architecture as stable cathode material for lithium-ion batteries. *RSC Adv* **10**, 18776-18783 (2020). https://doi.org/10.1039/d0ra03022h
124 Guan, X.-m., Li, G.-j., Li, C.-y. & Ren, R.-m. Synthesis of porous nano/micro structured LiFePO4/C cathode materials for lithium-ion batteries by spray-drying method. *Transactions of Nonferrous Metals Society of China* **27**, 141-147 (2017). https://doi.org/10.1016/s1003-6326(17)60016-5
125 Bauer, W. *et al.* Using Hierarchically Structured, Nanoporous Particles as Building Blocks for NCM111 Cathodes. *Nanomaterials (Basel)* **14** (2024). https://doi.org/10.3390/nano14020134
126 Li, L. *et al.* Structural and Electrochemical Study of Hierarchical LiNi1/3Co1/3Mn1/3O2 Cathode Material for Lithium-Ion Batteries. *ACS Applied Materials & Interfaces* **7**, 21939-21947 (2015). https://doi.org/10.1021/acsami.5b06584
127 Poozesh, S. & Bilgili, E. Scale-up of pharmaceutical spray drying using scale-up rules: A review. *Int J Pharm* **562**, 271-292 (2019). https://doi.org/10.1016/j.ijpharm.2019.03.047
128 Schmidt, M. *et al.* High Performance of Porous, Hierarchically Structured P2-Na0.6Al0.11 − xNi0.22 − yFex + yMn0.66O2 Cathode Materials. *Advanced Energy Materials* **14** (2024). https://doi.org/10.1002/aenm.202301854
129 Nandiyanto, A. B. D. & Okuyama, K. Progress in developing spray-drying methods for the production of controlled morphology particles: From the nanometer to submicrometer size ranges. *Advanced Powder Technology* **22**, 1-19 (2011). https://doi.org/10.1016/j.apt.2010.09.011
130 Wintzheimer, S. *et al.* Multifunctional, Hybrid Materials Design via Spray-Drying: Much more than Just Drying. *Adv Mater* **35**, e2306648 (2023). https://doi.org/10.1002/adma.202306648
131 Wagner, A. C. *et al.* Hierarchical Structuring of NMC111-Cathode Materials in Lithium-Ion Batteries: An In-Depth Study on the Influence of Primary and Secondary Particle Sizes on Electrochemical Performance. *ACS Applied Energy Materials* **3**, 12565-12574 (2020). https://doi.org/10.1021/acsaem.0c02494
132 Heyn, A. *et al.* Hierarchical Microstructured K3V2(PO4)3/C-Composite Electrode for Potassium-Ion-Batteries Through Scalable Spray-Drying Approach. *ChemSusChem* **18**, e202501111 (2025). https://doi.org/10.1002/cssc.202501111
133 Sostmann, T. A. *Syntheses and Electrochemical Characterization of KVOPO4/C-composites as a Cathode Material for Potassium Ion Batteries* Master of Science thesis, Karlsruhe Institute of Technology, (2025).
134 Psille, J. A. *Synthese und Charakterisierung von KTi2(PO4)3 als Anodenmaterial für K-Ionen-Batterien* Master of Science thesis, Karlsruhe Institute of Technology, (2025).
135 Panasenko, I., Bäuerle, M. & Jeschull, F. How reference electrodes improve our understanding of degradation processes in half and full cell potassium-ion battery setups. *Electrochimica Acta* **513** (2025). https://doi.org/10.1016/j.electacta.2024.145551
136 Lunezheva, E. S., Maksimov, B. A. & Mel'Nikov, O. K. Structure cristalline de KTi2(PO4)3; KTi2(PO4)3 crystal structure. *Kristallografiâ* **34**, 1119-1122 (1989).
137 Norberg, S. T., Thomas, P. A. & Tucker, M. G. A neutron total scattering study of local coordination in KTiOPO4 from room temperature to 900 °C. *Journal of Physics:*

Condensed Matter **23**, 175401 (2011). https://doi.org/10.1088/0953-8984/23/17/175401

138 Gesswein, H., Stuble, P., Weber, D., Binder, J. R. & Monig, R. A multipurpose laboratory diffractometer for operando powder X-ray diffraction investigations of energy materials. *J Appl Crystallogr* **55**, 503-514 (2022). https://doi.org/10.1107/S1600576722003089

139 Stüble, P. *et al.* From Powder to Pouch Cell: Setting up a Sodium-Ion Battery Reference System Based on Na3V2(PO4)3/C and Hard Carbon. *Batteries & Supercaps* **7** (2024). https://doi.org/10.1002/batt.202400406

140 Häringer, M. *Synthese und Hochskalierung hierarchisch strukturierter NASICON-Materialien als Kathodenmaterial für Natrium-Ionen-Batterien*. (2023).

141 Benhamada, L., Grandin, A., Borel, M. M., Leclaire, A. & Raveau, B. A new vanadium III potassium phosphate with a cage structure: K6V2P4O16. *Journal of Solid State Chemistry* **91**, 264-270 (1991). https://doi.org/https://doi.org/10.1016/0022-4596(91)90080-2

142 Hamid, N. A., Wennig, S., Heinzel, A., Schulz, C. & Wiggers, H. Influence of carbon content, particle size, and partial manganese substitution on the electrochemical performance of LiFexMn1-xPO4/carbon composites. *Ionics* **21**, 1857-1866 (2015). https://doi.org/10.1007/s11581-015-1366-6

143 Caracciolo, L., Madec, L., Gachot, G. & Martinez, H. Impact of the Salt Anion on K Metal Reactivity in EC/DEC Studied Using GC and XPS Analysis. *ACS Appl Mater Interfaces* **13**, 57505-57513 (2021). https://doi.org/10.1021/acsami.1c19537

144 Hosaka, T. *et al.* 1,3,2-Dioxathiolane 2,2-Dioxide as an Electrolyte Additive for K-Metal Cells. *ACS Energy Letters* **6**, 3643-3649 (2021). https://doi.org/10.1021/acsenergylett.1c01238

145 Xing, S. *et al.* Degradation of Styrene-Poly(ethylene oxide)-Based Block Copolymer Electrolytes at the Na and K Negative Electrode Studied by Microcalorimetry and Impedance Spectroscopy. *Journal of The Electrochemical Society* **171** (2024). https://doi.org/10.1149/1945-7111/ad3b72

146 Wildersinn, L., Stottmeister, D., Jeschull, F., Gross, A. & Hofmann, A. Decomposition of Binary Mixtures of DMC/EC, EMC/EC, and DEC/EC on Potassium Surfaces; GC, XPS, and Calculation. *ACS Appl Mater Interfaces* **17**, 10055-10072 (2025). https://doi.org/10.1021/acsami.4c17461

147 R. Dominko, M. B., M. Gaberscek, M. Remskar, D. Hanzel, S. Pejnovik and J. Jamnik. Impact of Carbon Coating Thickness on the Electrochemical Performance of $LiFePO_4$/C Composites. *Journal of The Electrochemical Society* **152**, A607-A610 (2005).

148 Raj, H. & Sil, A. Effect of carbon coating on electrochemical performance of LiFePO4 cathode material for Li-ion battery. *Ionics* **24**, 2543-2553 (2018). https://doi.org/10.1007/s11581-017-2423-0

149 Röder, C. *Finding Electrochemically Stable Electrolyte Components for High-Voltage Positive Electrodes in Potassium-Ion Batteries* Master of Science thesis, Karlsruhe Institute of Technology, (2023).

150 Amorós, P. *et al.* Crystal structure of a new polytype in the V–P–O system: is ω-VOPO4 a dynamically stabilised metastable network? *Journal of Physics and Chemistry of Solids* **62**, 1393-1399 (2001). https://doi.org/https://doi.org/10.1016/S0022-3697(01)00054-3

151 Lim, S. C. *et al.* Redox transformations of simple vanadium phosphates: the synthesis of ϵ-VOPO4. *Solid State Ionics* **84**, 219-226 (1996). https://doi.org/https://doi.org/10.1016/0167-2738(96)00007-0

152 Sadiq, M., Bensitel, M., Nohair, K., Leglise, J. & Lamonier, C. Effect of calcination temperature on the structure of vanadium phosphorus oxide materials and their catalytic

activity in the decomposition of 2-propanol. *Journal of Saudi Chemical Society* **16**, 445-449 (2012). https://doi.org/10.1016/j.jscs.2011.02.014
153 Bagnasco, G. *et al.* Tg/dta, Xrd and NH3-TPD Characterization of Layered VOPO4·2H2O and its Fe3+-Substituted Compound. *Journal of Thermal Analysis and Calorimetry* **52**, 615-630 (1998). https://doi.org/10.1023/A:1010136126445
154 Gopal, R. & Calvo, C. Crystal structure of βVPO5. *Journal of Solid State Chemistry* **5**, 432-435 (1972). https://doi.org/https://doi.org/10.1016/0022-4596(72)90089-8
155 Glaum, R. & Gruehn, R. Beiträge zum thermischen Verhalten wasserfreier Phosphate. *VI.* Einkristallstrukturverfeinerung der Metall(III)-orthophosphate TiPO4 und VPO4* **198**, 41-47 (1992). https://doi.org/doi:10.1524/zkri.1992.198.1-2.41
156 Jagger, B. *et al.* Potassium Alloy Reference Electrodes for Potassium-Ion Batteries: The K-In and K-Bi Systems. *ACS Mater Lett* **6**, 4498-4506 (2024). https://doi.org/10.1021/acsmaterialslett.4c01219
157 Dugas, R., Forero-Saboya, J. D. & Ponrouch, A. Methods and Protocols for Reliable Electrochemical Testing in Post-Li Batteries (Na, K, Mg, and Ca). *Chem Mater* **31**, 8613-8628 (2019). https://doi.org/10.1021/acs.chemmater.9b02776
158 Hosaka, T., Muratsubaki, S., Kubota, K., Onuma, H. & Komaba, S. Potassium Metal as Reliable Reference Electrodes of Nonaqueous Potassium Cells. *J Phys Chem Lett* **10**, 3296-3300 (2019). https://doi.org/10.1021/acs.jpclett.9b00711
159 Larhrib, B. & Madec, L. Toward Highly Reliable Potassium-Ion Half and Full Coin Cells. *Batteries & Supercaps* **6** (2023). https://doi.org/10.1002/batt.202300061
160 Jeschull, F. *et al.* Why Half-Cell Samples Provide Limited Insight Into the Aging Mechanisms of Potassium Batteries. *Advanced Energy Materials* **15** (2024). https://doi.org/10.1002/aenm.202403811
161 Cengiz, E. C., Rizell, J., Sadd, M., Matic, A. & Mozhzhukhina, N. Review—Reference Electrodes in Li-Ion and Next Generation Batteries: Correct Potential Assessment, Applications and Practices. *Journal of The Electrochemical Society* **168** (2021). https://doi.org/10.1149/1945-7111/ac429b
162 Costard, J., Ender, M., Weiss, M. & Ivers-Tiffée, E. Three-Electrode Setups for Lithium-Ion Batteries. *Journal of The Electrochemical Society* **164**, A80-A87 (2016). https://doi.org/10.1149/2.0241702jes
163 La Mantia, F., Wessells, C. D., Deshazer, H. D. & Cui, Y. Reliable reference electrodes for lithium-ion batteries. *Electrochemistry Communications* **31**, 141-144 (2013). https://doi.org/10.1016/j.elecom.2013.03.015
164 Whang, G., Huang, J., Le Pham, P. N., Kraft, M. A. & Zeier, W. G. Not All Lithium–Indium Counter Electrodes Are Made Equal: Probing the Inhomogeneities and Kinetics of Uniaxially Pressed Li–In Counter Electrodes in All Solid-State Batteries. *ACS Electrochemistry* **1**, 249-262 (2024). https://doi.org/10.1021/acselectrochem.4c00060
165 Han, M., Duan, J., Wang, Z., Wu, W. & Luo, W. Evaluation of Cathode Electrodes in Lithium-Ion Battery: Pitfalls and the Befitting Counter Electrode. *Small* **19**, e2208018 (2023). https://doi.org/10.1002/smll.202208018
166 McShane, E. J. *et al.* A Versatile Li0.5FePO4 Reference Electrode for Nonaqueous Electrochemical Conversion Technologies. *ACS Energy Letters* **8**, 230-235 (2022). https://doi.org/10.1021/acsenergylett.2c02190
167 Wei, Z. *et al.* Fabrication of Hierarchical Potassium Titanium Phosphate Spheroids: A Host Material for Sodium-Ion and Potassium-Ion Storage. *Advanced Energy Materials* **8** (2018). https://doi.org/10.1002/aenm.201801102
168 Huang, S. & Xu, G. KTi2(PO4)3 nanoparticles wrapped in 3D RGO as enhanced electrode for potassium-ion batteries. *Materials Letters* **361** (2024). https://doi.org/10.1016/j.matlet.2024.136156

169 Zhang, W., Liu, Y. & Guo, Z. Approaching high-performance potassium-ion batteries via advanced design strategies and engineering. *Science Advances* **5**, eaav7412 (2019). https://doi.org/10.1126/sciadv.aav7412
170 Liu, Y. *et al.* Boosting potassium-ion batteries by few-layered composite anodes prepared via solution-triggered one-step shear exfoliation. *Nat Commun* **9**, 3645 (2018). https://doi.org/10.1038/s41467-018-05786-1
171 Xu, K. Nonaqueous Liquid Electrolytes for Lithium-Based Rechargeable Batteries. *Chemical Reviews* **104**, 4303-4418 (2004). https://doi.org/10.1021/cr030203g
172 Sakao, M., Kijima, N., Akimoto, J. & Okutani, T. Synthesis, crystal structure, and electrochemical properties of hollandite-type K0.008TiO2. *Solid State Ionics* **225**, 502-505 (2012). https://doi.org/10.1016/j.ssi.2011.11.023
173 Qi, Y., Li, J., Zhong, W., Bao, S. & Xu, M. KTiOPO4: A long-life, high-rate and low-temperature-workable host for Na/K-ion batteries. *Chemical Engineering Journal* **417** (2021). https://doi.org/10.1016/j.cej.2020.128159
174 Pramanik, A., Manche, A. G., Clulow, R., Lightfoot, P. & Armstrong, A. R. Exploiting anion and cation redox chemistry in lithium-rich perovskite oxalate: a novel next-generation Li/Na-ion battery electrode. *Dalton Trans* **51**, 12467-12475 (2022). https://doi.org/10.1039/d2dt01447e
175 Pramanik, A. *et al.* KFe(C2O4)F: A Fluoro-oxalate Cathode Material for Li/Na-Ion Batteries. *ChemElectroChem* **10** (2023). https://doi.org/10.1002/celc.202300192

Use of Artificial Intelligence (AI)

In order to enhance the readability and grammatical quality of this thesis, the AI-tool DeepL Write (https://www.deepl.com/en/write) has been employed for a number of sections and sentences.

12 Appendix

Appendix 1: Nomenclature, composition and exact masses of used reactant for all different KVP/C samples.

Sample	NH_4VO_3 / g	$NH_4H_2PO_4$ / g	K_2CO_3 / g	Sucrose / g	β-Lactose / 50 g powder / g
KVP/C-1	25.00	36.871	22.16	4.42 (5 wt.%)	2.50 (5 wt.%)
KVP/C-2	30.02	44.25	26.58	8.20 (7.5 wt.%)	2.50 (5 wt.%)
KVP/C-3	30.04	44.28	26.60	11.33 (10 wt.%)	2.52 (5 wt.%)
KVP/C-4	30.04	44.28	26.58	5.41 (5 wt.%)	7.50 (15 wt.%)
KVP/C-5	30.01	44.29	26.61	8.20 (7.5 wt.%)	7.59 (15 wt.%)
KVP/C-6	30.00	44.27	26.59	11.21 (10 wt.%)	7.51 (15 wt.%)
KVP/C-2_650	30.02	44.27	26.61	8.19 (7.5 wt.%)	2.52 (5 wt.%)
KVP/C-2_700					
KVP/C-2_750					
KVP/C-2_800					
KVP/C-2_850					

Appendix 2: Composition and exact masses of used reactant for synthesis of the KVPO/C samples.

Sample	NH_4VO_3 / g	$NH_4H_2PO_4$ / g	K_2CO_3 / g	VPO_4 / g	$VOPO_4$ / g	β-Lactose / 50 g powder / g
VPO_4	32.56	31.97				
$VOPO_4$	20.36	19.99	-	-	-	-
$KVOPO_4$	-	-	18.85	19.79	22.01	-
KVPO/C	47.49 g KVPO					2.49

Appendix 3: Nomenclature, composition and exact masses of used reactant for synthesis of the KTP/C samples.

Sample	TiO_2 / g	$NH_4H_2PO_4$ / g	K_2CO_3 / g	β-Lactose / 50 g powder / g
KTP/C	19.97	43.14	9.52	5.72

Appendix 4: Nomenclature, composition and exact masses of used reactants for synthesis of the KTPO/C samples.

Sample	TiO_2 / g	$NH_4H_2PO_4$ / g	K_2CO_3 / g	Sucrose / g	β-Lactose / 50 g powder / g
KTPO/C	27.79	40.01	24.05	7.44	8.82

Appendix 5: Mass loading of cycled electrodes, either in half-cell, full-cell or 3-electrode setup.

Sample	Mass Loading Cathode / mg cm^{-2}	Mass Loading Anode / mg cm^{-2}	Setup
KVP/C-1	3.954 (C/20) 3.537 (C-Rate)	K-metal	Half-cell
KVP/C-2	3.678 (C/20) 3.827 (C-Rate) 6.841	K-metal	Half-cell *Operando* XRD
KVP/C-3	3.855 (C/20) 3.572 (C-Rate)	K-metal	Half-cell
KVP/C-4	5.111 (C/20) 3.466 (C-Rate)	K-metal	Half-cell
KVP/C-5	4.315 (C/20) 3.289 (C-Rate)	K-metal	Half-cell
KVP/C-6	3.692 (C/20) 3.820 (C-Rate)	K-metal	Half-cell
KVP/C-2-650	4.139	K-metal	Half-cell
KVP/C-2-700	4.026	K-metal	Half-cell
KVP/C-2-750	3.637	K-metal	Half-cell
KVP/C-2-800	3.532	K-metal	Half-cell
KVP/C-2-850	3.615	K-metal	Half-cell
KVP/C-2-CR	4.772 (C/20)	K-metal	Half-Cell
KVPO/C	6.854 (C-Rate) 6.549	K-metal	Half-cell *Operando* XRD

	6.414 5.303 5.996		CV CV CV
KTP/C	3.148 (C-Rate) 4.808 3.396	K-metal	Half-cell *Operando* XRD Self-discharge
KTPO/C	5.249 6.456 4.842	K-metal	Half-cell *Operando* XRD Self-discharge
KVP/C-2	5.049	K-Metal	3-El Cell with Ag / AgCl RE
KTP/C Re-Pin	1.76 mg	-	3-El-Cell RE
KVP/C-2-800	3.065	K-metal	3-El-Cell with KTP/C RE
KVPO/C	3.465	K-metal	3-El-Cell with KTP/C RE
KTPO/C	3.501	K-metal	3-El-Cell with KTP/C RE
KTP/C	2.249	K-metal	3-El-Cell with KTP/C RE
KVP/C-2-800 WE vs. KTPO/C DE	3.435 1.509	3.987 3.841	3-El-Cell Full Cell with KTP/C RE
KVP/C-2-800 WE vs. KTPO/C DE	1.726	3.945	Full-Cell
KFeOxF	1.813	K-Metal	Half-Cell

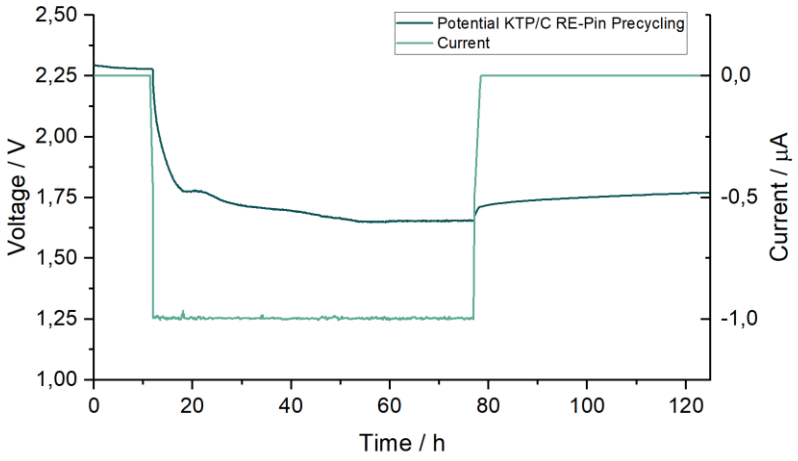

Appendix 6: Precycling procedure of a with KTP/C coated pin for cycling KTP/C to its voltage plateau around 1.6V vs. K/K^+ and the subsequent relaxation period. After the relaxation period the pin could be used as RE for evaluation of different electrode materials in PIB.

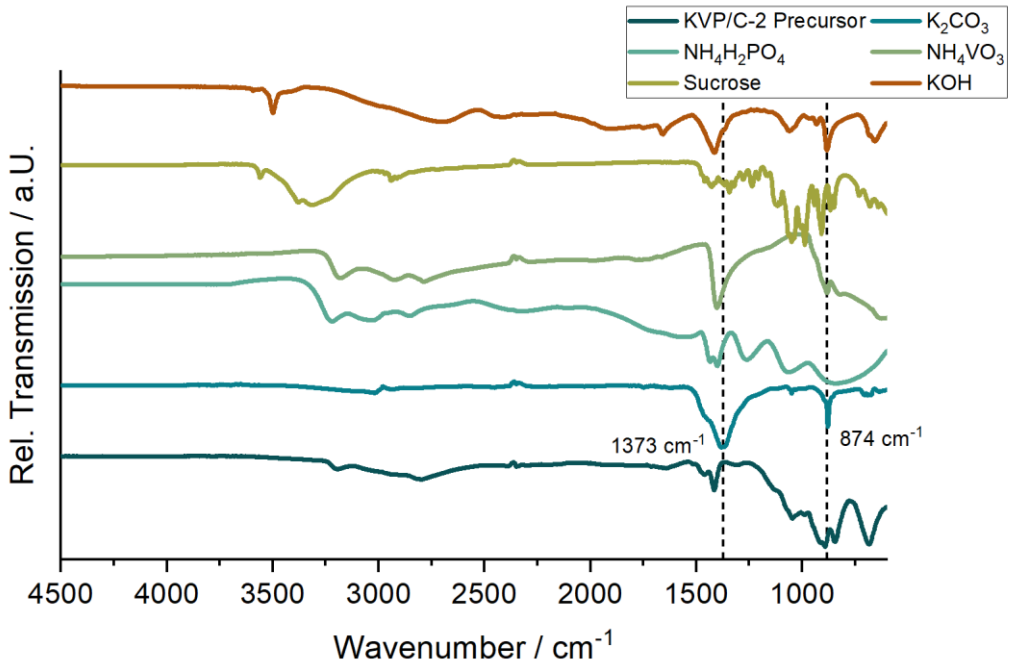

Appendix 7: FT-IR measurement on powders of the prepared KVP/C-2 precursor and the used reactants additional with KOH.

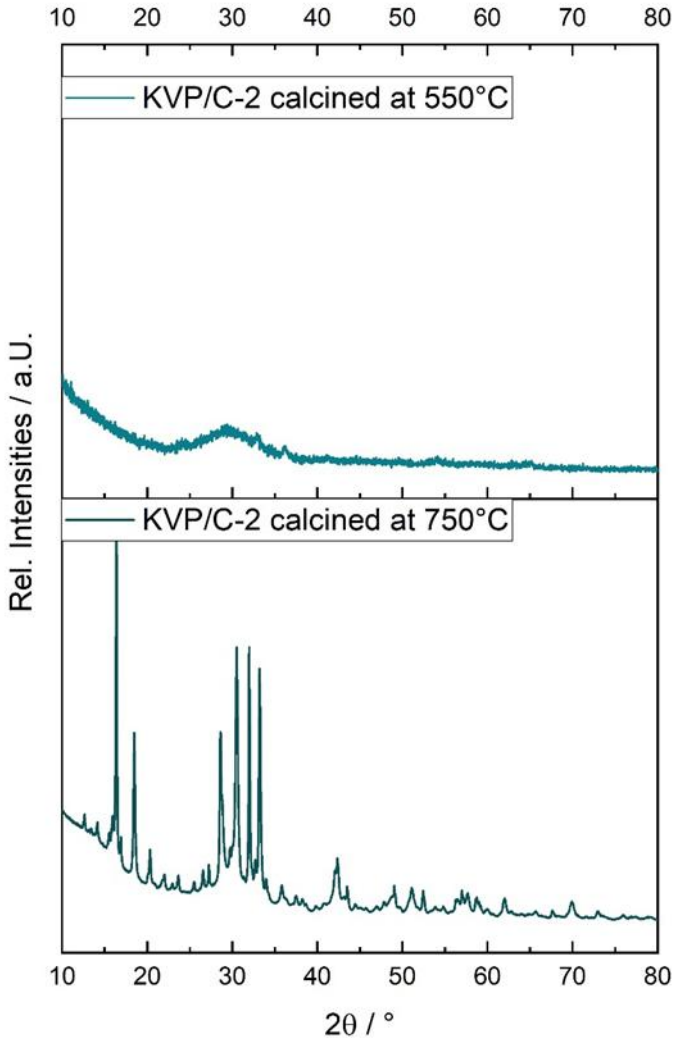

Appendix 8: Powder XRD of a KVP/C-2 precursor calcined at a temperature below 700 °C (top) and at 750 °C (bottom) under Ar + 3 % H_2-atmosphere for 48 h reproduced from Heyn et al.[132]

Appendix 9: Mass losses and onset temperatures determined by TG/DSC-IR analysis of the KVP/C-2 precursor combined with suggested decomposition products, adapted from Heyn et al.[132]

Onset Temperature / °C	**Weight loss / %**	**Decomposition product / Reaction process**
100	21.1	NH_4, H_2O, CO_2
300	6.6	CO_2
700	.	Crystallization KVP
800	6.3	CO, possible reaction of carbon matrix with KVP

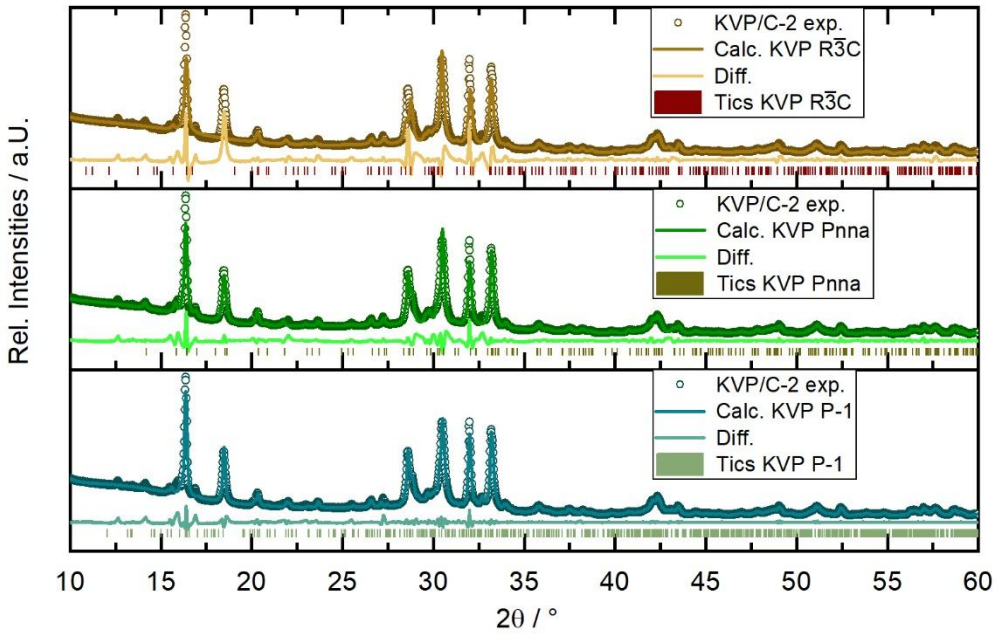

Appendix 10: Le-Bail Fits of the obtained diffraction pattern for KVP/C-2 based on different crystal structure models from literature with a) NASICON structure $R\bar{3}C$, b) orthorhombic Pnna structure and c) triclinic P-1 structure based on preliminary SAED results

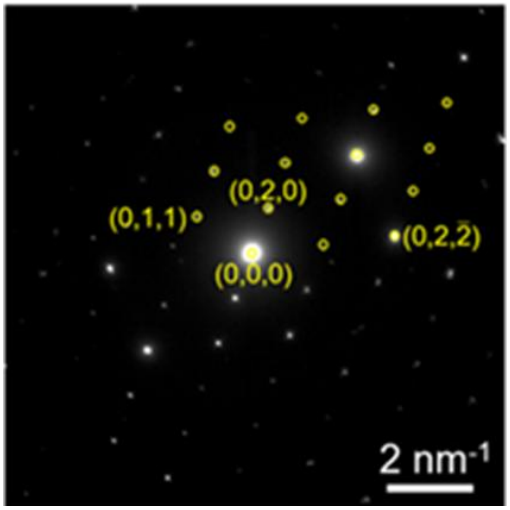

Fitted lattice parameters
in P-1 structure

a=11.0 Å
b=18.4 Å
c=6.8 Å
α=82.8°
β=82.6°
γ=95°

Appendix 11: SAED-pattern along the [100] zone axis of the KVP/C lattice (left) and the lattice parameters determined by SAED for a triclinic space group P-1 (right). Some of the simulated reflections obtained with the P-1 structure are indicated with yellow circles in the SAED-pattern.

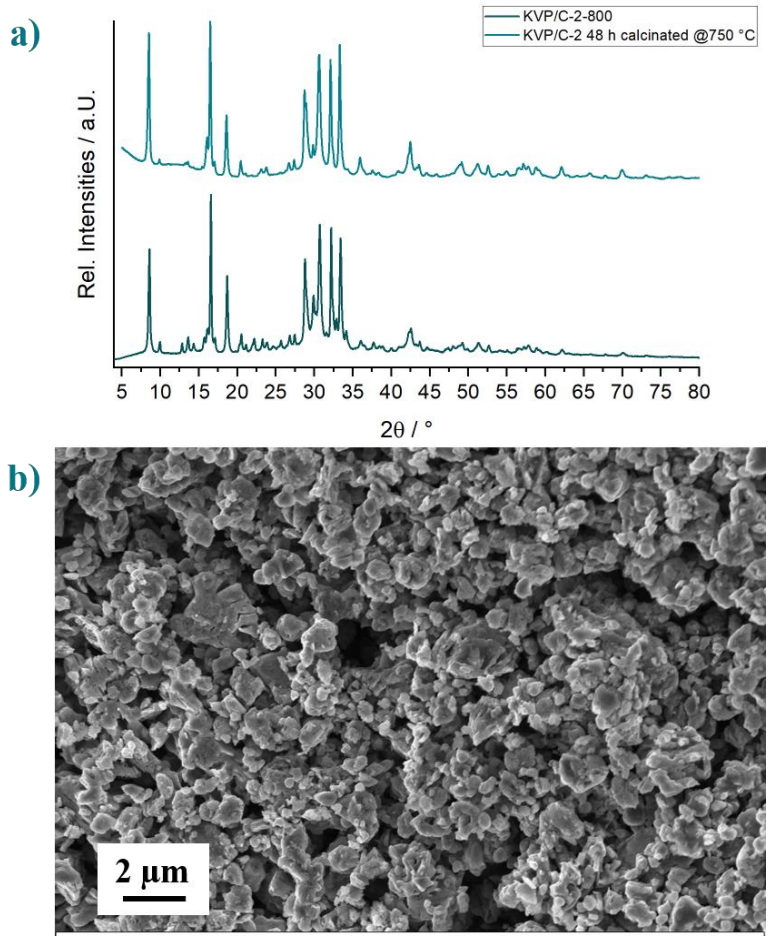

Appendix 12: a) Collected XRD pattern of large primary particles of KVP/C-2 calcinated for 48 h at 750 °C under Ar + 3 % H_2-atmosphere and KVP/C-2-800 granules, b) SEM images large primary particles of KVP/C-2 calcinated for 48 h at 750 °C under Ar + 3 % H_2-atmosphere.

Appendix 13: K:V:P ratio in wt. % of the KVP/C-2 composites based on an ICP-OES analysis.

Composite	**K** / **wt. %**	**V** / **wt. %**	**P** / **wt. %**
KVP/C-2	20.3 ± 0.2	17.9 ± 0.1	16.5 ± 0.1

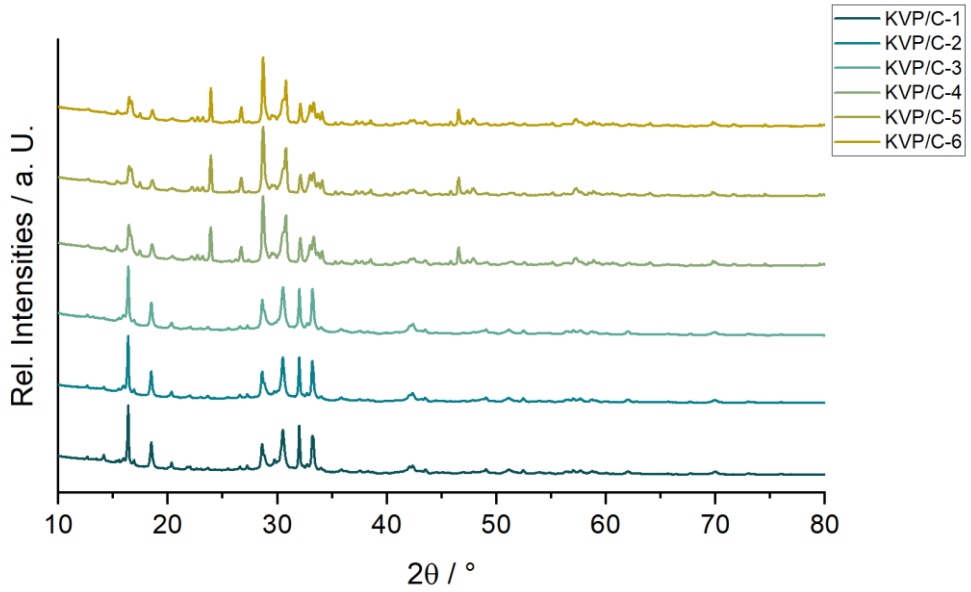

Appendix 14: Collection of all obtained X-ray powder diffraction pattern for the different KVP/C-composites witha) KVP/C-1, b) KVP/C-2, c) KVP/C-3, d) KVP/C-4, e) KVP/C-5, f) KVP/C-6.

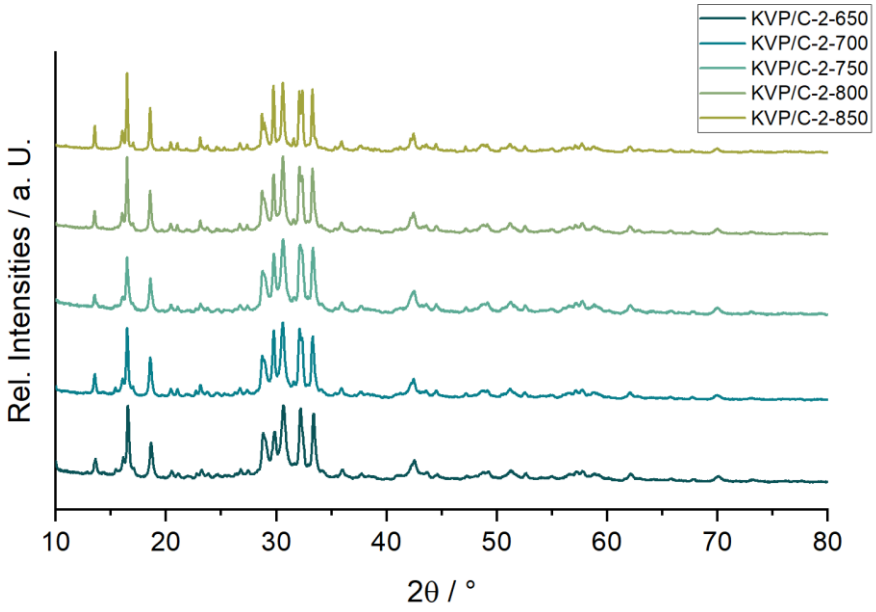

Appendix 15: Collected powder X-ray diffraction pattern of all KVP/C-2 composites sintered at different temperatures with a) 650 °C, b) 700 °C, c) 750 °C, d) 800 °C and e) 850 °C.

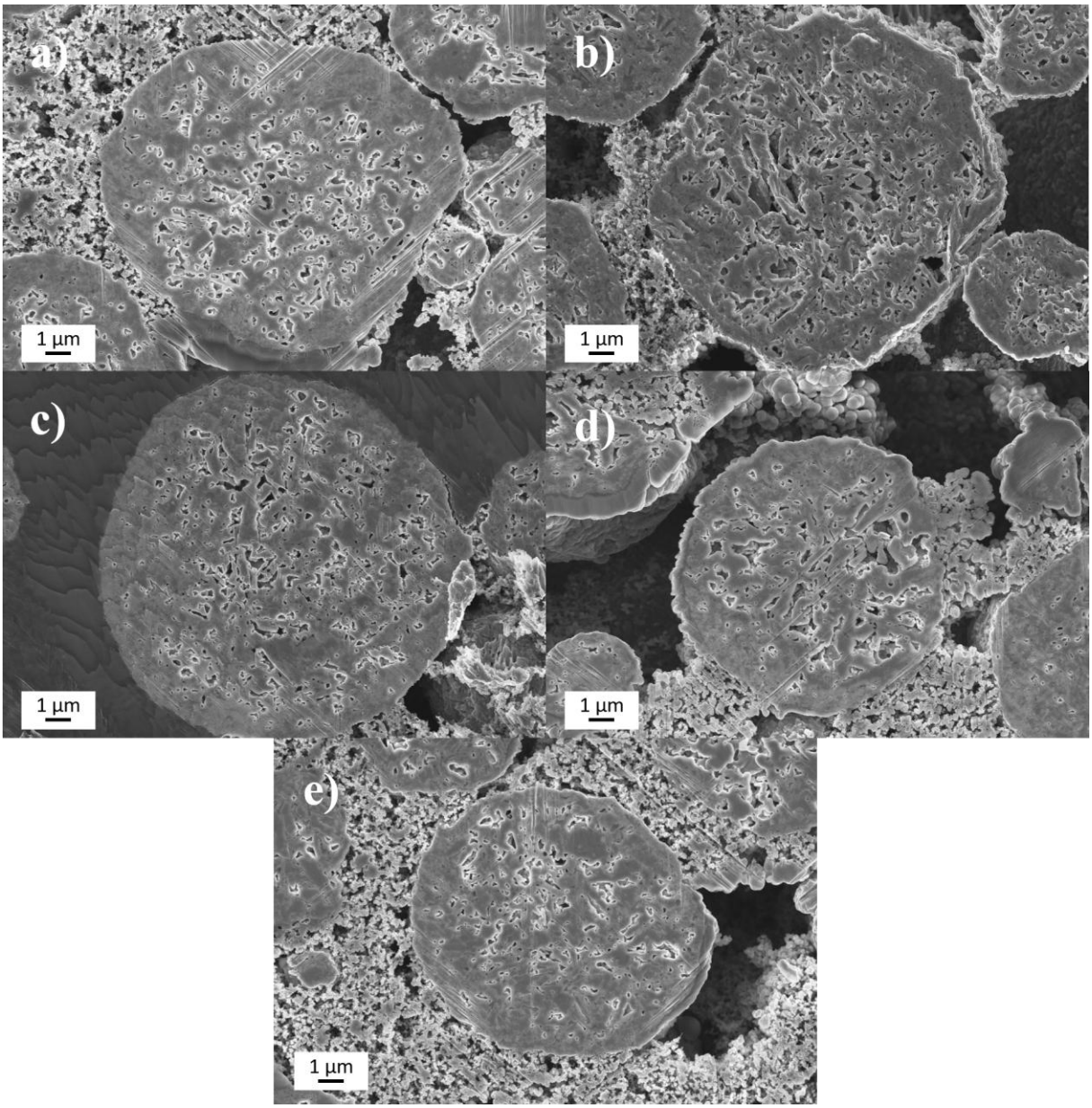

Appendix 16: SEM images of the cross-sections of different KVP/C-2 composites sintered at different temperatures with a) KVP/C-2-650 (650 °C), b) KVP/C-2-700 (700 °C), c) KVP/C-2-750 (750 °C), d) KVP/C-2-800 (800 °C) and e) KVP/C-2-850 (850 °C).

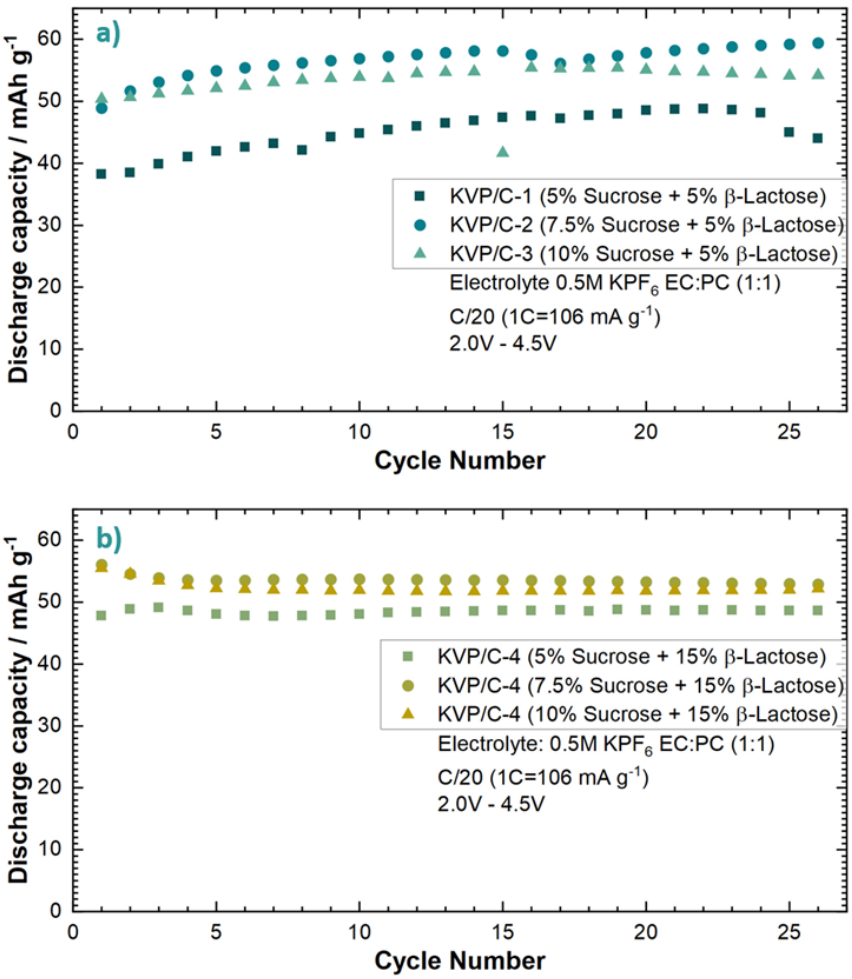

Appendix 17: Specific discharge capacities of KVP/C composites in PIB half-cells at C/20 without the contribution of the residual carbon for a) KVP/C composites with 5 wt. % β-lactose and b) KVP/C composites with 15 wt. % β-lactose, reproduced from Heyn et al.[132]

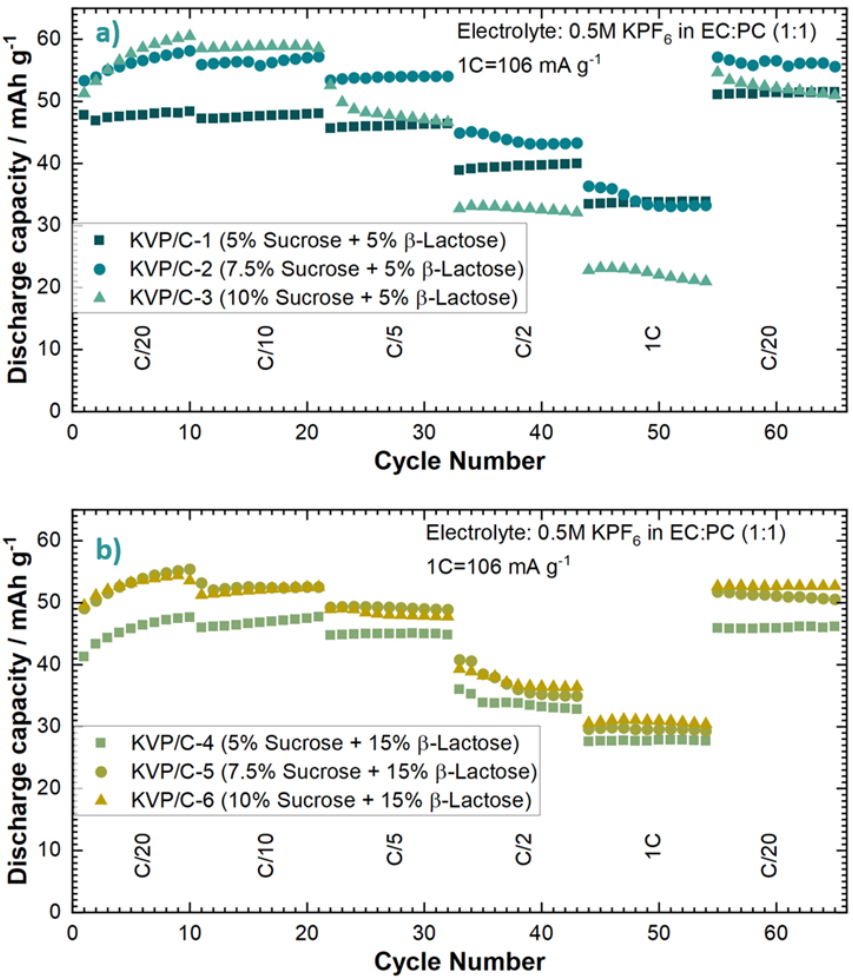

Appendix 18: C-Rate capability test of different KVP/C composites in PIB half-cell without the contribution of the residual carbon for a) KVP/C composites with 5 wt. % β-lactose and b) KVP/C composites with 15 wt. % β-lactose, reproduced from Heyn et al.[132]

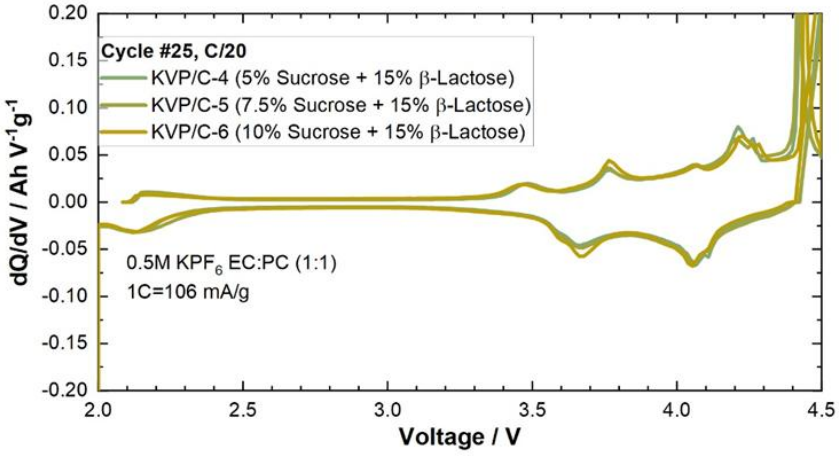

Appendix 19: dqdV-plot of KVP/C composites with 5 wt. % β-lactose in PIB half-cells at C/20 in the 25th cycle, reproduced from Heyn et al. [132]

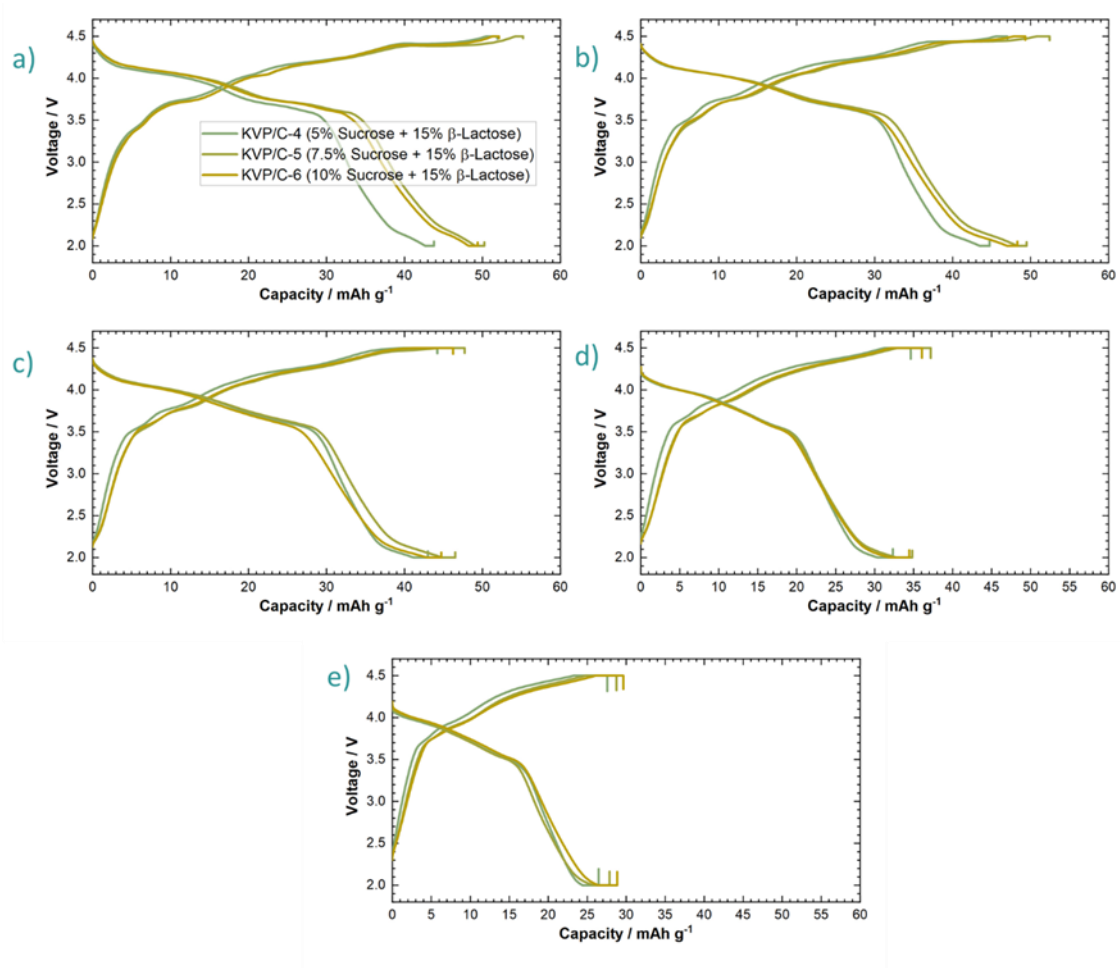

Appendix 20: Potential profiles of KVP/C composites with 15 wt.% of β-lactose in PIB half cells at different C-Rates in the 5th cycle at each C-rate. a) C/20, b) C/10, c) C/5, d) C/2 and e) 1C. 1C=106 mA g^{-1}, adapted from Heyn et al.[132]

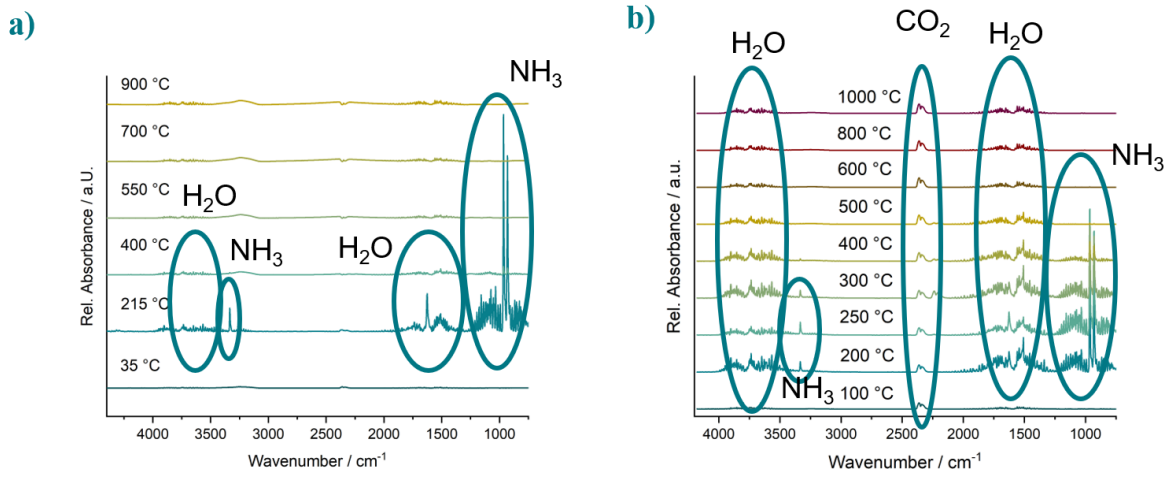

Appendix 21: Corresponding IR-sepctra collected during thermal analysis of the KVPO precursors a) VPO_4 and b) $VOPO_4$. CO_2 and continuous release of H_2O is caused by residual ambient atmosphere inside the gas IR-measurement cell.

Appendix 22: Onset temperature, weight losses and supposed decomposition products or reaction processes for the synthesis of the VPO_4 precursor based on TG/DSC-IR analysis.

Onset Temperature / °C	**Weight loss / %**	**Decomposition product / Reaction process**
200	29.2	NH_3, H_2O
650	-	Crystallization VPO_4

Appendix 23: Onset temperature, weight losses and supposed decomposition products or reaction processes for the synthesis of the $VOPO_4$ precursor based on TG/DSC-IR analysis.

Onset Temperature / °C	**Weight loss / %**	**Decomposition product / Reaction process**
200	31.4	NH_3, H_2O
300	-	Formation of intermediate reaction compounds
600	-	Crystallization of β-$VOPO_4$
600	0.8 (Mass gain)	
800	0.9	
820	-	Phase transition of $VOPO_4$ or further transition to high temperature phases in V:P:O system

Appendix 24: Onset temperature, weight losses and supposed decomposition products or reaction processes for the comproportionation reaction of KVPO based on TG/DSC-IR analysis.

Onset Temperature / °C	**Weight loss / %**	**Decomposition product / Reaction process**
150	1.9	CO_2, H_2O
300	9.1	Decomposition K_2CO_3, CO_2
650	-	Crystallization of $KVOPO_4$
850	-	Melting of $KVOPO_4$

Appendix 25: ICP-OES analysis of KVPO phase after the comproportionation reaction to determine the K:V:P-ratio in wt. %.

Composite	**K / wt. %**	**V / wt. %**	**P / wt. %**
KVPO	18.4 ± 0.1	25.3 ± 0.1	15.5 ± 0.1

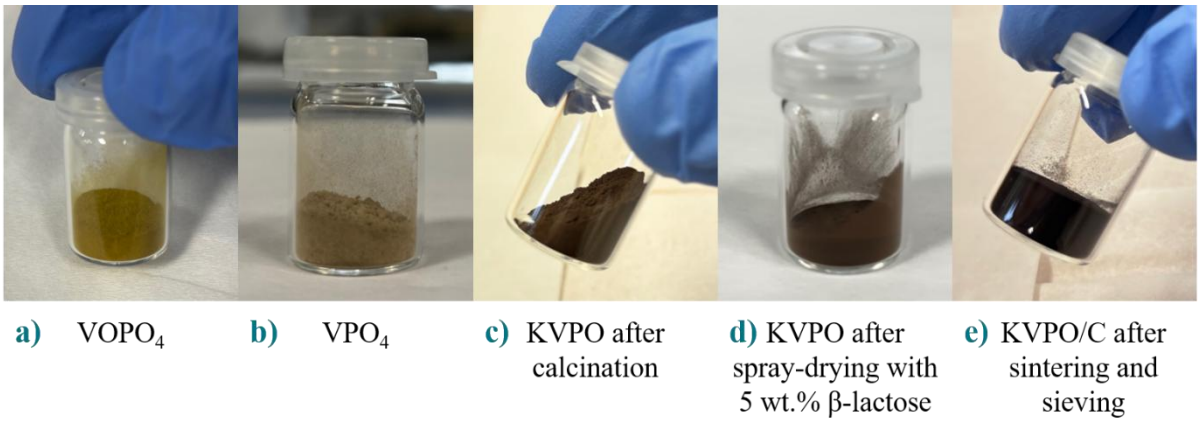

Appendix 26: Powder samples during the synthesis process of hierarchical structured KVPO/C composites with a) the $VOPO_4$ precursor, b) VPO_4 precursor, c) KVPO after the calcination / comproportionation, d) KVPO after spray-drying with 5 wt. % β-lactose and e) KVPO/C composites after completion of the whole synthesis process.

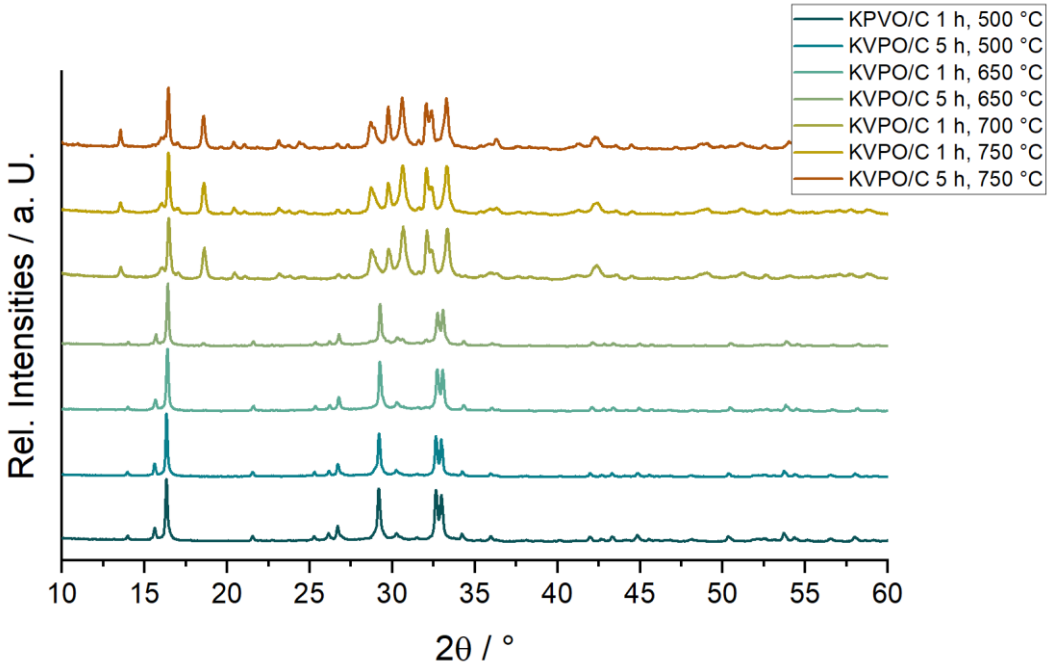

Appendix 27: Powder XRD of KVPO/C composites sintered at different temperatures and for different durations.

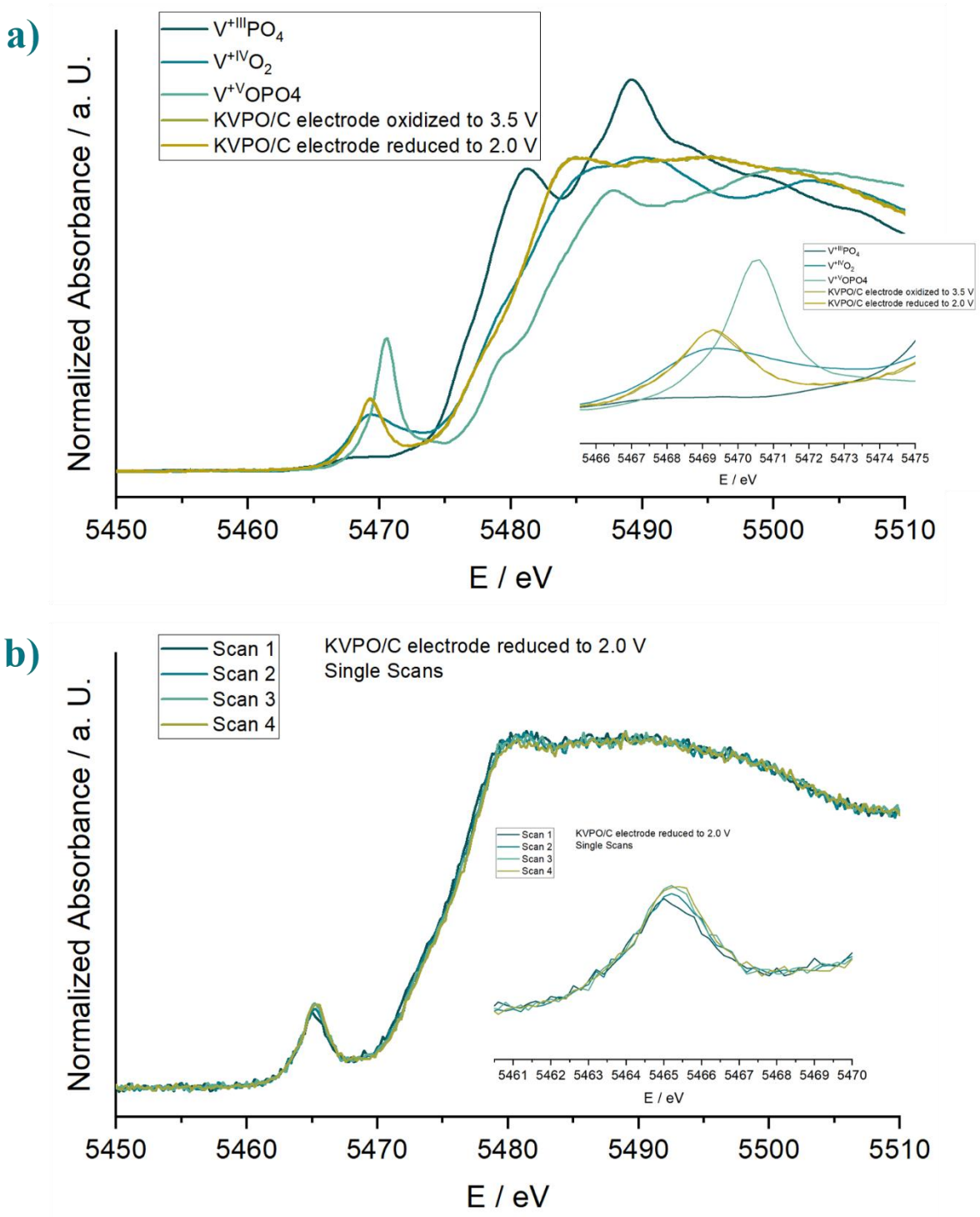

Appendix 28: XAS spectra for a) KVPO/C electrodes reduced to 2.0 V or oxidized to 3.5 vs. K^+/K in a PIB half-cell setup and corresponding references for different valent oxidation states of vanadium, b) single scans for a KVPO/C electrode reduced to 2.0 V vs. K^+/K in a PIB half-cell setup to visualize the stepwise oxidation of the KVPO/C during the measurement due to the contact with the ambient atmosphere.

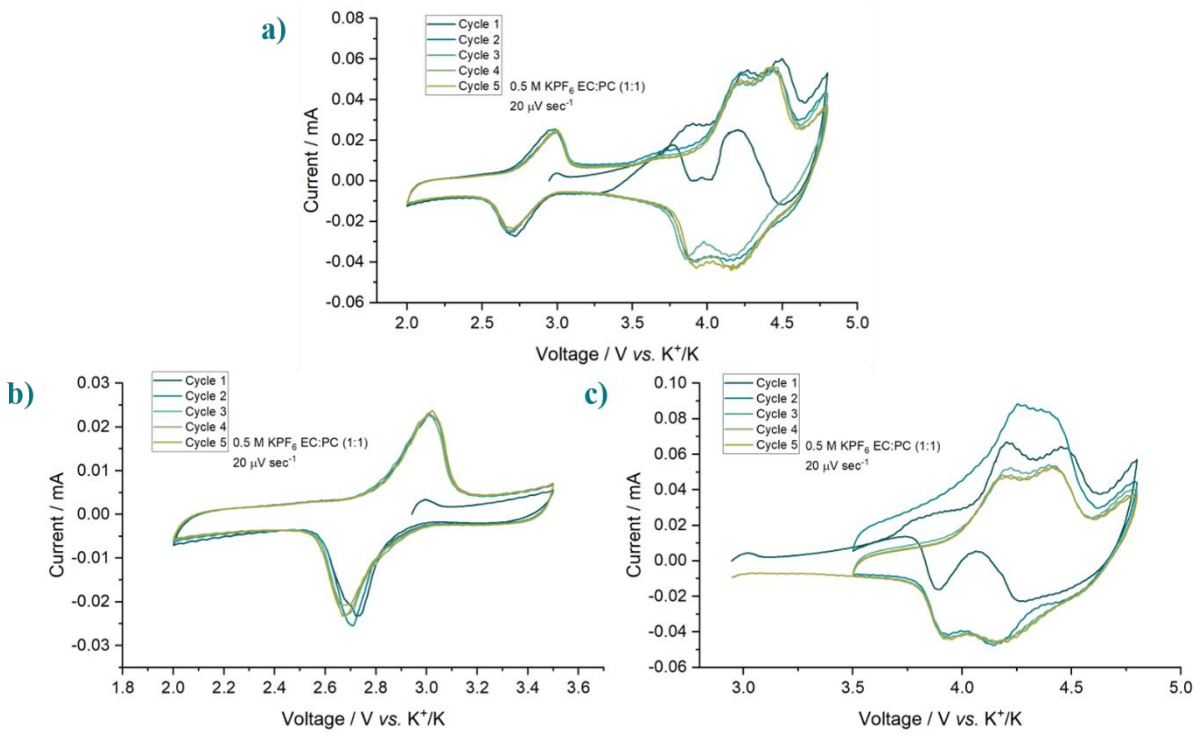

Appendix 29: CV measurements of KVPO/C composites in a conventional PIB half-cell setup with a scan rate of 20 µV sec^{-1} and in different voltage ranges: a) 2.0 V – 4.8 V, b) 2.0 V – 3.5 V, c) 3.5 V – 4.8 V. As an electrolyte 0.5 M KPF_6 in EC:PC (1:1) was used.

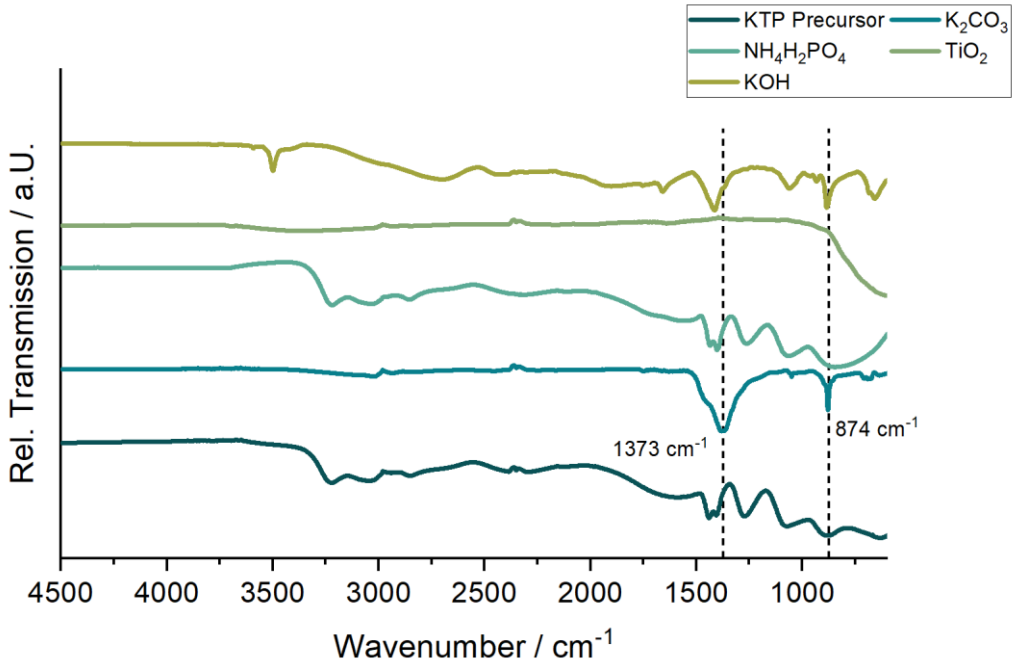

Appendix 30: FT-IR measurement on powders of the prepared KTP precursor and the used reactants additional with KOH

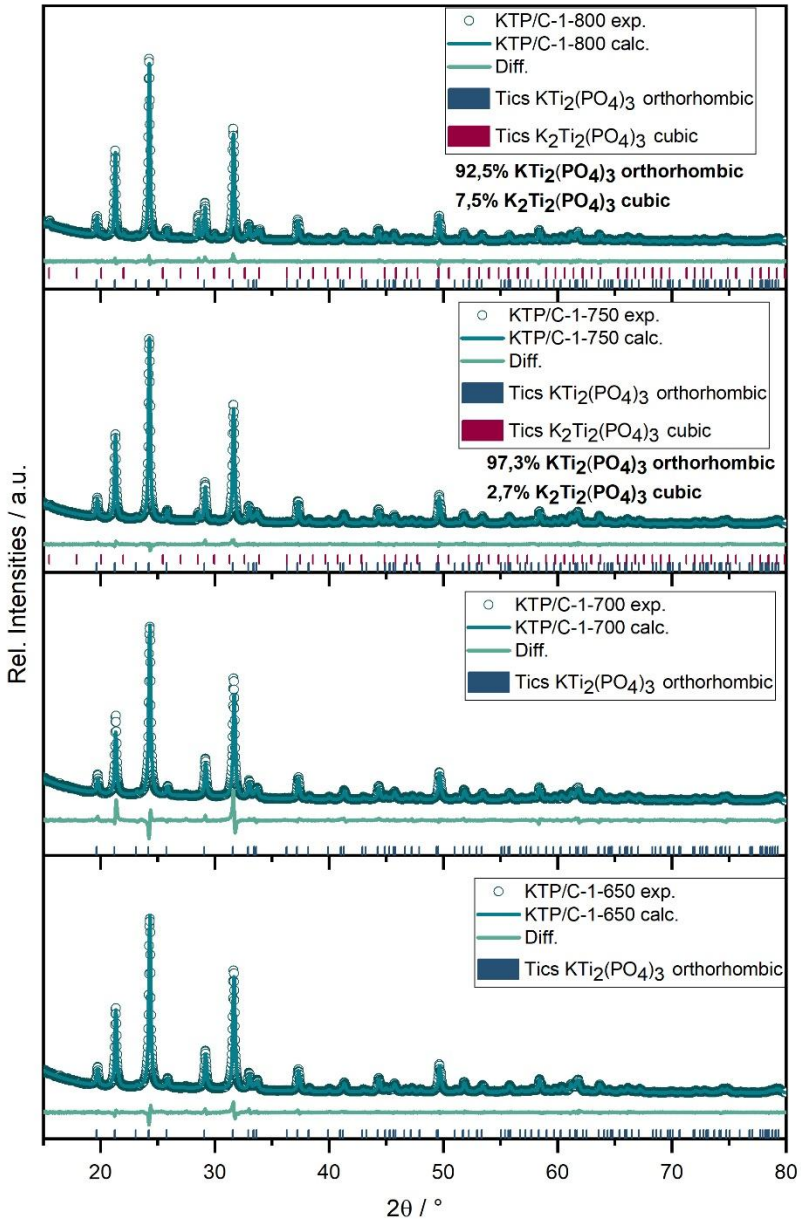

Appendix 31: Powder XRD pattern with performed Rietveldt-refinement for KTP/C composites sintered at different temperatures with the sintering temperatures ranging from 650 °C – 800 °C with 50 °C steps in between

Appendix 32: Onset temperature, weight losses and supposed decomposition products or reaction processes for the comproportionation reaction of KTPO/C based on TG/DSC-IR analysis.

Onset Temperature / °C	**Weight loss / %**	**Decomposition product / Reaction process**
100	13.6	CO_2, H_2O
300 - 850	1.7	CO_2
620	-	Crystallization of $KTiOPO_4$
850	4.5	Decomposition of $KTiOPO_4$

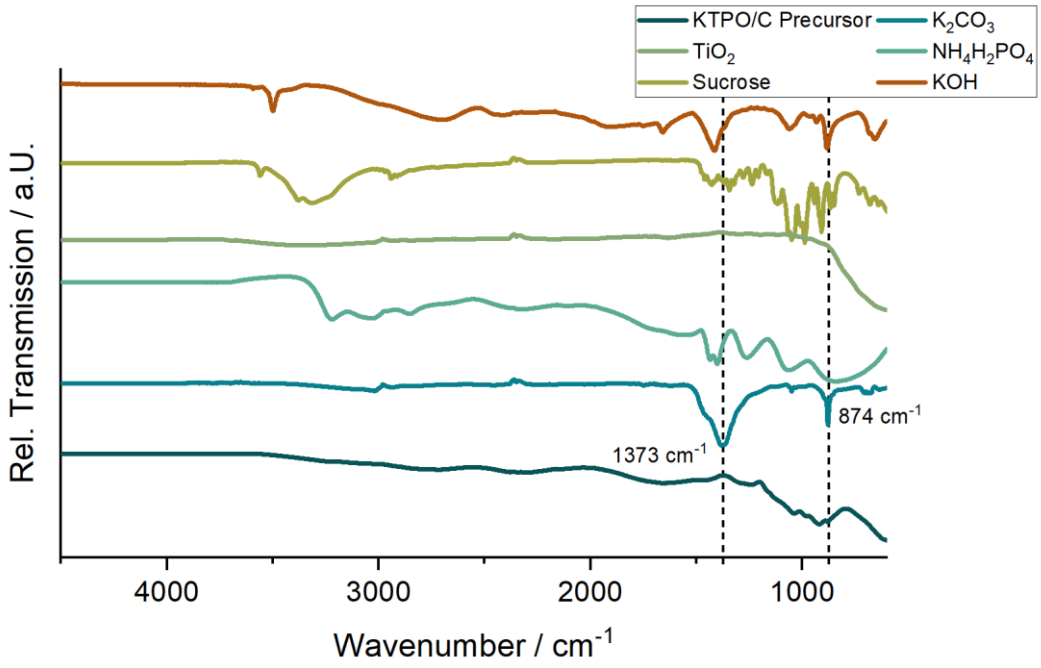

Appendix 33: FT-IR measurements on powders of the prepared KTPO/C precursor and the used reactants with additionally KOH.

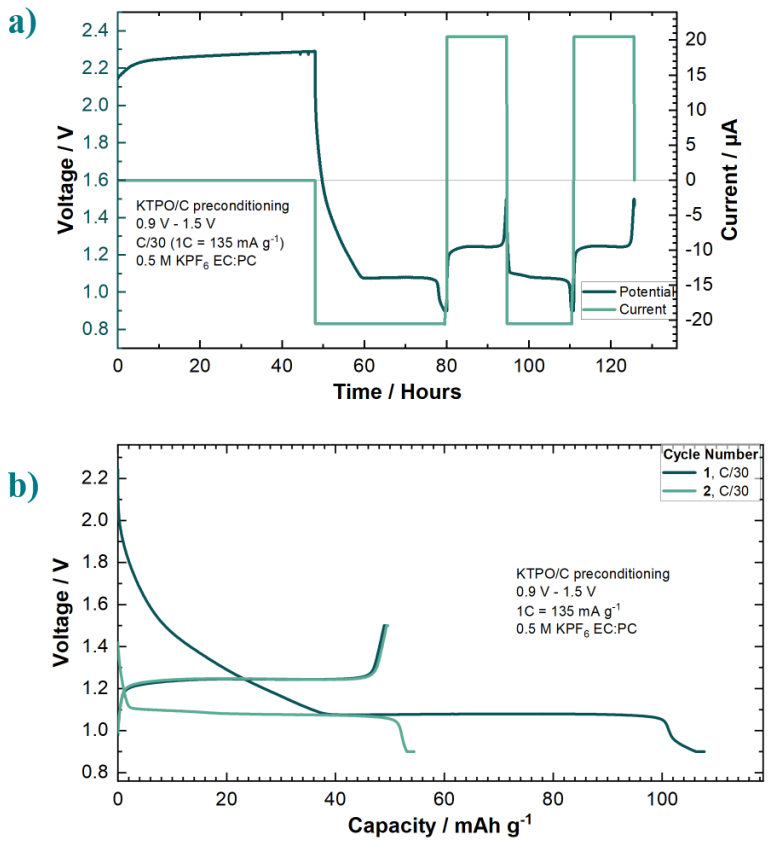

Appendix 34: Preconditioning procedure for the KTPO/C composite for its use as a diagnostic electrode. The KTPO/C composite was cycled in PIB half-cell for 2 cycles between 0.9 V – 1.5 V at C/30. As an electrolyte 0.5M KPF_6 EC:PC (1:1) was used.

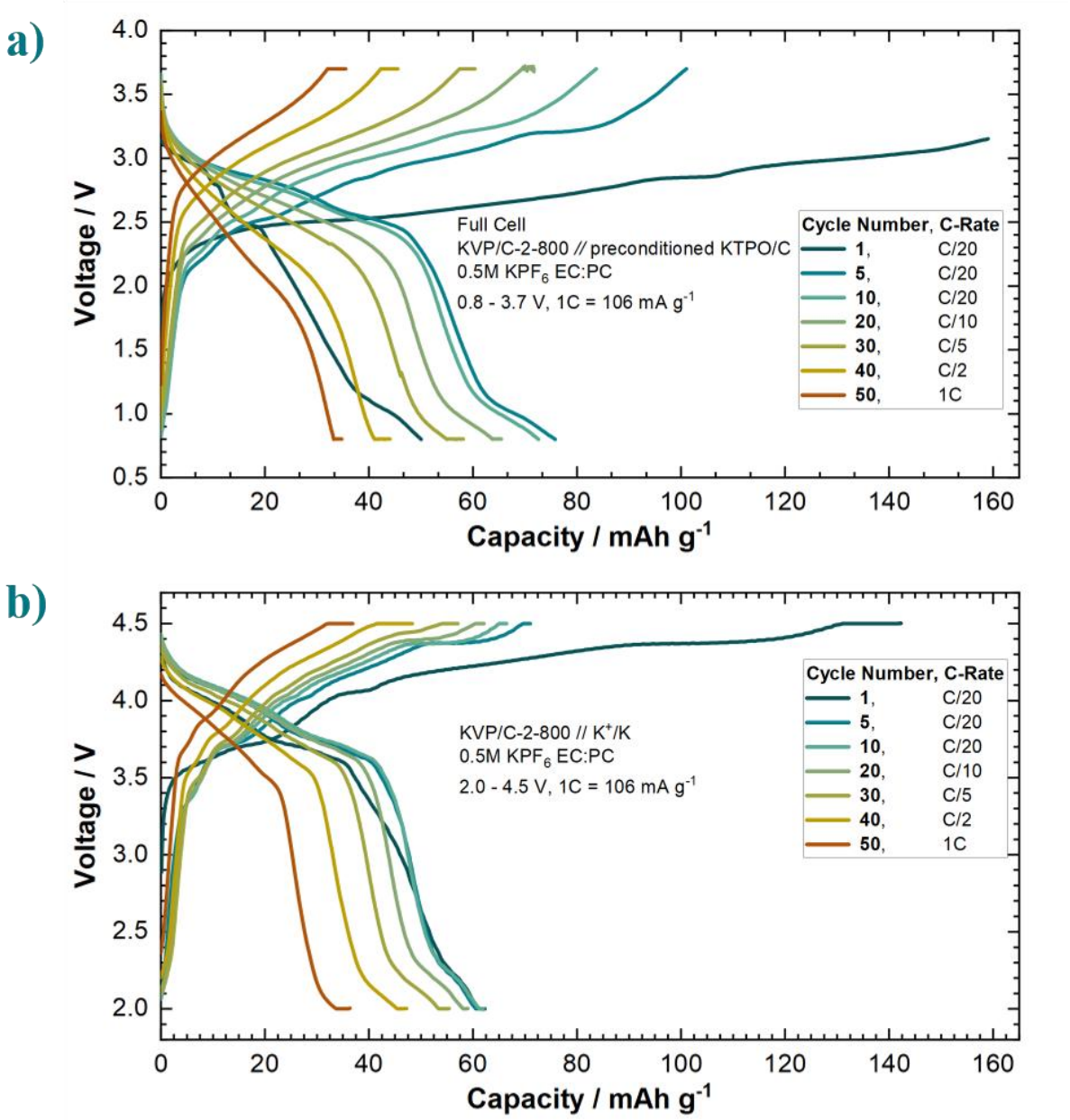

Appendix 35: Comparison of voltage profiles during C-rate capability test of a KVP/C-2-800 WE in a) a full-cell setup versus a preconditioned KTPO/C DE and b) a conventional half-cell setup versus a potassium metal CE.

Appendix 36: ICP-OES analysis on the two Ti-based electrode materials to determine the K:Ti:P-ratio in wt. %.

Composite	**K** / **wt. %**	**Ti** / **wt. %**	**P** / **wt. %**
KTP	9.7 ± 0.05	22.1 ± 0.1	22.0 ± 0.1
KTPO/C	18.8 ± 0.1	23.5 ± 0.1	14.6 ± 0.1

Appendix 37: Exemplary process for the synthesis of KFeOxF according to Pramanik et al.[175]

Mixing	**Reaction**	**Filtration & Washing**	**Ball milling**	**Ball Milling**	**Electrode Casting**
					
<u>Reactants</u> K_2CO_3 $H_2C_2O_4$*2 H_2O KBF_4 FeC_2O_4*2 H_2O **Molar Ratio (top to bottom):** 1:3:2:4	With H_2O 180°C 48h	2 times with Ehtanol and H_2O	Dry 15 min with 4* 10mm steel balls 400 rpm	Dry with C65 AM:C65 2:1 15 min with 4* 10mm steel balls 400 rpm	Casting onto C-coated Al-foil **AM:C:PVDF** **60:30:10**

List of Publications

a. Paper

Heyn, A., Röder, C., Geßwein, H., Ahmadian, A., Velazquez-Rizo, M., Bohn, N., Jeschull, F. and Binder, J.R., (2025), Hierarchical Microstructured K3V2(PO4)3/C-Composite Electrode for Potassium-Ion Batteries through Scalable Spray-Drying Approach. ChemSusChem 2501111. https://doi.org/10.1002/cssc.202501111

b. Conference Poster & Oral Presentations

Heyn, A., Jeschull, F., Bohn, N., Geßwein H., Panasenko, I. and Binder, J.R., How Reliable Are Potassium Ion Half-Cell Measurements? – Development of a Stable Polyanionic Quasi-Reference Anode for Characterization of High-Voltage Cathodic Materials for PIBs, Electrochemical Society Meeting Abstracts, 2025, MA2025-01, A03: Lithium Batteries and Beyond, https://doi.org/10.1149/MA2025-013171mtgabs

Heyn, A., Jeschull, F., Bohn, N. and Binder, J.R., Hierarchically Structured Potassium-Vanadium-Phosphate/C Composites As Possible High-Voltage Cathodic Materials for Potassium-Ion-Batteries, Electrochemical Society Meeting Abstracts, 2023, MA2023-02, A04: Next-Generation Batteries, https://doi.org/10.1149/MA2023-024560mtgabs

c. Supervised Student Projects

Sostmann. Tabea A., Student Internship (Deepening Project, Chemistry), Syntheses and Electrochemical Characterization of KVOPO4/C-composites as a Cathode Material for Potassium Ion Batteries, IAM-ESS, Karlsruhe Institute of Technology, (2025).

Psille, Joshua A., Master Thesis / Project (Material Science and engineering), Synthese und Charakterisierung von $KTi_2(PO_4)_3$ als Anodenmaterial für K-Ionen-Batterien, IAM-ESS, Karlsruhe Institute of Technology, (2025)